

THÈSE

En vue de l'obtention du

DOCTORAT DE L'UNIVERSITÉ DE TOULOUSE

Délivré par :

Université Toulouse 3 Paul Sabatier (UT3 Paul Sabatier)

Présentée et soutenue par :
Marc Núñez Eroles

Le Lundi 9 Novembre 2015

Titre :

Nanogravure et caractérisation structurale et électronique de rubans de graphène cristallins

---

École doctorale et discipline ou spécialité :
ED SDM: Nano-physique, nano-composants, nano-mesures – COP 00

Unité de recherche :
Centre d'Élaboration des Matériaux et d'Études Structurales (CEMES – CNRS UPR 8011)

Directeur de Thèse :
Erik DUJARDIN

Jury :

Erik DUJARDIN	Directeur de recherche – CEMES, Toulouse	Directeur de thèse
Johann CORAUX	Chargé de recherche – Institut Néel, Grenoble	Rapporteur
Vincent DERYCKE	Chercheur CEA – CEA, Saclay	Rapporteur
Brigitte CAUSSAT	Professeur – LGC, Toulouse	Examinatrice
Hanoko OKUNO	Chercheur CEA – CEA, Grenoble	Invitée
Raúl ARENAL	Chargé de recherche – LMA/INA, Zaragoza	Invité
Eric JOVER	Ministre de l'Éducation Supérieure – Andorre	Invité

Remerciements

Je veux, en premier lieu, remercier Alain Claverie de m'avoir permis d'effectuer mes stages de master 1 et 2, ainsi que mes trois ans de thèse dans ce laboratoire.

Deuxièmement, c'est Erik Dujardin que je tiens à remercier pour m'avoir donné l'opportunité de travailler sur ce sujet qui est maintenant le mien, sujet qui m'a permis de découvrir tant de champs différents de la physique, qui m'a tellement passionné et qui m'a permis de sortir le meilleur de moi. Je remercie Erik aussi pour sa confiance et la liberté de travail de laquelle j'ai bénéficié.

Ensuite, mais pas moins important, je remercie mon jury de thèse, Brigitte Caussat, Raúl Arenal, Hanako Okuno et Eric Jover mais tout particulièrement mes rapporteurs bienveillants Johann Coraux et Vincent Derycke qui, de part leur grande expérience, m'ont aidé à avancer et améliorer mon travail grâce à leur évaluation, corrections, questions, discussions et conseils.

Dono les gràcies al Govern d'Andorra, i en particular, al ministeri d'educació i recerca per haver me permès de fer aquesta aventura durant tres anys amb ells i per haver confiat en mi i el meu projecte de recerca. Per tot això i més dono gràcies à Helena Solé, Margarita Ceña, Meritxell Gallo i un cop més, à l'Eric Jover.

Si cette thèse a pu aboutir à des résultats, interprétations et conclusions satisfaisants, c'est grâce aux nombreuses personnes avec qui j'ai partagé mon temps de manip. Pour tous les rires, pour tout le soutien, pour tout ce qu'ils m'ont appris, aidé et tout le temps qu'ils ont dépensé pour moi, je remercie Philippe Salles, Raphael Laloo, David Martrou, Thierry Ondarçuhu, Olivier Guillermet, Raúl Arenal, Christian Bourgerette ainsi que Christian Girard pour son aide inestimable en plasmonique. Un énorme merci aussi à Maxime Berthe pour les semaines que j'ai passé avec lui, non seulement pour le travail sur le Nanoprobe, mais aussi pour les bières, sa bière, les discussions moto et son enthousiasme envers mes expériences.

Je remercie également Sébastien Gautier, Christian Joachim et Mohamed Hjilwa pour leurs conseils et discussions qui m'ont souvent débloqué. Merci aussi à Etienne Snoeck et TALEM pour m'avoir permis de travailler sur un Titan cube à Zaragoza qui a été d'une aide précieuse et pour les soirées tapas en ville. Je remercie de même Miguel Rubio Roy, Jorge Echeverría et Victor Freire pour leur travail mais aussi pour leur amitié, et pour m'avoir permis de parler en catalan dans mon bureau !

Un tel travail aurait été des dizaines de fois plus dur à accomplir si je n'avais pas compté sur le soutien inestimable de mes plus proches amis d'enfance : Andreu Casal, Roger Ribó et Sergio García qui ont toujours été là, qui m'ont encouragé jusqu'au dernier week-end quelques heures à peine avant ma soutenance ; je les remercie pour toutes les vallées et sommets que nous avons découverts ensemble et les nuits passées en montagne, ma grande passion qui n'aurait jamais été sans eux, tout comme la personne que je suis devenu.

Audrey, comme dit dans d'autres remerciements, tu as été le peps de ce laboratoire et de notre groupe. Toujours joyeuse et prête à déconner et à rigoler, il n'est pas toujours facile d'être comme ça et de garder la bonne humeur, mais avec toi cela a été bien plus simple, merci.

Roman, j'ai énormément apprécié le temps que j'ai passé avec toi, à faire de la moto, à rigoler, à randonner (à moins que ce ne soit randonnerer, ou randonnater …) à boire, à discuter, à faire des cochons au tournebroche et merci aussi pour ton hospitalité qui m'a beaucoup touché.

Agnès, merci à toi pour ton soutien sans faille, pour tes encouragements, pour remonter mon moral, pour être toujours là quand on a besoin d'un coup de main. Pour montrer qu'on peut faire beaucoup avec un sourire et un bonjour, et surtout parce que tu donnes l'envie à tout le monde d'être gentils et généreux comme toi.

Je remercie tous les autres chercheurs, doctorants, ingénieurs, pas ingénieurs, pour les bons moments, les discussions productives, les rires et les bêtises, en particulier Julien Dupré de Baubigny, Loranne Vernisse, Guru Kargal, Alexandre Teulle, Sviatlana Viarbitskaya, Agathe Fournier, Olivier Couturaud, Marie Hervé, Julien Coen, Xavier Bouju, Véronique Langlais, Christine Viala, André Gourdon, Jacques Bonvoisin, Claire Kammerer, Christophe Collard, Clémence Vidal, Rémi Arras, Romain Garbage, Romain Carru, Sébastien Joulié, Pascal Païva, Miguel Cortijo, Caroline Mortagne, Delphine Sordes, Benoit Eydoux, Cristina Mattioli et tous ceux que j'oublie…

Ma passion légendaire pour l'écriture et la rédaction me portent à mettre un terme à ces remerciements, qui de toute façon ne seront jamais suffisamment complets, en te remerciant toi, maman, pour t'être toujours inquiétée pour moi (peut-être même trop …) pour m'avoir soutenu et pour m'aimer si fort.

"One must conquer, achieve, get to the top […]
to know there's no dream that mustn't be dared.

Have we vanquished an enemy?
None but ourselves.

To struggle and to understand
Never this last without the other;
such is the law. . ."

George Leigh Mallory

Contents

Introduction..... 7

Chapter 1. Aim and context..... 9

1.1. History of graphene..... 9
1.2. Graphene properties..... 13
1.2.1. Structural properties and electronic bands of graphene..... 13
1.2.2. Electronic transport in graphene..... 16
1.3. Graphene Nanoribbons..... 18
1.3.1. Structural properties of graphene nanoribbons..... 18
1.3.2. Electronic structure of graphene nanoribbons..... 19
1.4. Experimental background..... 22
1.4.1. Graphene patterning techniques..... 22
1.4.2. Electronic transport measurements of GNR..... 28
1.5. References..... 33

Chapter 2. Sample fabrication and experimental Methods..... 37

2.1. Graphene sources and sample preparation..... 37
2.1.1. Starting material..... 37
2.1.2. Transfer of CVD graphene..... 39
2.1.3. Samples for TEM experiments..... 41
2.1.4. Sample fabrication for devices..... 42
2.1.5. Samples for STM in Ultra High Vacuum..... 43
2.1.6. Decontamination annealing..... 44
2.2. Scanning Electron Microscopy and Gas Injection System..... 46
2.2.1. Scanning Electron Microscope..... 46
2.2.2. Oxygen injection system..... 47
2.3. Structural analysis..... 49
2.3.1. Transmission Electron Microscope..... 49
2.3.2. Raman spectroscopy and mapping..... 51
2.3.3. Atomic Force Microscope..... 51
2.4. Cryo-magnetotransport..... 51
2.4.1. Device fabrication..... 51
2.4.2. Setup..... 53
2.4.3. Cryo-magnetotransport Measurements..... 54
2.5. References..... 55

Chapter 3. GNR fabrication by oxygen assisted e-beam etching..... 57

3.1. Electron Beam Induced Etching process..... 57
3.1.1. Principles..... 57
3.1.2. Water-induced etching on graphene..... 61
3.1.3. Oxygen-induced etching on graphene..... 63
3.1.4. Dose characterization..... 65
3.2. Making graphene nanoribbons..... 66
3.3. High Resolution structural analysis..... 69

3.3.1. High Resolution TEM imaging of simple EBIE cuts..... 69
3.3.2. Structural analysis of graphene nanoribbons..... 72
3.4. Discussion..... 74
3.5. Conclusion..... 77
3.6. References..... 78

Chapter 4. Electronic transport characterization of graphene nanoribbon devices... 79

4.1. Device fabrication and properties..... 79
4.1.1. Applying e-beam induced GNR cutting to device fabrication..... 79
4.1.2. Amorphization induced by backscattered electrons..... 82
4.1.3. Graphene devices over deep pools..... 90
4.2. Electronic transport properties measurements..... 92
4.2.1. Temperature dependence of nanoribbon conductance..... 92
4.2.2. Field effect in GNR devices..... 92
4.2.3. Magneto-transport..... 97
4.3. Discussion and Perspectives..... 99
4.4. Conclusion..... 100
4.5. References..... 102

Chapter 5. UHV-4probe STM study of graphene and graphene nanoribbons 103

5.1. 4-probe UHV-STM set up and samples..... 103
5.2. UHV-STM analysis of basal adsorption on graphene..... 107
5.3. Graphene SEM imaging under UHV and electrical annealing..... 110
5.4. Graphene electronic transport on dual-ribbon device..... 113
5.5. Conclusion..... 120
5.6. References..... 121

Conclusion and perspectives..... 123

Nomenclature..... 127

Annexe 1: Towards graphene/gold hybrid plasmonic systems..... 129

Annexe 2: Raman spectra of different graphene sources and transfer techniques..... 141

Résumé de la thèse..... 143

Introduction

Electronic devices of today's technology are based on silicon semiconductors. As processors power grows, their components are more and more miniaturized. As an example, most recent transistors are reduced to the limit, where the active zone measures ten nanometres. At those sizes a barrier is encountered when trying to keep reducing sizes. The physics dominating the phenomena at the nanometre size and below are the quantum mechanics. Indeed, if the evolution in electronics and its components is to keep reducing devices size, a new concept of components based on quantum mechanics has to be build up. The work presented in this manuscript is meant to contribute to a new technologic concept. Graphene has been shown to have particularly high electron mobility characteristics and give easy access to a 2-dimensionnal electron gas. Pristine graphene has a metallic behaviour, but the modification of its electronic states can lead to more complex functions. The structural modification of graphene will most probably reduce the mobility, starting with very high mobility material can allow to produce lower, but still high mobility devices. One way to modulate the electronic properties is to change the geometrical characteristics of a graphene sheet. There is still though a need for a technique that allows to pattern graphene while preserving its crystallinity and that is precise enough to apply modifications at the atomic scale. We present in this manuscript a graphene etching process where we propose to combine an electron beam to control the shape that triggers a chemical reaction giving crystalline directions affinity to reach atomic precision. The objects we chose to produce and analyse are graphene nanoribbons. Theoretically, when the two-dimensional electronic gas of the graphene is confined in a one-dimensional channel, the electrons transmitted through are subject to a similar effect than an electron confined in a box. As the confinement gets stronger, and the box smaller, the electron cannot access to an energy continuum anymore and the energy spectrum turns into discrete states. The effect in graphene would be the transition from continuous density of states at the Fermi level characteristic of metals to a non-continuous DOS where the states depend on the constriction properties, like width, defects, and edges. To the date no work has presented a patterning process for graphene device fabrication with electronic transport measurements of low disorder graphene nanoribbons. The manuscript is divided in six chapters.

In Chapter 1, graphene will be introduced and its main characteristics will be described as well as the theoretical properties of graphene nanoribbons. In

addition we will present the main patterning techniques of graphene and process to obtain nanometric ribbons. Furthermore some recent studies of electronic transport measurements through graphene nanoribbons will be summarized.

Chapter 2 is the experimental methods section. The equipment used in this work will be presented as well as techniques to produce CVD and exfoliated graphene, to pattern graphene and to characterize the structural properties down to the atomic resolution microscopy and the electronic properties by cryo-magnetotransport measurements.

The Electron Beam Induced Etching technique is presented in Chapter 3 as well as the structural analysis of EBIE-patterned graphene nanoribbons by Spherical Aberration Corrected Transmission Electron Microscopy (SACTEM). The analysis will focus on the crystallinity, edges arrangement as well as possible amorphization of the nanoribbon.

The Chapter 4 presents the transfer of the technology presented in chapter 3 to substrates for electronic transport measurements on suspended graphene nanoribbons. The electronic cryo-magnetotransport measurements of the graphene nanoribbon devices are also presented in this section. In particular, we will investigate the temperature, filed effect and magnetic dependency of the GNR conductance.

Chapter 5 gathers preliminary work on the next level of control of graphene-based technology at small dimensions. In this section graphene will be studied with a 4-probe Ultra High Vacuum Scanning Tunnelling Microscope. The devices are patterned by the EBIE technique developed and analysed on the previous chapters. We will focus on three aspects: the effect of Scanning Electron Microscopy on graphene in UHV environment compared to secondary vacuum, graphene decontamination, and finally some electronic transport measurements performed with two STM tips through a graphene crossed ribbon device.

Chapter 1

Aim and Context

CONTENTS

1.1 HISTORY OF GRAPHENE 9
1.2 GRAPHENE PROPERTIES 13
1.2.1 Structural properties and electronic bands of graphene 13
1.2.2 Electronic transport in graphene 16
1.3 GRAPHENE NANORIBBONS (GNR) 18
1.3.1 Structural properties of graphene nanoribbons 18
1.3.2 Electronic structure of Graphene Nanoribbons 19
1.4 EXPERIMENTAL BACKGROUND 22
1.4.1 Graphene patterning techniques 22
1.4.2 Electronic transport measurements of GNR 28
1.5 REFERENCES 33

1.1 History of graphene

Graphene is defined as a single layer of carbon atoms in a hexagonal honeycomb lattice and corresponds to a single layer of graphite. The history of graphene originates in the history of graphite. Graphite is a carbon crystalline conductor. Known since 1789, its atomic structure was potentially elucidated by W. L. Bragg in 1914 who measured the cleavage planes spacing in graphite by X-ray diffraction and found it to be 3.42 Å[1]. P. Ewald took a Laue photograph perpendicular to the crystal plane the same year, confirming the hexagonal symmetry of the planes. Two years latter, P. Debye and P. Scherrer fully determined the graphite structure by X-ray measurements[2].



Figure 1.1: From left to right, William L. Bragg, Peter Debye and Paul Scherrer

In 1924, J. D. Bernal solved the structure of graphite by single crystal diffraction of X-ray and he proposed an AA'AA' stacking of hexagonal arranged carbon atoms planes[3] (Figure 1.2).

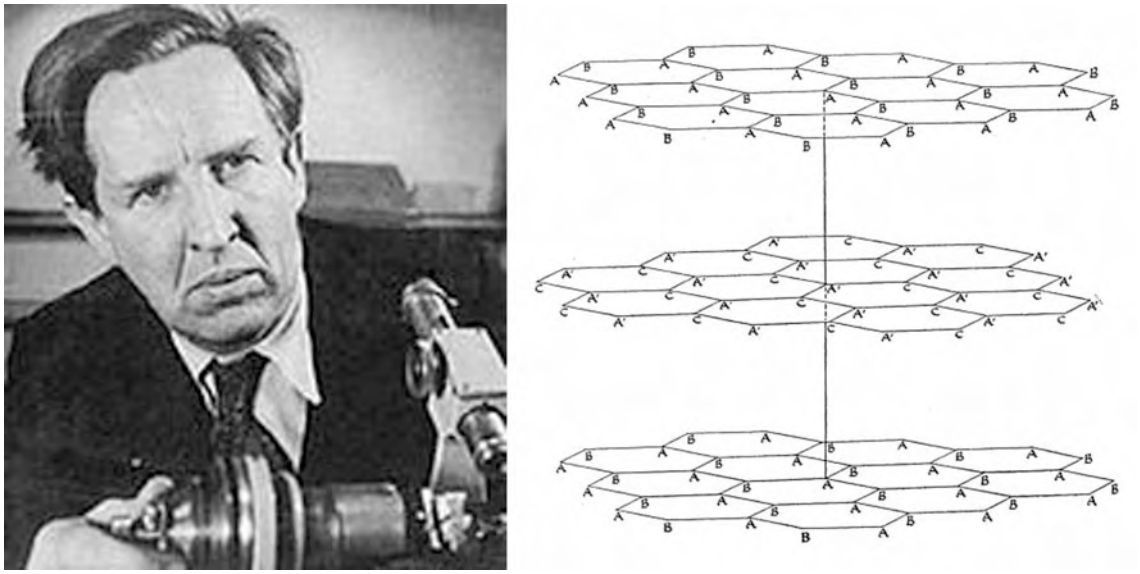


Figure 1.2: John Desmond Bernal and the graphite atomic arrangement determined by X-ray single crystal diffraction. Scheme adapted from [3].

While theoretically investigating the properties of graphite, P. R. Wallace introduced, in 1947, graphene as the basic unit constitutive of graphite. At the time, graphene was not though to exist by itself but a mere view of mind. Wallace defined the primitive cell (Figure 1.3a), the first Brillouin zone (Figure 1.3b) and used it to calculate, for the first time, electronic bands of graphene[4]. In so doing he also noted the linear dispersion relation around what we now call the Dirac points.

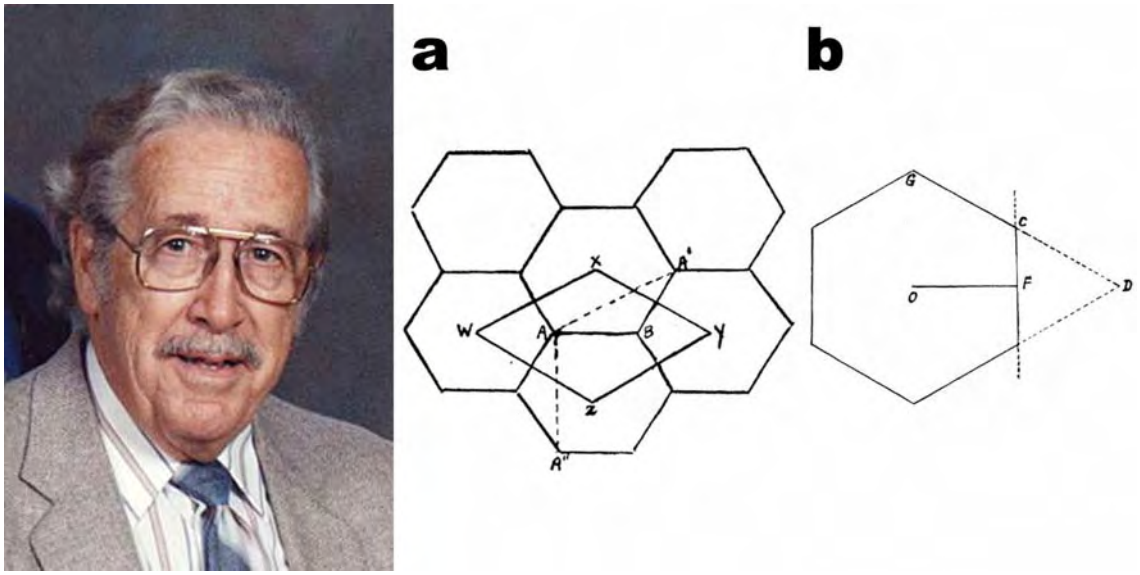


Figure 1.3: Phillip Russell Wallace, graphene scheme of primitive cell (a) and first Brillouin zone (b) adapted from [4].

In 1956, J.W. McClure published the wave propagation equation for excitations in graphene[5]. The similarity to the Dirac equation was then discussed in 1984 by G.W. Semenoff[6] (see also DiVincenzo and Mele[7]).

In 1970-2000 decades a big scientific endeavour was focused on producing insulated single-layer graphene[8]. Graphene single layer was observed by epitaxial growth on top of other materials such as silicon carbide[9-13], platinum carbide[14], tantalum carbide[15, 16], boron nitride[17] or titanium carbide[18]. In addition, single-walled carbon nanotubes had also been observed and analysed[19-21]. In 2004 A. Geim and K. Novoselov transferred monolayer graphene on oxidized silicon substrates[22]. They used a technique to cleave graphite successively on a piece of tape to reduce its thickness. This technique was used before for specimen analysis on electron microscopy in 1960[23]. The crucial difference is that a silicon substrate with a thin silicon dioxide layer on top would create optical interferences making mono-atomic layers of graphite identifiable by optical microscopy[24]. In their work they had shown how monolayers were deposited and measured by Atomic Force Microscopy (Figure 1.4a).

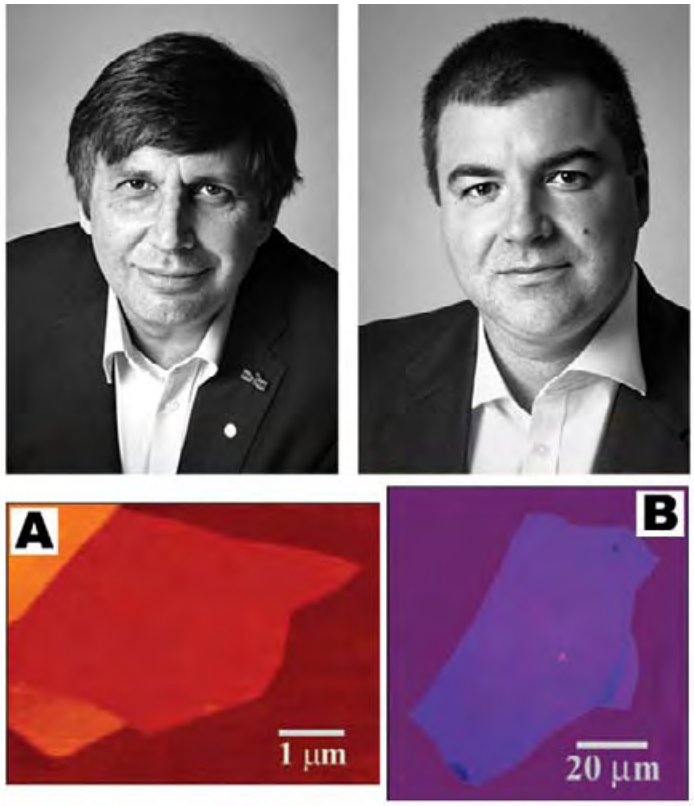


Figure 1.4: Upper left: Andre Geim, Upper Right: Konstantin Novoselov and their first published graphene single layer deposited by the tape technique on silicon dioxide on silicon substrates observed by (a) AFM and (b)optical microscopy. Adapted from [22].

The next year, in 2005, Geim and Novoselov as well as Philip Kim published the first experimental results evidencing the Dirac fermions [25, 26] and the ballistic behaviour of electronic transport in graphene.

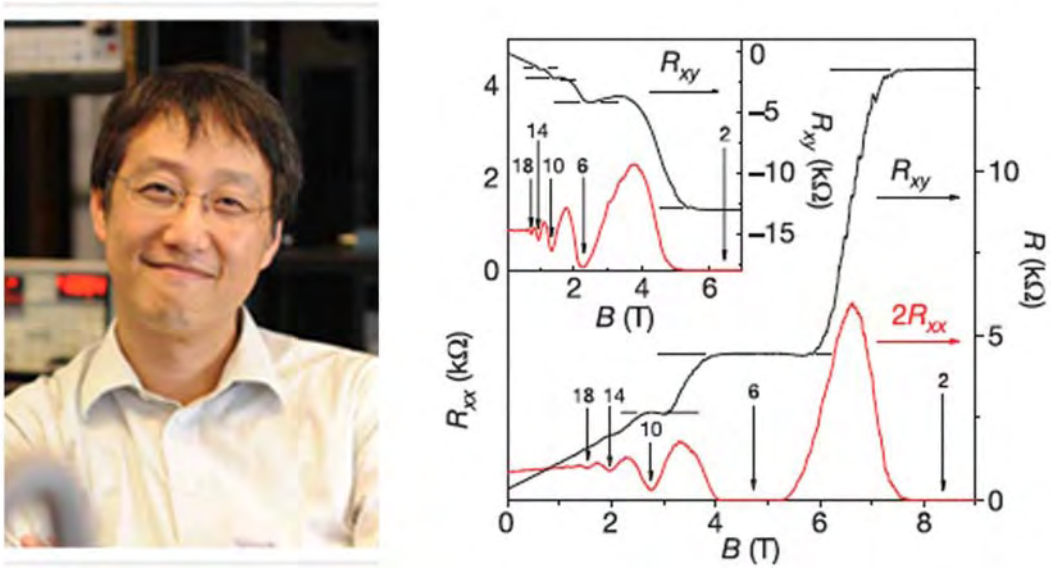


Figure 1.5: Upper left: Philip Kim, and his measurements of QHE in monolayer graphene. Adapted from [26].

As graphene was easier to produce than GaAs, cheaper and also presenting ballistic electronic transport, scientists around the world focused their attention on using this material.

1.2 Graphene properties

1.2.1 Structural properties and electronic bands of graphene

The hexagonal honeycomb lattice of graphene is shown in Figure 1.6a. The external electronic configuration corresponds to an s orbital and three p orbitals. The s orbital and the two in-plane p orbitals hybridize to form three sigma in-plane sp^2 molecular orbitals (Figure 1.6b). Those electrons are engaged in the carbon-to-carbon covalent bonds and therefore, do not contribute to electronic conductivity. The third p orbital, perpendicular to the graphene plane hybridizes forming bonding (π) and antibonding (π*) orbitals.

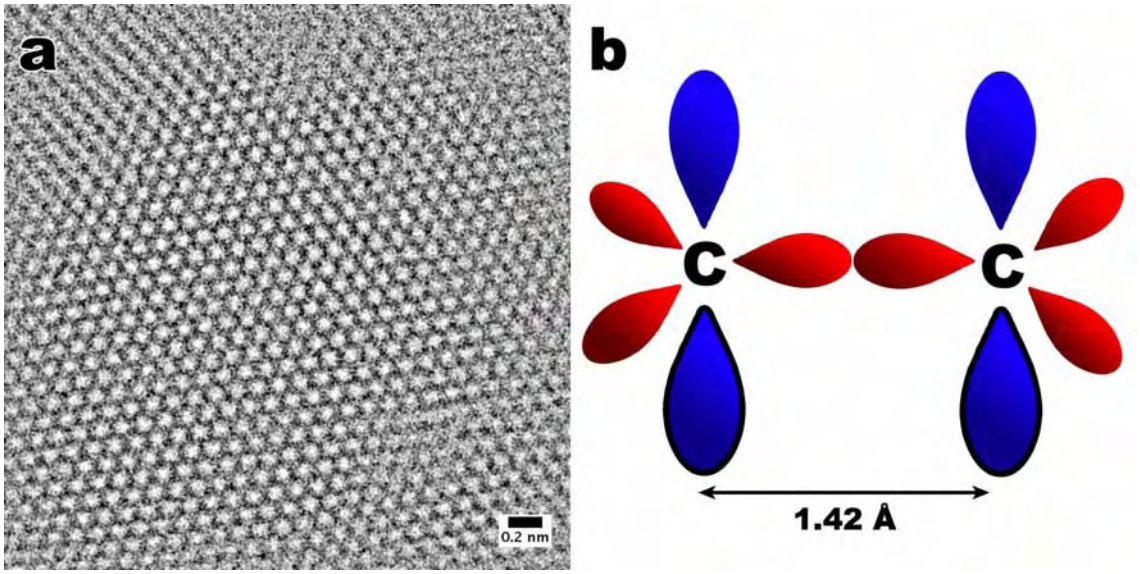


Figure 1.6: (a) TEM micrograph of monolayer graphene and (b) sp2 hybridized carbon atoms composing the structure of graphene.

The carbon-to-carbon bonding length is a = 1.42 Å (Figure 1.6b). Two main directions can be distinguished called armchair and zigzag (respectively x and y direction in Figure 1.7a). The lattice translation vectors $\mathbf{a_1}$ and $\mathbf{a_2}$ form a unit cell containing two non-equivalent carbon atom positions (black and blue) (Figure 1.7a).

$$\vec{a}_{1,2} = \frac{a}{2}\left(3 \cdot \vec{e}_x \pm \sqrt{3} \cdot \vec{e}_y\right) \qquad (1.1)$$

Vectors $\boldsymbol{\partial_{1,2,3}}$ are the nearest neighbour positions (Figure 1.7a).

$$\vec{\partial}_{1,2} = \frac{a}{2}\left(\vec{e}_x \pm \sqrt{3}\cdot\vec{e}_y\right);\ \vec{\partial}_3 = -a\cdot\vec{e}_x \tag{1.2}$$

The reciprocal lattice vectors are $b_{1,2}$ (Figure 1.7b).

$$\vec{b}_{1,2} = \frac{2\pi}{3a}\left(\vec{k}_x \pm \sqrt{3}\cdot\vec{k}_y\right) \tag{1.3}$$

The K and K' points in the borders of the Brillouin zone are particularly important for the physics of graphene. They are called the Dirac points and their positions in momentum space are:

$$K = \left(\frac{2\pi}{3a}, \frac{2\pi}{3\sqrt{3}a}\right);\ K' = \left(\frac{2\pi}{3a}, -\frac{2\pi}{3\sqrt{3}a}\right) \tag{1.4}$$

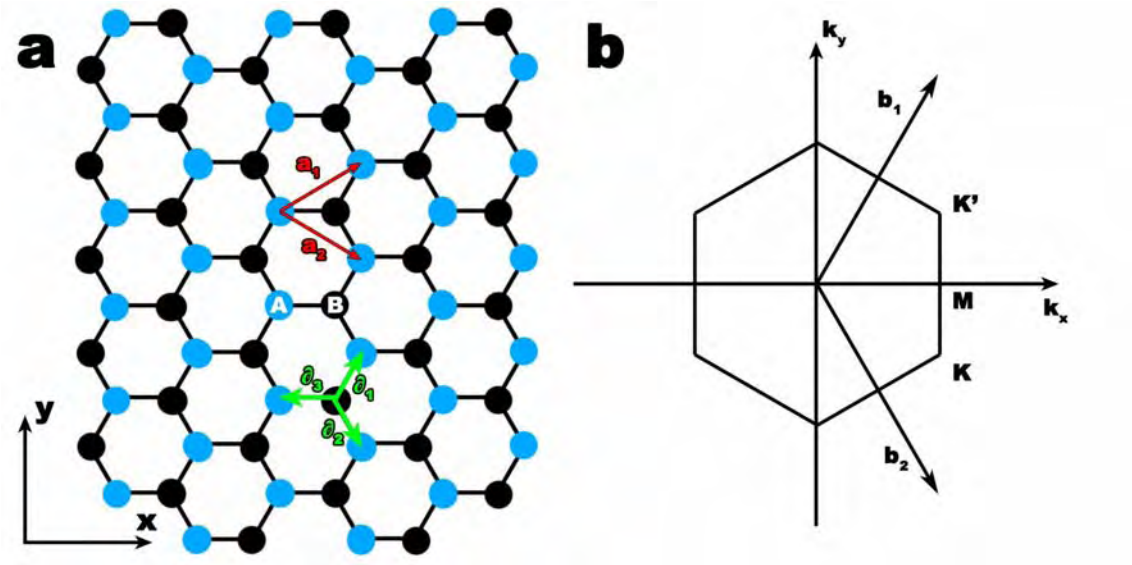


Figure 1.7: (a) Graphene honeycomb lattice composed of two triangular interpenetrating lattices (black and blue), a_1 and a_2 are the lattice unit vectors and ∂_1 ∂_2 and ∂_3 are the nearest-neighbour vectors. (b) The hexagonal 1st Brillouin zone is represented where b_1 and b_2 are the reciprocal vectors. Points K and K' correspond to the Dirac points.

The tight-binding Hamiltonian for electrons propagating in graphene, taking into account that electrons can hop to nearest and next-nearest atoms, has the following form [27] (with units such that $\hbar = 1$):

$$H = -t\sum_{<i,j>,\sigma}\left(a^{\dagger}_{\sigma,i}b_{\sigma,j} + H.c.\right) - t'\sum_{<<i,j>>,\sigma}\left(a^{\dagger}_{\sigma,i}a_{\sigma,j} + b^{\dagger}_{\sigma,i}b_{\sigma,j} + H.c.\right) \tag{1.5}$$

Where $a_{\sigma,i}$ ($a^{\dagger}_{\sigma,i}$) annihilates (creates) an electron with spin σ on site $\mathbf{R_i}$ on sublattice A (an equivalent definition is used for sublattice B), t ~ 2.8 eV is the nearest neighbour hopping energy (hopping between different sublattices represented by vectors $\boldsymbol{\partial_{1,2,3}}$), and t' ($0.02t \le t' \le 0.2t$) is the next nearest neighbour hoping energy (hopping in the same lattice represented by vectors $\mathbf{a_{1,2}}$). The electronic energy bands derived from this Hamiltonian are [4]:

$$E_{\pm}(\vec{k}) = \pm t\sqrt{3 + f(\vec{k})} - t' f(\vec{k}) \tag{1.6}$$

$$f(\vec{k}) = 2\cos(\sqrt{3}k_y a) + 4\cos\left(\frac{\sqrt{3}}{2}k_y a\right)\cos\left(\frac{3}{2}k_x a\right) \tag{1.7}$$

where the (+) sign corresponds to the conduction band (π*) and the (–) sign to the valence band (π). Figure 1.8 represents the band structure of graphene with a zoom in one of the Dirac cones position (at the K or K' position).

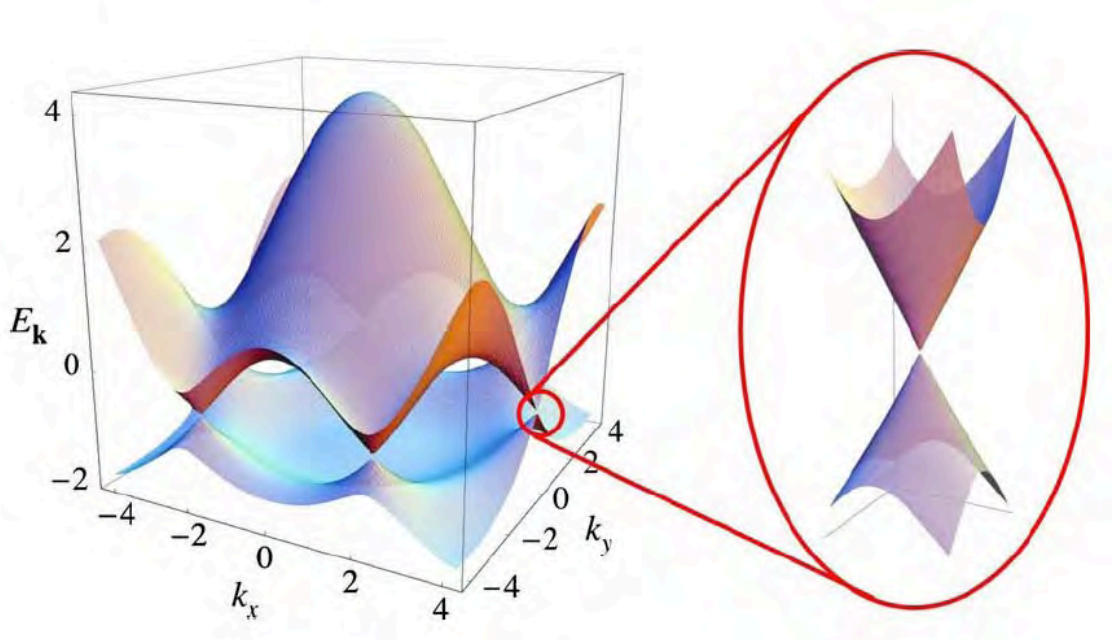


Figure 1.8: Representation of the two electronic bands (valence and conductance) of graphene. In inset, a zoom of one of the Dirac points. Adapted from [27].

The equation for the Dirac point dispersion is obtained by expanding Eq. (**1.7**) close to whether the **K** or the **K'** vectors (Eq. (**1.4**)) as $\mathbf{k} = \mathbf{K} + \mathbf{q}$ with $|\mathbf{q}| << |\mathbf{K}|$ [4].

$$E_{\pm}(\vec{q}) \approx \pm v_F |\vec{q}| + O\left[(q/K)^2\right] \tag{1.8}$$

where q is the relative momentum to the K (or K') point and v_F the Fermi velocity given by $v_F = 3ta/2$ and a value of $v_F \sim 1.10^6$ m.s^{-1}. This linear dispersion is similar to the energy of ultra-relativistic particles described by the massless Dirac equation and gives graphene some of its peculiar electronic properties.

1.2.2 Electronic transport in graphene

The most unusual electronic transport property of graphene is its high mobility (up to 250,000 cm^2/Vs[28]). In addition, due to the linear band structure, gated transport presents a resistance peak at a Fermi level corresponding to the junction of the conduction and valence bands where theoretically no electronic states are available. Away from that, I(V) characteristics are metal-like, linear, with constant resistance. But other magneto-transport phenomena take place on graphene. The properties of graphene under magnetic field are modified after patterning, and will be used in this work to evaluate edge transport. Hall effect, discovered in 1879 by Edwin Hall[29], is the apparition of a transversal bias on a conductive sample due to the Lorentz force applied to the charge carriers in a rectangular metallic bar with constant longitudinal current. The longitudinal voltage (V_{XX}) is then independent of the magnetic field whereas the transverse voltage will increase by the accumulation of charges due to the magnetic field (Figure 1.9). Its corresponding resistance is called the Hall resistance. While R_{XX} will be dependent on the bar sizes, the Hall effect is independent on the bar length and width. The resistance values follow the formula:

$$R_{XX} = \frac{L/W}{ne\mu} \qquad R_{XY} = \frac{\|\vec{B}\|}{ne} \tag{1.9}$$

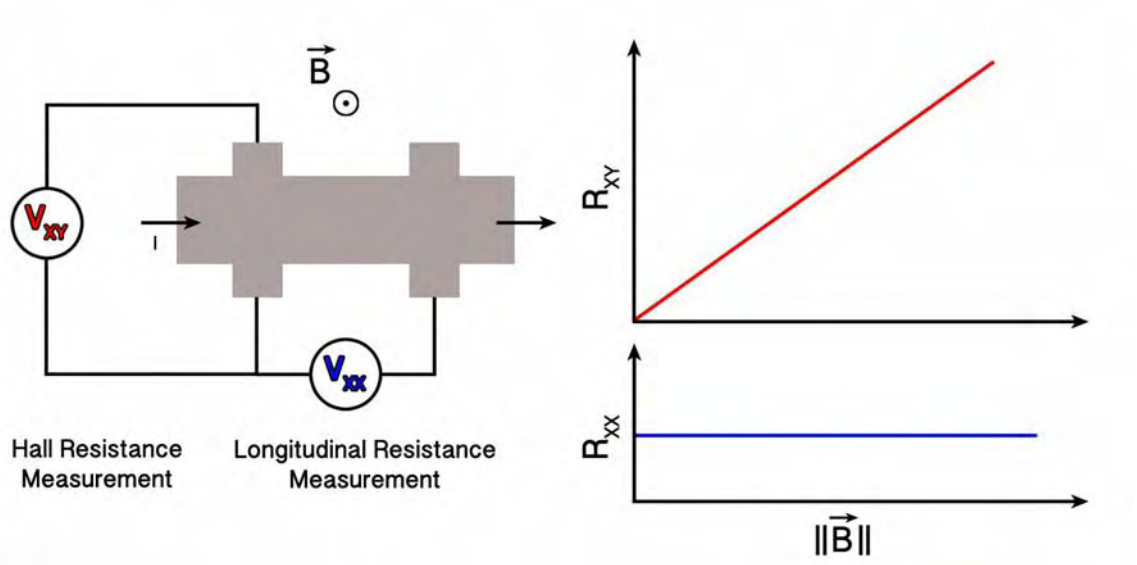


Figure 1.9: Measurement setup for the Hall effect and representation of the longitudinal as well as transverse resistance dependence on magnetic field intensity.

These formulas are based on the Drude model. This effect can be observed in any metallic conducting sample even at room temperature.

The Hall resistance measurement on graphene is different though. When graphene comprises a low enough density of defects, the transport can reach the ballistic regime where a quantisation appears in the presence of a magnetic field. In this case, the energy band split into Landau levels that degenerates then into spin up and spin down levels due to the Zeeman effect. As the magnetic field is increased, the Landau levels are more and more spaced. The eigenvalues for the Landau levels depending on magnetic field are given by:

$$E_N = \mathrm{sgn}(N)\sqrt{2e\hbar v_F B|N|} \tag{1.10}$$

Where N is an electron (N>0) or hole-like (N<0) index. The energy of the levels increases as the square root of the magnetic field. The Landau levels can be observed either by keeping the Fermi energy constant and by scanning the magnetic field or by setting a constant magnetic field (high enough to split the Landau levels) and raising the Fermi energy of the sample using the gate voltage (Figure 1.10a). We choose to describe an example where E_F is constant and the magnetic field intensity[26] is scanning between 0 and 9 T (Figure 1.10b).

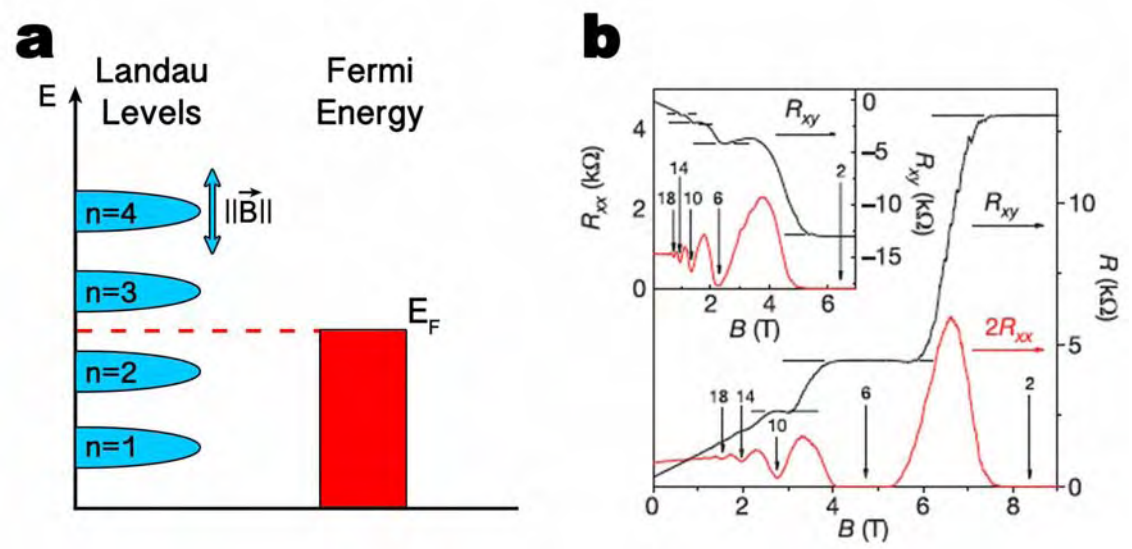


Figure 1.10: (a) Energy diagram of the filling mechanism of Landau levels by either variable magnetic field or Fermi energy level and (b) Graphene Hall bar measurements of longitudinal and transverse (Hall) resistance on variable magnetic field, adapted from [26].

In the example of Figure 1.10b the longitudinal (red) as well as the transverse (Hall) resistance (black) are measured. Even though the measurements at low magnetic field (from 0 to 1.5 T) are similar to the model of Figure 1.9, plateaux

appear in the Hall resistance as well as oscillations in the longitudinal resistance. This reveals the presence of Landau levels on the sample, which causes the increase of electronic states and also the resistance between the two sides. As the Landau levels correspond to electronic orbital states, they cause a sudden increase in the longitudinal resistance when they get across the Fermi level. This phenomenon is known as Shubnikov de Haas oscillations (SdH). Theoretically, there are no electronic states in between Landau levels and it would be impossible to stand between two of them. However in Figure 1.10b, we see that the steps are not perfectly straight. This is due to defects and imperfections in the sample that modify the potential allowing orbital states with energies different than the Landau levels. Those electronic states allow experimentally setting the Fermi level in between two Landau levels and performing a measurement.

1.3 Graphene nanoribbons (GNR)

1.3.1 Structural properties of graphene nanoribbons

The intrinsic electronic properties of bulk graphene are not sufficient to build complex mechanisms or devices. One needs to modify such properties to induce changes on its behaviour. One way to do it is by inducing confinement in a supplementary axis in order to evolve towards a one dimensional electron guide: graphene nanoribbons (GNR). GNR come in a variety of types depending on their geometrical size but also the structure of their edges. The length and width of the constriction will play an important role in the final electronic structure of the GNR. We define a zigzag (armchair) GNR as a zigzag (armchair) edged GNR, respectively aGNR and zGNR (Figure 1.11). Orientations in between those two possibilities will lead to a mixed GNR containing a non zero percentage α of armchair and $(1-\alpha)$ of zigzag edges (Figure 1.11) resulting in different GNR orientations.

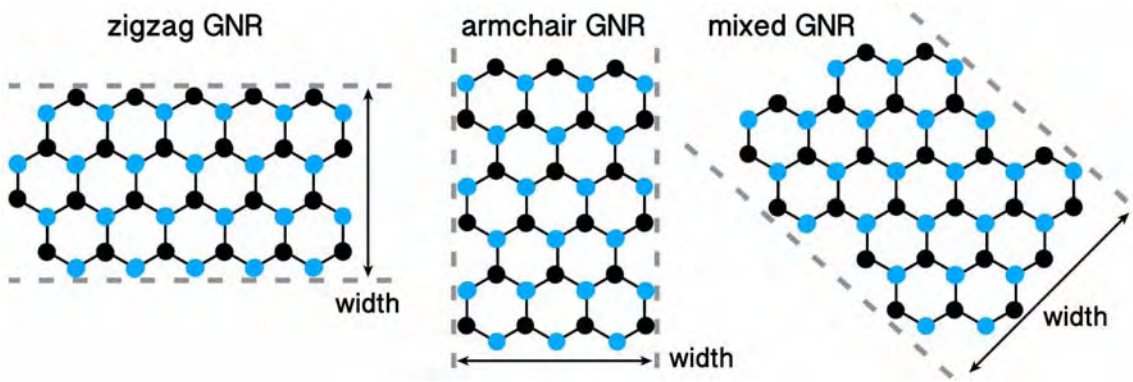


Figure 1.11: Representation of the three possible edge arrangements of graphene nanoribbons.

Furthermore, the geometry of the portion of graphene connecting the nanoribbon to the electrodes also contributes to the electronic behaviour. The GNR

can be connected to the rest of the graphene flake directly without additional patterning, or through a connection cone at an arbitrary angle (Figure 1.12).

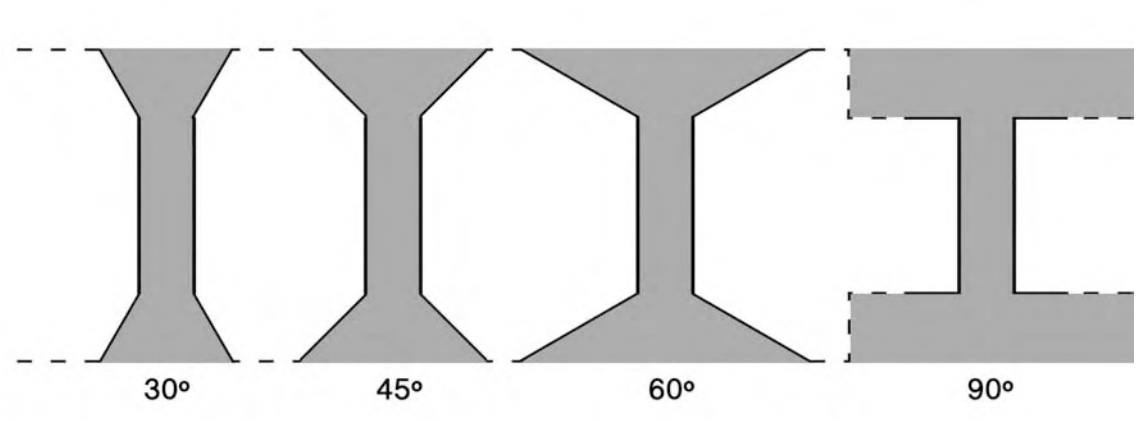


Figure 1.12: Scheme of graphene nanoribbons shape with different angle connections from 30° to 90°.

It has been theoretically shown that connection angles have an effect on the conductance in GNR-like constrictions[30], depending on the shape, and on the crystalline orientation of the connecting region.

1.3.2 Electronic structure of Graphene Nanoribbons

This section is divided into the zGNR and aGNR section as this parameter defines the electronic band structure and behaviour of the GNR. Those electronic properties are then modulated by the geometrical characteristics of the ribbon (width and length).

- *zigzag GNR*

The zGNR presents electronic states at the edges of the ribbon for any width [31, 32]. No matter what the width of the ribbon is, the device is metallic and the Density of States (DOS) does not change significantly with different sizes (Figure 1.13). No gap is present at any width, and edge states are always present at the Fermi level. Its energy band structure is comparable to the projection of graphene electronic band structure along a zigzag direction axis. The fact that the zGNR behaves as a metal can be useful for future metallic connections between devices using graphene strips. The conduction properties are though not adapted to the production of a semiconductor-like behaving graphene device.

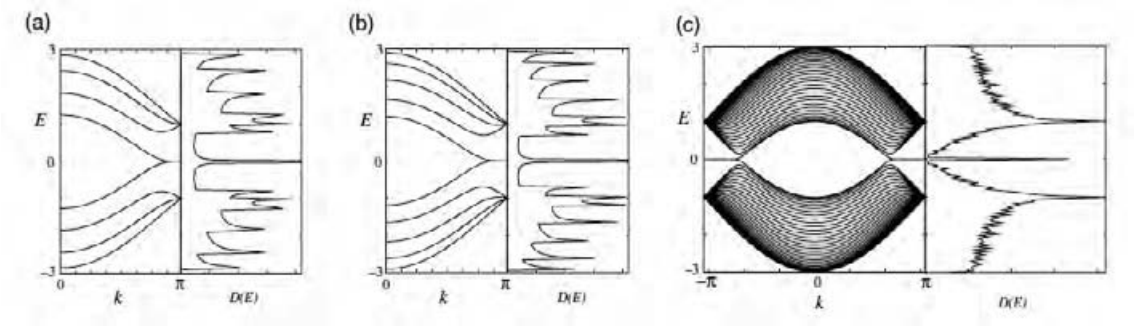


Figure 1.13: Energy band structure E(k) and density of states D(E) simulations of zigzag nanoribbons of widths (a) N=4, (b) N=5 and (c) N=30. Adapted from [32].

- *armchair GNR*

In contrast, the band diagram of aGNR depends significantly on the width and cannot then be extracted from a projection of the graphene electronic bands diagram. One characteristic of the armchair GNR is a gap between the conduction and valence bands depending on the GNR widths (Figure 1.14).

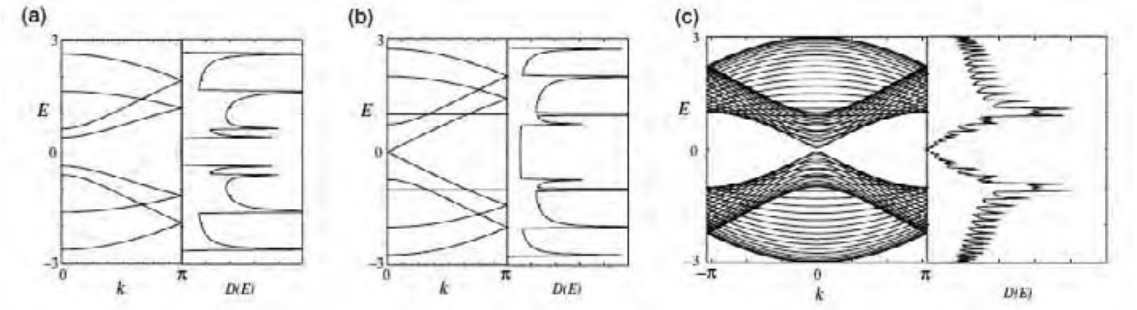


Figure 1.14: Energy band structure E(k) and density of states D(E) simulations of armchair nanoribbons of widths (a) N=4, (b) N=5 and (c) N=30 (3.6 nm). Adapted from [32].

The gap depends also on the number N of armchair chains contained on the ribbon. We can distinguish 3 families: N = 3p+1, 3p+2 and 3p, where $p \in N^*$. Simulations show that at same width (interpolated), ribbons of family N=3p+1 have the bigger gap energy compared to N=3p and N=3p+2 which has the lower energy gaps[33] (Figure 1.15). We can calculate the ribbon width from N using $W = \frac{\sqrt{3}}{2} a \cdot (N-1)$. For example N= 30 correspond to a W= 3.6 nm wide aGNR. From the calculations in Figure 1.15d we deduce a relation between the gap energy and the width as:

$$E_G = \frac{\alpha}{W} \qquad (1.11)$$

were $\alpha \approx 0.2 - 1.5$ eV.nm. The theoretical works show how atomic precision is important to achieve the desired device with given properties. GNR with similar width presents different characteristics at only one atom difference in width.

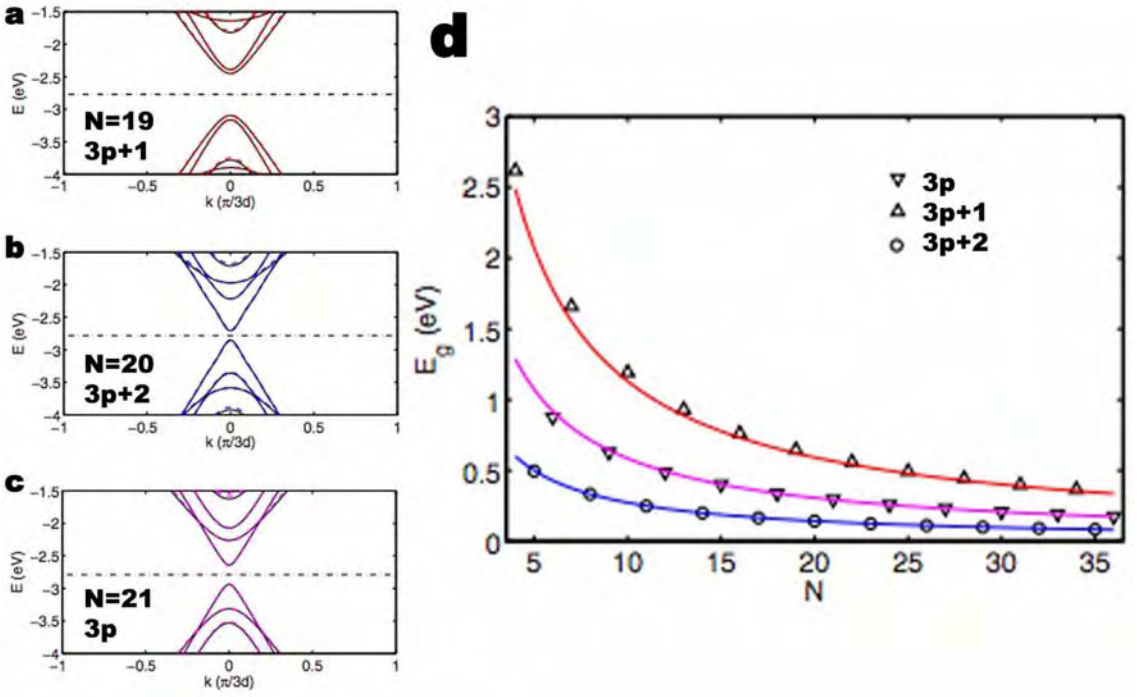


Figure 1.15: Electronic band calculations for (a) N=19, (b) N=20 and (c) N=21 armchair GNR and plot of gap energy versus N for the three types of ribbons N=3p, 3p+1 and 3p+2. The width is calculated using W= sqrt(3)/2*a*(N-1) with a=1.42 Å. Adapted from [33].

The values measured experimentally by electronic transport taking $\alpha = 0.2$ and considering an effective ribbon width W-W* (real width of the GNR – amorphized non conductive width) where in good agreement with those theoretical values[34].

- *GNR under Magnetic Field*

GNR under magnetic field are also subjected to the Zeeman effect, and so, to the energy bands splitting into Landau levels. While the centre of the ribbon reacts similarly to what we have described for 2D graphene, extra edge states arise from the 1D confinement. As a consequence, the dispersion of the Landau levels increases strongly near the GNR edges (Figure 1.16a). The flat regions of the Landau levels correspond to cyclotron orbits in the ribbon, edge states correspond to skipping orbits (Figure 1.16a). Skipping orbits are simply cyclotron orbits that hit the edge and are diffused forward. Finally higher energies with orbits bigger than the ribbon size will result in traversing orbits along the GNR (Figure 1.16b).

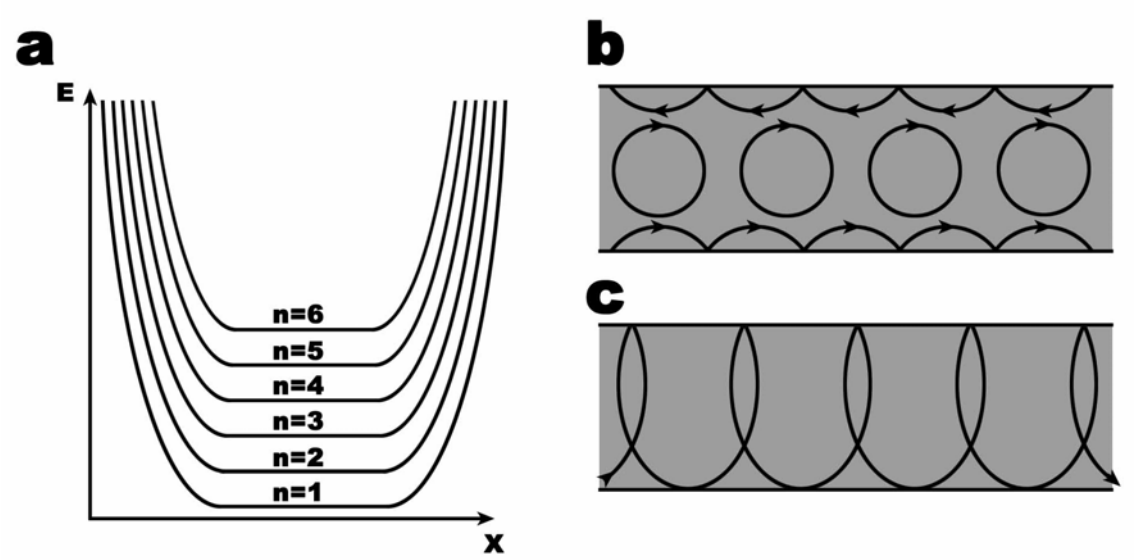


Figure 1.16: (a) Scheme of the Landau levels in a GNR under magnetic field and the three possible electron trajectories through the ribbon: (b) cyclotron orbits, skipping orbits and (c) traversing orbits.

This behaviour corresponds to ballistic transport regime. The presence of defects on the ribbon will cause the regime to change depending on the density. A low density of defects will cause a Landau states displacement, as the potential is locally modified by the defect, electron orbits are possible around it with cyclotron length, and so energy, different than normal levels. In addition, these defects can induce diffusion of electrons, perturbing their trajectories. At higher density, the channel is cut and the direct transmission of electrons is not longer possible and the only way for electrons to go through the ribbon is by hopping though the potential barriers, if barriers isolate graphene islands the conduction enters the Coulomb blockade regime.

1.4 Experimental background

1.4.1 Graphene patterning techniques

The most used and known technique to pattern GNR is the electron beam lithography (EBL) combined by metallization and reactive ion etching (RIE) of an exfoliated graphene sample[22, 25, 26, 34-47]. The species can be inert (argon) or reactive (oxygen) (schematic steps e and f in Figure 1.17). This procedure produces contacted graphene nanoribbons with a high success rate and down to 20 nm in width. But devices are supported (Figure 1.17). Moreover, because of the positive resist, the ribbon is irradiated by the electron beam and covered by resists, and during RIE the risk of ions implantation is high.

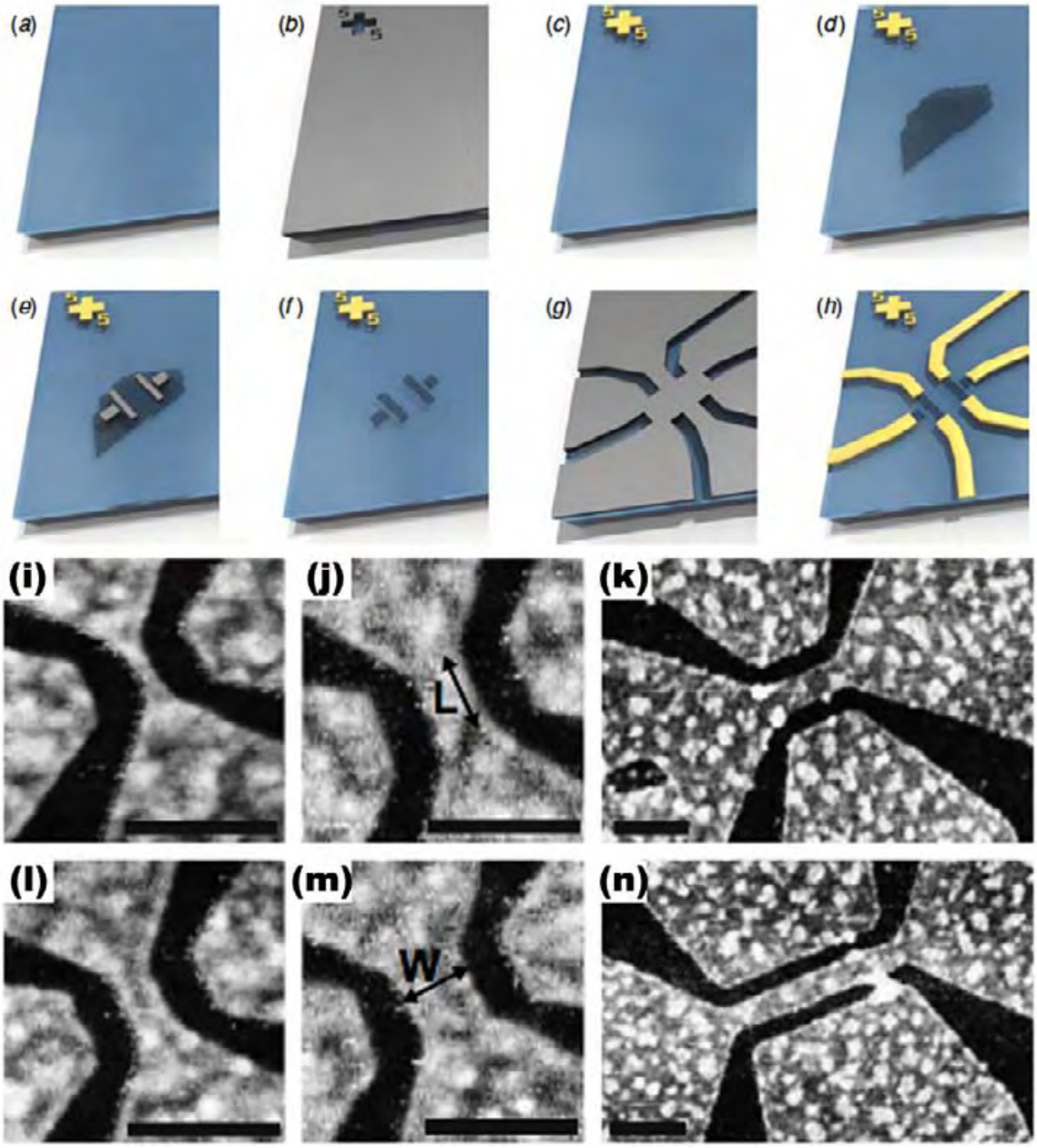


Figure 1.17: Graphene nanoribbon fabrication by the EBL+RIE technique. The samples are produced by (d) deposition of exfoliated graphene (e-f) patterned by Reactive Ion etching and (g-h) contacted by electron beam lithography. (i) to (n) Resulting GNR produced by this process imaged by AFM. Adapted from[37] and [38]. AFM scale bars are 200 nm

Ions can also be used by Focused Ion Beam (FIB) to etch graphene. Firsts GNR etching were made using gallium ions [48]. Gallium ions induced too much amorphization and damage to the GNR. Lighter ions such as helium[49, 50] with probe sizes down to 5 Å were used to pattern graphene reducing the ion implantation. This technique produces etched lines down to 10 nm in width on SiO_2 supported graphene. The schematic (Figure 1.18) shows that this technique has some backscattering issues, as it would also be possible for the EBL+RIE etching techniques. The backscattering of a (electron) beam on supported graphene will be further analysed in Chapter 4.

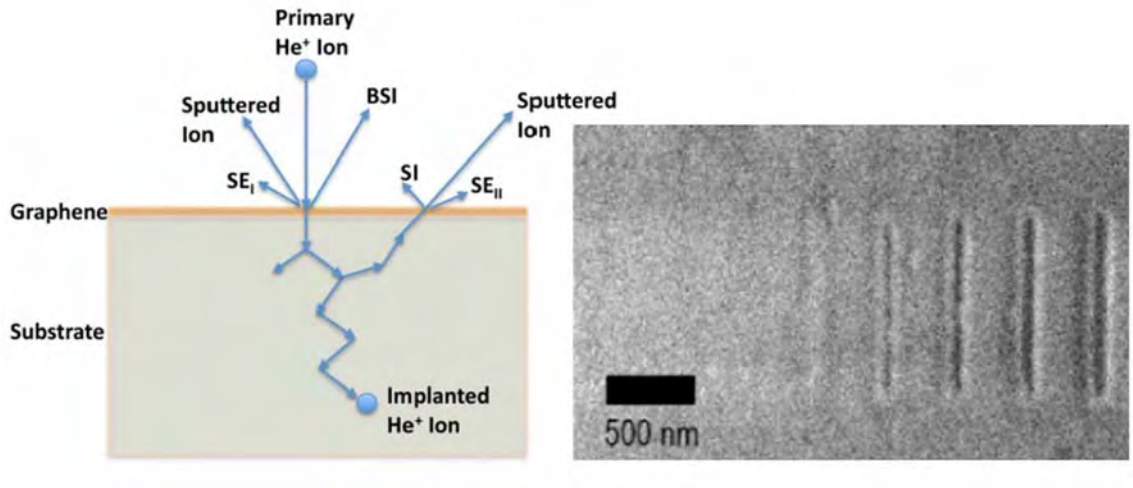


Figure 1.18: Helium Ion Lithography of graphene on silicon dioxide substrate. Adapted from [50].

Direct etching by a focused e-beam in order to knock atoms has been first evidenced by TEM[51-55]. In order to remove carbon atoms from the lattice (edge) a high energy electron beam is necessary, over 86 keV (50 keV)[51, 56, 57]. We find two main processes in the literature. The first one aims to produce by STEM a 20 nm large constriction. This constriction is then imaged continuously by standard TEM to narrow the constriction down to the atomic filament[52, 53, 55] (Figure 1.19). Although the edges produced by the TEM beam etching are smooth, the electron beam used to narrow the ribbon also produces damages in the core. Moreover, even if it is possible to slightly modify the evolution of the ribbon, no control on the shape or the width can be done. The ribbon is etched until it breaks and is no longer measurable. On the other hand it is possible to use the STEM (with Cs corrected probe) at 600°C with high-resolution probe and etch directly the final desired shape[54].

The three techniques presented here allow the patterning of arbitrary patterns by piloting the beam of a microscope, whether a lithography writer, FIB or TEM. Although etching precision reaches down to tens of nanometres, we will see in section 1.4.2 that the edge quality of the ribbons produced by those techniques is low, their crystallinity is lost to a large extent and the substrate and resist influence persist.

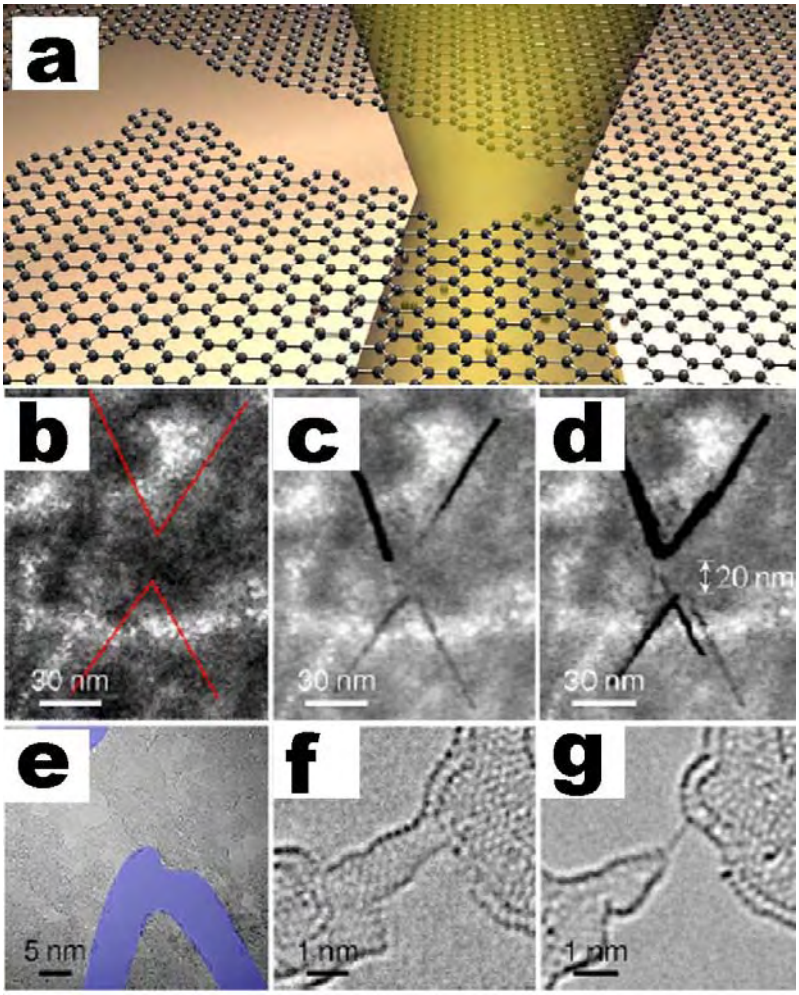


Figure 1.19: (a) Schematic of the TEM beam knock on on graphene. (b) to (g) HRTEM micrographs of the fabrication steps of the GNR. Adapted from[53].

Next is a chemical way to etch graphene: the catalytic etching of graphene by metallic nanoparticles under reactive gas[58-60]. Although the resulting edges are amongst the best quality edges in the literature with less than 1 nm of amorphization, the direction of diffusion and so the shape of the pattern is neither arbitrary nor controlled. However this shows that inducing a chemical reaction allows etching graphene by low energy activation. Furthermore the chemical reaction's preference for crystalline directions is strong enough in this case to force the direction of diffusion of the particles. This characteristic could be useful to perform relatively easy atomically precise patterning that has been shown to be crucial.

Chemical reactions are also used in order to open graphene nanotubes (Figure 1.20). The nanotube is locally oxidized to create a defect. This defect will then propagate following the longitudinal direction due to stress on the rolled graphene piece to unzip it. Carbon nanotubes opening lead to high quality graphene nanoribbons with low amorphization on the edges [61-63]. The ribbon width is close to $2\pi R$, with R the nanotube diameter, minus the burned away part.

Although their fabrication is relatively straightforward and with good results, the user does not choose the GNR position and complex device (multiribbon) fabrication would not be possible.

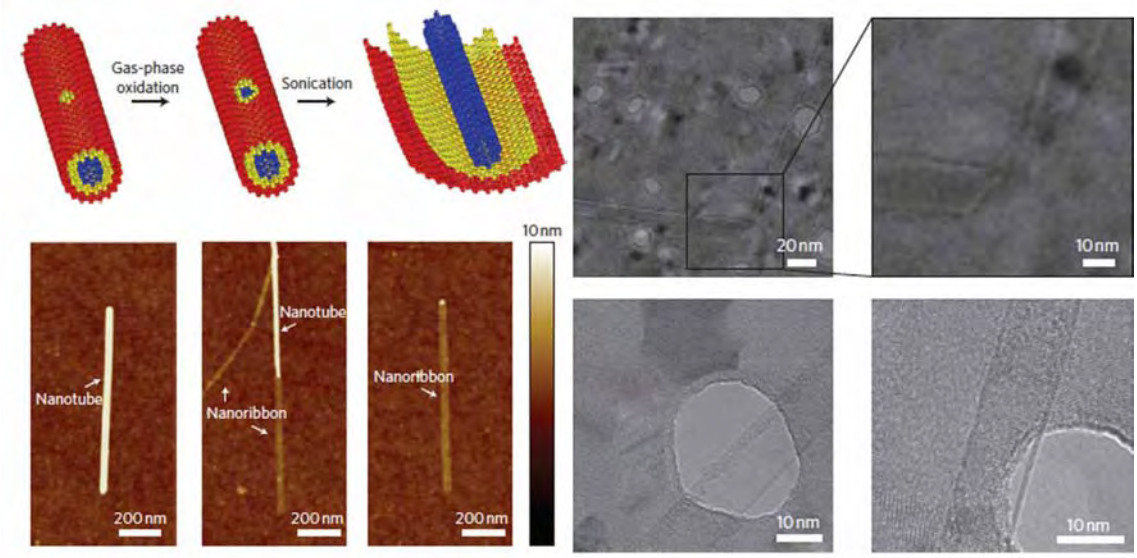


Figure 1.20: Carbon nanotube opening by gas-phase oxidation imaged by AFM as well as TEM microscopy techniques. Adapted from [62].

Finally the chemical synthesis of GNR (Figure 1.21) produces atomically perfect graphene ribbons[64]. The starting precursor defines the future morphology (edge structure, shape, width) of the GNR. For that reason every ribbon size or shape needs a whole new chemistry (precursor, reaction and conditions). Though the quality and size precision of this technique is the best in the literature, difficulties are encountered to insulate one single ribbon in order to contact and proceed to transport measurements. Moreover the GNR are synthesized over a metallic surface compromising the electronic transport measurements without changing the substrate. The fact that chemistry is so precise and capable of producing high quality objects can be helpful if we succeed to find a process combining chemistry with an arbitrary shape patterning technique.

The chemical approaches produce objects with high structural quality. The crystallinity of graphene is preserved and the edges present a roughness of 0.5 nm or less. On the other hand the use of those techniques makes it difficult to arbitrarily choose the geometries, sizes and position on the sample of the targeted object.

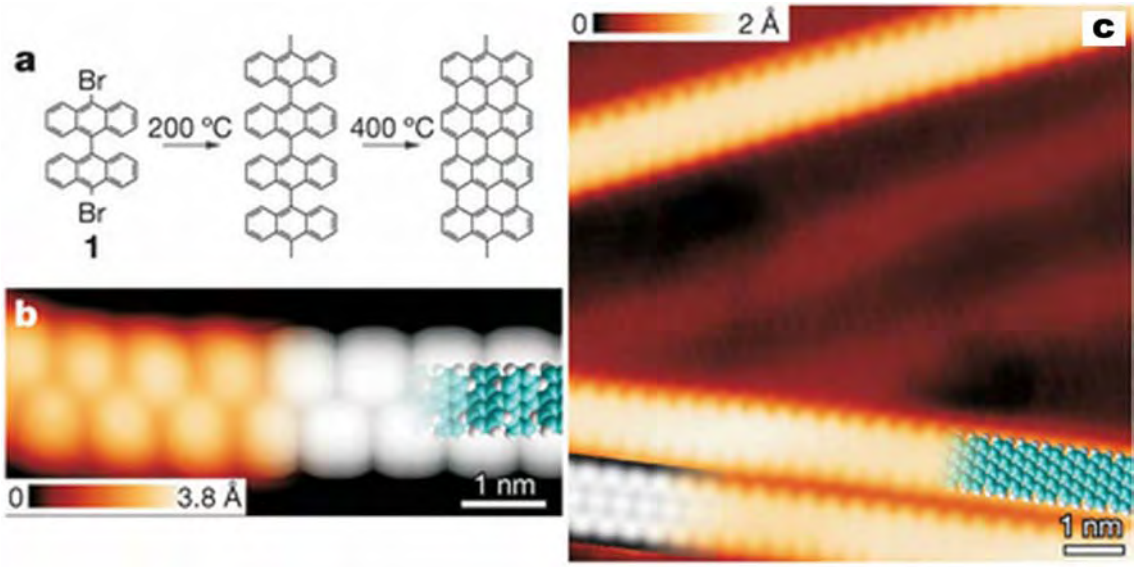


Figure 1.21: Chemical synthesis and near field imaging of graphene nanoribbons. Adapted from [64].

There are some chemical candidates that can be used to etch graphene. For example, water (ice) has been proved to form species that reacts with graphene removing it from the surface[65]. Furthermore this technique allows the production of silicon dioxide supported single-layer graphene nanoribbon arrays of widths down to 50 nm. Even though this technique is quite effective, no high-resolution study analyses the resulting devices. Furthermore water, or ice, is not the best candidate for vacuum chambers or for chemical reactivity.

Another possibility is to use oxygen. Oxygen is a more reactive gas than water is and is easier to pump away from the microscope chamber afterwards. In addition the presence of oxygen in an SEM chamber has been shown to induce hexagonal crystalline edged holes in graphite samples when exposed to an electron beam[66](Figure 1.22).

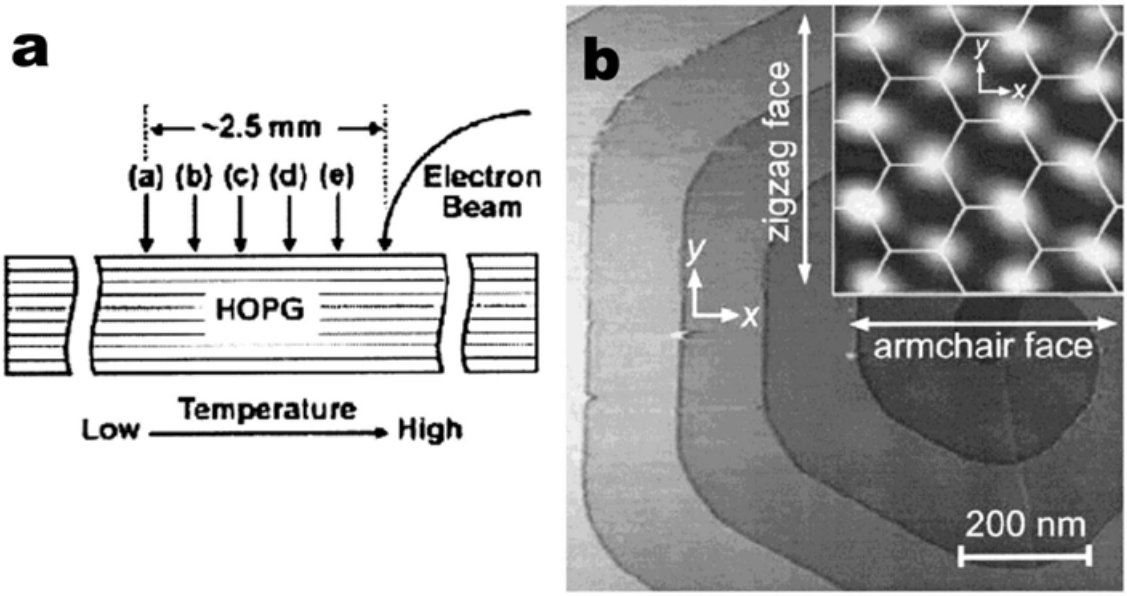


Figure 1.22: Oxygen induced etching of graphite during e-beam exposition (a) and (b). Adapted from [66].

This last technique is potentially combining a crystallographic dependent chemical etching of graphene, with an activation of the reaction by an electron beam that we can control. The work presented in this manuscript is inspired in this last etching technique and will aim to perform graphene patterns by activating such reaction with a controlled focused electron beam.

1.4.2 Electronic transport measurements of GNR

Not all the graphene nanoribbons fabrication methods shown in the previous section are presented with electronic transport measurements. We present in this part some of the most representative electron cryo-transport and cryo-magneto transport measurements performed on graphene nanoribbons. Two fabrication techniques are represented: EBL + RIE plasma etching of graphene sheets and carbon nanotubes unzipping. All the following results correspond to graphene ribbons supported on silicon dioxide substrate.

We find in literature works in which graphene nanoribbons are patterned by RIE for example (Figure 1.23) and measured. The measurements show indeed wide gap opening (around 50 meV). This gap energy though seems quite high compared to the theoretical energy gap discussed before in section 1.3.2 for the patterned ribbon width.

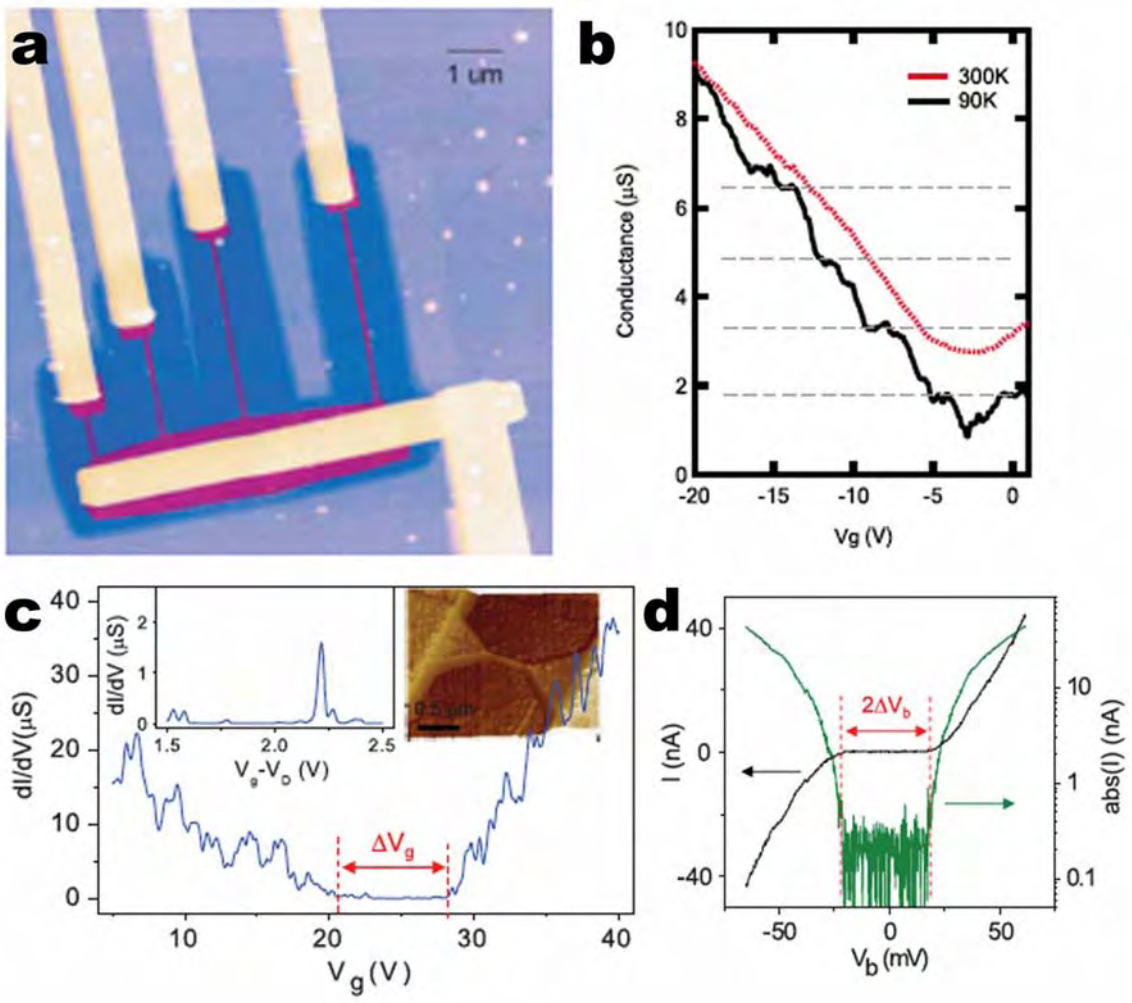


Figure 1.23: Backgate measurements of graphene nanoribbons patterned by EBL and RIE of (a) 1.7 µm measured at 90 K (b) and backgate and I(V) measurements of a 36 nm GNR measured at 1.5 K (c) and (d). Adapted from [45] and [39].

Those GNR measurements show characteristics related to a phenomenon other than electron confinement taking place, increasing the gap energy.

Other studies (Figure 1.24)[37, 40] have shown those nanoribbons to present coulomb diamonds in the conductance versus backgate voltage and bias diagram. These results show that the graphene nanoribbons do not have transport properties of devices with ballistic transport regime. The conduction regime on those devices is therefore different, much probably due to defects. As seen before, defects in a GNR will induce the transport regime to change to diffusive or to electron hopping depending on their density.

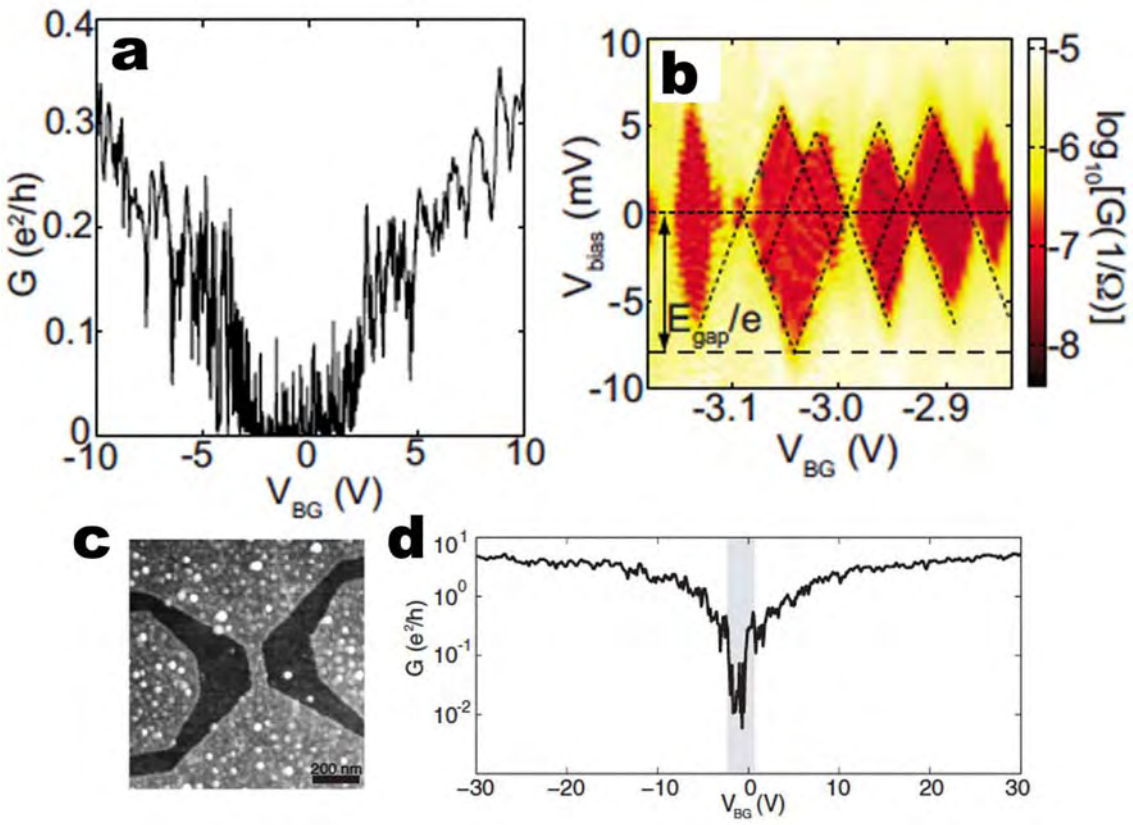


Figure 1.24: (a) Electronic transport measurements of plasma etched graphene nanoribbons in (c). Transport gap measurement of a 85 nm wide ribbon and its conductance versus gate voltage and bias (b). (c) Graphene nanoribbon of 75 nm width with (d) backgate measurement of the gap and its conductance versus backgate voltage and bias diagram (e). Adapted from [37] and [40].

The junctive diamonds of suppressed conductance are an indication of coulomb blockade regime, dominated by edge roughness and defects. We define edge roughness as the distance between the outer limit of the edge and the inner limit of the edge. This regime is the result of a GNR composed of islands. The electrons travel from source to drain by hopping from one island to the adjacent one consecutively. The nanoribbon islands can come from two different origins. The first and most obvious one is to have crystalline islands surrounded by an amorphized area. This have certainly been induced during the patterning process.

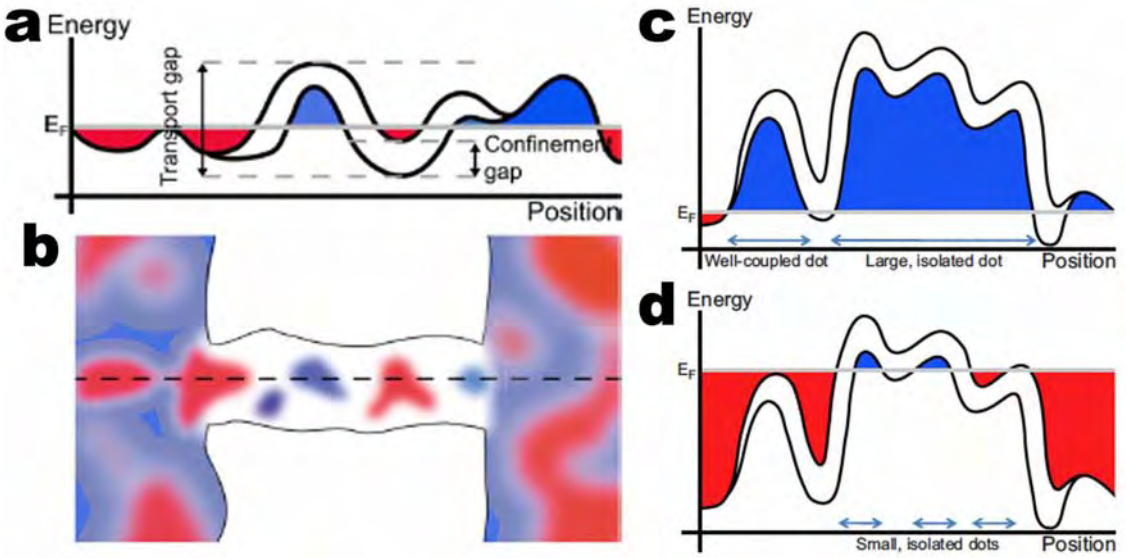


Figure 1.25: Schematic mechanism of dots creation by the surface potential fluctuation induced by the substrate and diffusive edges. Hole doping is represented in blue and electron doping in red. Adapted from [42].

The second one is the creation of dots along the GNR by the combination of substrate induced potential fluctuations and the real confinement gap of the GNR. The flat and constant Fermi energy will cross the energy gap a few times creating electron and hole doped areas separated by the confinement gap (Figure 1.25 a and b). This model explains how changing the Fermi energy in a complex fluctuation of this potential may cause the system to switch in between different states such as large or small dots and isolated and well-coupled dots [42](Figure 1.25 c and d).

The patterning techniques presented before (EBL+RIE) had been proved to be inefficient though. Even if the etching is performed, the remaining material is defective, in the ribbon as well as the edges. This density of defects prevents the electrons from high mobility transport regime. As we want to preserve them as much as possible, the challenge is to pattern graphene nanoribbons, by preserving the graphene crystallinity and producing low roughness and low defected edges.

Experiments on unzipped carbon nanotubes have shown to have transport properties under magnetic field similar to a GNR with only Gaussian disorder[67]. The simulated current distribution in such GNR shows the backscattering mechanism due to localized states that successively disappears with the creation of magnetic edges (Figure 1.26). This mechanism that concentrates the current flow in the smooth edges enhances the transmission and so induces a positive magneto conductance.

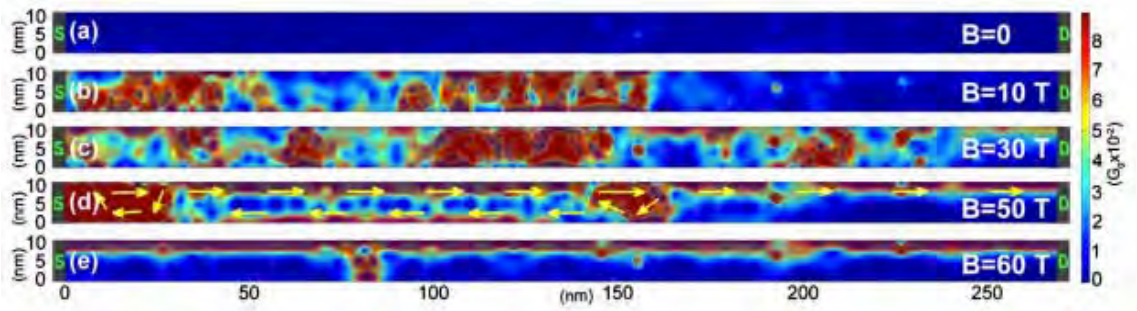


Figure 1.26: Current distribution at E= 200 meV for a 90 nm aGNR with only Gaussian disorder at different magnetic fields. Adapted from [67].

In this experiments backscattering due to edge roughness and amorphized GNR have been removed by using high quality GNR from carbon nanotubes. There is though one last source of scattering that has not been eliminated, which is the substrate itself. By reducing the substrate-GNR interaction, the last source of backscattering remaining would be removed.

This work will focus on the production of graphene nanoribbons by preventing from those scattering phenomena. The sample fabrication and specially the patterning procedure has to produce arbitrary shaped ribbons of nanometric size (~ 20 nm) with crystalline edges as well as non-amorphized ribbon core by using an induced chemical reaction. The final main challenge is to produce ribbons, free of the influence of the substrate, that are measurable by electronic transport techniques.

1.5 References

[1] W. H. Bragg, in *X rays and crystal structure*, London: G. Bell, 1915, 131.
[2] P. S. P. Debye, Vol. 18, 1917, 291.
[3] J. D. Bernal, Proceedings of the Royal Society of London A: Mathematical, Physical and Engineering Sciences 1924, 106, 749.
[4] P. R. Wallace, Physical Review 1947, 71, 622.
[5] J. W. McClure, Physical Review 1956, 104, 666.
[6] G. W. Semenoff, Physical Review Letters 1984, 53, 2449.
[7] D. P. Divincenzo, E. J. Mele, Physical Review B 1984, 29, 1685.
[8] C. Soldano, A. Mahmood, E. Dujardin, Carbon 2010, 48, 2127.
[9] A. J. Vanbommel, J. E. Crombeen, A. Vantooren, Surf. Sci. 1975, 48, 463.
[10] I. Forbeaux, J. M. Themlin, J. M. Debever, Surf. Sci. 1999, 442, 9.
[11] A. Charrier, A. Coati, T. Argunova, F. Thibaudau, Y. Garreau, R. Pinchaux, I. Forbeaux, J. M. Debever, M. Sauvage-Simkin, J. M. Themlin, Journal of Applied Physics 2002, 92, 2479.
[12] C. Berger, Z. M. Song, T. B. Li, X. B. Li, A. Y. Ogbazghi, R. Feng, Z. T. Dai, A. N. Marchenkov, E. H. Conrad, P. N. First, W. A. de Heer, Journal of Physical Chemistry B 2004, 108, 19912.
[13] I. Forbeaux, J. M. Themlin, J. M. Debever, Physical Review B 1998, 58, 16396.
[14] T. A. Land, T. Michely, R. J. Behm, J. C. Hemminger, G. Comsa, Surf. Sci. 1992, 264, 261.
[15] B. S. Itchkawitz, P. F. Lyman, G. W. Ownby, D. M. Zehner, Surf. Sci. 1994, 318, 395.
[16] A. Nagashima, H. Itoh, T. Ichinokawa, C. Oshima, S. Otani, Physical Review B 1994, 50, 4756.
[17] C. Oshima, A. Nagashima, Journal of Physics-Condensed Matter 1997, 9, 1.
[18] M. Terai, N. Hasegawa, M. Okusawa, S. Otani, C. Oshima, Applied Surface Science 1998, 130, 876.
[19] S. Iijima, Nature 1991, 354, 56.
[20] A. M. Cassell, J. A. Raymakers, J. Kong, H. J. Dai, Journal of Physical Chemistry B 1999, 103, 6484.
[21] M. S. Dresselhaus, G. Dresselhaus, A. Jorio, A. G. Souza, M. A. Pimenta, R. Saito, Accounts of Chemical Research 2002, 35, 1070.
[22] K. S. Novoselov, A. K. Geim, S. V. Morozov, D. Jiang, Y. Zhang, S. V. Dubonos, I. V. Grigorieva, A. A. Firsov, Science 2004, 306, 666.
[23] F.-M. H., J Appl Phys 1960, 31.
[24] P. Blake, E. W. Hill, A. H. Castro Neto, K. S. Novoselov, D. Jiang, R. Yang, T. J. Booth, A. K. Geim, Applied Physics Letters 2007, 91, 3.
[25] K. S. Novoselov, A. K. Geim, S. V. Morozov, D. Jiang, M. I. Katsnelson, I. V. Grigorieva, S. V. Dubonos, A. A. Firsov, Nature 2005, 438, 197.
[26] Y. B. Zhang, Y. W. Tan, H. L. Stormer, P. Kim, Nature 2005, 438, 201.
[27] A. H. Castro Neto, F. Guinea, N. M. R. Peres, K. S. Novoselov, A. K. Geim, Reviews of Modern Physics 2009, 81, 109.
[28] M. Orlita, C. Faugeras, P. Plochocka, P. Neugebauer, G. Martinez, D. K. Maude, A. L. Barra, M. Sprinkle, C. Berger, W. A. de Heer, M. Potemski, Physical Review Letters 2008, 101.

[29] E. H. Hall, American Journal of Mathematics 1879, 2, 287.
[30] J. Wurm, M. Wimmer, I. Adagideli, K. Richter, H. U. Baranger, New Journal of Physics 2009, 11.
[31] K. Nakada, M. Fujita, G. Dresselhaus, M. S. Dresselhaus, Physical Review B 1996, 54, 17954.
[32] K. Wakabayashi, Y. Takane, M. Yamamoto, M. Sigrist, New Journal of Physics 2009, 11.
[33] D. Gunlycke, C. T. White, Physical Review B 2008, 77, 115116.
[34] M. Y. Han, B. Oezyilmaz, Y. Zhang, P. Kim, Physical Review Letters 2007, 98.
[35] C. Stampfer, E. Schurtenberger, F. Molitor, J. Guettinger, T. Ihn, K. Ensslin, Nano Letters 2008, 8, 2378.
[36] X. Liu, J. B. Oostinga, A. F. Morpurgo, L. M. K. Vandersypen, Physical Review B 2009, 80.
[37] F. Molitor, A. Jacobsen, C. Stampfer, J. Guettinger, T. Ihn, K. Ensslin, Physical Review B 2009, 79.
[38] C. Stampfer, J. Guettinger, S. Hellmueller, F. Molitor, K. Ensslin, T. Ihn, Physical Review Letters 2009, 102.
[39] M. Y. Han, J. C. Brant, P. Kim, Physical Review Letters 2010, 104.
[40] S. Droescher, H. Knowles, Y. Meir, K. Ensslin, T. Ihn, Physical Review B 2011, 84.
[41] J. Guttinger, F. Molitor, C. Stampfer, S. Schnez, A. Jacobsen, S. Droscher, T. Ihn, K. Ensslin, Rep. Prog. Phys. 2012, 75, 24.
[42] P. Gallagher, K. Todd, D. Goldhaber-Gordon, Physical Review B 2010, 81.
[43] J. B. Oostinga, B. Sacepe, M. F. Craciun, A. F. Morpurgo, Physical Review B 2010, 81, 4.
[44] Z. Chen, Y.-M. Lin, M. J. Rooks, P. Avouris, Physica E-Low-Dimensional Systems & Nanostructures 2007, 40, 228.
[45] Y.-M. Lin, V. Perebeinos, Z. Chen, P. Avouris, Physical Review B 2008, 78.
[46] Y. Wu, Y.-m. Lin, A. A. Bol, K. A. Jenkins, F. Xia, D. B. Farmer, Y. Zhu, P. Avouris, Nature 2011, 472, 74.
[47] X. Wang, H. Dai, Nature Chemistry 2010, 2, 661.
[48] J.-F. Dayen, A. Mahmood, D. S. Golubev, I. Roch-Jeune, P. Salles, E. Dujardin, Small 2008, 4, 716.
[49] D. C. Bell, M. C. Lemme, L. A. Stern, J. Rwilliams, C. M. Marcus, Nanotechnology 2009, 20.
[50] M. C. Lemme, D. C. Bell, J. R. Williams, L. A. Stern, B. W. H. Baugher, P. Jarillo-Herrero, C. M. Marcus, Acs Nano 2009, 3, 2674.
[51] C. O. Girit, J. C. Meyer, R. Erni, M. D. Rossell, C. Kisielowski, L. Yang, C.-H. Park, M. F. Crommie, M. L. Cohen, S. G. Louie, A. Zettl, Science 2009, 323, 1705.
[52] Y. Lu, C. A. Merchant, M. Drndic, A. T. C. Johnson, Nano Letters 2011, 11, 5184.
[53] F. Boerrnert, L. Fu, S. Gorantla, M. Knupfer, B. Buechner, M. H. Ruemmeli, Acs Nano 2012, 6, 10327.
[54] Q. Xu, M.-Y. Wu, G. F. Schneider, L. Houben, S. K. Malladi, C. Dekker, E. Yucelen, R. E. Dunin-Borkowski, H. W. Zandbergen, Acs Nano 2013, 7, 1566.
[55] Z. J. Qi, J. A. Rodriguez-Manzo, A. R. Botello-Mendez, S. J. Hong, E. A. Stach, Y. W. Park, J.-C. Charlier, M. Drndic, A. T. C. Johnson, Nano letters 2014, 14, 4238.

[56] J. C. Meyer, F. Eder, S. Kurasch, V. Skakalova, J. Kotakoski, H. J. Park, S. Roth, A. Chuvilin, S. Eyhusen, G. Benner, A. V. Krasheninnikov, U. Kaiser, Physical Review Letters 2012, 108.
[57] T. Susi, J. Kotakoski, R. Arenal, S. Kurasch, H. Jiang, V. Skakalova, O. Stephan, A. V. Krasheninnikov, E. I. Kauppinen, U. Kaiser, J. C. Meyer, Acs Nano 2012, 6, 8837.
[58] S. S. Datta, D. R. Strachan, S. M. Khamis, A. T. C. Johnson, Nano Letters 2008, 8, 1912.
[59] L. C. Campos, V. R. Manfrinato, J. D. Sanchez-Yamagishi, J. Kong, P. Jarillo-Herrero, Nano Letters 2009, 9, 2600.
[60] F. Schaeffel, M. Wilson, A. Bachmatiuk, M. H. Ruemmeli, U. Queitsch, B. Rellinghaus, G. A. D. Briggs, J. H. Warner, Acs Nano 2011, 5, 1975.
[61] L. Jiao, L. Zhang, X. Wang, G. Diankov, H. Dai, Nature 2009, 458, 877.
[62] L. Jiao, X. Wang, G. Diankov, H. Wang, H. Dai, Nature Nanotechnology 2010, 5, 321.
[63] R. Ribeiro, J.-M. Poumirol, A. Cresti, W. Escoffier, M. Goiran, J.-M. Broto, S. Roche, B. Raquet, Physical Review Letters 2011, 107.
[64] J. Cai, P. Ruffieux, R. Jaafar, M. Bieri, T. Braun, S. Blankenburg, M. Muoth, A. P. Seitsonen, M. Saleh, X. Feng, K. Mullen, R. Fasel, Nature 2010, 466, 470.
[65] J. A. Gardener, J. A. Golovchenko, Nanotechnology 2012, 23.
[66] H. Hiura, Journal of Materials Research 2001, 16, 1287.
[67] J. M. Poumirol, A. Cresti, S. Roche, W. Escoffier, M. Goiran, X. R. Wang, X. L. Li, H. J. Dai, B. Raquet, Physical Review B 2010, 82, 4.

Chapter 2

Sample Fabrication and Experimental Methods

CONTENTS

2.1 GRAPHENE SOURCES AND SAMPLE PREPARATION 37
2.1.1 Starting material *37*
2.1.2 Transfer of CVD graphene *39*
2.1.3 Samples for TEM experiments *41*
2.1.4 Sample fabrication for devices *42*
2.1.5 Samples for STM in Ultra High Vacuum *43*
2.1.6 Decontamination annealing *44*
2.2 SCANNING ELECTRON MICROSCOPY AND GAS INJECTION SYSTEM 46
2.2.1 Scanning Electron Microscope *46*
2.2.2 Oxygen injection system *47*
2.3 STRUCTURAL ANALYSIS 49
2.3.1 Transmission Electron Microscope *49*
2.3.2 Raman spectroscopy and mapping *51*
2.3.3 Atomic Force Microscope *51*
2.4 CRYO-MAGNETOTRANSPORT 51
2.4.1 Device fabrication *51*
2.4.2 Setup *53*
2.4.3 Cryo-magnetotransport Measurements *54*
2.5 REFERENCES 55

2.1 Graphene sources and sample preparation

2.1.1 Starting material

Two different types of graphene were used in order to fabricate the samples. The first one is mechanically exfoliated graphene from graphite flakes and secondly, graphene grown on metals by chemical vapour deposition (CVD).

Mechanically exfoliated graphene was produced starting from commercial graphite flakes (from Astiburry Company Inc, USA) [1, 2]. Those flakes are Kish graphite, produced during the cooling of carbon saturated hot iron in the steel

fabrication process (see Figure 2.1a). As shown in Figure 2.1b, one flake is placed onto a rectangular piece of wafer handling tape and cleaved off repeatedly, about 20 times (Figure 2.1c), until the tape is covered by a shiny layer of graphite as shown on Figure 2.1d. The material must be spread all over the tape to decrease its thickness.

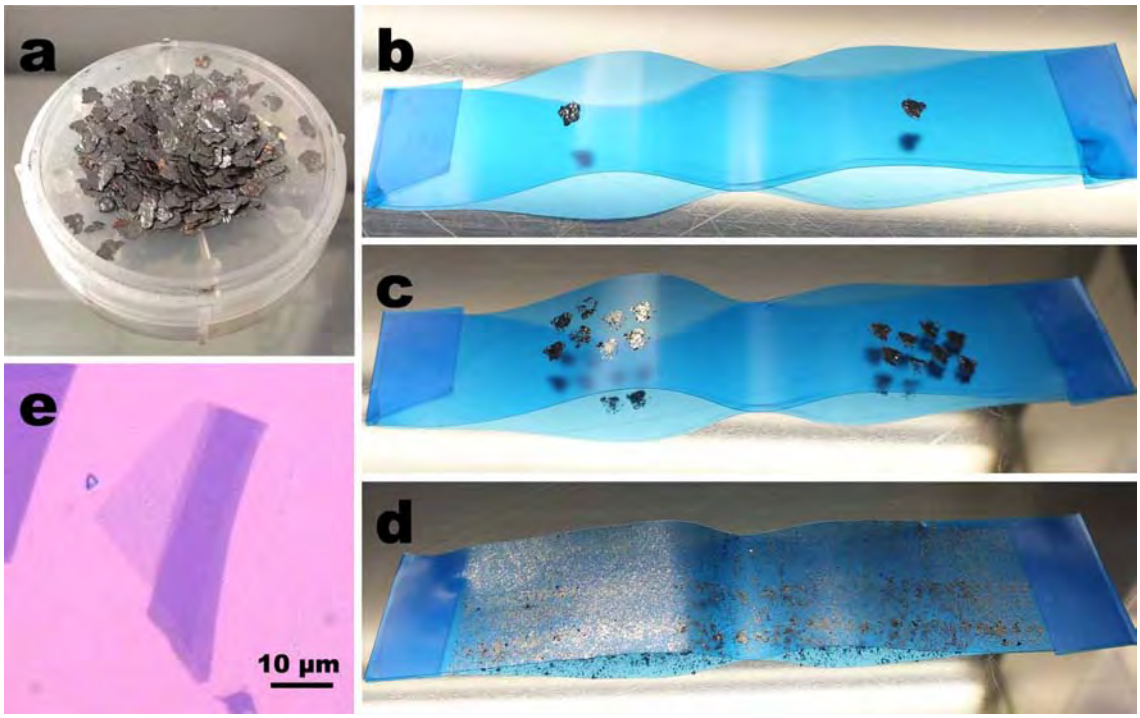


Figure 2.1: (a) The graphene source is a pile of graphite flakes.(b) Graphite flake is glued to a piece of wafer handling tape. Successive exfoliations lead to step (c) and finally to a tape fully covered by a homogeneous graphite layer (d). (e) Example of graphene flake on SiO_2 obtained by this process.

Once the tape is ready, it is pressed onto a pre-cleaned substrate and pealed off to induce the transfer of graphite pieces of variable thickness. The entire process is made under laminar flow hood inside a class 1000 cleanroom facility to avoid contamination during exfoliation. In Figure 2.1e, an example of a graphene monolayer deposited on a silicon dioxide substrate is shown.

Another graphene source is obtained from the Chemical Vapour Deposition of hydrocarbon precursors on metals. The process consists in the chemical decomposition of a carbon precursor (such as ethylene, methane, hexane, etc)[3] at high temperature around 1000 °C, over a metallic surface in the presence of hydrogen[4] and argon. The growth of graphene has been demonstrated on different metals: cobalt, nickel, copper, ruthenium, iridium, palladium, platinum gold, etc.[3]. We consider two potential CVD: grown on nickel and copper. Those two options have different growing mechanisms and results.

On the production of CVD graphene on nickel, carbon precursors are reduced by hydrogen during the high temperature step, carbon atoms are

deposited over the metal and diffuse to form a solid solution of carbon and nickel. Once the desired quantity of carbon is diluted in the metal, the temperature is slowly decreased. As the solubility of carbon on nickel depends on the temperature, carbon precipitates out of the metal in graphitic arrangement.[5]

On the other hand, carbon solubility on copper is too low to allow this mechanism. The current hypothesis is that partly dehydrogenated carbon precursors (reduced in gas phase by hydrogen) adsorbs at the copper surface[6]. Those species are free to diffuse over the surface. Further precursor influx induces the formation of nuclei that grow into one-layer graphitic flowers of carbon up to full surface coverage[7, 8]. The presence of adsorbed hydrogen promotes the formation of single layers of graphene[9, 10] by etching out the multilayers.

We decide to use CVD graphene grown on copper, as its growth mechanism is prone to produce monolayers. Although CVD techniques produces better graphene every day[11] enhancing the monolayer ratio and underlying metal crystalline properties[12]. The density of structural defects and thus the effective electronic mobility still remains below the one of exfoliated graphene values[8, 11, 13]. This is one of the reasons why the use of CVD graphene will be restricted the structural characterization of EBIE pattern etching rather than device production.

In this work, three sources of CVD graphene on copper are used: commercial CVD graphene on 4" circular copper foil of 18 μm thick with grain size up to 10μm and more than 95% coverage from Graphene Supermarket as well as Graphenea; and graphene produced by pulsed CVD by the team of Vincent Bouchiat at the Institut Néel in Grenoble[11].

2.1.2 Transfer of CVD graphene

In order to prepare GNR devices, CVD graphene is transferred onto a suitable substrate, typically consisting of thermal SiO_2 on Si. The first crucial step is to separate the graphene layer from copper. The metal is removed by soft chemical etching at the surface of ammonium persulfate. The reaction responsible for the dissolution of metal is the following:

$$\begin{aligned} &(NH_4)_2S_2O_8 + 2H_2 \rightarrow NH_3(g) + S_2O_8^{2-}(aq) + 2H_3O^+(aq) \\ &S_2O_8^{2-}(aq) + Cu(s) \rightarrow 2SO_4^{2-}(aq) + Cu^{2+}(aq) \end{aligned} \qquad (2.1)$$

The presence of NH_4^+ in solution stabilises the solution's PH and avoids the induction of structural defects (as it is the case for Na^+ for example). A slow etching rate is needed for getting pieces of graphene large enough to cover a typical 6x6 mm substrate. If the etchant is too concentrated and the reaction too fast, copper is etched into a multitude of little grains with sizes of a few hundreds of

microns. Those copper grains fall and break the graphene layer. The standard etchant concentration used is limited to 10^{-2} mol.L^{-1}. Even though it takes 48 to 72 hours to completely dissolve the copper foil. When a piece of graphene coated copper is floated on top of the solution surface, as shown in Figure 2.1a, the graphene layer is found floating at the liquid surface (Figure 2.2b).

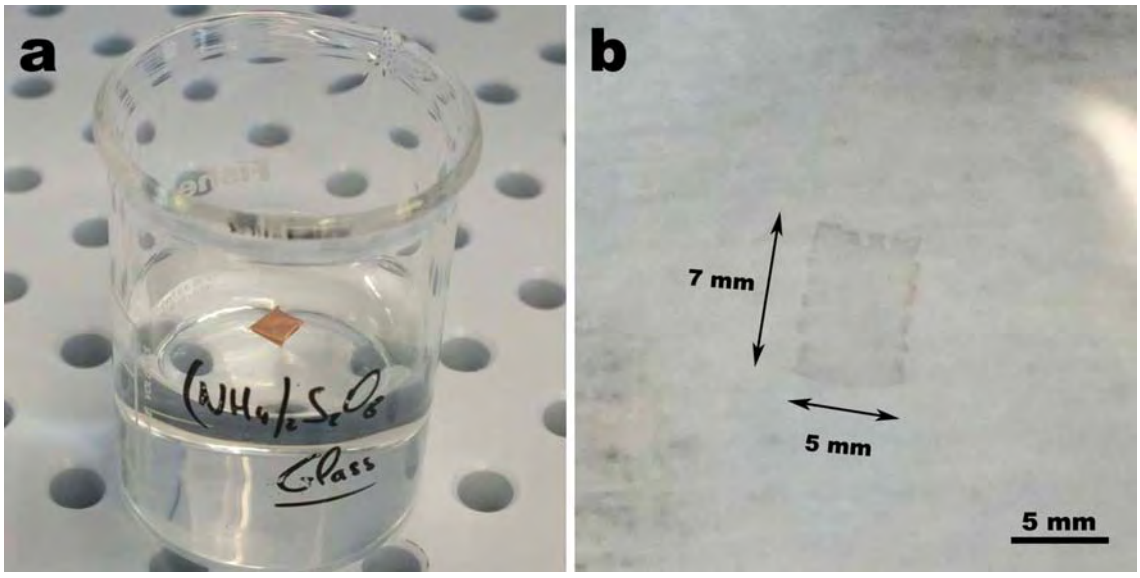


Figure 2.2: Removal of metal from a CVD graphene on copper sample.(a) Sample of graphene on copper stands at the surface of an aqueous solution of ammonium persulfate for the metal etching. (b) Remaining graphene layer after the complete removal of the copper.

The volume of etching solution must be adapted to the amount of copper to dissolve. For a typical piece of 5x5 mm of 18 µm thick copper, there is around $6.33.10^{-5}$ mol of atoms to oxidize. For that, the minimal volume of the solution of 10^{-2} mol.L^{-1} is 6,33 mL. The volume effectively used is 4 times higher (20 mL) to keep the reaction speed from decreasing too much during the reaction. At the end of this process, the underlying solution turns blue indicating the presence of Cu^{2+} ions in solution. Using more solution than theoretically needed is also useful to decrease the copper ions concentration at the end of the etching and limit Cu^{2+} contamination on the graphene. The floating graphene layer is transferred onto a deionised water to further remove possible contamination of copper ions and etching products. Finally the target substrate is immersed below the graphene and lifted-up. When the two materials are in contact, graphene sticks to the surface and can then be taken out from the liquid.

The CVD transfer process is easier to perform using unclean CVD samples. Indeed the lack of support during the transfer, such as resist[5, 14, 15], requires a delicate handling of the floating graphene. Otherwise, the manipulation induces damages such as cracks, holes, ripples and folds. At this stage, a sample covered by hydrocarbons has increased thickness as well as its visibility and strength that makes transfer easier.

2.1.3 Samples for TEM experiments

The Transmission Electron Microscopy (TEM) experiments were carried out on dedicated substrates consisting of a 3mm silicon discs with a central square, over which a silicon nitride membrane covered by a matrice of holes is suspended (see Figure 2.3a).

CVD graphene is deposited on the SiN_x membrane. As the TEM grids are light it is possible to improve the transfer process and avoid folding and breaking the graphene layer. By placing the grid directly on top of the CVD graphene on copper at the beginning of the copper etching (Figure 2.3b). The resulting grid is completely covered as seen in Figure 2.3c and the suspended areas typically looked like Figure 2.3d. In the suspended region, graphene layer, folds and multilayer areas can be seen, yet micron size free standing graphene monolayers could be readily prepared by this approach.

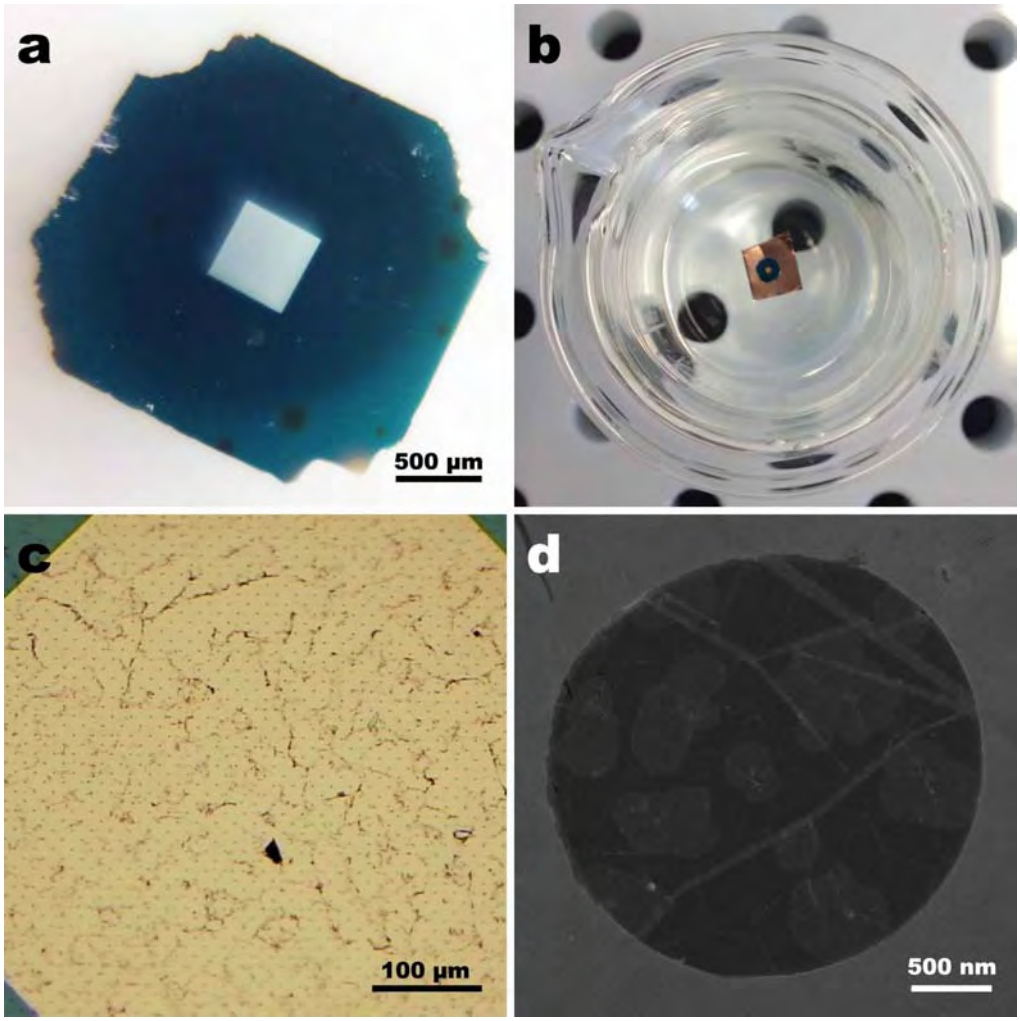


Figure 2.3: (a) Example of TEM silicon nitride grid used in this work for transmission electron microscopy experiments. (b) Transfer of CVD graphene from the copper to the grid, the result of this transfer is shown in (c), ripples are evidence of graphene deposited over the membrane. (d) Scanning Electron micrograph of one of the pores in the SiN membrane.

2.1.4 Sample fabrication for devices

Devices fabrication and electronic transport measurements were carried out on larger silicon dioxide on silicon substrates in order to contact graphene and to use the backgate electrode for field effect experiments[16]. The substrates are 290 nm thick silicon dioxide made by thermal oxidation on n-doped silicon. Photolithography combined with electronic beam metal evaporation was used to deposit a square cross mark matrix with 200 µm pitch size labelled from A to Z and from 1 to 26. In order to locally suspend graphene, pools were etched using Bosch process making a matrice of deep pools on the surface. The Bosch process uses an alternation of etching with plasma combined to SF_6 and C_4F_8 surface passivation to protect the sides of the pools. Following this method, developed by M. Rubio Roy (CEMES) in LAAS Renatech facility, we reach a depth value of 6 µm and a size of 1 per 5 µm. Finally, the wafer is diced into 6x6 mm substrates. A typical substrate is shown in Figure 2.4a.

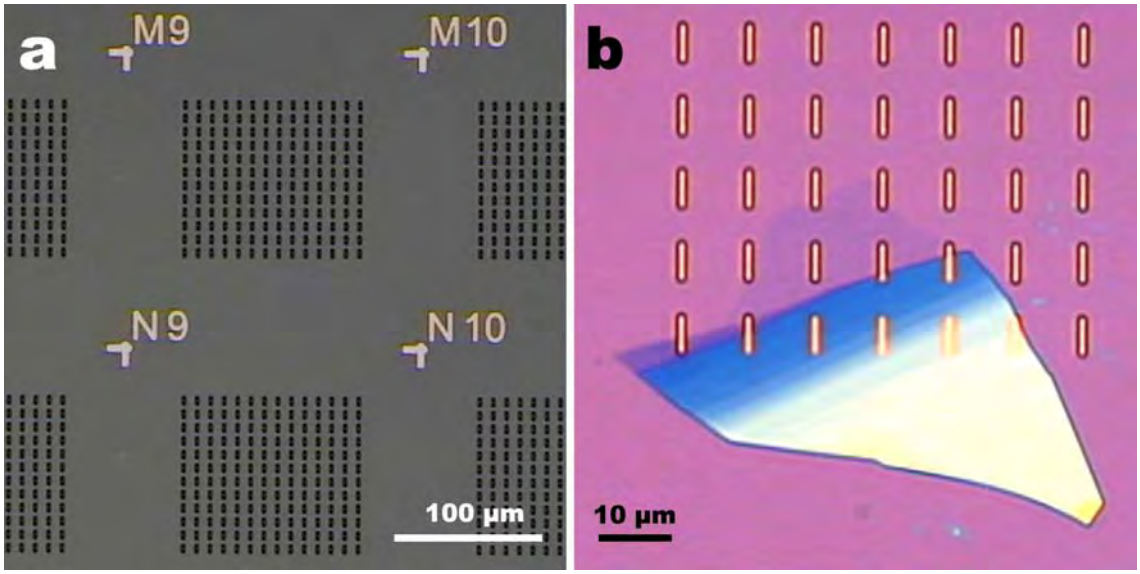


Figure 2.4: (a) Silicon dioxide on silicon samples with marks and pools used for transport measurements purposes. The marks matrice covers the 6x6 mm sample from A to Z and from 1 to 26. The holes are 6µm deep, 1 to 1,5 µm wide and 5 µm long. (b) Partially suspended graphene deposited by mechanical exfoliation on silicon dioxide on silicon samples with pools matrix.

Before graphene deposition, the substrate is cleaned using n-methyl-2-pyrrolidone (NMP) in a sonicator during 15 min followed by acetone (ACE) and isopropyl alcohol (IPA). Afterwards, the substrate is placed in a piranha solution (sulphuric acid 97% + hydrogen peroxide 30% 3:1 in volume ratio) during three hours. Then the substrate is rinsed in deionized water, IPA and dried. Finally oxygen plasma is applied for 4 min right before graphene deposition.

For electronic transport, exfoliated graphene is deposited rather than large graphene sheets from CVD growth so that single devices could be produce in a chosen graphene flake of about 10 to 30 µm by side, and because of the higher graphene quality[8]. Indeed in millimetre sized CVD graphene deposit, such device would have needed to be electrically isolated from the rest of the sheet which would have requested a detrimental etching step. The deposition is performed as described previously in this chapter (see section 2.1.1).

The resulting sample shown in Figure 2.4b is composed of partially suspended graphene over the pools on silicon dioxide.

2.1.5 Samples for STM in Ultra High Vacuum

For ultra high vacuum Scanning Tunnelling Microscopy (STM) experiments, TEM grids samples as well as silicon substrates with pools covered by CVD graphene are used. The silicon substrates were obtained by removing the silicon dioxide layer of the Si/SiO_2 substrates with 50% concentrated hydrofluoric acid (HF) followed by piranha. The CVD graphene transfer was performed as described in section 2.1.2.

Though this process produces satisfactory samples, a similar method to the CVD graphene deposition on TEM grid that increases the coverage of the sample, with less ripples and holes was attempted. The principle is the same as the TEM sample preparation, but the 6x6 mm silicon substrate is too heavy to be placed over a floating piece of copper. We use a vacuum pencil to keep the copper and substrate afloat, as well as a motorized plate that slowly lifts-up the beaker to compensate for the water evaporation over 48 to 72h. The setup is shown in Figure 2.5.

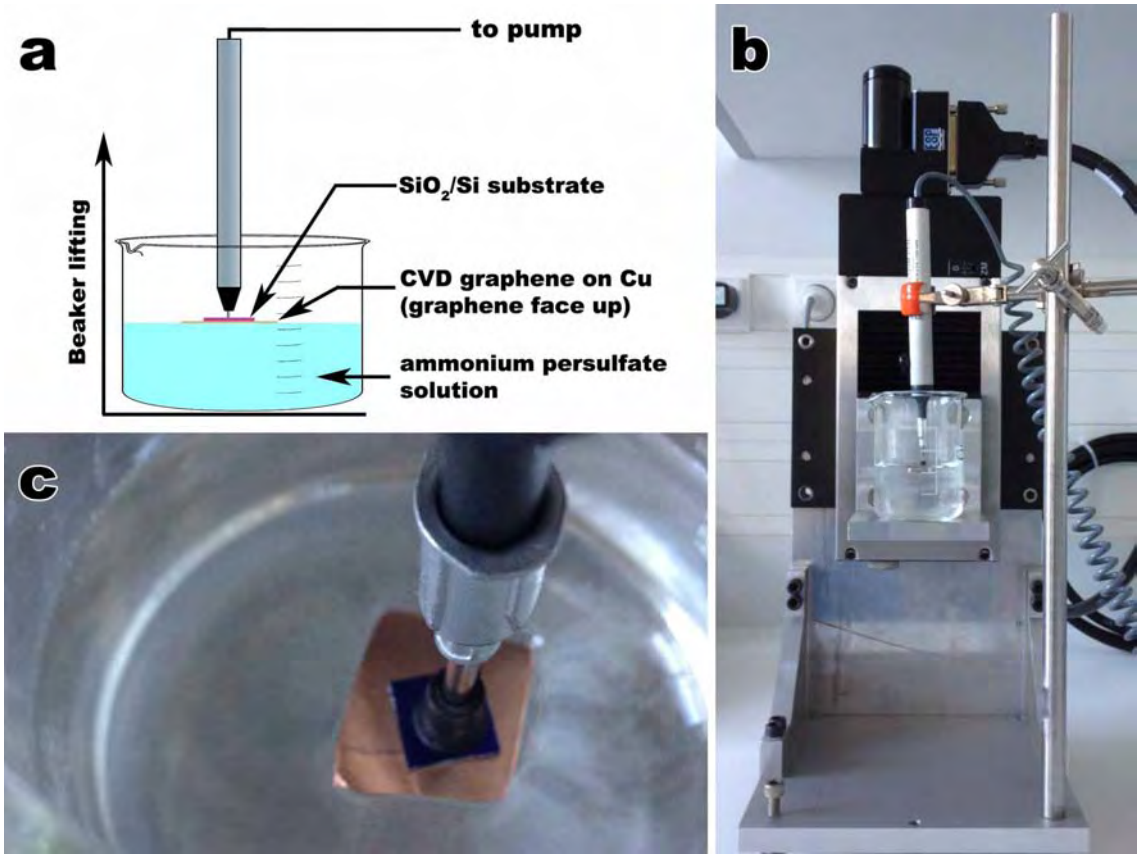


Figure 2.5: (a) Scheme of the CVD graphene deposition by placing the substrate directly over the graphene layer from the start of the etching. (b) and (c) Pictures of the lifting table and the vacuum pen setup.

The development of this process was not achieved but produced promising results. This technique, if further improved, can enhance CVD graphene depositions on heavy substrates, if they are not too hydrophilic or hydrophobic.

2.1.6 Decontamination annealing

After exfoliation of graphite or after CVD deposition, graphene is rapidly covered with adsorbates[17]. They are mainly composed of ambient carbonaceous materials like hydrocarbons or amorphous carbon. They induce modifications to graphene such as strain, doping (in addition to the doping induced by the substrate) and of course contamination. Those adsorbates have to be removed before the patterning or analysis of the material; otherwise the result will be modified by their presence. Yet graphene itself should not be damaged by the cleaning procedure. In our work graphene is cleaned by thermal annealing into an oven under reducing atmosphere (Ar, H_2). The reducing atmosphere will chemically remove the adsorbates transforming them into volatile products at moderate temperature (350 to 500 °C)[18].

The set up is shown in Figure 2.6 and was prepared by M. Monthioux, M. Delmas and L. Noé (CEMES). The sample is exposed to argon and hydrogen and temperature raised to activate the reaction between the hydrogen and the amorphous carbon of the sample but not enough to activate the hydrogen-graphene reaction. An Argon flow of 300 sccm ensures the H_2 feed and removal of by-products. Although the parameters of maximum efficiency should be the same for any graphene source, every substrate imposes different temperature limits.

The protocol for silicon dioxide on silicon samples is as follows. After introducing the sample into the oven, the tube is flushed with argon at 300 sccm during 10 minutes to remove air and dry the tube. Then temperature is set to 250 °C. Once the setpoint is reached (at 5 °C/min), the hydrogen inlet is open at 75 sccm during 4 hours. Afterwards, hydrogen inlet is closed and heating turned off. The sample is then naturally cooled at 1 to 2 °C/min under argon flow.



Figure 2.6: Quartz tube annealing oven. The gas inlets are on the right (lower flowmeter corresponds to argon, and upper one to hydrogen). On the left the outlet is filtered through a solution of dichloromethane.

For TEM silicon nitride grids, the annealing is performed at 550 °C under argon flow only during 4 hours. A second annealing step under hydrogen is performed at 350 °C instead of 250 °C to improve reaction efficiency.

We observed that annealing silicon dioxide samples at 550 °C resulted in tearing the suspended graphene flakes. This does not happen with graphene on the ultra high vacuum silicon samples neither in TEM silicon nitride grids. One possible reason is that the dilatation coefficient of the silicon dioxide induces stress to graphene during the annealing. Indeed there is a large difference of thermal expansion coefficient among those three materials. At working temperatures between 200 °C and 550 °C, silicon nitride membranes (Si_3N_4) have a coefficient of α_{SiN}= 2.6 to 3.2 K^{-1}, silicon α_{Si}= 3 K^{-1} whereas for silicon dioxide

α_{SiO2}= 9 K^{-1}. More stress is applied to suspended graphene on silicon dioxide during annealing than on silicon or silicon nitride. This interpretation is supposing that the graphene flake is large enough and adheres to the substrate.

Gold or copper type TEM grids are not recommended, as our experiments shown that metallic particles diffuse from the grid over the entire sample at temperatures as low as 240 °C.

2.2 Scanning Electron Microscopy and Gas Injection System

2.2.1 Scanning Electron Microscope

The microscope used for graphene patterning is a FEI DualBeam Helios NanoLab 600i Focused Ion Beam (FIB) (Figure 2.7). The main characteristics are a Tomahawk gallium ion column and a Scanning Electron Microscopy (SEM) Elstar UHR immersion lens FESEM column.

The FIB column produces a gallium beam with energies from 0.5 to 30 keV and currents from 1.1 pA to 65 nA. The column is also equipped with a Time-Of-Flight correction (TOF) to enhance low dwell time patterns.

The SEM column produces a focused electron beam with landing energy range from 20 eV to 30 keV and current from 1.3 pA to 22 nA. The electron beam maximum resolution at optimum working distance (and 4 mm) is 0.8 nm at 30 kV (STEM), 0.9 nm (0.9 nm) at 15 kV and 1.4 nm (2.5 nm) at 1 kV. There are two imaging modes; the classic mode is called field-free, the second one is called immersion and uses an additional lens located around the pole piece. The magnetic field of this lens covers the sample and optimizes the focalization giving a smaller probe size and better resolution. Five detectors are available: Scanning Transmission Electron Microscopy detector (STEM-BF/DF/HAADF), Through Lens Detector (TLD-SE/BSE), Concentric ring Back Scattered detector (CBS), Ion Conversion and Electron detector (ICE-SI/SE) and Everhart-Thornley detector (ETD-SE).



Figure 2.7: FIB/SEM FEI DualBeam Helios NanoLab 600i

The electron and ion beam coincidence point is at SEM analytical working distance of 4 mm and the angle between the two beams is 52 °. The main chamber vacuum can reach 10^{-7} mbar as a lower limit. Five gas injection systems are available for platinum, cobalt, tungsten and carbon precursors as well as oxygen. The sample is installed on a 5-axes motorized stage in which bias can be applied for beam deceleration from -50 V to -4 kV. In addition the machine is equipped with the following items: plasma cleaner (for sample and chamber), liquid nitrogen (LN_2) cryopumping reservoir, in-chamber infrared camera, Omniprobe AutoProbe 200 in situ sample lift-out system and FIB charge neutralizer.

In addition a Zeiss 1450 XB crossbeam with a Zeiss Gemini SEM column was used for imaging purposes. Its electron beam landing energy is between 2 and 30 kV. The default energy used in this work is 20 keV with a resolution of 1 nm. Six diaphragms are available of 7.5, 10, 20, 30, 60, and 120 µm leading respectively to nominal current values of 12.8, 28.1, 97.7, 763.7 pA and 2.91 nA at operating tension of 20 kV.

2.2.2 Oxygen injection system

Graphene etching is trigged by e-beam under oxygen using a gas injection system on the microscope. An oxygen cylinder (H_2O < 3 ppm) supplies the injection system through the yellow tube shown in Figure 2.8a. A pressure regulator sets the microscope inlet pressure to 1.5 bar. At the microscope, a pneumatic valve opens and closes the inlet followed by a needle valve used to

regulate the flow supplied to the nozzle (see Figure 2.8b). The high-pressure security of the microscope is setted to 10^{-4} mbar, the chamber pressure is raised just below this limit.

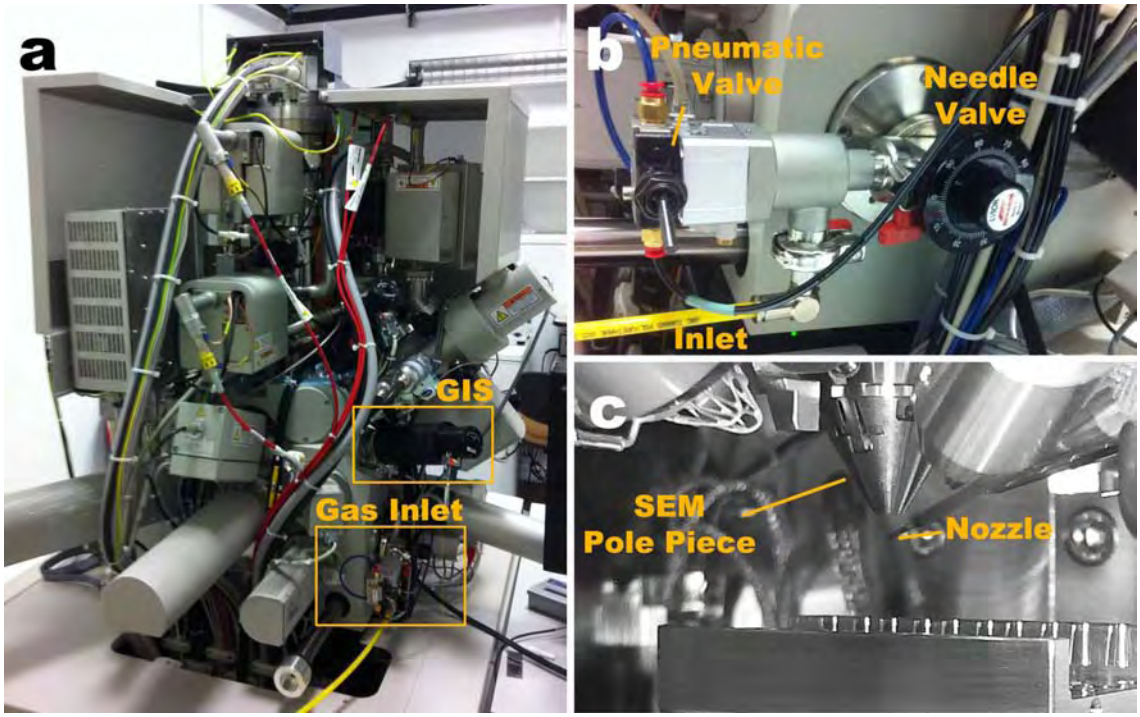


Figure 2.8: Detail of the oxygen injection system of the FEI Helios.(a) Rear part of the microscope, the gas inlet and the nozzle introducer. (b) Detail of the oxygen inlet. (c) View of the inside of the chamber through the infrared camera while nozzle inserted.

The gas from the injection system shown in Figure 2.8a enters the chamber by a pneumatic system. The end of the injection nozzle target is at 3.9 mm from the SEM pole piece in the z-axis for a sample WD of 4 mm (see Figure 2.8c).

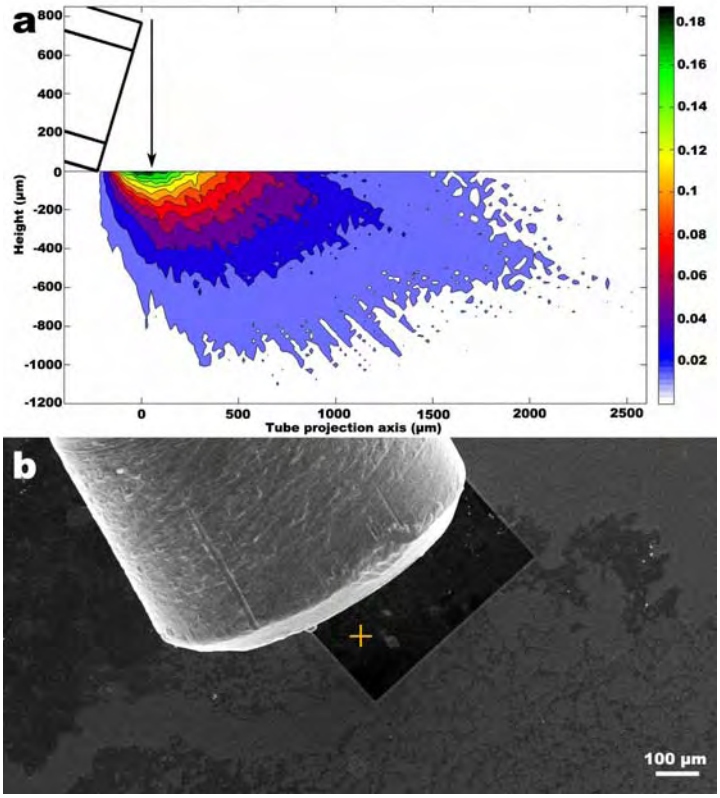


Figure 2.9: (a) Simulation of oxygen molecules impacts below the nozzle in arbitrary units (provided by FEI Company). (b) Position of the nozzle relative to the beam centre position (yellow cross).

In Figure 2.9a a simulation of the oxygen flow outside the nozzle show that the higher gas density is at the closer proximity of the nozzle. The position of the nozzle was fixed at around 50 µm of the electron beam centre position as shown in Figure 2.9b.

2.3 Structural analysis

2.3.1 Transmission Electron Microscope

An FEI Tecnaï F20 equipped with a CEOS image corrector is used. This microscope is set to 100 kV of operating tension and preliminary studies are performed with it before the lower energy analysis. On the other hand no microscope at CEMES was adapted to perform together high resolution and low acceleration tension (60 - 80 kV) microscopy.

In order to perform such analysis Transmission Electron Microscopy was performed in the LMA facility in Zaragoza using a FEI Titan^3 Cubed 80-300 (Figure 2.10) with the assistance of Raúl Arenal and made possible by the TALEM project. The operating acceleration tension can be set between 60 and 300 kV. The microscope is located in a box to fully insulate from acoustic, mechanical, thermal and light perturbations. The electron beam is produced by a Schottky gun emitter

FEG. High Resolution HRTEM images acquisition is made with a Gatan CCD camera 2 k x 2 k. For high resolution TEM, this microscope is also equipped with a SuperTwin objective lens as well as a CETCOR Cs-objective image corrector from CEOS Company raising the resolution to 0.8 Å.

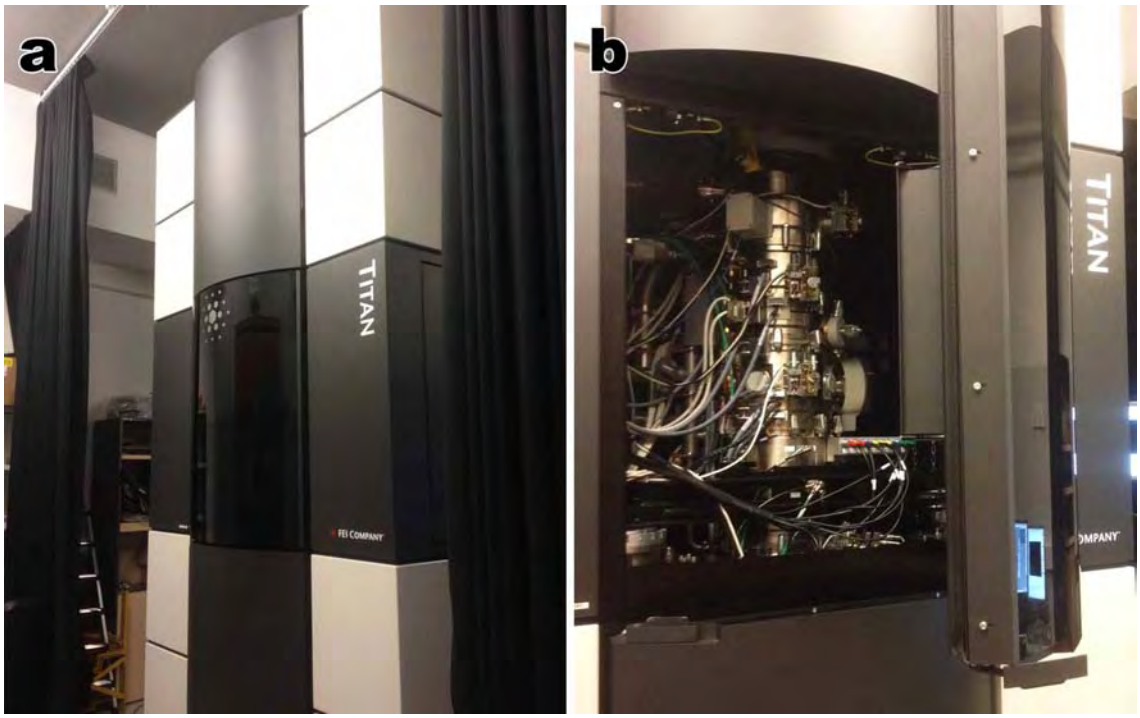


Figure 2.10: FEI Titan cubed S/TEM with image aberration corrector in the Laboratorio de Microscopías Avanzadas – Instituto de Nanociencia de Aragón in Zaragoza (SPAIN).

Moreover basic STEM facilities (BF and DF detectors) are installed in this machine as well as a Gatan Energy Filter Tridiem 863 allowing EELS experiments with an energy resolution of around 0.7 eV. A Lorentz lens and an electrostatic biprism are also available.

A heating sample holder Gatan Heating Holder 652 with temperature range from room temperature up to 1000 °C has been used in combination with the machine.

Once the sample is installed on the TEM holder it is heated up to 400ºC over night under secondary vacuum (around 10^{-7} mbar). Prior to the introduction in the Titan column, the operating tension is pre-set to 80 kV 8 to 10 hours before in order to have a stable electron beam. The extraction tension is 3950 V, slightly lower than the normal tension (~4200 V). TEM imaging of the sample is performed as usual. Work areas are firstly inspected at low magnification and acquisition parameters are optimized in the close vicinity of the area of interest. The sample is imaged with minimum or no previous exposure. To avoid any modifications due to electron exposition.

2.3.2 Raman spectroscopy and mapping

Raman spectra were measured using a Horiba Xplora-MV2000 spectrometer. The machine is equipped with three semiconductor lasers (λ_{green} = 532 nm, λ_{red} = 638 nm and $\lambda_{infrared}$ = 785 nm) with a maximum power of 40 mW. In addition a 500 µm confocal hole is used as well as a 100 µm slit. The spectra are collected by a CCD detector of 1024 pixels. Four gratings are available: 300, 600, 1800 and 2400 l.mm^{-1}. The spatial resolution of the microscope is 1 µm and the spectral resolution is down to 1.8 cm^{-1}/pixel at 532 nm and 1.1 cm^{-1}/pixel at 785 nm.

For Raman mapping a step-by-step motorized x-y table is used, the Raman spectra are then analysed by a homemade Fortran script. A typical 50x50 pixel map takes about 2 hours to be recorded. This acquisition timescale and the stage assembly require surveillance, as the non-motorized z-scale axis is prone to drift.

2.3.3 Atomic Force Microscope

Atomic Force Microscopy (AFM) is performed in tapping mode using one of two Veeco microscopes, either a Veeco Dimension 3000 or a Picoforce. The tips are Olympus OTESPA type with square pyramidal shape, made of silicon with a resonance frequency between 290 and 345 kHz and rigidity between 12 and 103 Nm^{-1}.

2.4 Cryo-magnetotransport

2.4.1 Device fabrication

In addition to the generic process described in section 2.1.4, graphene has to be electrically contacted and bonded to a suitable sample holder.

Two lithography techniques were performed by M. Rubio Roy and C. Bourgerette to contact graphene: Electron Beam Lithography (EBL) as well as laser lithography. The EBL writer is a RAITH 150 located in the Laboratory for Analysis and Architecture of Systems in Toulouse. The resolution is 20 nm and the positioning precision is 2 nm. The acceleration voltage can be selected from 1 to 30 kV. A PMMA 996 coating of 37 g/L is used as resist for this step to deposit a 150 nm thick layer.

The laser lithography machine is a Kloé Dilase 650 ultra violet laser lithography (see Figure 2.11a). It is equipped with two semiconductor lasers of λ_{uv1} = 375 nm and λ_{uv2} = 405 nm. Two different optic lines resulting on three different spot sizes can be selected: the 0.5 µm, 2 µm and the 20 µm line. Its feature precision goes down to 0,5 µm.

Metal (often Au monolayer followed by Pd) was deposited all over the sample by electron sputtering deposition.

After lift off made with acetone, the substrate is glued to a cryostat sample holder using silver paint as it is shown in Figure 2.11c.

A normal Kulicke & Soffa model 4523 wedge bonder machine is used to connect the lithography pads to the sample holder pins (Figure 2.11b). The wire used is 25μm thick and can be either gold or aluminium. The sample is heated during the bonding process to 80°C. The wire is welded by applying around 30ms of sonication (for aluminium) and pressure to the wedge.

Examples of lithography as well as wire bonding on cryostat holder are shown in Figure 2.11c and d.

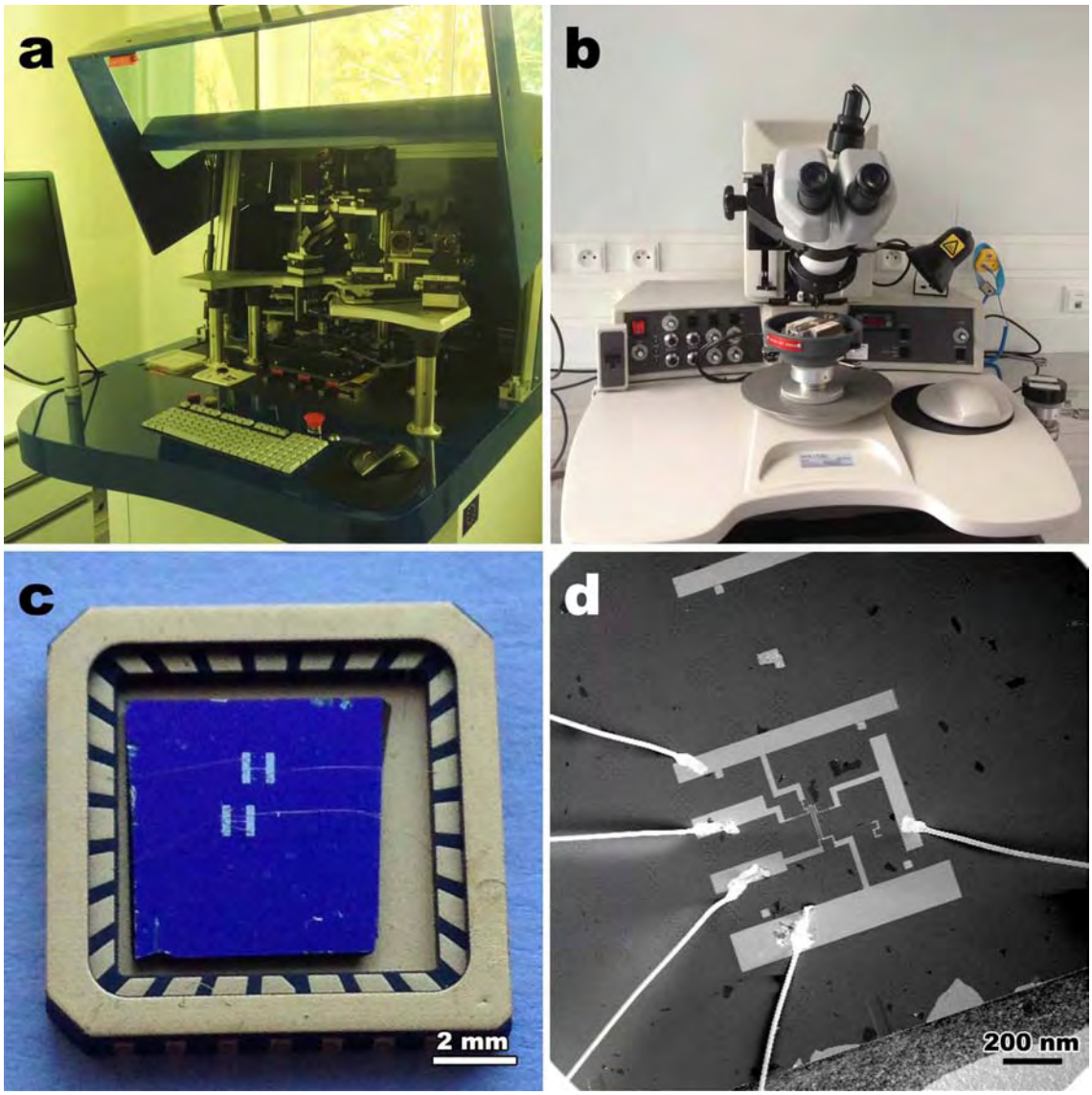


Figure 2.11: (a) The Kloé Dilase 650 photolithography writer. (b) K&S 4523 wedge bonder.(c) Silicon substrate with lithography devices glued and bonded to a 300 mK sample holder. (d) SEM micrograph of a device after lithography and bonding.

2.4.1 Setup

Cryo-magnetotransport measurements were performed in an Oxford Instruments liquid Helium (He^4) cryostat (see Figure 2.12a). A Sumitomo Cryogenics F-70H helium compressor and SRP-082B cryocooler cold head recondensate the helium vapours to avoid losses. The main chamber operating temperature is 4.38 K, but it can be pumped down to the triple point in order to decrease the temperature to 2.2 K.

In the main chamber a 32.4 H superconducting cryomagnet (see Figure 2.12d) produces a vertical magnetic field up to 14 T at 4.38 K and 16 T at 2.2 K at the sample position.



Figure 2.12: (a) Oxford Instruments liquid Helium^4 cryostat setup. (b) Variable Temperature Insert. (c) VTI installed and connected into the cryostat and cryostat top assembly. (d) Superconductive solenoid cryomagnet. (e) Sample holder socket and sample stick with electrical connections and thermometer. This machine has been used thanks to P. Salles (CEMES-CNRS).

In this cryostat, a Variable Temperature Insert (VTI) is placed (see Figure 2.12b). The VTI is insulated from the helium bath by a vacuum barrier. Liquid Helium from the main bath can be pumped into the VTI through a needle valve and through the bottom of the insert while gaseous He is pumped away at the top of the VTI. The inlet is a copper piece with a thermic resistance that can set the helium supply temperature from the bath temperature to 280 K. As the VTI chamber is continuously pumped the temperature range inside can reach down to 1.4 K and

up to 280 K. When the VTI is inserted as shown in Figure 2.12c, the bottom is placed in the coil.

The sample is installed in a socket at the end of a rod. This rod is introduced into the VTI in such a way that the sample is in the middle of the coil and facing down to the helium inlet of the VTI (magnetic field is perpendicular to the sample surface). A calibrated Si sensor is installed in the socket for temperature monitoring (Figure 2.12e).

For electronic measurements, Keithley electronics were used. For source and drain bias we used a 2635A simple channel sourcemeter, a 2612 dual channel sourcemeter for back gate potentials, as well as a 2000 multimetre all connected to the sample through a 707A switching matrix and finally a 2182A nanovoltmetre connected to a low noise 7001 switch. All this equipment is controlled using a LabView interface to control the temperature of the sample, and the electronic measurements.

2.4.2 Cryo-magnetotransport Measurements

Different types of measurement routines are possible depending on the chosen variable. Typical I(V) measurements were performed from the sourcemeter once the VTI temperature is stable. The electronics measure currents and tensions, resistance, conductance and normalized conductance are deduced from it.

Back-gated measurements are made by two different ways. The first is to measure the current at constant sample bias at different backgate voltages. The second one, is the measurement of a I(V) characteristic at every different backgate value. The first one is less exhaustive and can be extracted from the information obtained with the second method.

The same options are available for measurements under magnetic field. During magnetic field, a constant gate voltage can be applied simultaneously to keep the graphene sample at the Dirac point during the experiment.

2.5 References

[1] K. S. Novoselov, A. K. Geim, S. V. Morozov, D. Jiang, Y. Zhang, S. V. Dubonos, I. V. Grigorieva, A. A. Firsov, Science 2004, 306, 666.
[2] K. S. Novoselov, D. Jiang, F. Schedin, T. J. Booth, V. V. Khotkevich, S. V. Morozov, A. K. Geim, Proceedings of the National Academy of Sciences of the United States of America 2005, 102, 10451.
[3] Y. Yao, Z. Li, Z. Lin, K.-S. Moon, J. Agar, C. Wong, Journal of Physical Chemistry C 2011, 115, 5232.
[4] M. Losurdo, M. M. Giangregorio, P. Capezzuto, G. Bruno, Physical Chemistry Chemical Physics 2011, 13, 20836.
[5] A. Reina, X. Jia, J. Ho, D. Nezich, H. Son, V. Bulovic, M. S. Dresselhaus, J. Kong, Nano Letters 2009, 9, 30.
[6] I. Vlassiouk, M. Regmi, P. F. Fulvio, S. Dai, P. Datskos, G. Eres, S. Smirnov, Acs Nano 2011, 5, 6069.
[7] C. Hwang, K. Yoo, S. J. Kim, E. K. Seo, H. Yu, L. P. Biro, Journal of Physical Chemistry C 2011, 115, 22369.
[8] X. Li, C. W. Magnuson, A. Venugopal, J. An, J. W. Suk, B. Han, M. Borysiak, W. Cai, A. Velamakanni, Y. Zhu, L. Fu, E. M. Vogel, E. Voelkl, L. Colombo, R. S. Ruoff, Nano Letters 2010, 10, 4328.
[9] X. Li, C. W. Magnuson, A. Venugopal, R. M. Tromp, J. B. Hannon, E. M. Vogel, L. Colombo, R. S. Ruoff, Journal of the American Chemical Society 2011, 133, 2816.
[10] L. Tao, J. Lee, H. Chou, M. Holt, R. S. Ruoff, D. Akinwande, Acs Nano 2012, 6, 2319.
[11] Z. Han, A. Kimouche, D. Kalita, A. Allain, H. Arjmandi-Tash, A. Reserbat-Plantey, L. Marty, S. Pairis, V. Reita, N. Bendiab, J. Coraux, V. Bouchiat, Advanced Functional Materials 2014, 24, 964.
[12] J. D. Wood, S. W. Schmucker, A. S. Lyons, E. Pop, J. W. Lyding, Nano Letters 2011, 11, 4547.
[13] X. Li, W. Cai, J. An, S. Kim, J. Nah, D. Yang, R. Piner, A. Velamakanni, I. Jung, E. Tutuc, S. K. Banerjee, L. Colombo, R. S. Ruoff, Science 2009, 324, 1312.
[14] Z.-Y. Juang, C.-Y. Wu, A.-Y. Lu, C.-Y. Su, K.-C. Leou, F.-R. Chen, C.-H. Tsai, Carbon 2010, 48, 3169.
[15] W. Regan, N. Alem, B. Aleman, B. Geng, C. Girit, L. Maserati, F. Wang, M. Crommie, A. Zettl, Applied Physics Letters 2010, 96.
[16] P. Blake, E. W. Hill, A. H. Castro Neto, K. S. Novoselov, D. Jiang, R. Yang, T. J. Booth, A. K. Geim, Applied Physics Letters 2007, 91, 3.
[17] Z. Li, Y. Wang, A. Kozbial, G. Shenoy, F. Zhou, R. McGinley, P. Ireland, B. Morganstein, A. Kunkel, S. P. Surwade, L. Li, H. Liu, Nature Materials 2013, 12, 925.
[18] Y.-C. Lin, C.-C. Lu, C.-H. Yeh, C. Jin, K. Suenaga, P.-W. Chiu, Nano Letters 2012, 12, 414.

Chapter 3

GNR Fabrication by Oxygen Assisted E-Beam Etching

CONTENTS

3.1 ELECTRON BEAM INDUCED ETCHING PROCESS 57
3.1.1 Principles *57*
3.1.2 Water-induced etching on graphene *61*
3.1.3 Oxygen-induced etching on graphene *63*
3.1.4 Dose characterization *65*
3.2 MAKING GRAPHENE NANORIBBONS 66
3.3 HIGH RESOLUTION STRUCTURAL ANALYSIS 69
3.3.1 High Resolution TEM imaging of simple EBIE cuts *69*
3.3.2 Structural analysis of graphene nanoribbons *72*
3.4 DISCUSSION 74
3.5 CONCLUSION 77
3.6 REFERENCES 78

3.1 Electron Beam Induced Etching process

High-energy electron beam has been shown to be efficient to etch graphene by knocking-on carbon atoms from the lattice[1-7]. Our first aim in this chapter is to set a combined chemical etching that allows to control faceting with controllability of a guided beam. The second objective is to use this new process to pattern graphene nanoribbons. Finally we want to analyse the cuts and graphene patterned objects in atomic resolution to characterize the process performance.

3.1.1 Principles

Electron Beam Induced Etching (EBIE) consists in activating a reaction between the surface of a material and a reactive gas with the energy provided by an electron beam[8] (Figure 3.1a). The direct etching of materials by a focused electron beam often requires high energy to reach the knock-on threshold. Graphene for example, can be directly etched by an e-beam if its energy exceeds 86 keV[9] for bulk atoms and 50 keV for edge atoms[1, 5, 10]. Yet, in the presence of a

reactive gas, knock-on events can be replaced by activated reactions that require much less energy input. The gain in input energy provided by the e-beam will depend on the characteristics such as the activation energy and the chemical species produced. In our case, it is important to choose a gas that can react with graphene, while generating volatile by products. The advantages of this approach are numerous. Using this technique gives access to chemical properties such as crystalline directions affinities. Anisotropic chemical etching has been longer used for micrometre scale patterning, for example, of silicon[11, 12]. If usually used for shape-inducing process, we could benefit from this characteristic to produce high atomic edge quality GNR. The use of SEM at lower energy than TEM accelerations reduces the beam damage. Also it is possible to use a wider range of substrates beyond typical 3 mm diameter, electron transparent TEM substrates. One restrictive condition is to use conductive enough substrates to avoid charging; typically the sample should be able to evacuate currents in the range of 100 nA, usually surface conduction is sufficient. The beam path can be easily programmed to follow any arbitrary pattern and being fast blanked to avoid damage around the pattern.

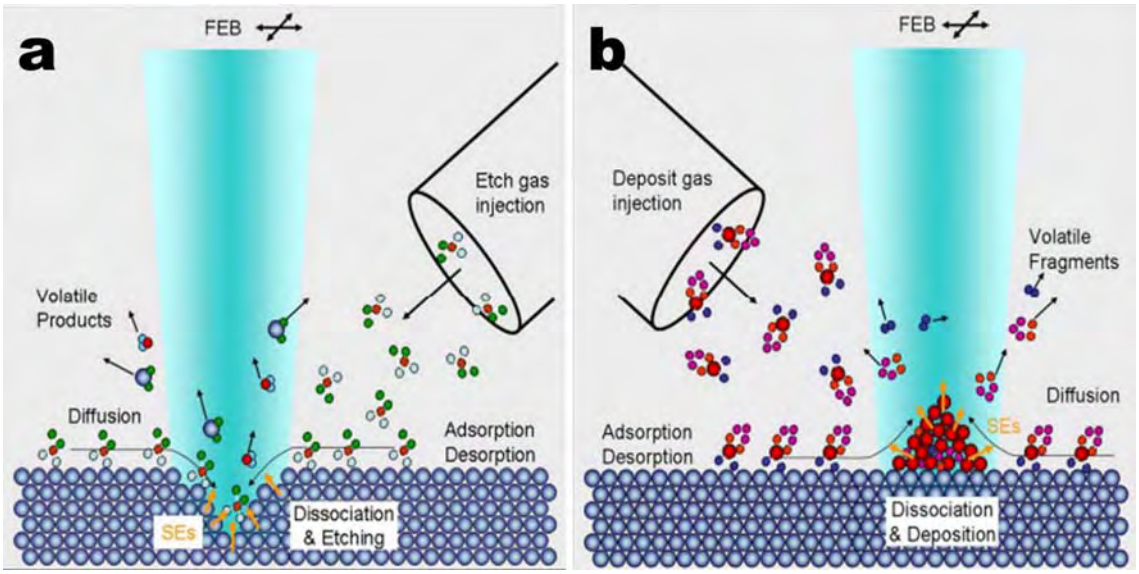


Figure 3.1: (a) Illustration of the EBIE and (b) EBID process, adapted from [8].

We should mention that etching process usually co-exist with e-beam induced deposition. Instead of a reaction between the gas and the sample, the beam energy can break the molecules in the gas near the focal point, thus producing non-volatile materials that deposit over the sample [13-17] (Figure 3.1b). The etching and depositing processes do not evolve at the same rate when changing beam parameters. The goal here will be to set parameters like dose, acceleration tension and gas flow to enhance graphene etching, and minimize deposition of amorphous carbon. The gas flow ensures the reactant replenishment at the reaction site. The dose (electrical charge delivered per area) must be high

enough to prevent or eliminate deposits while avoiding to deplete all reactive gas at the etching area.

For graphene etching, several reactions are conceivable, the simplest ones using water vapour[18], oxygen, hydrogen, ammonia, etc. In our case two possibilities are compatible with the SEM microscope chamber: water and oxygen, which can be injected in small amounts directly near the sample.

Programming the microscope is crucial for a good etching quality. The electron probe path is controlled digitally. Instead of following a path with a constant speed (analogic control), the beam executes a series of exposures at given coordinates. The sample is exposed spot by spot with exposure time and positions chosen by the user. To etch lines, the relevant parameters are the overlapping between two successive expositions (or the pitch), exposure time per pixel and number of scans per line (Figure 3.2).

The first concern is the overlap parameter, as edge roughness depends highly on it and it is one important step to calculate the dose. The overlap, O_p, is set in percentage on the microscope and corresponds to the step size (pitch) over probe size (P_s) ratio (see equation (**3.1**)). The effective probe size can be measured by analysing the smallest producible hole and comprises around 95% of the probe dose (Figure 3.2a). It depends on microscope acceleration tension, diaphragm (current), magnification and working distance. For a 20 keV beam at 1.7 nA and 4 mm of working distance, the probe size is 8 nm.

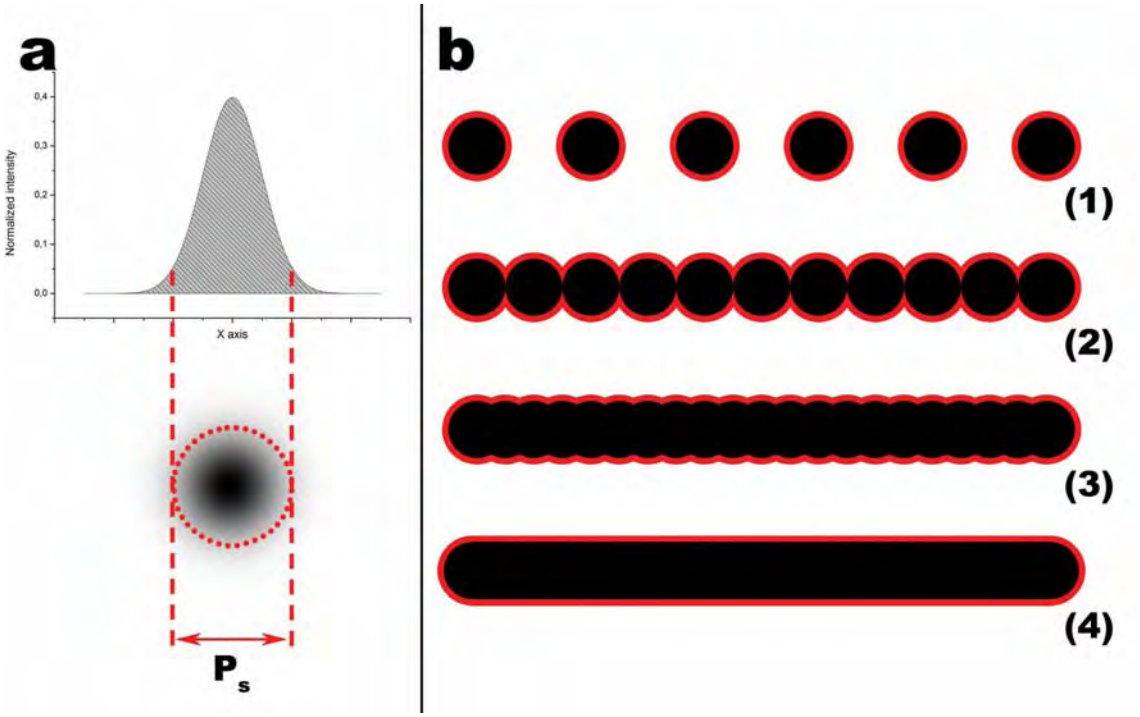


Figure 3.2: (a) Electronic distribution of the probe and probe size definition. (b) Scheme of lines exposed at different overlapping parameter: (1) -100%, (2) 0%, (3) 50% and (4) 95%.

The formula for the overlapping ratio is the following:

$$O_p = \frac{Pitch}{P_s} \tag{3.1}$$

Etching with steps bigger than the probe size, results in a series of dots as seen in Figure 3.2b (1). As the overlap is increased, the holes become tangent and a continuous line can be etched. But as we observe in Figure 3.2b (2) (overlap = 0%) the etching of a series of circular dots leads to arch-shaped edges. To avoid this phenomenon and get edges as smooth as possible, the overlap was increased progressively to reduce edge roughness (see Figure 3.2b (3)) while concomitantly reducing the dose per dot. As the overlap is limited by the resolution of the microscope, the final value, used all along this work, extracted from experimental observations, was 95% of overlap (Figure 3.2b (4)).

The irradiation dose unit is C.nm^{-2}, for one single spot irradiation the dose is given by the following formula:

$$D_s = \frac{I \cdot t_e}{\pi \cdot \left(\frac{P_s}{2}\right)^2} \tag{3.2}$$

Where I is the SEM probe current, t_e the exposition time and P_s the probe size. In the case of a straight line with overlap the dose becomes:

$$D_l = \frac{I \cdot t_e \cdot \left(\frac{L}{(1-O_p)\cdot P_s} + 1\right)}{L \cdot P_s + \pi\left(\frac{P_s}{2}\right)^2} \cdot N \tag{3.3}$$

Where L is the line length, O_p is the overlap ratio and N the number of scans. If we consider $L >> P_s$ we can simplify the relation as:

$$D_l \approx \frac{I \cdot t_e}{(1-O_p)\cdot P_s^2} \cdot N \tag{3.4}$$

A dose equivalency can be found between overlapped and non-overlapped etching:

$$t_l \approx \frac{4 \cdot (1-O_p)}{\pi \cdot N} \cdot t_s \tag{3.5}$$

Where t_l is the exposition time for a line with overlap O_p and t_s the exposition time for a single dot. Using this geometrical model allows us to perform and analyse dose experiments by etching single dots and transpose the results to line etching (see section 3.1.4).

3.1.2 Water-induced etching on graphene

The first part of the work was done in the Zeiss microscope. Those experiments are used as a reference and comparative point for the rest of this thesis.

In the following experimental tests, two available precursors to etch graphene are used: fluorine and water (Figure 3.3). The pristine suspended graphene sample (Figure 3.3a) is first flushed by fluorine precursor while scanning with the e-beam between the two arrows (Figure 3.3b). As result neither etching nor deposition is observed at the graphene level, whereas the underlying silicon seems to be etched by this process. We conclude that this precursor does not interact efficiently with graphene or carbon but does so with silica.

The second test is performed using water vapour instead. Graphene is etched (Figure 3.3c) along 6 different lines. Hence water is indeed reacting with graphene as expected and conditions are favourable for graphene etching. Interestingly, a supplementary test with fluorine destroys the layer (Figure 3.3d). We deduce that silicon has deposit below the graphene layer and held the layer in place. Amongst all possibilities, we know that water is a good candidate to etch graphene and we will now characterize the performance of this process.

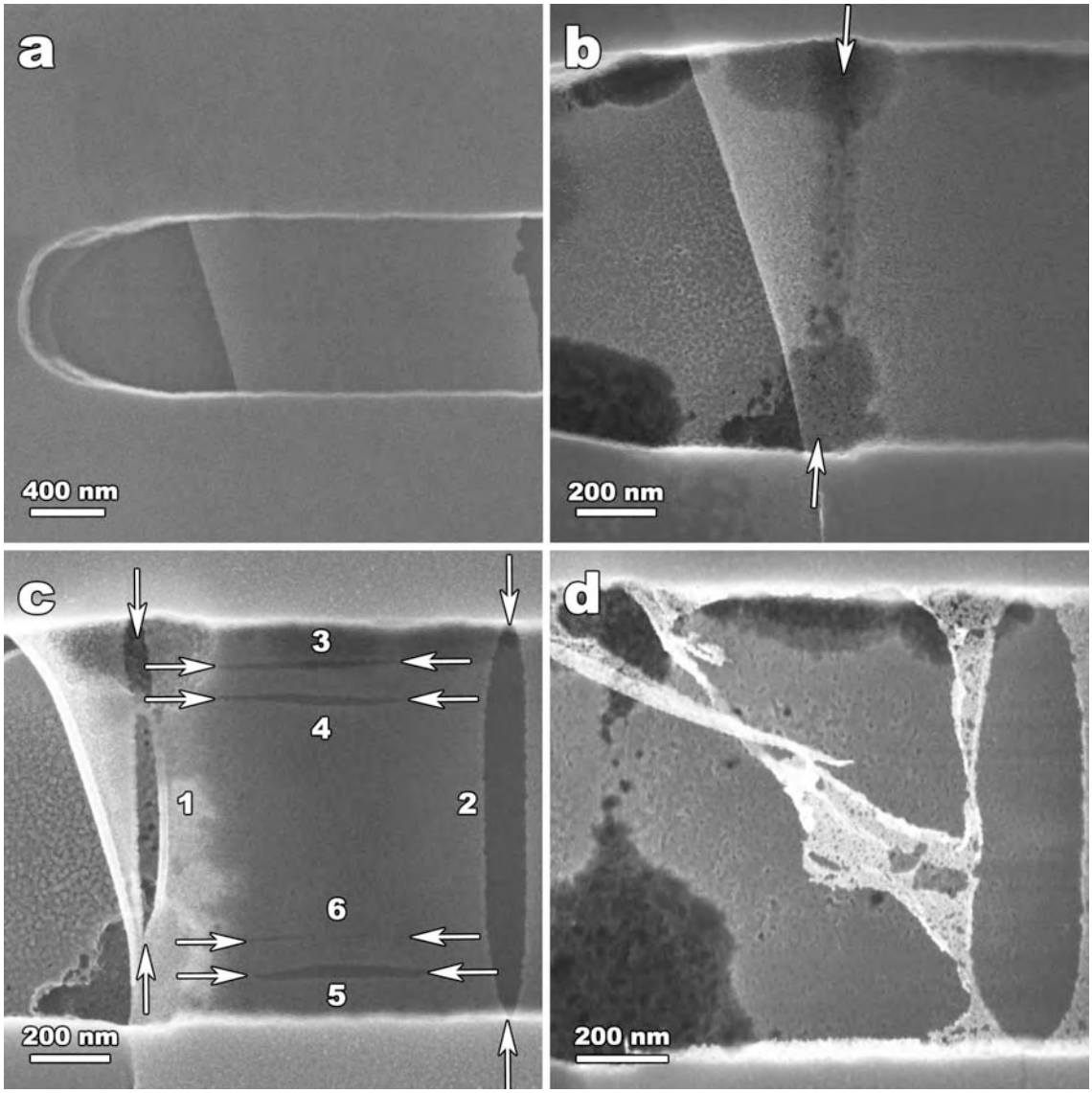


Figure 3.3: Experimental test etching using fluorine on graphene. (a) Pristine pseudo-suspended graphene sample. (b) Test using fluorine with e-beam. (c) Water-EBIE etching of cuts until saturation. (d) Fluorine has been used again during EBIE.

Other water assisted EBIE tests were performed on TEM grids as well as silicon dioxide substrates with pools. The Figure 3.4 shows the difference between the etching results using water on annealed samples (Figure 3.4a) and samples covered by amorphous carbon (Figure 3.4b).

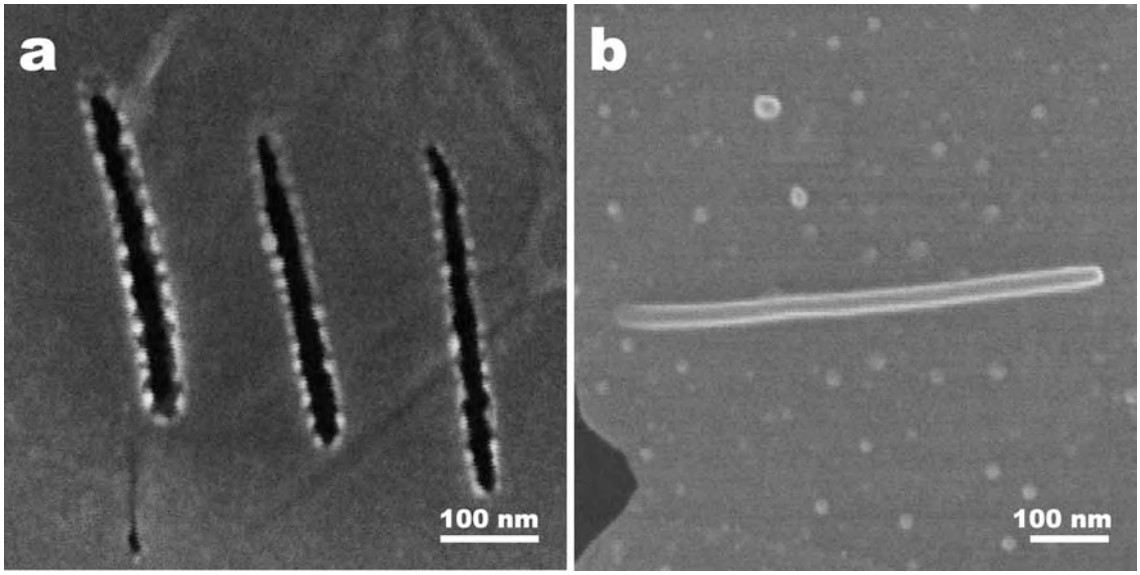


Figure 3.4: Cuts on graphene using water assisted EBIE. (a) Clean sample etched successfully and (b) an unsuccessfully etching on a non-properly clean graphene sample.

The results of Figure 3.4a show the effectiveness of the etching. The graphene layer has been perforated along three lines successfully. Those lines are around 25 nm wide. One can notice insulating (white contrast), pearl-shape debris deposited on the edges. This material is most provably amorphous carbon deposited during the etching. Even taking into account the deposition, the edge roughness is around 5 nm. We define the edge roughness as the amplitude between the least and the most protruding parts of the edge (Figure 3.4a). Figure 3.4b illustrates the impact of contamination present on the sample before cutting. In this case the e-beam induced processes are dominated by the deposition of amorphous carbon. No effective cutting is observed. It is therefore crucial to perform extensive sample cleaning to reach conditions where etching is effective and deposition is minimal (see Chapter 2 section 2.1.6). In spite of this we have observed that H_2O assisted EBIE is always prone to a finite amount of re-deposition. We interpret this as the result of H_2O vapour condensation near the focal zone of water vapour drops and EBIE by products that favours re-deposition. We thus considered changing the reaction gas.

3.1.3 Oxygen-induced etching on graphene

The oxygen assisted EBIE etching technique is similar to the water assisted EBIE process, only the reactive gas is changed. Oxygen has lower dew point (-62 °C) compared to water (18 °C for 90% of humidity at 20 °C). In addition oxygen is more reactive and water can carry or trap hydrocarbons that contaminates the sample. Oxygen is less likely to condensate on the graphene surface and cause deposition of amorphous carbon. We now apply the EBIE process using oxygen in

order to analyse the resulting effect (Figure 3.5a). If the process allows to pattern graphene we will proceed to optimize the process.

To draw a line, the shape, overlap ratio, pixel exposition and number of scans are set and the pattern is positioned with respect to the last SEM image. The sample is flushed with oxygen and e-beam patterning is launched. After a few minutes of pumping, the result is imaged with minimal exposure. Next, the patterned graphene can either be studied by further SEM imaging or preserved for other analysis.

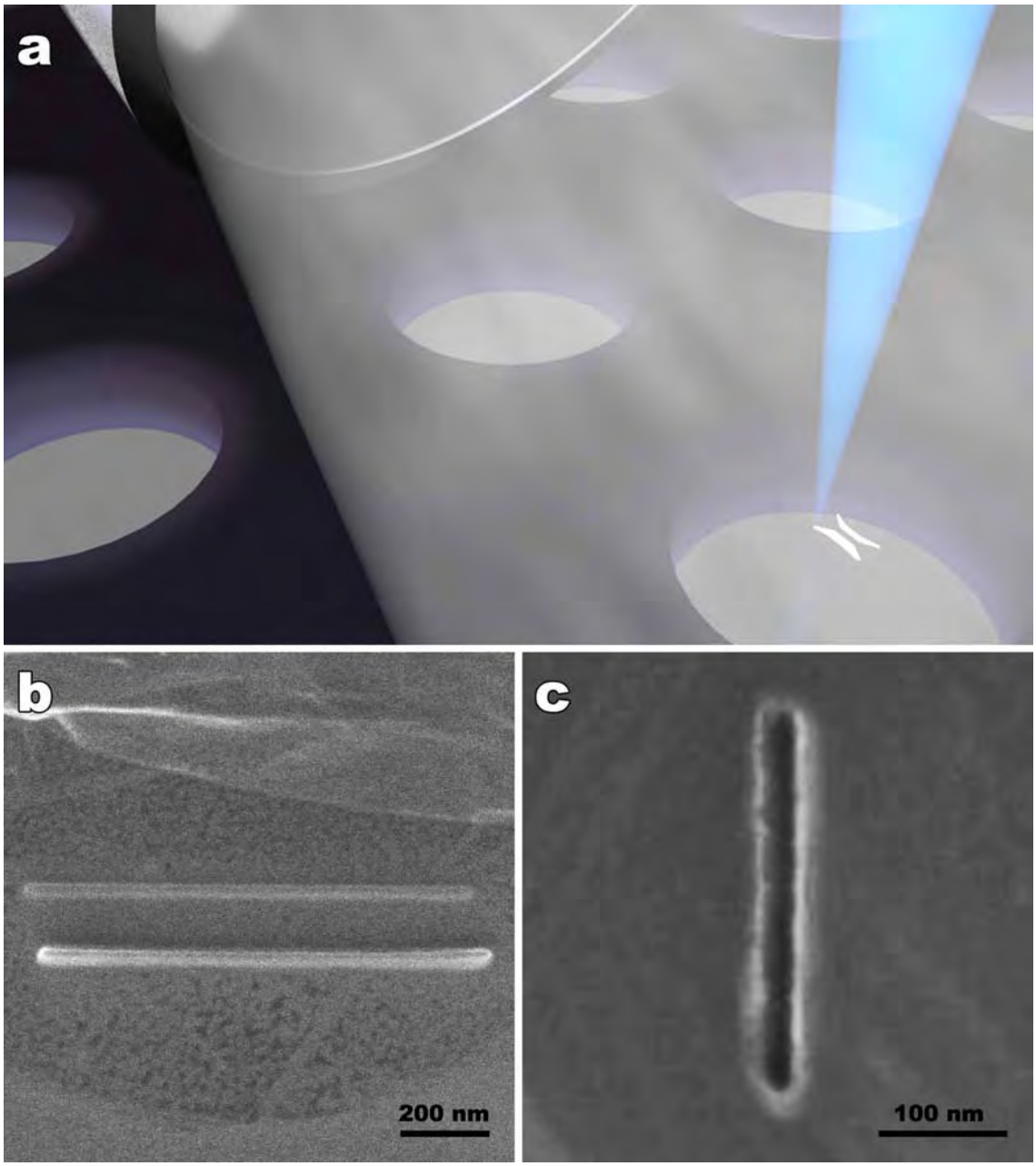


Figure 3.5: (a) Schematic of the oxygen EBIE etching on TEM grids for SEM and SACTEM analysis. (b) Result of an EBIE etching at low current. (c) Etching performed with 1.7 nA.

The main parameter determining the etching result is the dose (equation (**3.3**). Patterning with low probe current (below 1 nA) leads to high deposition rate, and no net etching (Figure 3.5b). The first successful etching is observed using the 1.4 nA diaphragm (current value around 1.7 nA) and an exposition time of 100 ms/pixel (50% overlap) and 12 scans at 10 KeV. Those parameters correspond to a dose of $D = 5.5 \cdot 10^{7}$ C.m^{-2}. Once the etching is effective, the parameters can be adjusted to find the minimal exposition time requested for faster patterning. The minimal exposition producing a continuous and straight cut at 1.7 nA is 6 to 8 ms/pixel at 95% of overlap and 2 scans (Figure 3.5c). The cut measures 300 nm long by 20 nm wide. The corresponding dose is $D = 2.76 \cdot 10^{6}$ C.m^{-2}. Depending on graphene quality and the presence of amorphous carbon on the sample those values could double this minimal dose. The etching is effective at 5, 10 or 20 kV acceleration tension. Using a different acceleration tension mostly changes the line width, which is reduced at higher acceleration voltage. The aim is to etch with minimal amorphization and minimal deposition rate. For properly cleaned graphene, the lower the exposition, the lower the amorphization and the a-C re-deposition. For samples with a big amount of a-C, big enough to force the increase of the dose, even if a higher dose can allow drilling the layers, cutting will always cause an important deposit of a-C in the etching close environment.

3.1.4 Dose characterization

In this section we present a study of the dose effect when etching graphene with oxygen assisted EBIE (Figure 3.6). As we can see in the plot of etched surface versus the dose, the dose required to activate the reaction is at around $0.5 \cdot 10^{8}$ C.m^{-2}. The etching rate first increases rapidly with increasing and then saturates after $D = 2 \cdot 10^{9}$ C.m^{-2}. The fact that those values are high compared to experimental values is probably due to the small nominal probe size taken into account by the microscope. The measurements present an important standard deviation (148.72 nm^2 at $4 \cdot 10^{9}$ C.m^{-2}). We deduce, and we associate this value, to important variations of the contamination from one sample to the other. Indeed more contaminants makes the etching harder, and increases the a-C re-deposition on the working area.

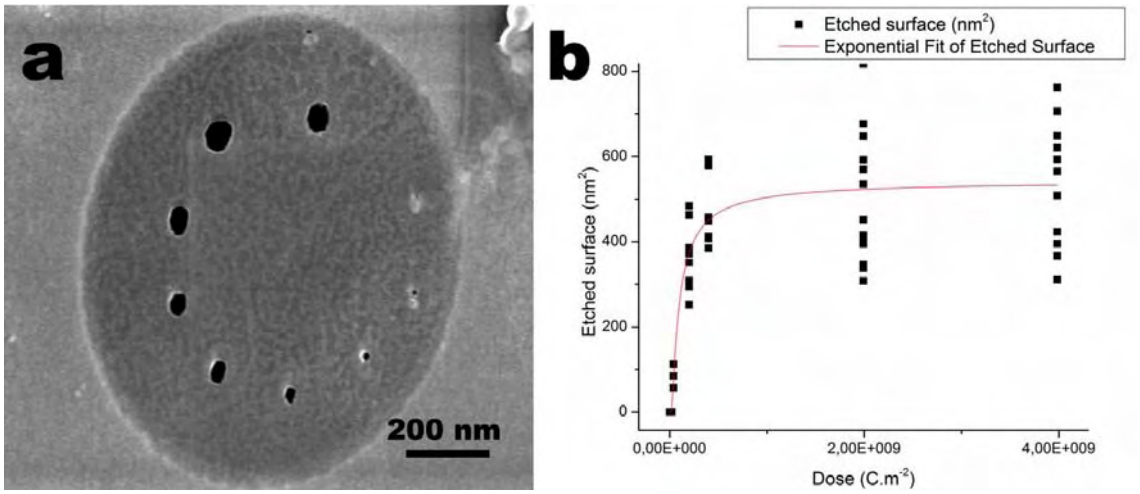


Figure 3.6: Dose experiment of surface etched versus dose supplied. (a) SEM micrograph of increasing exposure (2 s, 4 s, 7 s, 10 s, 15 s, 20 s, 30 s, 40 s and 50 s), as well as a (b) plot and fit of all data.

The smallest hole we could perforate was using a 1 s exposure. If we use the equation ((**3.4**, seen in section 3.1.1), we deduce that for 95% overlap and 2 scans, a maximum exposition time of 31.8 ms per pixel should be enough to perform straight cutting.

3.2 Making graphene nanoribbons

The challenge in fabricating GNR is to etch two parallel lines, within less than 100 nm of each other.

The etching of the graphene nanoribbon must be realized in one single shot. Indeed, imaging the area between the cutting of two lines would produce unwanted carbon deposition making the following cut harder or even impossible. The pattern chosen for our graphene nanoribbons is displayed in Figure 3.7a. The length and separation of the two sides of the ribbon will change depending on the desired GNR length and width. The V shaped areas will be used for electrode connection and will not change during this work. Those connections are set at a $\pi/6$ angle compared to the ribbon to minimize the contact impedance as described in Chapter 1[19].

A second important issue to take into consideration are the over-exposed areas at the meeting point of two lines. An inaccurate positioning or realization of the cuts can double the exposure. As a consequence, the GNR could be constricted at this position, .This proximity effect is particularly probable at both ends of the GNR where four cuts converge on a 100x100 nm area resulting in amorphized or damaged graphene that will directly impact the electronic properties of the GNR. As it corresponds to a corner, there is no need of a high overlap to produce a straight edge. The two lines need to be close enough to break the graphene between them. In principle, an overlap or even a coincidence is not necessary.

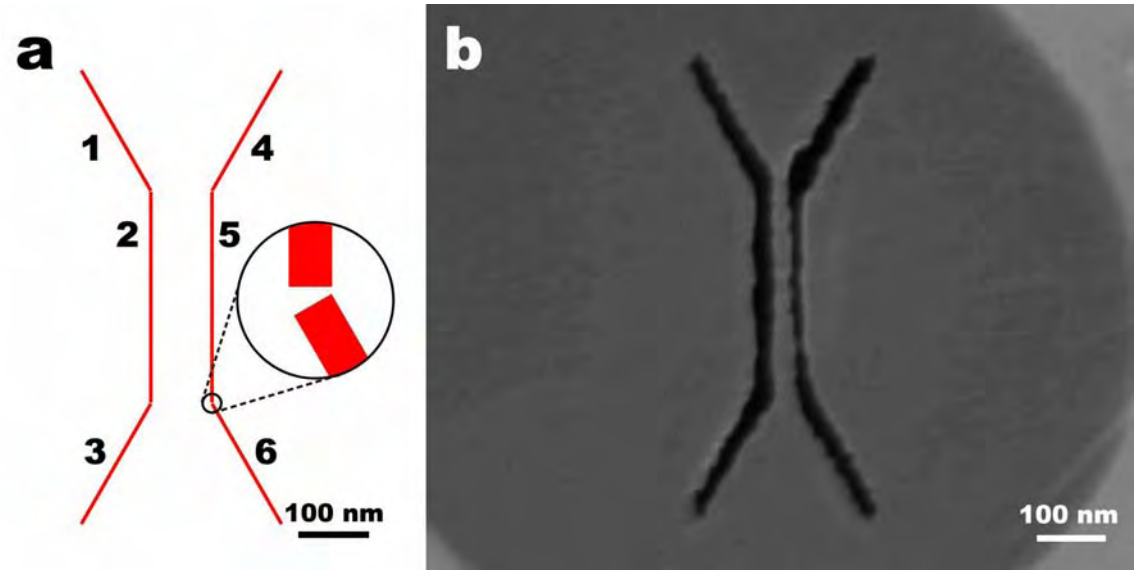


Figure 3.7: (a) correspond to the GNR pattern shape chosen for the ribbons fabrication. Length and width can be adapted. (b) is an example of oxygen EBIE etching of pattern in (a)

To etch a GNR, the total cutting length in the Figure 3.7a is about 1µm. Since the optimal parameters are 6ms/pixel, two passes, an overlap of 95% and a nominal probe size of around 1 nm, we obtain a total etching time of 280 s (4 min 40 s). But the microscope will need about 5 min due to beam repositioning. If the sample requires higher exposition, the etching time can rise up to around 8 min for an 8 ms/pixel exposure. Therefore the system needs to show a remarkable stability to avoid stage, sample or beam drift by more than a few nanometres over 5 to 10 min.

The EBIE technique allows the etching of GNR of variable size down to 4 nm and lengths up to the micron range. Changing the width will not affect the etching time, but it will increase in proportion to the length of the ribbons. Examples of different widths and lengths of GNR are shown in Figure 3.8. Although the SEM can reach large imaging fields (in this case up to 1 mm), resolution criteria to allow the beam to execute 0.05 nm steps imposes a maximum field of view of around 2 µm (with our column). Long range etching with high edge quality require stage repositioning, which is another instrumental challenge.

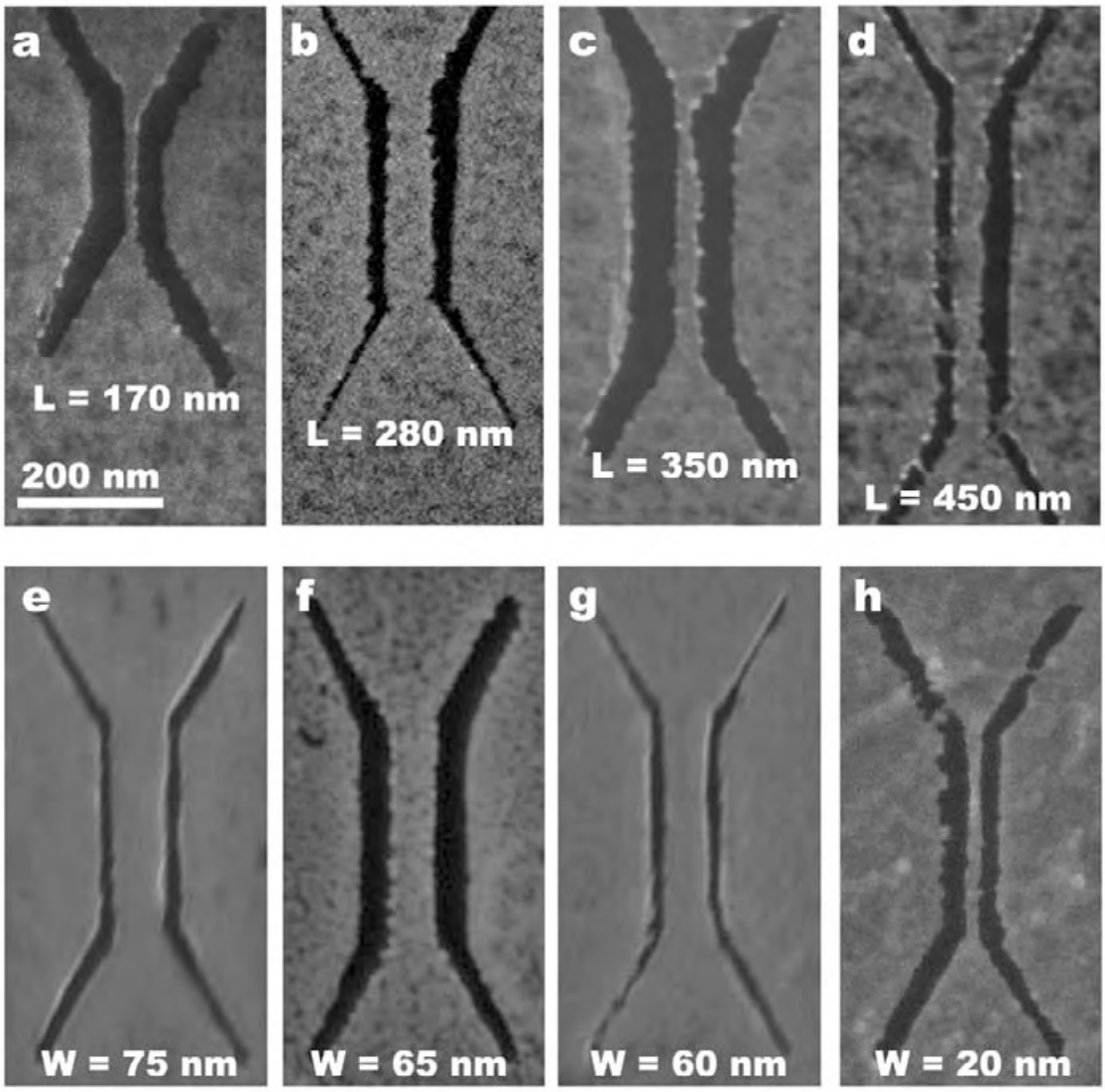


Figure 3.8: Examples of oxygen-EBIE etched GNR on suspended graphene on SiN TEM grids. Top line shows different lengths from (a) 170 nm, (b) 280 nm, (c) 350 nm and to (d) 450 nm. At the bottom line are presented different widths: (e) 75 nm, (f) 65 nm, (g) 60 nm and (h) 20 nm.

The process, once optimized, is robust, reproducible and reliable and allow to make, at will, any ribbon geometry within a given range. (Figure 3.8). At times, the resulting GNR can be contaminated by a-C, causing bridges and making the ribbon thicker. Consequently GNR were cleaned by a post-fabrication annealing step as described in section 2.1.6 before further and higher resolution analysis (see Chapter 2 section 2.1.6).

3.3 High Resolution structural analysis

Spherical Aberration Corrected Transmission Electron Microscopy (SACTEM) allows to analyse suspended graphene with atomic resolution. In order to turn EBIE into a generic on-demand graphene patterning technique, one needs to assess the quality of the resulting ribbons. In particular, the structure of the edges cut by oxygen assisted EBIE. The edges could be amorphized, rough, full of adsorbed amorphous material or, on the contrary, crystalline, straight and adsorbate-free. Similar assessment is required for the core of the GNR. This material has to be characterized to determine if it is still graphene, if the lattice has been damaged and if the edges of it are the same quality as for the cut, better or worse. Such analysis was conducted at 100 kV and 80 kV to prevent TEM electrons from damaging the graphene.

3.3.1 High Resolution TEM imaging of simple EBIE cuts

In order to establish a reference, we first analyse water-assisted EBIE cuts and edges (Figure 3.9). The cut in Figure 3.9a is imaged at 100 keV. The edges appear to have a roughness around 3 nm. This roughness is in the state of the art compared to chemical etching techniques[20-22] which produces edges with 1 nm of roughness. At the edge we can observe one graphene crystalline domain. No other similar situations, where the graphene lattice is visible until the edge, have been observed amongst the other samples. The rest of this edge does not present straight lines, which could indicate the presence of graphene underneath a thick amorphous coating. The lattice around the cut is not visible, therefore no quantitative evaluation of the lattice quality could be made.

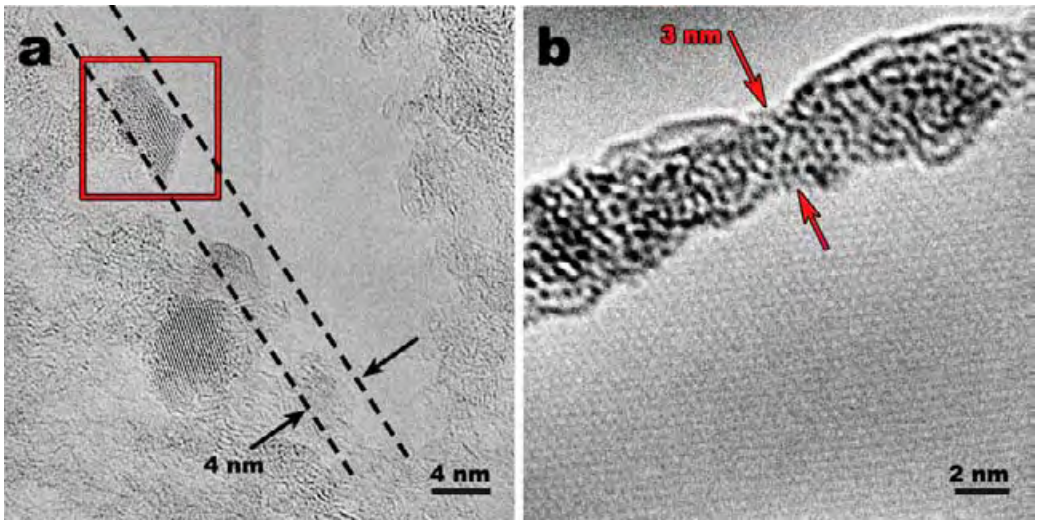


Figure 3.9: (a) SACTEM micrograph of a water-EBIE etched line imaged at 100 keV at the Tecnaï. (b) GNR edge etched by water-EBIE imaged at the Titan³ at 80 keV.

Figure 3.9b shows a similar result. A 3 nm to 5 nm band of amorphous carbon is visible along the graphene edge. Beyond this band, graphene appears as crystalline. The amorphous band could not be removed even by prolonged exposure to the high voltage beam and prevented any characterization of the edge underneath. The first possible explanation is that graphene is present, although not observable, beneath the amorphous. Then, the maximum roughness of the edge is about 4 nm, corresponding to the mean width of the a-C band. Alternatively, graphene terminates at the a-C band. In this case, the effective roughness is set by the graphene/a-C interface and is limited to about 1 nm.

Therefore SACTEM results do not confirm if water-assisted EBIE can produce crystalline edges. In addition the use of water was always associated with basal and edge contamination by amorphous carbon. The rest of the chapter will report the effects obtained by replacing H_2O by O_2 while preserving most of the developed protocol

Figure 3.10 shows the analysis of typical EBIE cuts and edges performed with oxygen. In Figure 3.10a we see both edges of a line cut. Firstly, all along the edge, graphene hexagonal arrangement is visible up to the very edge and no a-C band is present here. The edge roughness is limited to 0.8 nm. This roughness is in the range of high energy STEM etched graphene edges. Secondly, the graphene crystal all around the cut is intact and no important amorphization is visible.

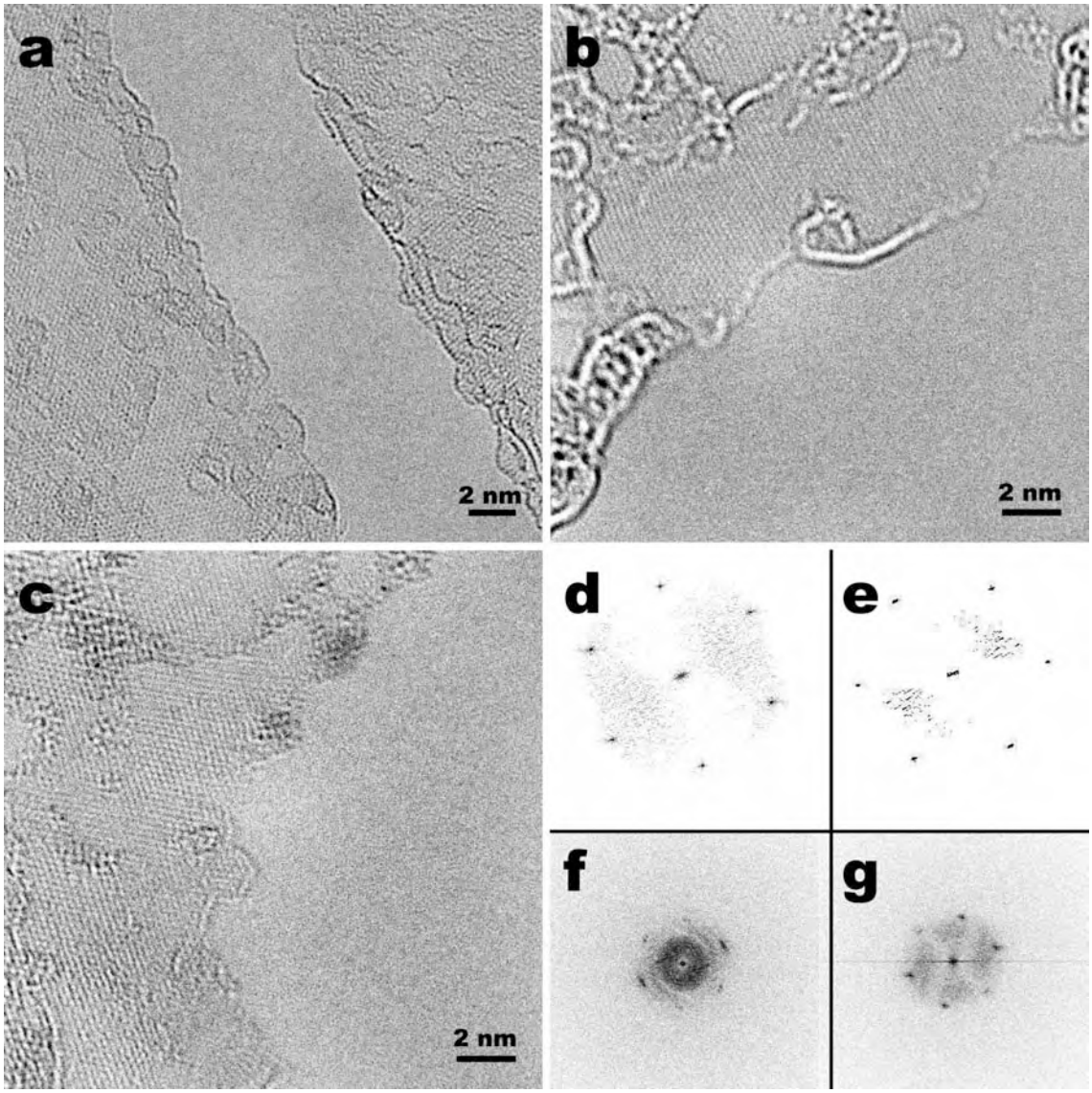


Figure 3.10: TEM micrographs of single EBIE cuts made with oxygen. (a) Side-to-side cut imaged at the Titan³ at 80 keV, (b) and (c) examples of edges imaged at the Tecnaï at 100 keV.(d) FFT of graphene in (a) left, (e) in (a) right, (f) of picture (b) and (g) of picture (c)

Figure 3.10b and c show the edges of two additional oxygen EBIE cuts. Figure 3.10b confirms that crystallinity of graphene is maintained up to the edge. Moreover, the edge roughness at short range is relatively low (2 nm). The atomic arrangement of the edge is not disordered and some parts are straight as if they were cut along a specific crystalline direction. Figure 3.10c also shows the crystallinity of patterned graphene all along the edge. In this image we also notice that the edge is made of straight lines separated by marked angles of values multiple of 60° as one would expect from atomically oriented edges. From the micrograph's FFT (Figure 3.10g) we deduce the presence of armchair oriented edges. It thus appears that oxygen EBIE etching produce non-amorphized edges eventually crystalline and provide substantially better quality etching than the water based equivalent.

3.3.2 Structural analysis of graphene nanoribbons

While single cuts have been improved by using O_2, we must investigate the quality of graphene nanoribbons when two cuts are performed in close vicinity. Figure 3.11 shows the results of the SACTEM observation of oxygen EBIE patterned GNR at 80 keV. Two parts of the GNR are analysed: the centre of a 16x320 nm ribbon and one of the connections. In the connection micrograph we see a part of the edge, which appears smooth and straight. From this edge, the graphene crystal lattice is continuously visible all the way to the middle. In the ribbon's micrograph we see the GNR edges. We notice that a significant fraction of the GNR is covered by a very thin layer of amorphous carbon. Indeed, the graphene lattice is still visible through the a-C deposition. The edges are straight all across the image, especially for the bottom one, and he upper edge appears slightly folded.

A closer look to a GNR (Figure 3.11b) displays smooth and straight edges even at relatively low magnification. The higher resolution micrograph (Figure 3.11c) shows the atomic arrangement of the edge. The roughness of the edge is limited to the sub-benzenoid ring size. Although direct visualisation of the atomic configuration of the edge orientation could not be recorded, it can be solved by a comparison to the Fast Fourier Transform (FFT). The insert of Figure 3.11c corresponds to the FFT of the micrograph where graphene signal maxima are surrounded by red circles. If we compare the orientation of the FFT pattern to the edge, we can conclude that the arrangement of the edge is armchair. This observation is confirmed by the analysis of the TEM contrast collected at the edge of the GNR. Figure 3.11d is the cross sectional intensity collected along the edge. Its Fourier transform is shown in Figure 3.11e. The FFT reveals a spatial frequency of $1/2.08$ Å^{-1}. The contrast collected includes 3 pixels, so probably correspond to two atomic rows. The spatial frequency corresponds to the frequency of an armchair edge, which has a repetition distance of 2.12 Å.

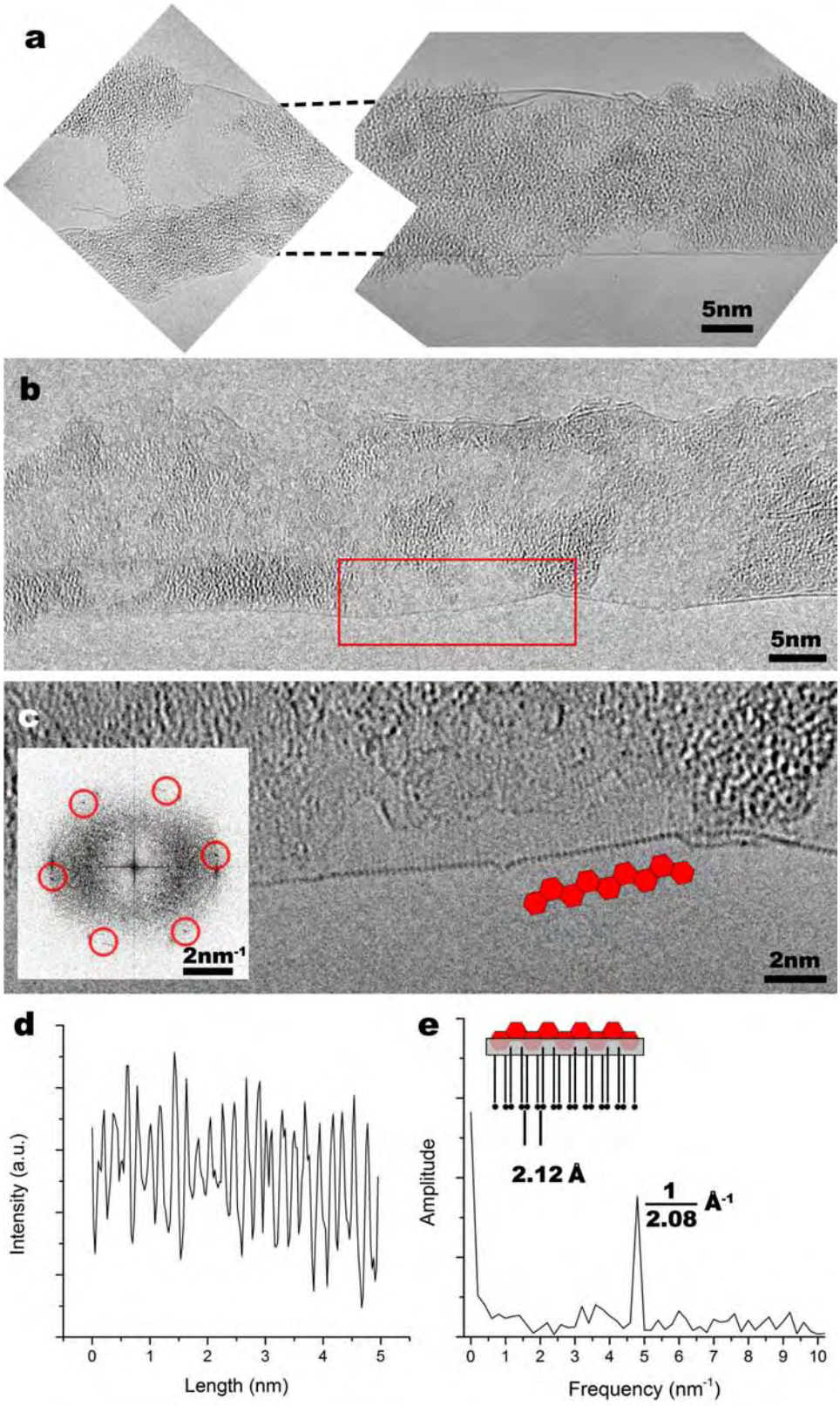


Figure 3.11: Spherical aberration corrected TEM analysis of a 320nm long and 14nm wide graphene nanoribbon. (a) Micrograph of the centre (right) of the ribbon as well as the V shaped connection at one end (left). (b) Micrograph of the middle of another graphene nanoribbon of 320nm long and 16nm wide. (c) Zoom of the micrograph in (b) at the edge area. The insert of (c) corresponds to the Fast Fourier Transform of the image. (d) Profile of the edge in (c) in front of the red-hexagon diagram, and (e) it's Fourier transform.

3.4 Discussion

EBIE etching assisted by oxygen has revealed better results than fluorine and water, but what is the reaction mechanism? We will discuss the edge as well as connections morphology produced by this process. We will also focus on an important GNR morphology parameter: its width. In addition we will discuss the contaminants present on our samples and their origins. Finally the TEM observations are performed at least at 4 times higher energy than SEM, could this be modifying graphene characteristics?

Even using clean samples, after the etching, a-C deposition is visible around the work area. Immediately after patterning, SEM imaging of etched GNR by EBIE provides some indications of the quality of the ribbon. The contrast of a pristine and clean graphene layer is particularly dark (conductive) and many details are visible such as grain bounds, bilayers and macroscopic defects. When an a-C layer covers graphene, the contrast is brighter (insulating) and the sharpness of details is covered by a cotton-like blur. The amorphous material deposited can have three origins. First one is the amorphous carbon present on the sample itself. This sample has probably been contaminated because of atmosphere hydrocarbons. Those contaminants are vaporised by the e-beam and re-deposited around the pattern area. Most of this contamination is removed by the annealing described in Chapter 2. The amorphous carbon can react in reducing atmosphere before graphene gets damaged or modified. Amorphous carbon is also produced by the decomposition of residual contaminants present in the SEM chamber, under the rastering e-beam. Finally the by products produced by the EBIE reaction are prone to be re-deposited all around the patterns. Though the third one can hardly be avoided, we can limit the effect of the others by annealing the sample, and working on a clean microscope chamber in as high vacuum as possible.

As the knock-on energy of graphene is 86 keV[9, 10], which is higher than the TEM energy, the energy is too low to damage bulk graphene but the beam can help removing amorphous carbon from the surface of graphene [4]. Although it is insufficient to damage bulk graphene, 50 keV[1, 5] are enough to remove atoms at edge position or reorganize them. Experiments at 80 keV in the same beam conditions show that edges are unchanged during our analysing time range (from 1 to 5 min). Samples need to be imaged in TEM using minimal exposition to avoid such modifications.

Concerning the crystalline edges we have produced, the chemical reaction between oxygen and graphene is responsible for it. But we do not know yet what is the reaction taking place. We propose two hypotheses for the mechanism of the

reaction. The first is the graphene combustion producing carbon monoxide and dioxide. The activation energy required for this reaction (~40000 cal/mol = 17.3meV/atom [23]) is more than 10^6 times lower than SEM beam energy. This reaction though is not known for being crystalline selective, therefore it is not responsible for the etching. The second mechanism involves the formation of ozone and oxygen radicals from the gas injected under the electron beam. This reactive species react with graphene to break carbon-carbon bonds. Yet the oxygen inlet is 800µm in diameter and so the ozone and radicals distribution at the graphene surface would be on the range of the inlet diameter size around the beam's target. We deduce that such species are produced with oxygen adsorbed on graphene. This solution explains both line width and crystallinity.

The atomic arrangement observed at the edge is armchair-like. It is unlikely though that armchair direction corresponds exactly to the cuts orientation. Thus the edge is most probably a combination of armchair and zigzag segments. The edge can change its orientation by tuning the zigzag/armchair ratio of the edge. In Figure 3.11c, the right part of the edge would be zigzag according to the micrograph's FFT proving this hypothesis. Even if graphene lattice orientation had been observed before patterning, which could be possible by STEM and FFT in the SEM chamber, grain boundaries changes crystal orientation. This shows the need of big crystals in CVD graphene if we want to produce GNR with the same edge properties all along.

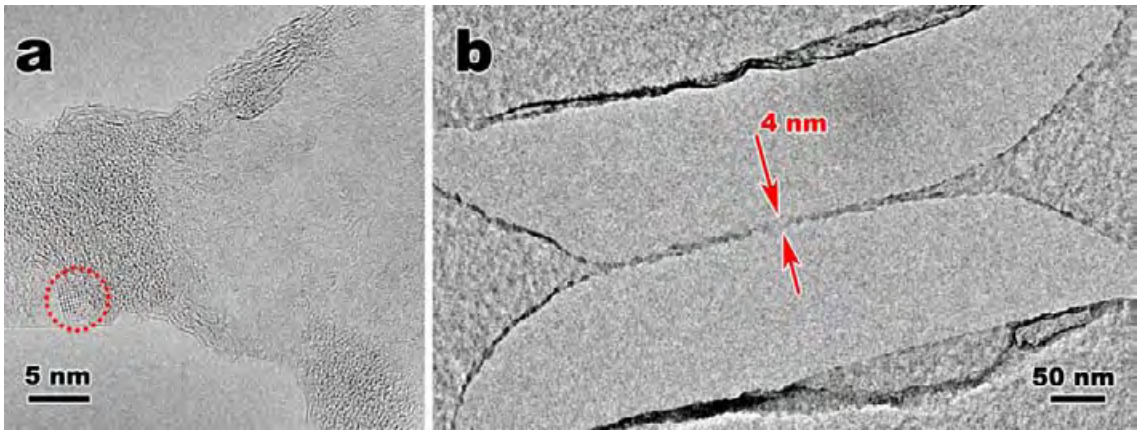


Figure 3.12: SACTEM Titan³ micrographs at 80 keV of (a) a GNR connection and (b) one of the narrowest GNR observed.

Figure 3.12a shows an example of a GNR connection. This area can be overexposed by connection cuts misplacement. In this example, graphene lattice is apparent and no important defects can be seen. Edge roughness is not higher than what has been observed before for a-C deposited areas (see Figure 3.11a). The start of the graphene nanoribbon is visible as well as an atomic straight bottom edge. Therefore, if a 16 nm GNR does not present defects due to misplacement imprecision, it will not be a problem for bigger ribbons either.

Another detail visible is a metallic particle deposited over connection (surrounded by red dotted circle). Considering the emplacement of this particle, that no other particles are observed looking randomly over the sample, it is more likely contamination deposited during the EBIE etching, or the imaging in the SEM. The interatomic distance of this particle (~3.12 Å) corresponds to the lattice parameter of tungsten (=3.165 Å). Tungsten is one of the metallic materials available inside the Helios chamber. Residues of its last use could have remained in the chamber or the nozzle could leak. This raises the importance to work in a clean chamber, as every material in the chamber can be deposited by the e-beam. SEM observations in the Nanoprobe shows that metallic particles are indeed deposited all around the patterned areas. As shown in Figure 3.13, in the SEM pictures we can see rectangular fields of those particles all around the zones of interest analysed and patterned in the Helios chamber.

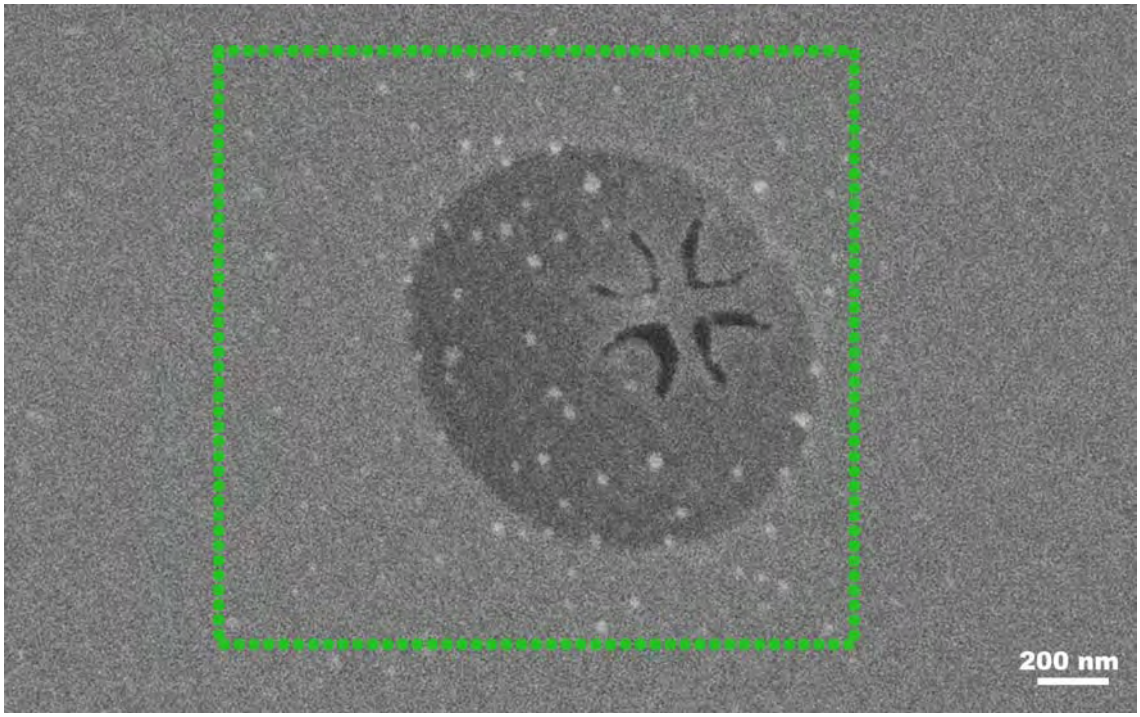


Figure 3.13: SEM micrograph of an area etched and scanned in the Helios chamber (green rectangle), as seen in the NanoProbe.

Figure 3.12b shows the limits of this process as such. A ribbon as narrow as 4 nm was fabricated by the technique described here. The theoretical energy gap value for a 4 nm GNR is around 50 meV, far enough for FET purposes. Even if this width is not performed routinely the previous ribbons width, which are 15 nm and 18 nm wide are reproducible.

We move now to the effect of annealing on the GNR width. The GNR width observed at the SEM right after etching often differs from the width observed at the TEM after annealing. Two interpretations can explain this. First, the GNR is surrounded by amorphous carbon right after etching that makes it appear larger.

Cleaning it removes the amorphous material and reveals de GNR itself. The second one is that the hydrogen annealing is responsible of additional etching. It is unlikely that annealing in H_2/Ar is reducing the GNR width as it would also ocure for water-assisted EBIE, which was not observed.

3.5 Conclusion

The oxygen assisted EBIE etching process presented and optimized here is effective and graphene is readily etched when exposed to the e-beam. The process allows etching arbitrary patterns, for example graphene nanoribbons. Graphene nanoribbons can be produced with width down to 15 nm, and length of at least 320 nm. At this size-range, no damages observable in high resolution TEM are induced by the EBIE out from the etched area. In addition, the edges of the oxygen-assisted process are free of amorphized carbon, crystalline, and amongst the best edges quality found in literature. The orientation of the edges so-produced, can either present zig-zag or armchair atomic arrangement.

3.6 References

[1] C. O. Girit, J. C. Meyer, R. Erni, M. D. Rossell, C. Kisielowski, L. Yang, C.-H. Park, M. F. Crommie, M. L. Cohen, S. G. Louie, A. Zettl, Science 2009, 323, 1705.
[2] J. H. Warner, M. H. Ruemmeli, L. Ge, T. Gemming, B. Montanari, N. M. Harrison, B. Buechner, G. A. D. Briggs, Nature Nanotechnology 2009, 4, 500.
[3] Y. Lu, C. A. Merchant, M. Drndic, A. T. C. Johnson, Nano Letters 2011, 11, 5184.
[4] F. Boerrnert, L. Fu, S. Gorantla, M. Knupfer, B. Buechner, M. H. Ruemmeli, Acs Nano 2012, 6, 10327.
[5] J. Kotakoski, D. Santos-Cottin, A. V. Krasheninnikov, Acs Nano 2012, 6, 671.
[6] Q. Xu, M.-Y. Wu, G. F. Schneider, L. Houben, S. K. Malladi, C. Dekker, E. Yucelen, R. E. Dunin-Borkowski, H. W. Zandbergen, Acs Nano 2013, 7, 1566.
[7] Z. J. Qi, J. A. Rodriguez-Manzo, A. R. Botello-Mendez, S. J. Hong, E. A. Stach, Y. W. Park, J.-C. Charlier, M. Drndic, A. T. C. Johnson, Nano letters 2014, 14, 4238.
[8] I. Utke, P. Hoffmann, J. Melngailis, Journal of Vacuum Science & Technology B 2008, 26, 1197.
[9] B. W. Smith, D. E. Luzzi, Journal of Applied Physics 2001, 90, 3509.
[10] J. C. Meyer, F. Eder, S. Kurasch, V. Skakalova, J. Kotakoski, H. J. Park, S. Roth, A. Chuvilin, S. Eyhusen, G. Benner, A. V. Krasheninnikov, U. Kaiser, Physical Review Letters 2012, 108.
[11] E. Bassous, Ieee Transactions on Electron Devices 1978, 25, 1178.
[12] K. E. Bean, Ieee Transactions on Electron Devices 1978, 25, 1185.
[13] H. W. P. Koops, R. Weiel, D. P. Kern, T. H. Baum, Journal of Vacuum Science & Technology B 1988, 6, 477.
[14] S. J. Randolph, J. D. Fowlkes, P. D. Rack, Critical Reviews in Solid State and Materials Sciences 2006, 31, 55.
[15] K. Furuya, Science and Technology of Advanced Materials 2008, 9.
[16] M. Song, K. Furuya, Science and Technology of Advanced Materials 2008, 9.
[17] Y. Guan, J. D. Fowlkes, S. T. Retterer, M. L. Simpson, P. D. Rack, Nanotechnology 2008, 19.
[18] H. Hiura, Journal of Materials Research 2001, 16, 1287.
[19] J. Wurm, M. Wimmer, I. Adagideli, K. Richter, H. U. Baranger, New Journal of Physics 2009, 11.
[20] F. Schaeffel, M. Wilson, A. Bachmatiuk, M. H. Ruemmeli, U. Queitsch, B. Rellinghaus, G. A. D. Briggs, J. H. Warner, Acs Nano 2011, 5, 1975.
[21] S. S. Datta, D. R. Strachan, S. M. Khamis, A. T. C. Johnson, Nano Letters 2008, 8, 1912.
[22] L. C. Campos, V. R. Manfrinato, J. D. Sanchez-Yamagishi, J. Kong, P. Jarillo-Herrero, Nano Letters 2009, 9, 2600.
[23] T. PA, 8th Symo.(Intl.) on Combust., Williams and Wilkins, Baltimore 1962, 807.

Chapter 4

Electronic Transport Characterization of Graphene Nanoribbon Devices

CONTENTS

4.1 DEVICE FABRICATION AND PROPERTIES 79
4.1.1 Transposing e-beam induced GNR cutting to device fabrication 79
4.1.2 Amorphization induced by backscattered electrons 82
4.1.3 Graphene devices over deep pools 90
4.2 ELECTRONIC TRANSPORT PROPERTIES MEASUREMENTS 92
4.2.1 Temperature dependence of nanoribbon conductance 92
4.2.2 Field effect in GNR devices 92
4.2.3 Magneto-transport 97
4.3 DISCUSSION AND PERSPECTIVES 100
4.4 CONCLUSION 101
4.5 REFERENCES 102

This chapter is dedicated to electron transport measurements of graphene nanoribbons patterned by oxygen assisted EBIE. The main challenge address here is the transposition of the method developed in chapter 3 to suspended, back gated and electrically contacted GNR, in order to probe their electronic properties. The dependence of electronic transport on temperature, backgate field-effect and perpendicular magnetic field will be investigated.

4.1 Device fabrication and properties

4.1.1 Transposing e-beam induced GNR cutting to device fabrication

Samples for electronic transport measurements where prepared by exfoliating graphene onto SiO_2/Si substrates by the tape technique. The substrates are covered by a matrix of micrometre sized pools (1x5 µm) as described in Chapter 2 to produce locally suspended graphene. Monolayer graphene flakes

covering pools are identified by optical microscopy and Raman spectroscopy and contacted either by laser or e-beam lithography followed by Au/Pd electron sputtering. For e-beam lithography, lift-off is carried out by an over-night acetone bath to remove the PMMA. Afterwards, the sample is flushed with fresh acetone to break and remove the undesired part of the metal layer.

The protocol for graphene patterning presented in Chapter 3 has to be modified in order to adapt it to the substrates with pools and electrodes. More complicated and longer patterning is necessary to fabricate devices measurable by electronic transport experiments (Figure 4.1a and b).

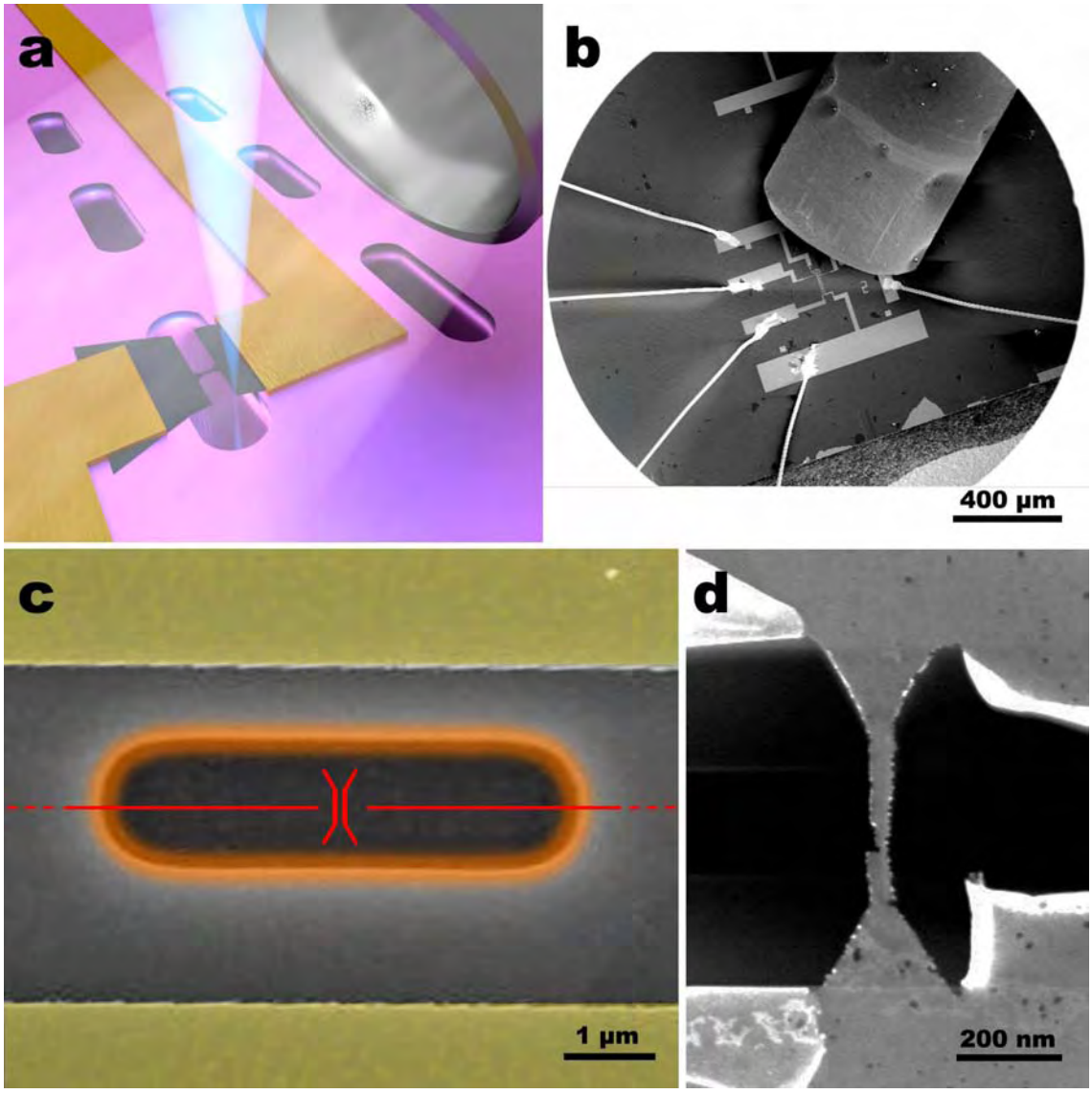


Figure 4.1: (a) Scheme of the oxygen assisted EBIE fabrication of samples for electronic transport measurements. (b) SEM micrograph of an example of sample configuration during GNR etching on a contacted and bonded pseudo-suspended graphene flake on silicon dioxide sample. A zoom of this kind of sample is shown in (c). Colours represent: metallic contacts in yellow, damaging area due to backscattering in orange and pattern items in red. (d) Example of GNR etched on pseudo-suspended graphene after electrical insulation by EBIE by SEM.

The central nanoribbon pattern has to be isolated from the rest of the graphene. This implies a significantly larger EBIE time (Figure 4.1c). Yet this time should be minimized to limit carbon re-deposition.

We want to measure the properties of the electronic transmission through the ribbon, therefore anything electrically connecting the source and drain electrodes but the GNR must be cut. In this case two pieces of graphene, one on each side of the ribbon, need to be sectioned. Thus we add to the pattern two straight lines to cut the graphene around the pattern and isolate the ribbon. Those insulation cuts have to get from the close GNR environment to the graphene border. This graphene border can be on the suspended area, or reach the silica and be supported. Although it is less contaminating to etch the pool region on one shot, the supported area cutting is not critical and can be etched using more steps. We chose to perform those cuts centred on the pool's width (Figure 4.1c). The pool is around 1.5 μm wide and the oxide thickness is 290 nm. This means that even if theoretically the pool walls have been oxidized, if the insulation cut is performed close to the edge, the piece of graphene that will fold down is big enough to touch the pool wall below the oxide and create a shortcut to the backgate (Figure 4.2).

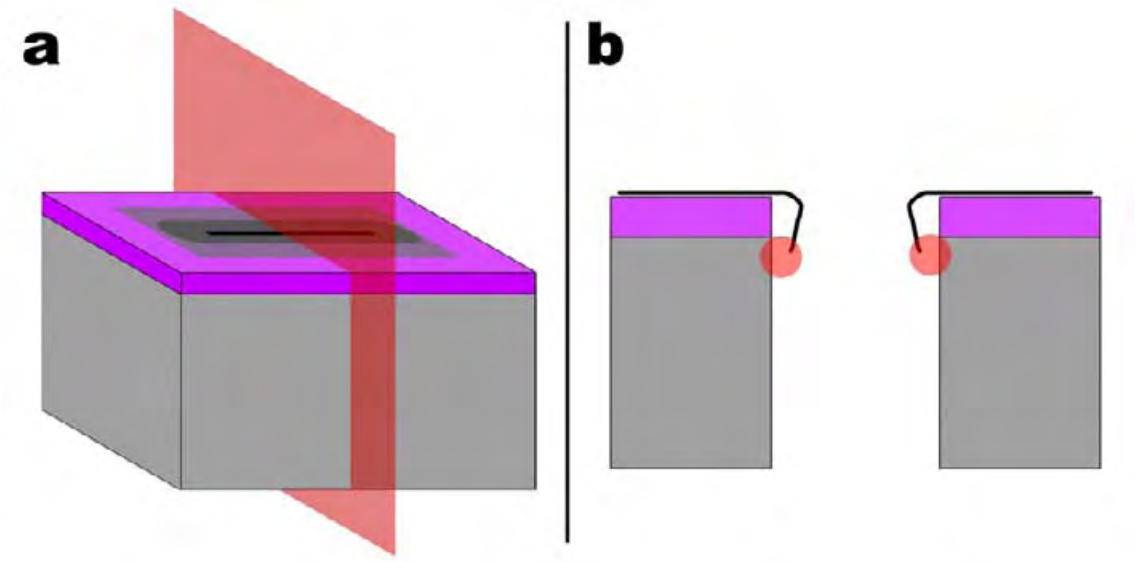


Figure 4.2: (a) 3d scheme of a etched graphene flake suspended over a silicon dioxide on silicon substrate with pools. (b) 2d scheme of the pool following the red plane showing the folding of the graphene layer after been etched. The red circles shows where graphene gets close to the grid.

The isolation cuts need to be etched very close to the GNR. This could damage the ribbon if we cause an overexposed area as seen before for the V shape connections etching. The further the isolation cuts can be made from the GNR, the better.

An example of resulting GNR is shown in Figure 4.1d. We notice a few holes on graphene, they could have been produced by backscattered electrons produced at the bottom of the pool. In addition a constriction is noticeable in the middle of the GNR. Its origin is the insulation cut, placed too close to the GNR. Even though, the

pattern has been performed with precision, edges are straight, and the GNR has been successfully insulated from the rest of the graphene sheet.

As for the case of SACTEM samples, electron beam irradiation of the ribbon during imaging is minimized to avoid depositions, or damage due to residual oxygen in the chamber.

Overall, we see that a careful protocol leaves three potential damaged zones. If the insulation and the connections cuts are not properly executed, they can cause amorphization or constrictions in the nanoribbon. The GNR would then be composed of two crystalline sections surrounded by damaged graphene areas. On the other hand we notice that the EBIE cuts on exfoliated graphene, even after being exposed to PMMA, are thinner and better defined than previous cuts observed by SEM on CVD graphene on TEM grids. This indicates that the material is less contaminated.

4.1.2 Amorphization induced by backscattered electrons

The most stricking difference between the GNR produced on top of a pool on a SiO_2/Si substrate and a free standing GNR is the presence of defects visible in SEM.

One example of graphene etching over 250 nm deep pools is shown in Figure 4.3. The graphene layer has been perforated all along, including around and inside the GNR. The poor structural quality of such GNRs will deteriorate its intrinsic electronic transport properties.

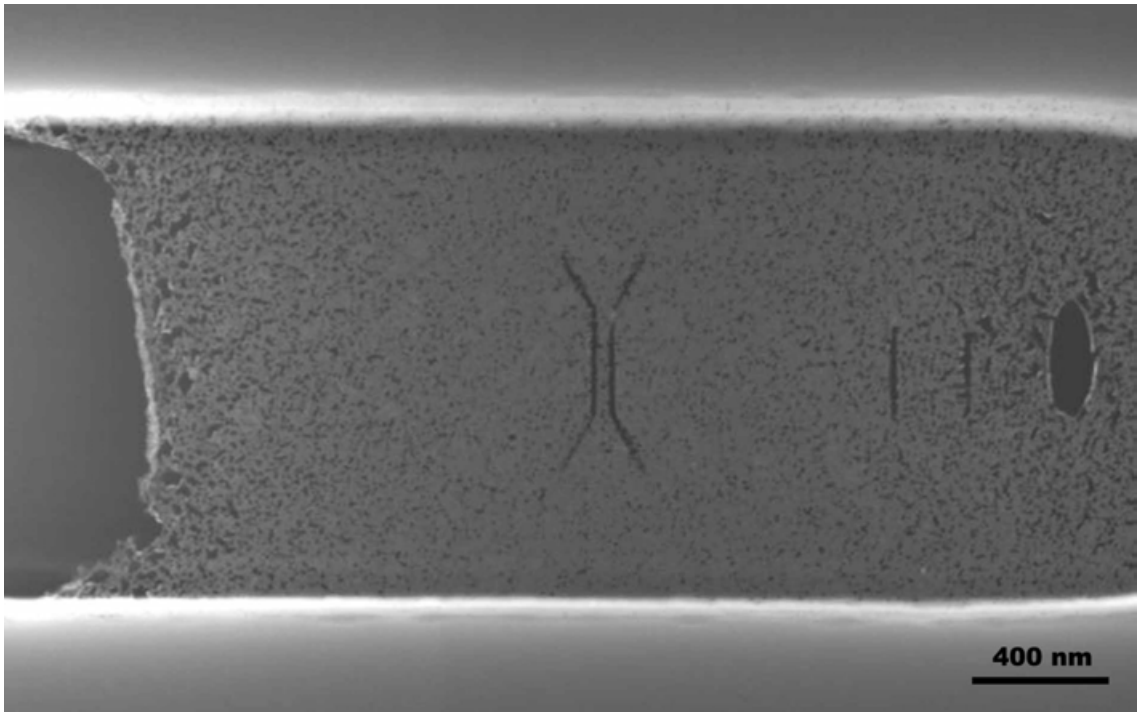


Figure 4.3: SEM example of oxygen-EBIE etching on graphene pseudo-suspended on 250 nm pools.

We attribute this large area damaging to back scattered electrons produced by the incident electron beam hitting the substrate, 250 nm below the suspended graphene. Those electrons emerging from the pool at any angle, hit over a large area. Since this happens during the etching and in the presence of oxygen, back scattered electrons trigger a parasite EBIE resulting in nanometer size holes scattered on graphene's suspended area.

To support this interpretation, we present a study by simulation of the e-beam behaviour on different graphene samples. The simulations have been performed using CASINO v3.2 software. The CASINO software calculates the trajectories of secondary and backscattered electrons induced in an arbitrary substrate (morphology and composition) under an e-beam irradiation. The program is based on a Monte-Carlo simulation method. The energy of the beam is set to 20 keV and number of electrons to 10^4. Note that graphic representation of the electrons trajectories presented in the following figures shows only 50 of them.

Figure 4.4a corresponds to the configuration used for water-EBIE etching where graphene is directly supported on the SiO_2/Si substrate. In Figure 4.4a, an SEM image of a typical cut illustrates the dramatic effect of the series of processes induced by the incident beam. Three areas can be distinguished. The first one is the etched region in the centre of the cut. It is narrow (~100 nm) although one order of magnitude larger than standard cut of suspended graphene. Around it is a 500 nm wide area where graphene is fully etched. One can also notice that the supporting SiO_2 has been roughened. Finally, within a 80 nm wide band centred on the cut, the graphene layer is still present in part but seriously cracked and damaged. This configuration is modelled in Figure 4.4b by simulating the electronic beam scattering on supported graphene on silicon dioxide sample.

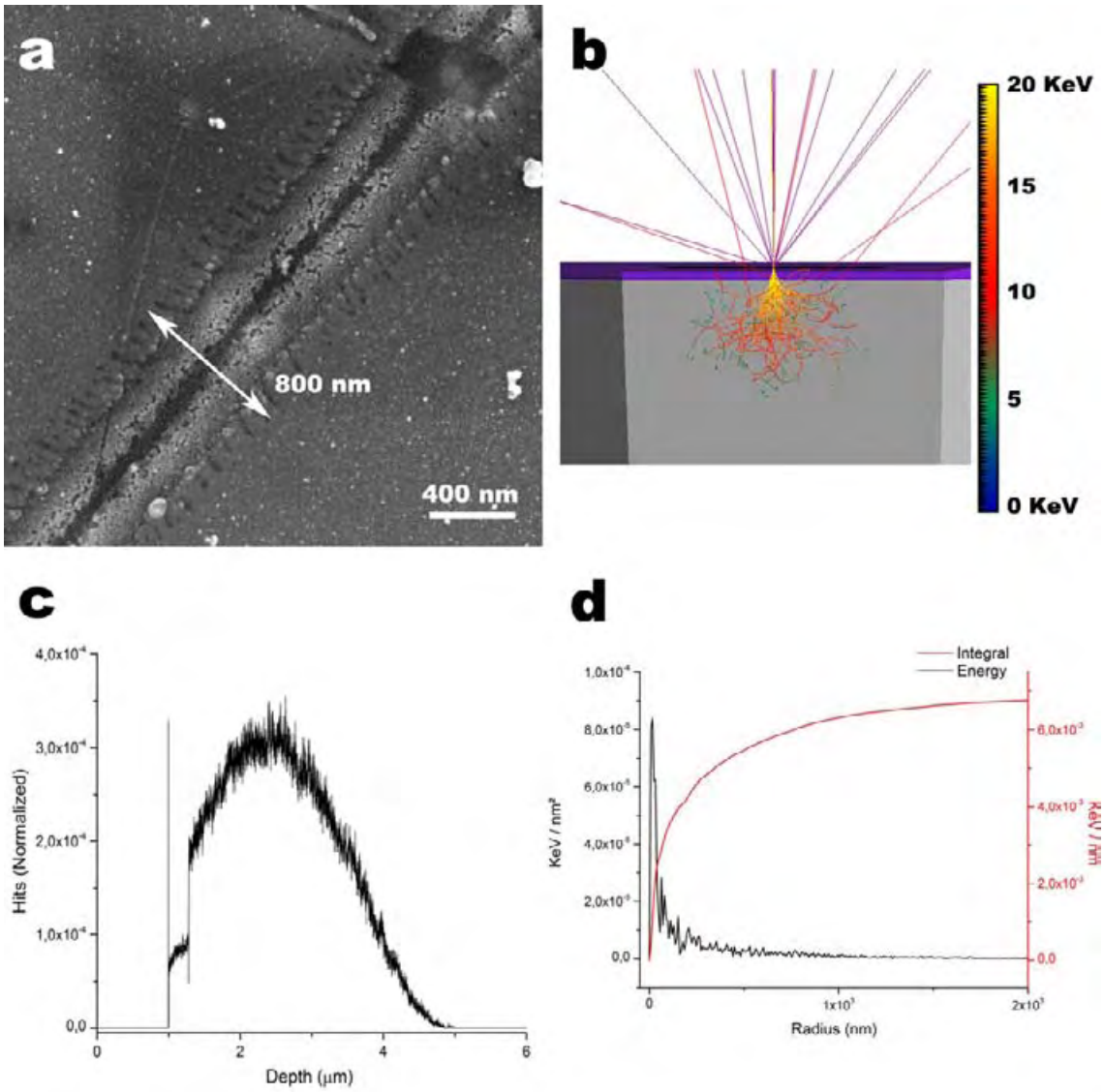


Figure 4.4: Study of the EBIE etching on supported graphene samples. (a) SEM picture of a water-EBIE cut performed on a supported graphene on silica sample. (b) Simulation of backscattered and secondary electrons produced on a supported graphene on silica sample. In this picture 50 electrons trajectories (out of 10000) are shown. The results of number of hits versus the depth and the energy at the surface versus the radius correspond respectively to graphs (c) and (d).

Backscattered electrons (in purple) and secondary electrons (in red) that are indeed produced come back to the graphene layer with a shallow angle, away from the impact point. The electron production takes place within 3 µm from the surface (Figure 4.4c). Hence the probability of an electron reaching back to the surface is high. The spatial distribution of the electron energy at the surface is shown in Figure 4.4d, it shows an area of influence of 400 nm. This implies that during an EBIE etching, graphene within 400 nm around the incident beam is also subject to a significant flux of energetic BSE and SE that can also trigger EBIE. This simulation matches our experimental observation of serious damage within a 400 nm band along a line cut. This obviously impairs high-resolution patterning

and justifies the need to minimize BSE and SE by suspending graphene at least locally.

In this work we implemented the local suspension of graphene by creating arrays 1x5 μm pools the depth of which was initially kept smaller than the oxide thickness (295 nm). Figure 4.5 shows the results of beam backscattering simulations on 250 nm (Figure 4.5a) pools while setting the beam target at the centre of the suspended graphene.

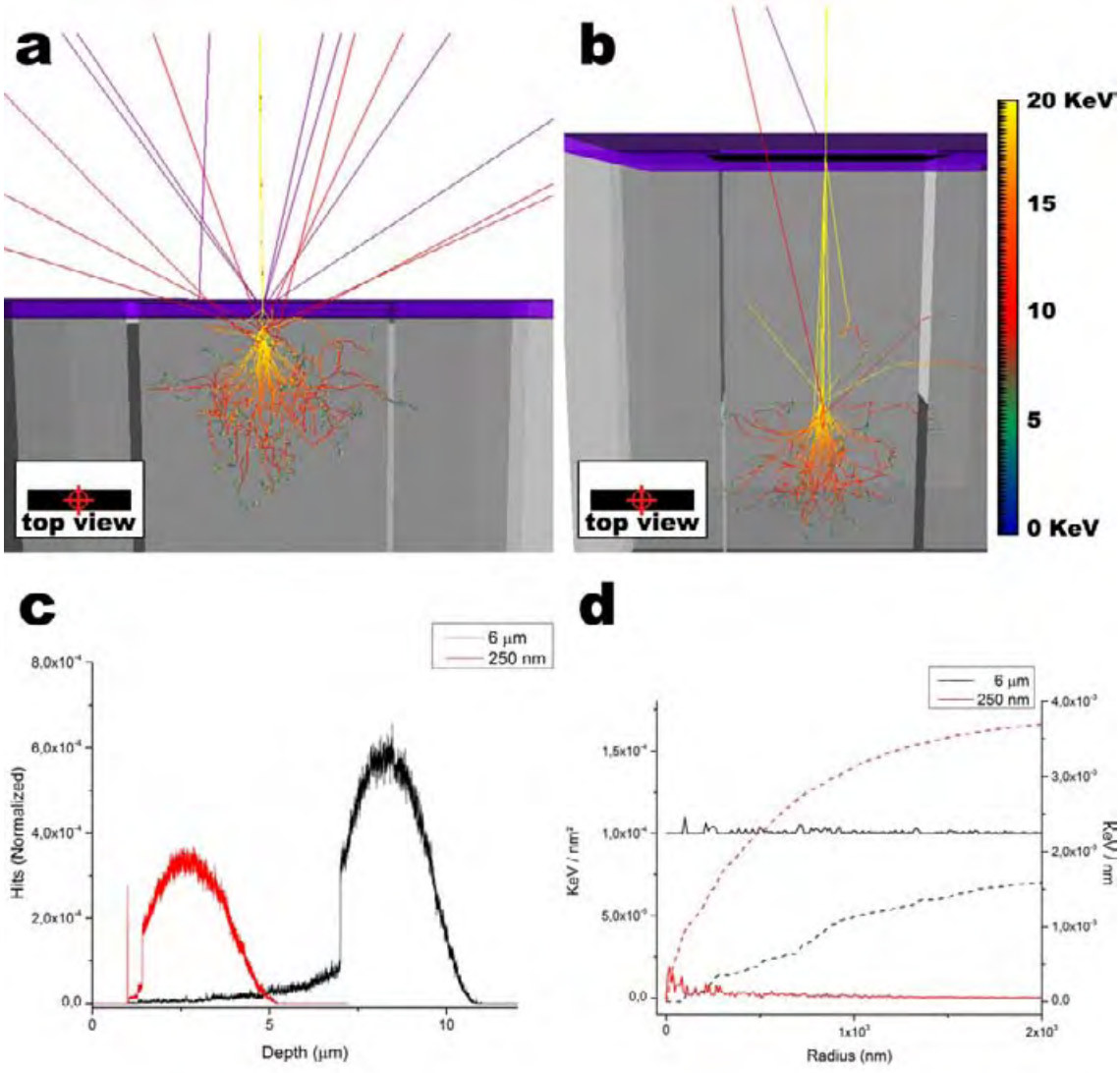


Figure 4.5: Simulation of electron backscattering and secondary electrons on (a) 250 nm deep pools and (b) 6 μm deep pools, backscattered electrons are shown in purple. (c) Electron collisions versus the depth and (d) backscattered energy repartition on the surface (integration in dash plot, right scale).

In Figure 4.5a, we notice in the simulation that an important amount of backscattered and secondary electrons is generated below the floor of the pool, a significant fraction is able to travel back to the graphene layer. In Figure 4.5c (red curve) we see that the electrons are mostly within 3 μm depth in the substrate. This simulation confirms our interpretation that backscattered electrons are produced at the bottom of 250 nm deep pools and are able to reach the suspended graphene and induce EBIE on.

Next, we consider implementing much deeper pools in order to increase the solid angle from which electrons produced at the bottom could reach the suspended graphene. For this we performed the Bosch process (see Chapter 2) that allows etching a few micrometre deep even for 1x5 μm sized pools. In our ultra-deep pool samples, the depth was adjusted to 6 μm.

In Figure 4.5b, the simulations corresponding to graphene over 6 μm pools, electron activity is mainly between the bottom of the pool (6 μm) and 2 μm deeper (Figure 4.5c). The portion of backscattered electrons reaching the graphene is lower compared to the 250 nm pools situation (Figure 4.5d). As electron activity is kept far from the working area, the probability of backscattered and secondary electrons at the graphene level is indeed lower. The simulation confirms the relevance of our modification of the pool depth.

We now verify whether our choice of acceleration voltage based on the experimental observations of the minimal damage induced was confirmed. For this, simulations with a 10 keV incident beam were performed in the same configuration as Figure 4.6b, i.e. for graphene over a 6 μm deep pools and a beam positioned at the centre of the suspended graphene. This simulation shows that more backscattered and secondary electrons reach the graphene layer. The electron activity and the backscattered electrons production occurs in a thinner layer of silicon at the bottom of the pool between 1 and 1.5 μm below the surface (Figure 4.6b and c). Electrons have more probabilities to travel back in the pool and reach the graphene. The higher the energy, the deeper the BSE and SE will be diffused, and so fewer electrons will travel back and they will have a lower energy, thus reducing the probability of damage. These results reinforce the technical choice of performing EBIE at 20 keV, which provided the smallest feature size and limits the damages.

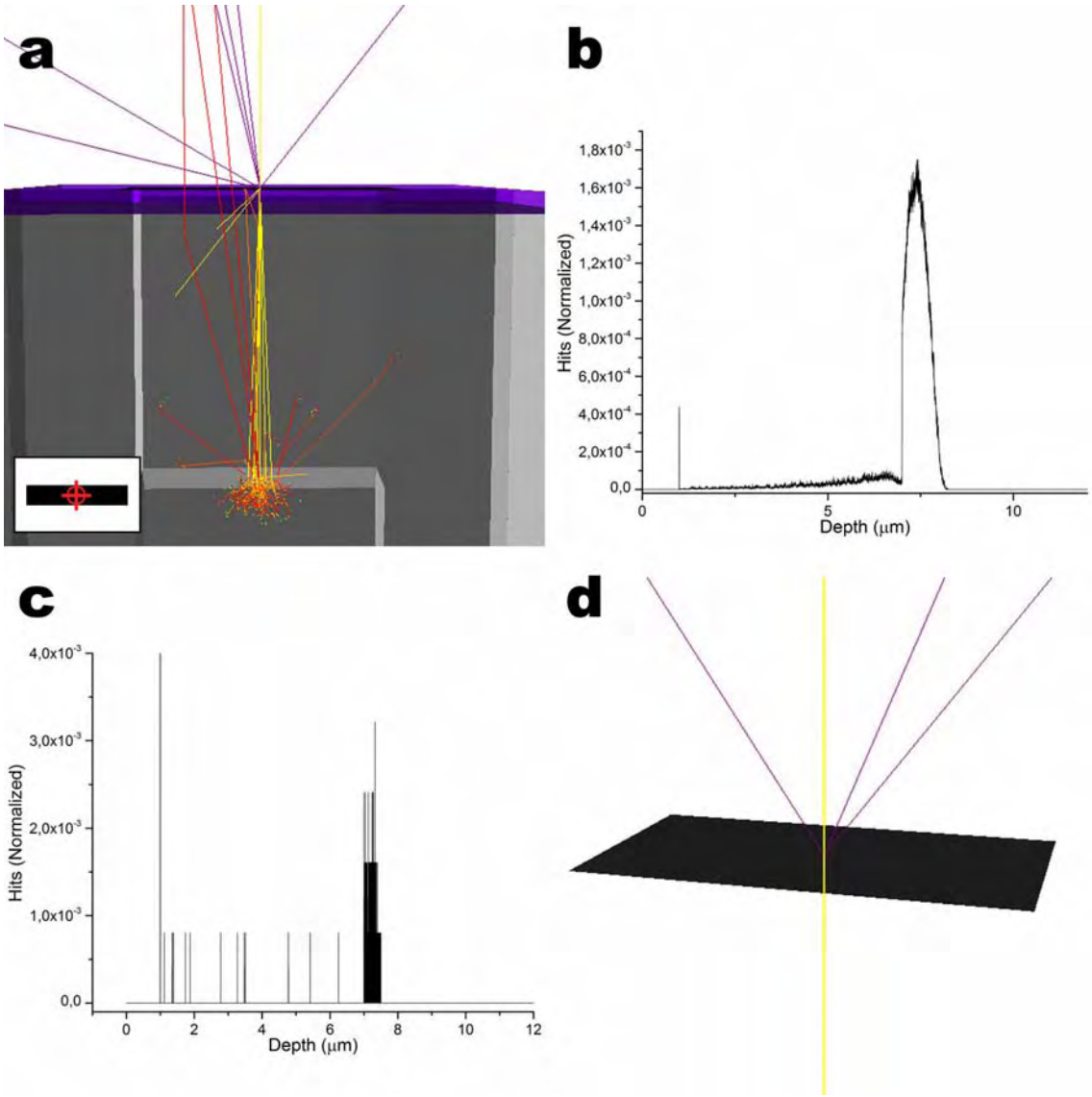


Figure 4.6: Casino simulations of backscattered electrons. (a) Electronic simulation of a 10 keV e-beam on a 6 μm deep pools sample, (b) electrons collisions versus the depth and (c) backscattered electrons produced versus the depth. (d) Simulation on completely suspended graphene.

Figure 4.6d corresponds to a simulation using only a graphene layer, without support. This corresponds to the TEM grids used for structural analysis. As we can see in this case the problem of backscattered and secondary electrons damaging the sample does not exist. The only backscattered electrons are produced at the graphene level and cannot produce damage.

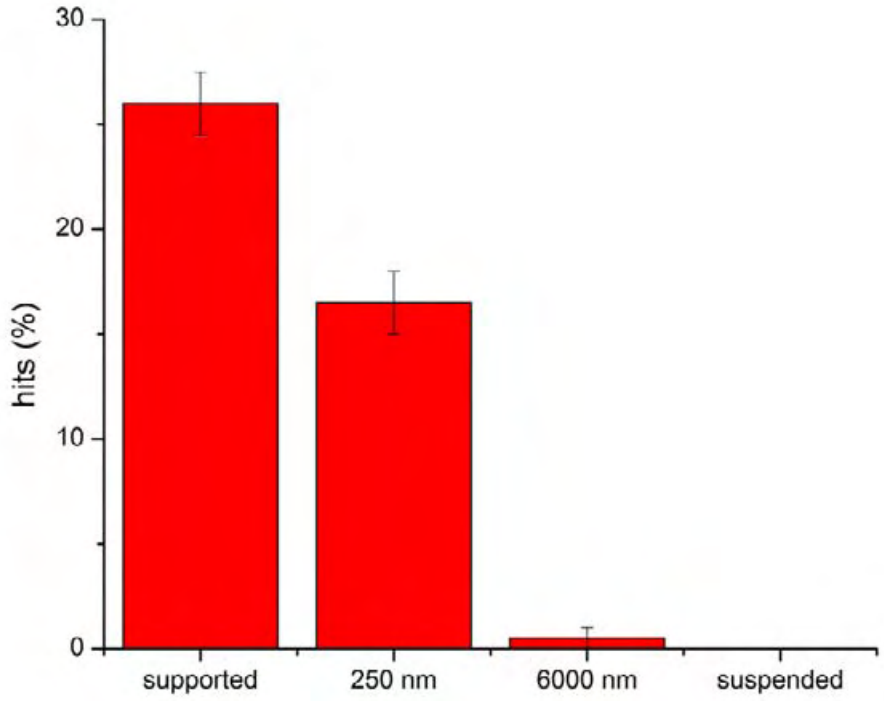


Figure 4.7: Resume of the backscattered hits to suspended graphene on the four different configurations

EBIE is performed on the suspended but also supported region. One particular attention was paid to the region where the beam passes over the edge of the pool. Figure 4.8a, b and c corresponds respectively to a beam focused inside the pool at 10 nm of the border, at the edge and outside the pool at 10 nm of the edge. The simulation with the beam positioned inside the pool (Figure 4.8a) gives results very close to those of the central area of the suspended graphene (Figure 4.5b). The amount of secondary and backscattered electron activity close to the surface is relatively low (Figure 4.8d and e black plots). On the contrary the two other configurations lead to the production of a much larger amount of BSE and SE that goes towards the rest of the suspended graphene sheet where they can potentially induce damage.

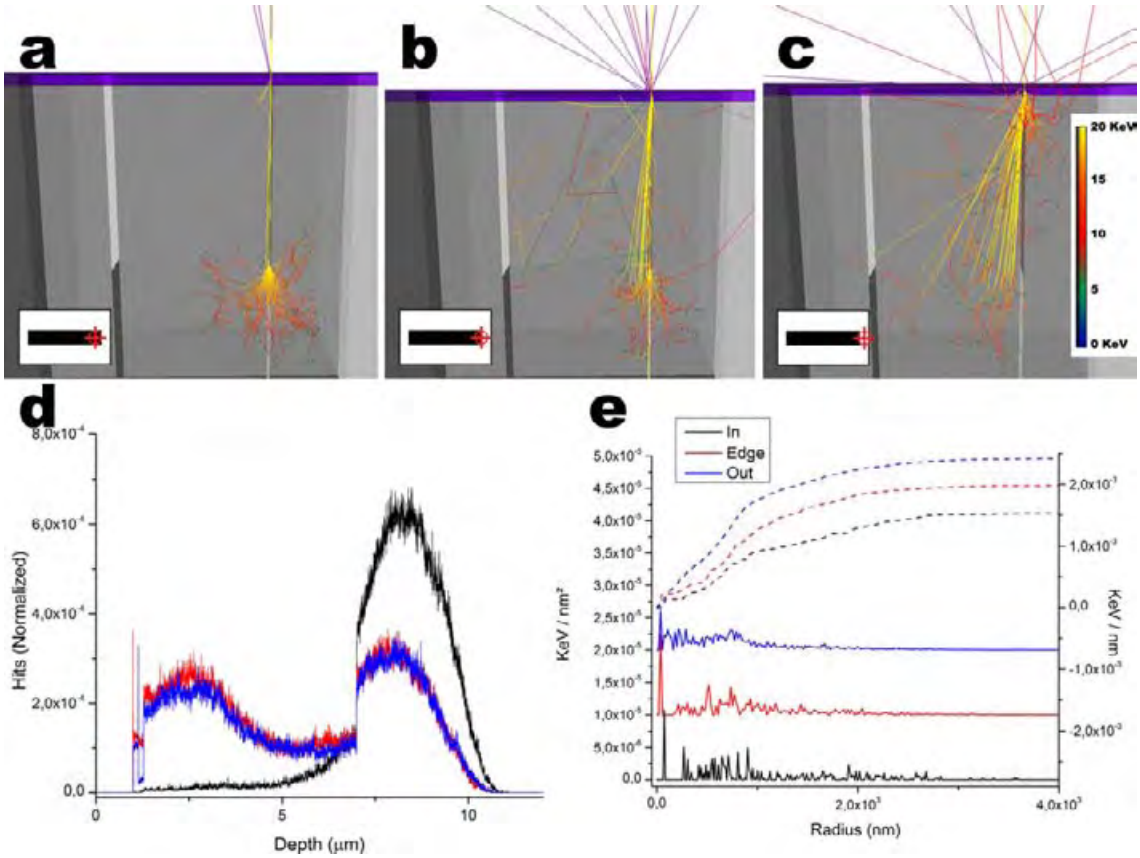


Figure 4.8: Simulation of electron scattering when etching close to the pool's edge. (a) E-beam's target is inside the pool at 10 nm of the edge. (b) Beam is focused at the edge position, and (c) outside the pool at 10 nm of it. (d) Electron collisions versus the depth and (e) backscattered energy repartition on the surface (integration in dash plot, right scale).

For impacts just outside the pool (Figure 4.8c) the number of secondary electrons going across the graphene is further increased compared to Figure 4.8b. This irradiation comes from electrons that have penetrated into the substrate and then emerge inside the pool travelling up towards the graphene. This irradiation does not only enlarge cuts as seen before (Figure 4.5) due to the substrate but also compromises all the suspended graphene area. The energy repartition on the surface increases when passing over the edge and onto the substrate Figure 4.8d.

In conclusion, Monte Carlo simulations show that the etching of graphene patterns is only conceivable on graphene suspended over deep pools (~6 µm). In this configuration, the patterning is performed by the sole effect of the incident beam electrons and the effect triggered by BSE and SE is negligible. The CASINO simulation of backscattered electrons indicate that only a little fraction of the energy comes back to the graphene layer at 20 kV when using 6 µm deep pools. But we have also shown that this result is a lot different at 10 kV where electrons do not penetrate the silicon too deep, and can re-emerge in the pool. The patterning close to the pool edges can generate enough BSE travelling to the GNR to damage it. This can be an issue if the graphene flake covers the whole pool and

isolating EBIE side cuts are necessary. Therefore the geometrical and structural properties, of pseudo-suspended and contacted GNR are close to the one of fully suspended. Yet one should bear in mind that some unwanted damage may have been caused by peripheral etching steps.

Although peripheral to the main pattern, the isolation of the GNR from the large graphene flakes requires etching step close or on the supporting substrate. These portions of the global pattern where shown to have potential consequences on the GNR itself.

To summarize, patterning of device would reach the quality certified on TEM grids if two conditions are respected: (i) pattern paths should remain at least 10 nm away from the pool edges and (ii) to use e-beam energy of 20 keV or higher.

4.1.3 Graphene devices over deep pools

After establishing the optimized protocol, hundreds of flakes have been produced and analysed over tens of substrates. Several dozens have been contacted by EBL but eventually only two have reached electrical measurement after a successful EBIE patterning and annealing. After oxygen assisted EBIE we obtain two GNR displayed in Figure 4.9. Sample A is multi-layered and measures 90 nm by 320 nm long. Sample B is monolayer and measures 60 nm by 320 nm.

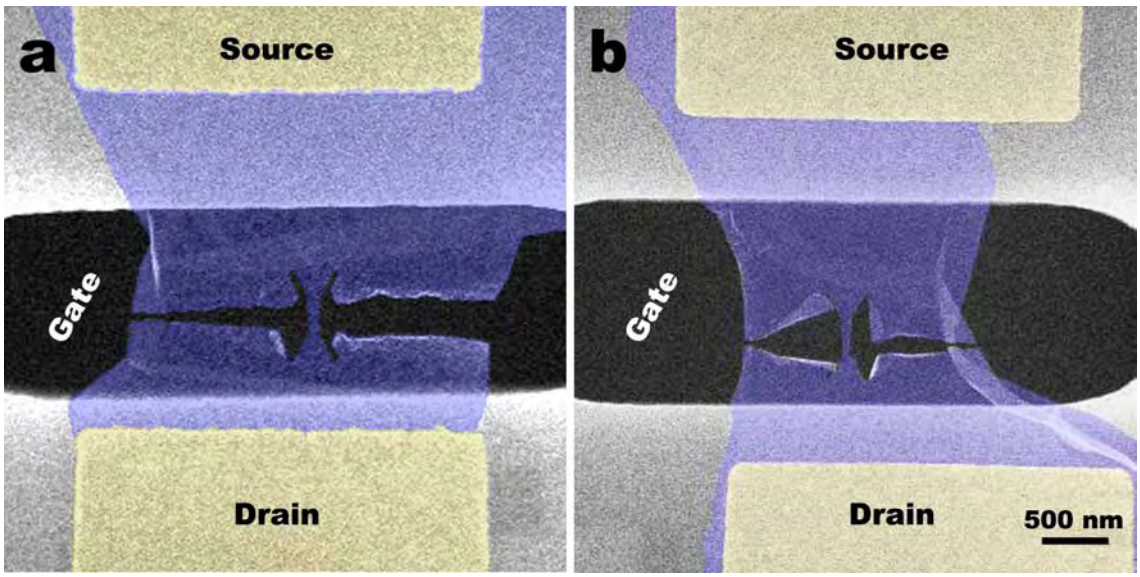


Figure 4.9: SEM micrographs of the suspended and contacted GNR obtained by oxygen assisted EBIE etching of graphene. (a) Sample A, the GNR size is 90 nm wide by 320 nm long, (b) Sample B, the GNR size is 60 nm wide by 320 nm long.

The conductance of the two ribbons is tested at room temperature using a manual probe station. I(V) current-voltage measurements show that both samples are conductive (Figure 4.10). At ambient temperature, sample A has a 2-probe

resistance of R_a = 11.43 kΩ and sample B, R_b = 5.40 kΩ. The I(V) characteristics are linear in both samples and we can proceed to further analysis. Those resistance values are similar to the resistance of non patterned graphene samples with same aspect-ratio (length/width) (20 by 4 μm) which have a value of R ~ 1 kΩ[1].

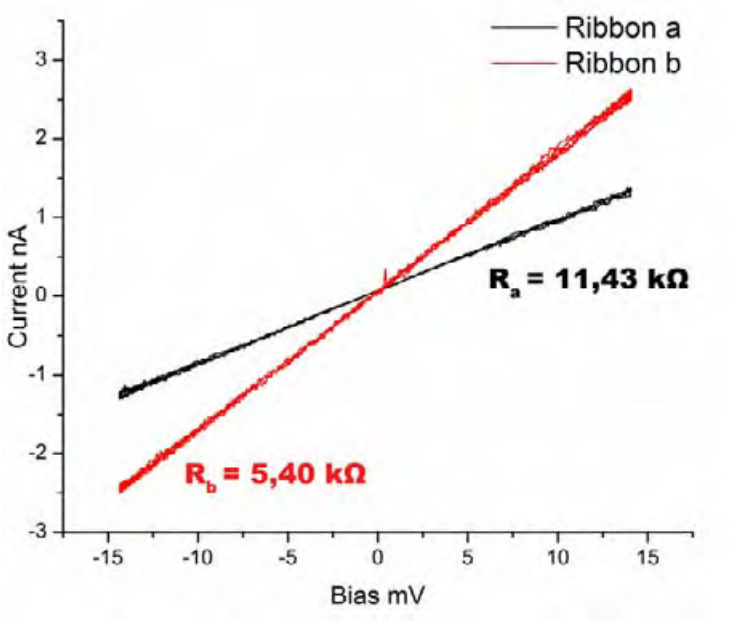


Figure 4.10: Current vs. bias measurements on ambient conditions of ribbons a and b

Sample A presents a higher resistance in ambient conditions and the ribbon is wider. I(V) measurements at 65 K still show only ohmic behaviour. One possible explanation for this higher resistance is the contact with pads. As we can see in Figure 4.9a, the lower pad seems to have a restricted surface contact to the graphene layer. Sample A will not give any supplementary information as it broke during those measurements. The following results are measured on the 60 nm wide ribbon of Sample B.

4.2 Electronic transport properties measurements

4.2.1 Temperature dependence of nanoribbon conductance

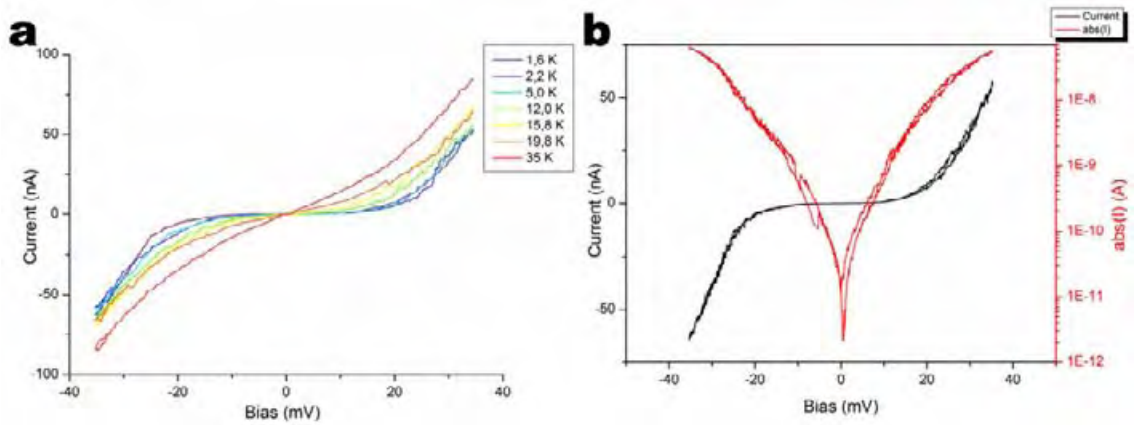


Figure 4.11: (a) Current versus bias measurements at temperatures from 35 K to 1.6 K (a). (b) In black a measurement at 1.4 K and its absolute value in log scale in red.

Figure 4.11 shows the measured current versus the bias voltage at different temperatures from 35 K down to 1.4 K. As the temperature drops, a non-linearity appears and becomes more pronounced (Figure 4.11a). The non-linear behaviour appears mostly below 50 K. The I(V) characteristic at 1.4 K measurement in log scale is also shown in Figure 4.11b. The slope of the abs(I) plot increases strongly around 0 V. We observe no gap in this measurement. If we zoom around 0 V we observe a noised flat region. We estimate this region to around 0.5 to 1 mV. The theoretical gap for such width is 3 meV. We do not know at this stage where the Fermi level is, which could be lowering it, but it is in the same range of energy. In comparison, gap measurements reported for 60 nm ribbons patterned by EBL and RIE are around 6 to 8 meV[2]. Those energies are higher than the theoretical energy, which implies that other phenomena are occurring. The transport measurements show that the conduction is dominated by Coulomb blockade, edge disorder and substrate influence. Our GNR, suspended and patterned by oxygen assisted EBIE, have theoretically less defects and better edges. That would explain such a low energy. A much narrow ribbon would present a gap easier to measure with our instruments.

4.2.2 Field effect in GNR devices

The variation of the GNR conductance with the backgate voltage at V_{SD}= 5mV at T= 1.4 K is measured in Figure 4.12a. The aim was to find the Dirac peak of the sample. The measured signal corresponds to a series of reproducible peaks and dips overlayed on a V-shape background (2 scans perfectly superposed are shown). First we pay attention to the background that reach its minimum

conductance at around V_g = - 1.3 V. From the slopes of this background we can extract a mobility value for the holes (μ_h) and electrons (μ_e) side using the following equation.

$$\mu_{FET} = \frac{\delta G}{\delta V_{BG}} \cdot \frac{L^2}{C_g} \tag{4.1}$$

with:

$$C_g = \varepsilon_0 \frac{W \cdot L}{d} \tag{4.2}$$

Where L is the length, W the width of the GNR, d its distance to the grid, G the conductance, V_{BG} the back gate voltage and ε_0 the vacuum electrical permittivity.

Using the conventional parallel plate capacitor model to calculate the GNR mobility from equation (**4.1**) we get $\mu_{FET,h}$= 4041 cm²/Vs for the holes mobility and $\mu_{FET,e}$= 1643 cm²/Vs for electron mobility. As the GNR is suspended in vacuum we know that the grid potential felt at the GNR position is lower than what it would be in SiO_2 supported graphene. To refine this estimation, we proceed to a simulation in order to evaluate the electric potential induced by the grid over the pool. Figure 4.12b is the result of an electrostatic potential simulation at the substrate surface level. The potential at the silicon surface reaches a value close to the potential of the backgate. On the other hand the potential decreases over the pool. When considering 1.5x5x6 µm pools and taking into account the two electrodes (at 0V and 5mV), we find that the potential at the GNR position is around 49% of the silicon potential. If we apply this correction due to low field effect efficiency we get to $\mu_{FET,h}$= 8247 cm²/Vs and $\mu_{FET,e}$= 3353 cm²/Vs. This result only takes account of the capacitance in between the ribbon and the parallel bottom of the pool, but not the other silicon faces. The surface of the projection of the ribbon to those other faces is none, but considering that they are at closer distance of the ribbon they could affect the mobility value.

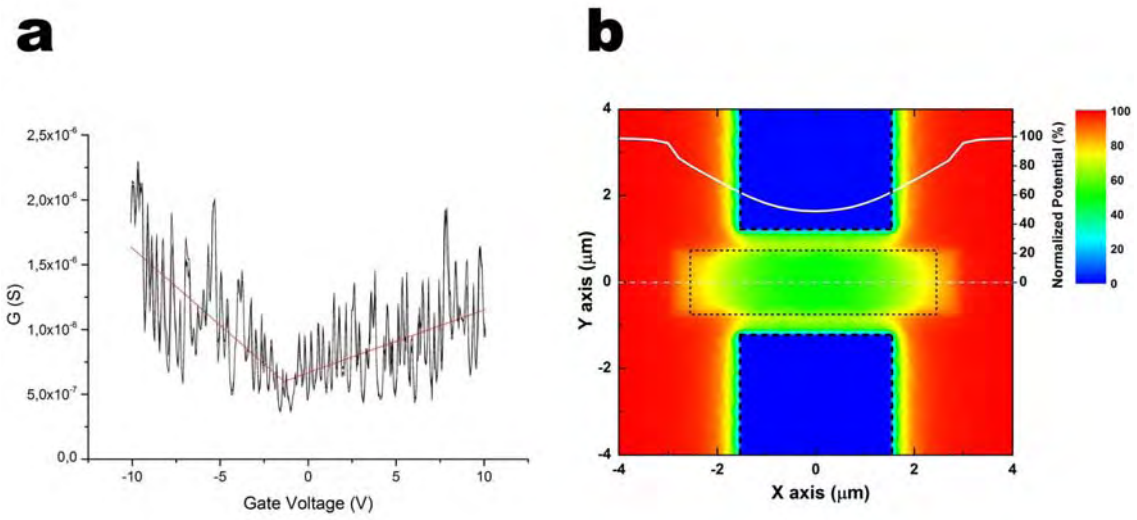


Figure 4.12: Measurement of the conductance versus the gate voltage (a) at 5 mV bias. Red lines are a linear fit of the background. (b) Gate potential simulation over the pool at the silicon dioxide surface. Nominal value is plotted in white.

A minimal mobility value can be obtained by considering a plane below the GNR at a distance corresponding to the closest silicon (Figure 4.13a). In that case, we consider a plane at 850 nm of the GNR (Figure 4.13b) resulting on a mobility of $\mu_{FET,h}$= 1168 cm^2/Vs. This scenario though, is overestimating the capacitance and so underestimating the mobility but can be used as a lower limit.

Only few works on the literature report electron mobility for GNR. We can compare our results with the 2700 cm^{-2}/Vs electron mobility for GNR on SiC[3], and the electron mobility of opened carbon nanotubes reported up to around 1600[4] and 1200 cm^{-2}/Vs[5]. These values are in the same range of mobility as the one estimated for electrons in our samples, we can deduce that our ribbons are at least of same quality as opened carbon nanotubes. However our devices present a typical contact resistance of ~5-10 kΩ instead of typically hundreds of kΩ for opened carbon nanotubes.

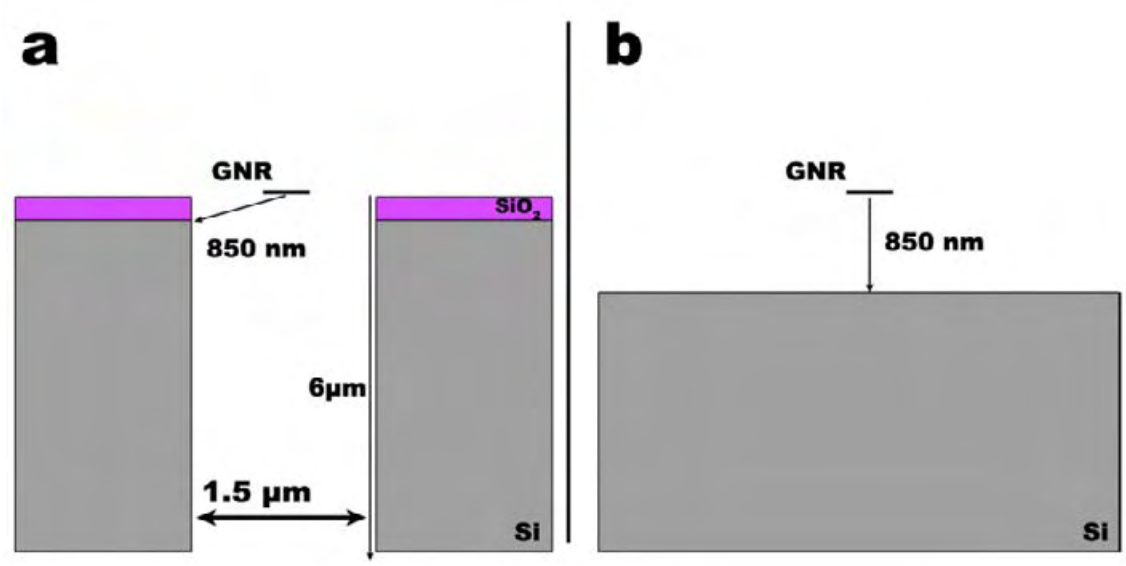


Figure 4.13: (a) Scheme of the configuration of the sample measured. (b) Schematic of the approximation used for the calculation of the maximum capacitance of the device.

These mobility values are high compared to the mobility of other similar size supported GNR patterned by EBL and RIE [6, 7] and comparable to non-patterned supported large graphene flakes[8]. As seen previously in Chapter 1, the substrate can induce potential fluctuations causing diffusion centres and hopping. The fact that the ribbon is suspended removes the scattering by the substrate-induced potential and could account for the preserved mobility. The reproducible oscillations on back-gated measurements can indicate a Coulomb blockade regime[2, 6, 9-11]. Thus some barriers are still influencing the electron transport on our ribbon. If that is the case we can analyse this signal deeper and should be able to extract a domain size to help evaluate the ribbon quality.

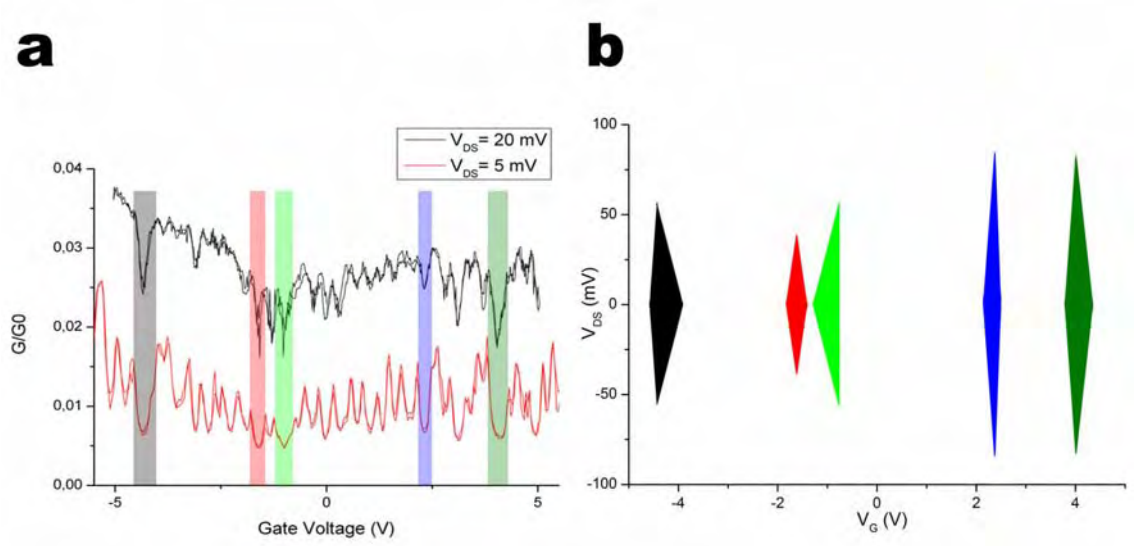


Figure 4.14: Current versus backgate voltage at 5 and 20 mV (a). (b) Diamonds extracted from extrapolation on gate measurements of (a).

In Figure 4.14a, gate voltage sweeps produce regular oscillations of the conductance. The width of the peaks and dips vary with the bias voltage. One possible origin of such behaviour is the existence of confined area of graphene acting as quantum dots (QD) with discrete levels of energy. For a given bias, the gate voltage modulates the relative position of the levels of the QD. High conductance corresponds to the situation where the QD level is aligned with the Fermi level of the electrodes, while in between levels, the conductance is suppressed. The usual analysis of such system consist in recording G (V_b ,V_g) which often shows diamond-like patterns. The V_b size of these patterns provides an indication of the charging energy, which corresponds to the spacing between consecutive levels and is directly related to the dot size. Although preliminary measurements could be performed, sample B did not survive to yield a complete G (V_d , V_g) set. We notice, though that the valleys are indeed wider at V_{SD}=5 mV than V_{SD}=20 mV. To extract some information of this experiment, we extrapolate rough diamond coordinates from two curves to estimate the charging energy. Those values are then taken as an indicator of the dot size with equation (**4.3**)[11]. Where d is the dot diameter, e the elementary electric charge, ε_0 the vacuum electrical permittivity and E_c the dot charging energy.

$$d = \frac{e}{4\varepsilon_0 E_c} \qquad (4.3)$$

We get size ranges of dots between 50 to 180 nm (around 6 barriers across the ribbon). Since no substrate can influence the ribbon, we assure that the dots are created by the physical interruptions in the crystalline ribbon. The 180 nm is comparable to the half of the GNR. It could be related to amorphous barriers in the

middle and at the ends of the GNR. Those are the positions where the isolation cuts and the V-shaped connections have been made.

Through the mobility values calculated previously, we notice a significant difference between holes and electrons mobility. In our samples holes have higher mobility (x2.5) than electrons. In addition, the minimal conductivity during backgate measurements is displaced to the negative values of gate voltage. One possible interpretation is in direct relation with the Coulomb barriers estimated right before. If we consider those barriers to be the result of a potential fluctuation in graphene induced by the adsorbates observed in TEM, the resulting mobility differences can be caused by a non electron-hole symmetric potential. If we consider the potential of the GNR to be mainly flat with 2 to 7 hollow-like barriers (Figure 4.15a), then holes mobility would be lower than electrons. On the other hand, if the potential is mainly flat with pic-like barriers by local n doping (Figure 4.15b), then electrons mobility will be affected. If we make the hypothesis that adsorbates have a homogeneous composition, we get to the conclusion that adsorbates are electron donor type. This also affords for the conductance minima at negative gate potential. The adsorbates could then be oxygen/ozone from the etching, alkanes, or other electron donor molecules[12-14].

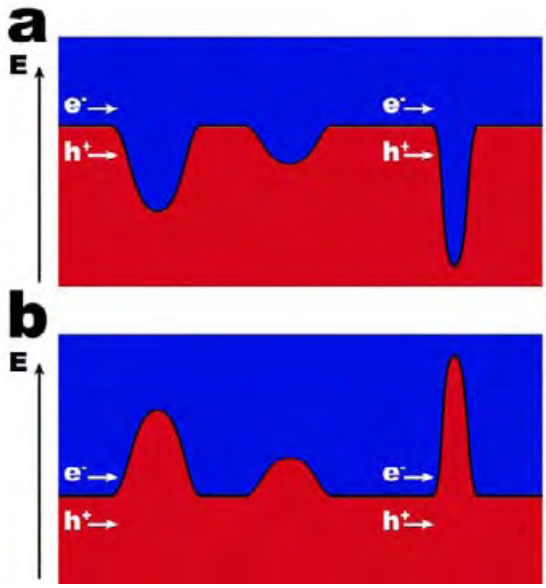


Figure 4.15: Longitudinal ribbon diagram of the influence of (a) electron acceptor and (b) electron donor adsorbates on the electrostatic potential of a suspended graphene layer and effect on electrons and holes propagation

4.2.3 Magneto-transport

When a perpendicular magnetic field is applied to the GNR, its conductance is intensely modified. We first focus on magnetic field scans (from -12 to 12 T) at 1.4 K and different V_{SD} values (10, 20 and 30 mV) (Figure 4.16a). We notice that at any bias value, conductance of the ribbon increases with increasing magnetic field. Large magneto-conductance on graphene nanoribbons has already been

predicted[15] and reported[16, 17]. Taking into account the resistance values at 0 T and 12 T at 10 mV R_0 = 57 kΩ and R_{12} = 22.7 kΩ and using the following formula:

$$MR = \frac{\Delta R}{R_0} = \frac{R_{12} - R_0}{R_0} \tag{4.4}$$

We get MR = -60.2 % at 1.4 K and 12 T. This value can be considered high.

This magneto-conductance is the consequence of a good edge crystallinity. As the magnetic field intensity increase the current is confined towards one side of the ribbon. As only one edge and its close environment are used, the number of diffusion centre encountered by electrons is reduced. This is in good agreement with the SACTEM analysis presented previously in Chapter 3.

The measurements are symmetric compared to the 0 T value which affords for similar structural characteristics of both edges. This result is crucial for our experiments as the electronic properties of the edges are the quality sensors for the patterning technique, which has been observed in direct space by atomic resolution microscopy and finds some confirmation in these preliminary magneto-transport measurements.

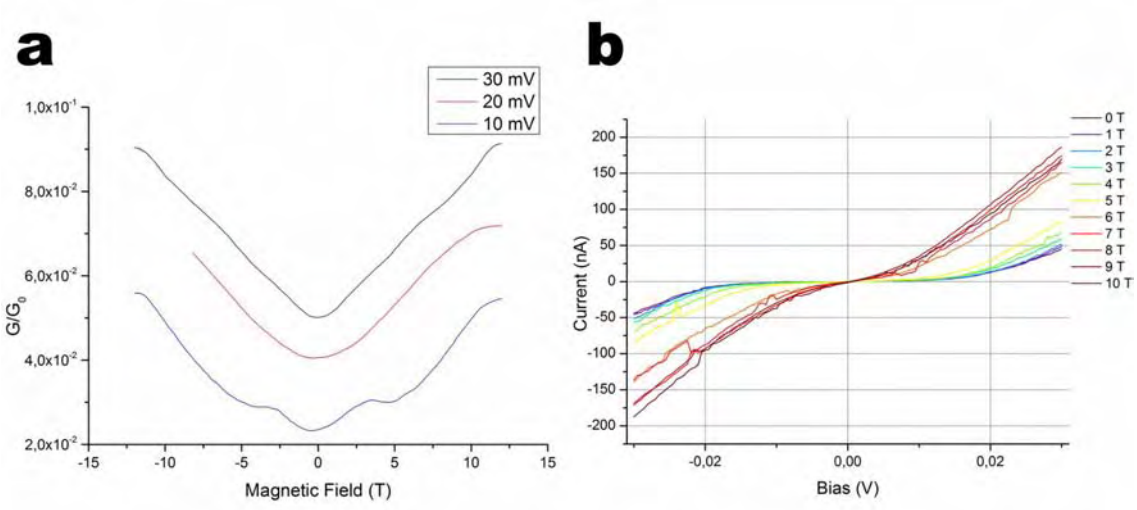


Figure 4.16: Perpendicular magnetic field scan measurements of the conductance of the GNR. (a) Measurements at constant bias and variable magnetic field, and (b) measurements at constant magnetic field and variable bias.

In addition we notice a conductance oscillation in the 10 mV measurements, which is symmetrical in magnetic field, at around 2.5 T. Those oscillations could be interpreted as Shubnikov de Haas oscillations induced by the occupation of cyclotron orbits when energy reaches a Landau level. We compare that to the Landau levels diagram calculated for a 50 nm ribbon (Figure 4.17a) adapted from[15]. At 1.4 K and 10 meV, the energy level we consider is equivalent to

E = 116 K (using $T=E/k_B$). We notice that, at this energy level and taking into account that at 60 nm levels are slightly lower, a Landau level is present for a magnetic field of around 2.5 to 3 T. It is therefore possible that the two oscillations are related to cyclotron orbit bulk states, which would further confirm the integrity of the crystallinity in the ribbon. We can now compare this with the cyclotron length versus the magnetic field (Figure 4.17b) using equation (**4.5**)[16] and deduce that orbits are around 15 nm wide. This is conceivable given the ribbon width as well as the estimated dot sizes. When energy is raised to 232 K (20 mV) and 348 K (30 mV), the Landau level is very close to 0 T and explain why it is no longer visible.

$$l_B = \left(\frac{\hbar}{eB}\right)^{1/2} \tag{4.5}$$

In addition, when measuring current versus bias at different field values (Figure 4.16b) we observe that the non-linearity is less and less pronounced as we increase the magnetic field. We interpret that as a magnetic field weakening of the confinement and lowering coulomb barriers[16]. In this case, the energy of the magnetic field acts as a temperature increase and allows electrons to access to higher energy levels.

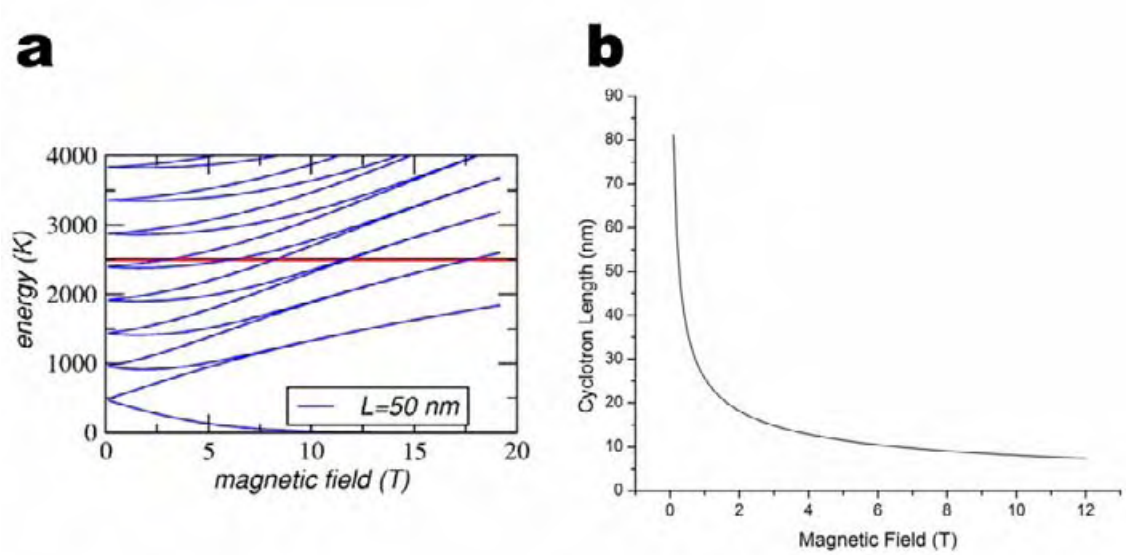


Figure 4.17: (a) Laundau levels for a 50 nm wide GNR as a function of magnetic field, adapted from [15]. (b) Plot of the cyclotron length of an electron versus the magnetic field.

4.3 Discussion and Perspectives

Two topics will be discussed in this section, concerning the electronic measurements just presented. First, the GNR properties extracted from the electronic transport results, such as the dot sizes estimated, compared to the SACTEM observations of the previous chapter. Secondly, the peculiar and bi-stable behaviour that this sample presented at high temperature (> 70 K). Finally, a comparison between the two ribbons will be treated.

The cryomagneto-transport measurements have mainly shown two things. The first one is that the GNR on sample B is composed of 6 dots. The second one is that the electronic transport through the edges results in better conductance than transport through the whole ribbon width (without magnetic field). Those results are in agreement with the SACTEM analysis presented previously on Chapter 3: good ribbon crystallinity and atomically smooth edges. It is possible that the few barriers across the ribbon are avoided by edge conduction. The SACTEM measurements show that adsorbates are indeed less present at the edges than in the core. Those adsorbates, by inducing potential fluctuations could therefore be partially responsible for the few isolated islands measured in the ribbon by field effect measurements. On the other hand no amorphization inside the GNR was observed in SACTEM, which affords for this interpretation and for the mobility we measured. In any case the estimated lower dot size of 50 nm is in the range of the high resolution SACTEM micrograph size.

Defects on the ribbon could also explain the field measurements. As no defects were spotted in SACTEM, their origin must be the SiO_2/Si substrate. Backscattered electrons could have induced the defects during EBIE. Even if the fraction of energy backscattered to the graphene layer is low, it exists and becomes measurable by electronic transport when patterning is long enough (10 to 15 mn).

One way to avoid this problem would be to fully remove the pool bottom, which is unfortunate as this would stronger reduce grid efficiency. Another option would be to install the backgate after EBIE patterning of the ribbon, which could be possible even if highly delicate. In addition, the need for electrical insulation imposes additional etching close to the GNR, enhancing the damage probabilities on the ribbon. Those are the principal differences compared to SACTEM experiments that could explain the presence of 50 to 180 nm dots on the ribbon.

4.4 Conclusion

In this chapter the results of the electron transport experiments on the oxygen assisted EBIE patterned GNR are presented. If the 90 nm wide GNR shows a linear I(V) characteristic, the 60 nm wide GNR presents a non-linearity and a flat conductance region of ~1-0.5 meV at low temperature. This energy is similar to the theoretical gap energy for a 60 nm GNR. Back-gated measurements show that some barriers still exist through the ribbon potential, inducing electron localization. Backscattering electrons damage during EBIE or isolation cuts close to the ribbon combined by the adsorbates observed in SACTEM could be the origin of those 7 barriers existing through the ribbon. On the other hand, magneto-transport could show important magneto-conductance and Landau level plateaus that indeed suggest high mobility in the sample. This result is consistent with the SACTEM observation of the nanoribbon edges (Chapter 3).

4.5 References

[1] Y. B. Zhang, Y. W. Tan, H. L. Stormer, P. Kim, Nature 2005, 438, 201.
[2] S. Droescher, H. Knowles, Y. Meir, K. Ensslin, T. Ihn, Physical Review B 2011, 84.
[3] M. Sprinkle, M. Ruan, Y. Hu, J. Hankinson, M. Rubio-Roy, B. Zhang, X. Wu, C. Berger, W. A. de Heer, Nature Nanotechnology 2010, 5, 727.
[4] L. Jiao, X. Wang, G. Diankov, H. Wang, H. Dai, Nature Nanotechnology 2010, 5, 321.
[5] R. Ribeiro, J.-M. Poumirol, A. Cresti, W. Escoffier, M. Goiran, J.-M. Broto, S. Roche, B. Raquet, Physical Review Letters 2011, 107.
[6] P. Gallagher, K. Todd, D. Goldhaber-Gordon, Physical Review B 2010, 81.
[7] J. B. Oostinga, B. Sacepe, M. F. Craciun, A. F. Morpurgo, Physical Review B 2010, 81, 4.
[8] A. K. Geim, K. S. Novoselov, Nature Materials 2007, 6, 183.
[9] C. Stampfer, J. Guettinger, S. Hellmueller, F. Molitor, K. Ensslin, T. Ihn, Physical Review Letters 2009, 102.
[10] M. Y. Han, J. C. Brant, P. Kim, Physical Review Letters 2010, 104.
[11] J. Guttinger, F. Molitor, C. Stampfer, S. Schnez, A. Jacobsen, S. Droscher, T. Ihn, K. Ensslin, Rep. Prog. Phys. 2012, 75, 24.
[12] J. Yan, M. S. Fuhrer, Physical Review Letters 2011, 107.
[13] Z. Luo, N. J. Pinto, Y. Davila, A. T. C. Johnson, Applied Physics Letters 2012, 100.
[14] H. Pinto, A. Markevich, Beilstein Journal of Nanotechnology 2014, 5, 1842.
[15] N. M. R. Peres, A. H. Castro Neto, F. Guinea, Physical Review B 2006, 73, 4.
[16] J. Bai, R. Cheng, F. Xiu, L. Liao, M. Wang, A. Shailos, K. L. Wang, Y. Huang, X. Duan, Nature Nanotechnology 2010, 5, 655.
[17] J. M. Poumirol, A. Cresti, S. Roche, W. Escoffier, M. Goiran, X. R. Wang, X. L. Li, H. J. Dai, B. Raquet, Physical Review B 2010, 82, 4.

Chapter 5

UHV 4-probe STM Study of Graphene and Graphene Nanoribbons

CONTENTS

5.1 4-PROBE UHV-STM SET UP AND SAMPLES 103
5.2 UHV-STM ANALYSIS OF BASAL ADSORPTION ON GRAPHENE 107
5.3 GRAPHENE SEM IMAGING UNDER UHV AND ELECTRICAL ANNEALING 110
5.4 ELECTRONIC TRANSPORT ON GRAPHENE CROSS DEVICE 113
5.5 CONCLUSION 120
5.6 REFERENCES 121

5.1 4-probe UHV-STM set up and samples

The production of graphene suspended devices requires multiple steps of sample processing, several steps of which create contamination or damage the pristine crystallinity and eventually degrades the device performances. Among them, adsorbates and lithography related contamination could be obviated by working in UHV environment and probing directly graphene. Moreover our ultimate goal is a control of graphene edge with atomic resolution, which further pleads in favour of STM observation of GNR devices.

In this chapter we present the SEM and STM study of CVD graphene and graphene devices under UHV conditions. Scanning Tunnelling Microscope was brought to function in Zürich by the two IBM researchers Gerd Binnig and Heinrich Rohrer in 1981[1]. Since then a new field in material physics has opened for surface analysis. The principle of this microscope is to use the tunnel current established between two metal electrodes that are not in electrical contact. The tunnelling current varies exponentially with the distance between them. By choosing a metallic tip as one electrode and a flat metallic or semiconducting surface as the other electrode, a local tunnelling current can be established between the last few atoms of the tip and the surface. A topography map of the surface can be

performed maintaining a constant current setpoint by approaching or retracting the tip while scanning. Other experiments such as bias spectroscopy and molecular orbitals imaging are possible thanks to this microscope down to sub-atomic resolution (Figure 5.1a). More recently multiple tip STM have been developed in order to access to a whole new field of measurements: parallelized measurement and manipulation, or probe-to-probe measurements. In the case of multiple tip STM developed by Omicron, four STM scanners are mounted around the sample and each probe is at around 45 º of the vertical position and at 90 º from each other on the (x;y) plane. A FEG SEM column on top of the setup monitors tips approach and manipulation. In our case, a 4-probe STM is ideal for high-resolution imaging, manipulating and electrically measuring graphene devices. This machine allows performing electronic transport measurements through a patterned graphene object avoiding lithography and bonding. For this work we use an Omicron Nanoprobe 4-probe STM at the Institut d'Electronique de Microélectronique et de Nanotechnologie in Lille (France).

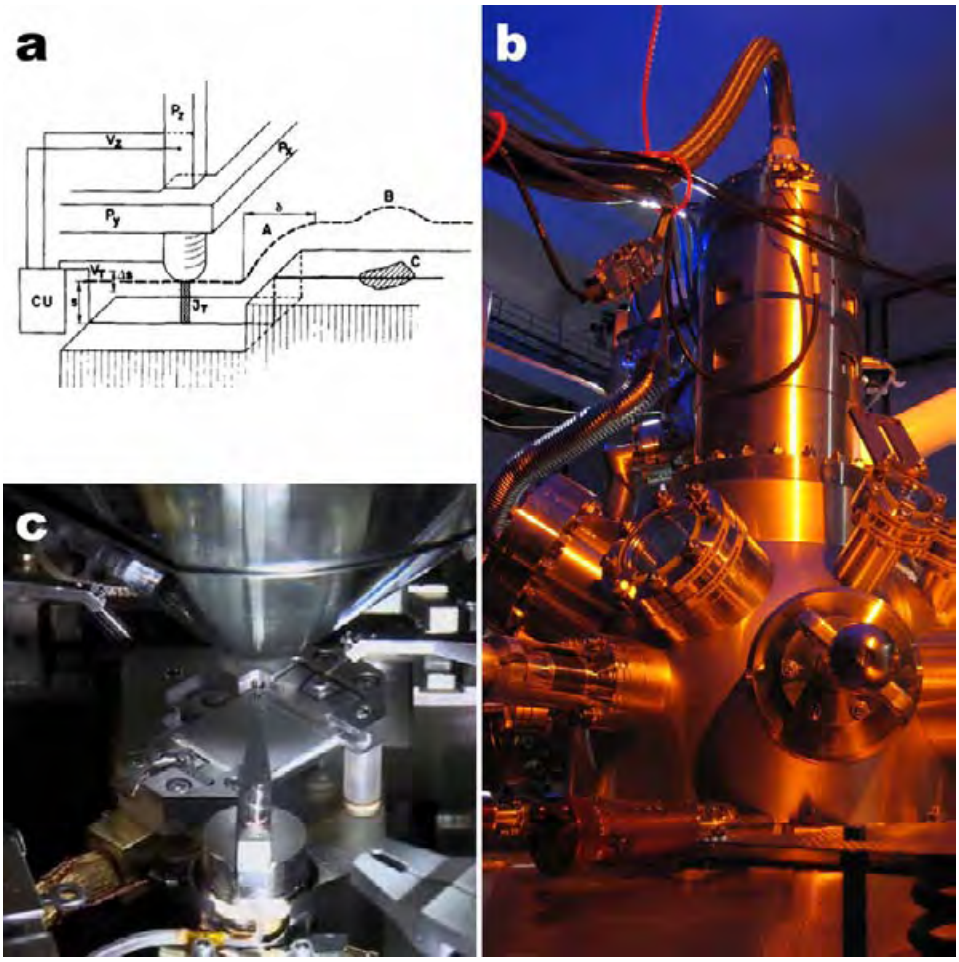


Figure 5.1: (a) Scheme of the STM adapted from[1]. Px Py and Pz are the piezzo controlling the three axes, J_t is the tunnel current and the dashed line corresponds to the STM trajectory to maintain the tunnel current setpoint. Adapted from [1]. (b) The Omicron NanoProbe 4-probe STM from outside with view to the SEM column. (c) Picture of the inside of the microscope, at the top the SEM pole piece surrounded by the 4 STM tips disposed over the sample holder.

The first generation of Omicron Nanoprobe is composed of 4 STM microscopes and one Zeiss Gemini SEM column identical to the one described in the section 2.2.1. The STM scanners are three low resolution STM's and one high resolution tip. The high-resolution scanner is the only one that is precise enough to reach atomic resolution. The high-resolution tip is placed at the bottom right position on all SEM pictures presented here. Four Nanonis controllers interface the four STM tips. All the equipment is in a UHV chamber at $\sim 10^{-10}$ mbar. In addition another UHV chamber is available for tip preparation and sample annealing.

The tips are made of tungsten wire etched by electrochemical process. The wire is dipped in a NaOH solution and a voltage is applied between the tungsten wire and another electrode (often graphite) inside the solution. As the tungsten is etched, the solution meniscus retracts. As a result, a sharp tungsten tip is formed. In the preparation chamber, the tips are heated up for around 5 hours to clean them of any adsorbents. Once the chamber pressure drops below 10^{-9} while the tip is red hot, it is cooled down to room temperature and installed on its corresponding piezo scanner. The resulting tips are shown in Figure 5.1 and 5.2.

The sample connection to ground for classic STM can be unplugged to perform probe-to-probe measurements using a Keithley source-meter[2].

STM has already been used for suspended graphene analysis[3-9]. The ideal sample for this study would be graphene deposited over an atomically flat metallic substrate with holes (with no bottom to avoid any backscattering). Indeed two areas would then be accessible simultaneously: graphene on atomically flat surface for structural analysis of the graphene adsorbents and suspended for graphene properties measurement and suspended patterned graphene for device measurements. The samples prepared for this work are CVD graphene deposited on TEM membranes as well as silicon [1,0,0] substrates with pools (SiO_2 on Si substrates used for transport in which oxide is removed by HF etching). After deposition the samples are annealed under hydrogen and argon as described in Chapter2. The sample is heated up to around 400°C for 24h[3], once introduced in the Nanoprobe.

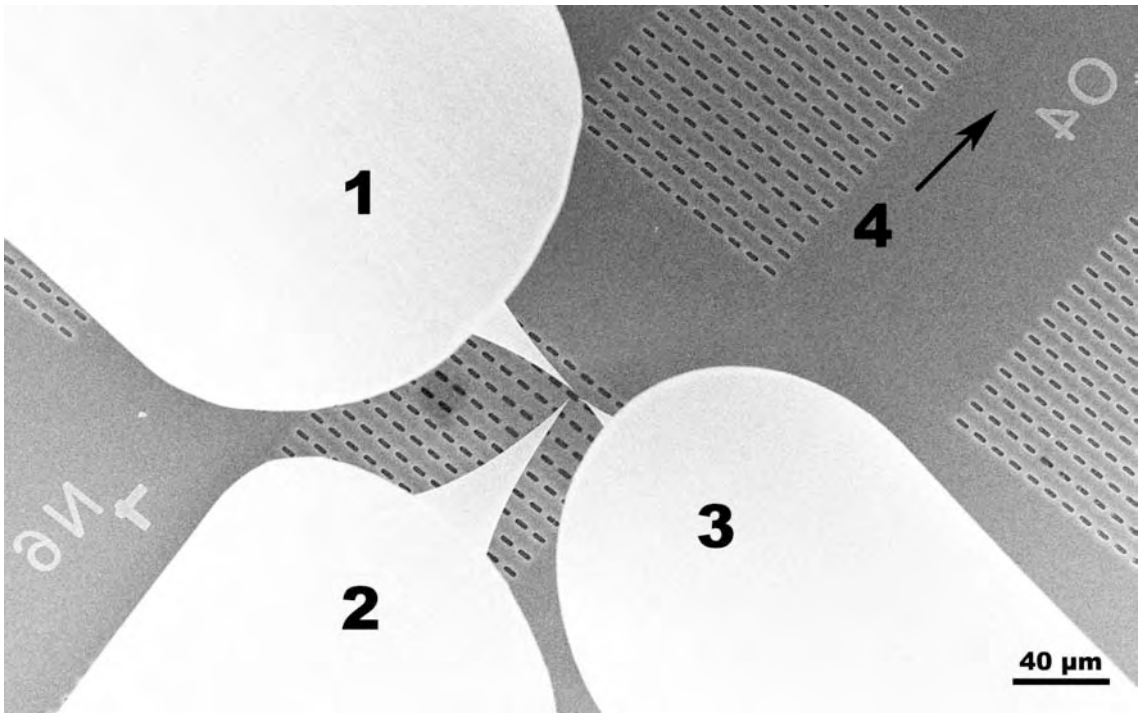


Figure 5.2: SEM micrograph of 3 of the 4 tips installed on the Nanoprobe scanners

To land a probe on the sample for probe-to-probe measurements, all the area is scanned by the STM tip to find points of reference and its landing position. The tip is placed in STM mode at the desired position and control loop is opened. The tip is then slowly lowered using the piezzo until STM current rises suddenly and saturates. The tip is now in contact with the substrate. The same procedure is followed for the second tip. Once both tips are in contact with the sample, at least one of them is set to ground voltage. The sample needs to be unplugged from the ground to eliminate shortcuts and force the tip-to-tip current path. The microscope is ready. The probes are connected to a source-metre, bias is applied between probes and the current measured.

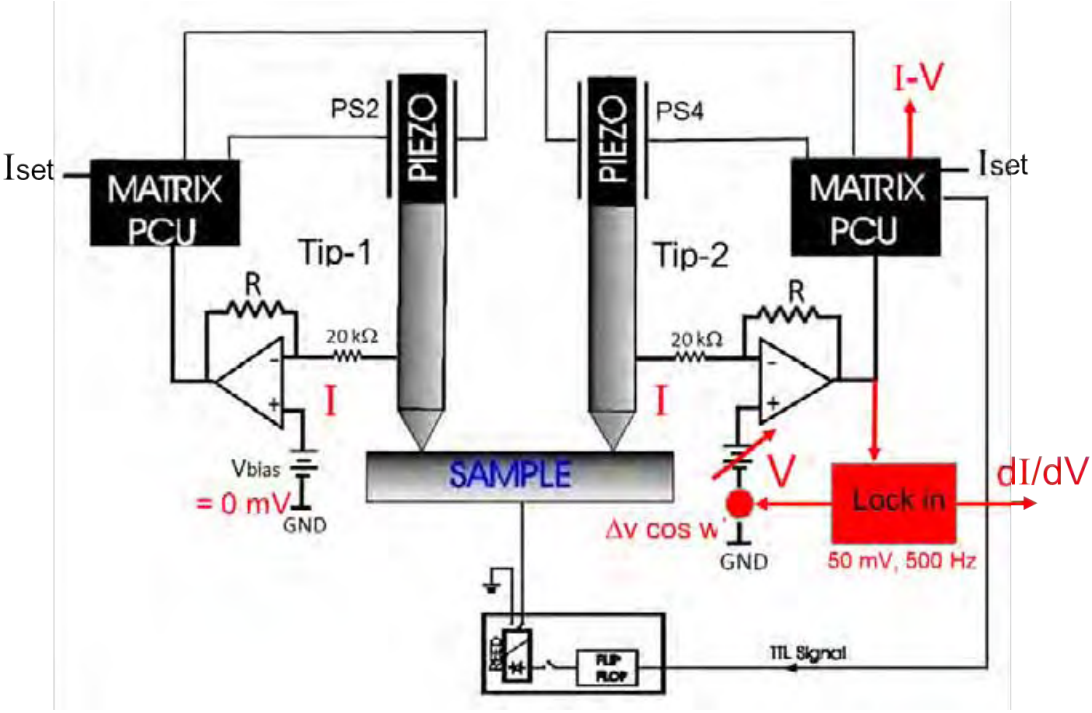


Figure 5.3: Nanoprobe setup for probe-to-probe electronic transport measurements through the sample. Courtesy of C. Joachim (CEMES, CNRS).

5.2 UHV-STM analysis of basal adsorption on graphene

Epitaxial graphene has been shown to be clean in UHV conditions[10-12]. This section presents the results of our SEM and STM analysis of our graphene samples. We can choose between two techniques to produce graphene: tape micro-cleaving and CVD graphene. The use of tape is not adapted to UHV, and CVD is often transferred using resist techniques such as PMMA transfer[13-15] outside the UHV chamber.

Another way to get clean graphene in UHV is the in-situ growth of graphene, or a direct connection between the CVD oven and UHV chamber. Some works had been done on ruthenium[10-12]. For our purposes there is the need to have graphene on insulators though. The CVD graphene on metal should be transferred, which is not possible in UHV with actual techniques. It is though possible to perform CVD growth on other than metallic substrates. A few reports of the direct CVD growth of graphene on insulators have recently been published. One example is the growth of graphene on SiC[16-20]. This process produces samples directly measurable by multi-probe STM. A second example is the growth of graphene on mica[21]. This technique produces graphene on top of little isolated pieces of mica, which would need to be grounded individually in order to analyse them on STM or SEM. Epitaxial graphene produced on SiC by silicon sublimation leads to wafer scale graphene layer. Graphene ribbons can be produced, but not arbitrary

patterns. An interesting approach consists in growing graphene by metal catalysed CVD but using thin films to allow graphene to grow at the lower interface of the metal [22]. Besides the classical layer formed at the metal-vacuum face, another graphene layer is formed at the silica-metal interface. The metal can then be removed, leaving interfacial CVD graphene on top of the insulating substrate. Unfortunately, it appears that this approach is difficult to control and requires silica substrate, which is difficult to keep atomically smooth.

There is no technique today to bring pristine suspended graphene into UHV chambers avoiding atmosphere exposure to the material. We attempted the graphene transfer from HOPG by direct contact. One experiment has been carried out to try and transfer graphite in UHV to a flat silicon dioxide substrate. In order to do this we used a press that brings into contact two omicron pads. This press is part of the Dynamo UHV Factory (DUF) (Figure 5.4 a and b). In one of the sides a silicon dioxide on silicon sample is installed that has been pre-cleaned and annealed in UHV. A crystal of HOPG freshly cleaved before inserting in UHV chamber is annealed at 400ºC overnight. It is then installed on the other side of the press. By pressing the surfaces against one another, graphene layers are transferred. By this process the surface that has been exposed to atmosphere lies face down to the substrate and a clean cleaved surface is accessible for STM measurements. The experiment resulted in very poor transfer yield between the two sides that were analysed by optical microscopy. Two objects were identified (Figure 5.4c and d). Figure 5.4c shows a thick piece of graphite whereas the Figure 5.4d shows a thinner deposit. This deposit has straight borders and could correspond to graphene. The optical contrast corresponds to less than 3 or 4 layers. This result indicates that, even if difficult and with poor success, the transfer of HOPG to another surface could be performed in UHV by friction. Silicon dioxide samples are certainly not the most appropriate candidate for this process as its surface is too rough.

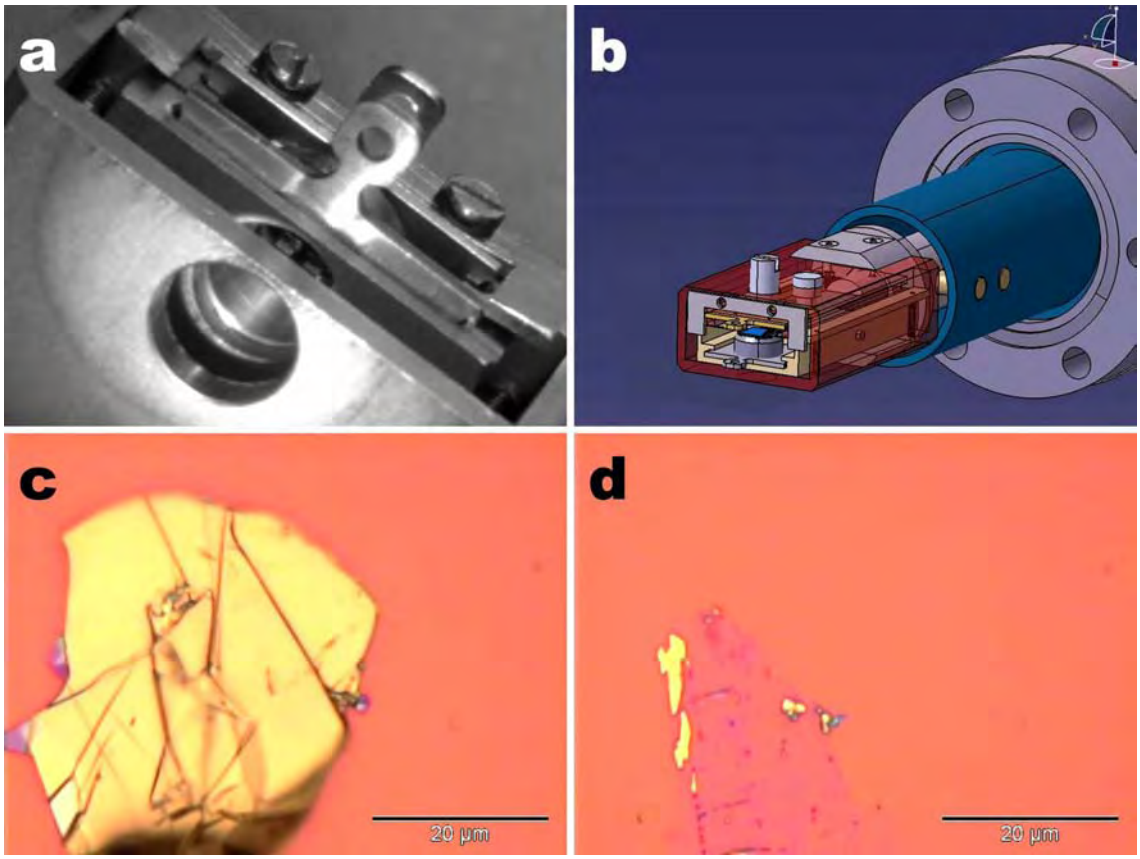


Figure 5.4: (a) Picture and (b) scheme of the UHV press, courtesy of D. Martrou (CEMES, CNRS). Images (c) and (d) are optical microscope pictures of the objects spotted on the silicon dioxide substrate after the HOPG transfer experiment.

If we consider the possibility to transfer CVD grown on metal onto another substrate, we know that the usual technique using PMMA leaves some residues behind that are not removable[23]. Transferring graphene without resist as we do (see Chapter 2), the sample is only covered by an a-C layer. This material is easier to remove than the PMMA and after annealing in reducing atmosphere followed by an UHV annealing only some thin layer a-C persists (Figure 5.5). In addition, local annealing by joule effect is a relatively effective process, even if it does not remove all kind of contaminants[24].

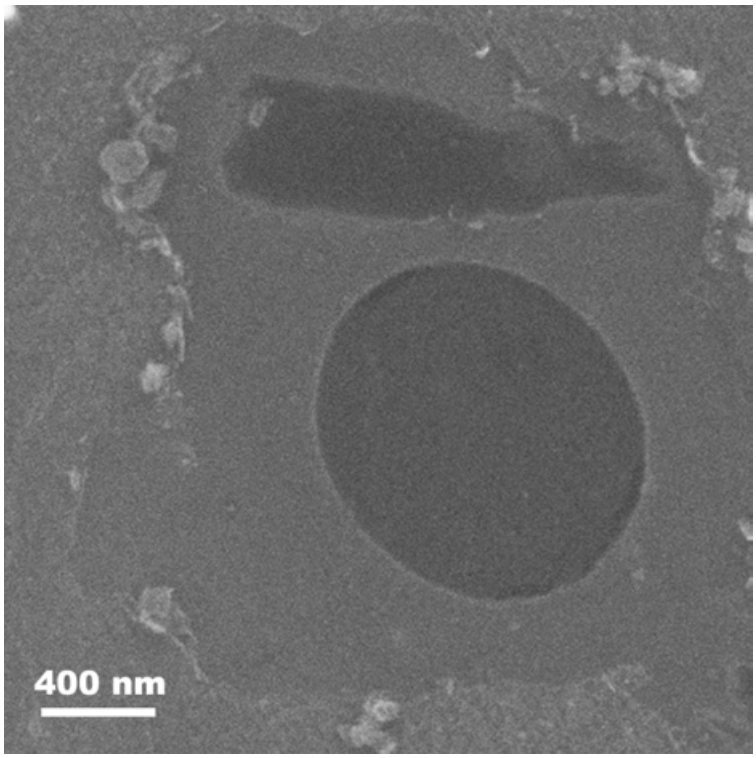


Figure 5.5: SEM micrograph of CVD graphene area on TEM grid after STM scanning at low setpoint.

5.3 Graphene SEM imaging under UHV and electrical annealing

As described previously, in Chapter 3, there are three sources of graphene contamination: the microscope chamber, the carbon present on the sample itself and products from the EBIE reaction. So far this contamination has been observed in the Helios without performing any etching. The amorphous carbon layer grows as imaging proceeds. Figure 5.6 shows a comparison between areas exposed to e-beam in both microscopes. Figure 5.6a shows a pristine suspended CVD graphene on its first SEM scan after H_2/Ar annealing. The contrast is sharp and many details such as folds and multilayers are visible. After an etching test and another scan (D_1~7.86 10^{-9} C/μm^2) operated at P=10^{-7} mbar , Figure 5.6b shows that graphene has been covered by amorphous material, multilayers are no longer visible and graphene contrast turned to white. In this case even folds are hard to see after imaging. Figure 5.6c shows a suspended CVD graphene in which multilayers and some grain boundaries are visible. Figure 5.6d shows the same area 16 min later and after many scans (D_2~6.07 10^{-8} C/μm^2) at P=10^{-10} mbar . In this second micrograph no changes are observed compared to the first one. The same details can be seen and graphene has kept the same dark contrast. Performing the EBIE and the SEM imaging in a cleaner, or a UHV, chamber would therefore not generate as much amorphous carbon adsorption as what was observed in chapters 3 and 4,

thus further advocating for the implementation of our EBIE protocol in yet cleaner UHV environment.

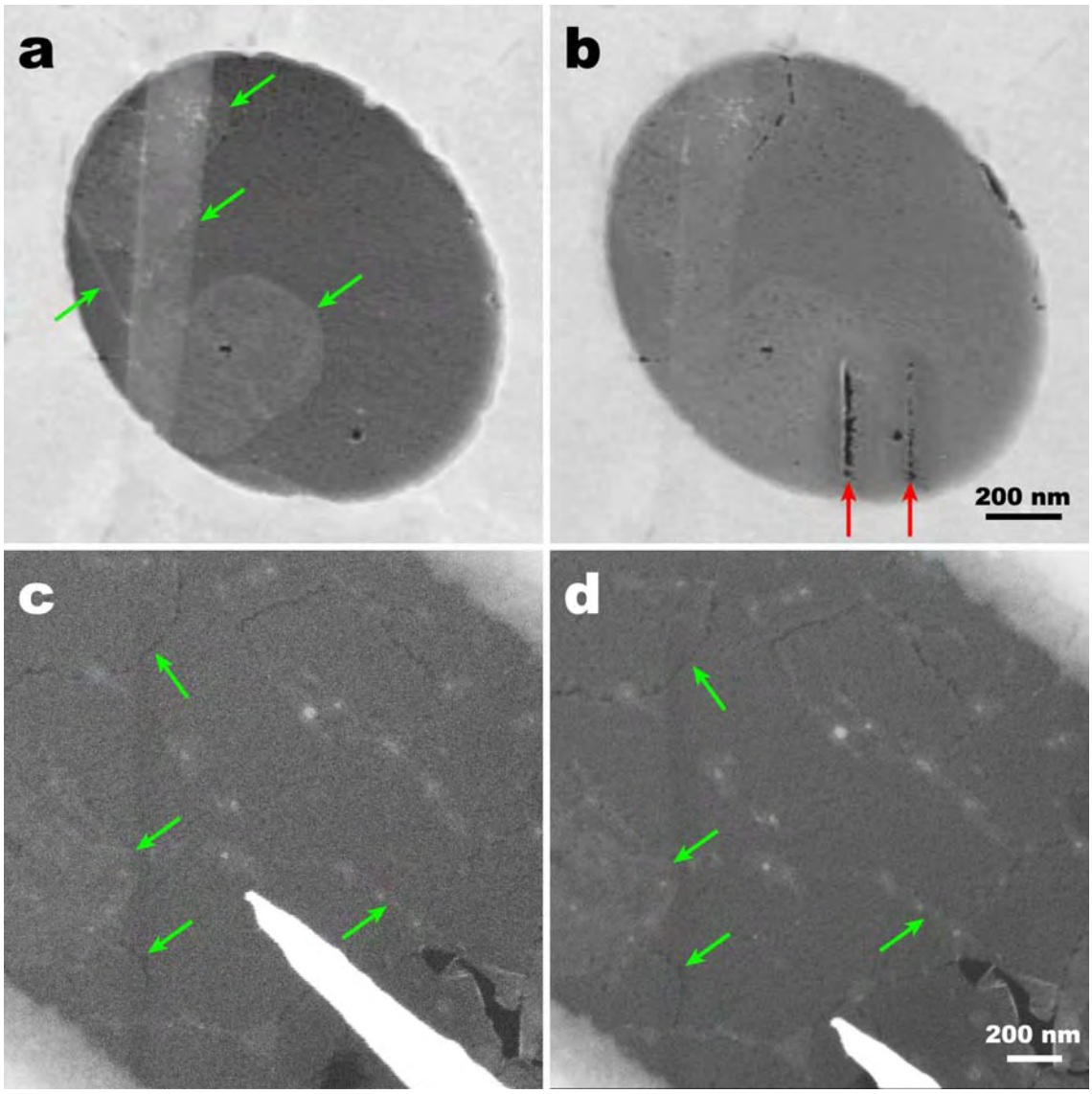


Figure 5.6: Comparison of SEM imaging in secondary vacuum (10^{-7} mbar in the Helios) and in UHV (10^{-10} mbar in the NanoProbe). (a) SEM picture of suspended CVD graphene taken in the Helios chamber, (b) is the same as (a) after 2 SEM scans and some etching (red arrows) (D_1~7.86 10^{-9} C/µm²)(same scale). (c) Suspended CVD graphene region imaged in the Nanoprobe chamber, and (d) the same area 16 min and many scans later (D_2~6.07 10^{-8} C/µm²)(same scale).

If adsorbents are not removed by the successive annealing and desorption steps, electrical annealing can also be performed locally between two STM tips. The advantage is that the probes are placed anywhere in order to clean chosen local areas. An example is shown in Figure 5.7. Once in contact the bias is raised in order to establish a current that heats the area by Joule effect. The two probes are 376 nm from each other, which is comparable to the length of our standard graphene ribbons (see Figure 5.7a). The bias is raised from 0 to 1.6 V by 0.1 V steps and kept at maximal value. The measured current between the probes is around

1 µA. After 5 min the current has doubled and 10 min later the current reaches 209 µA. When the current eventually saturates, the bias is lowered back down to zero by 0.1 V steps (see Figure 5.7b and Figure 5.8). We estimate the maximum power to 0.3 mW.

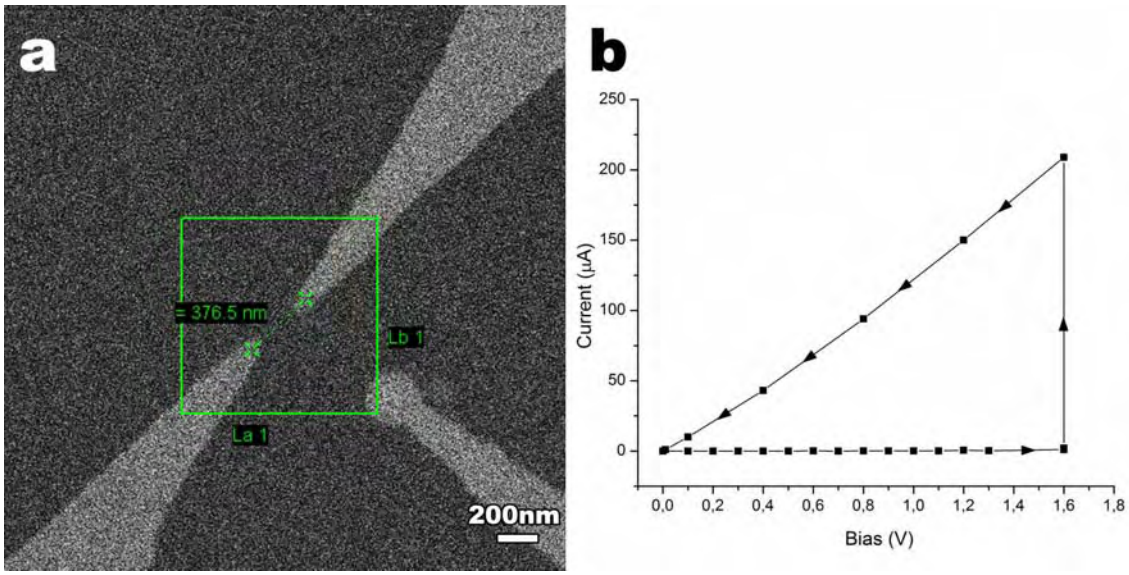


Figure 5.7: Electrical annealing experiment in the NanoProbe. (a) SEM picture showing the STM tips setup of the experiment; tips 2 and 4 (lower left and upper right) are in contact to the surface. (b) Electrical path of the annealing, each step increasing and decreasing the bias is performed in a few seconds and the bias is maintained at 1.6 V during 10 min.

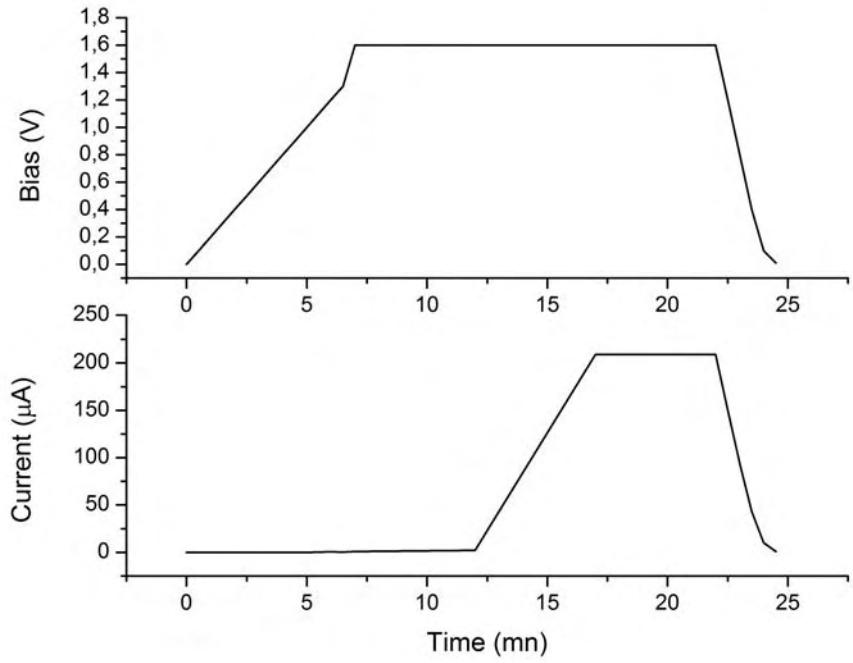


Figure 5.8: Bias and current versus time profiles of the electrical annealing of graphene using probe-to-probe current.

In the current-voltage graph displayed in Figure 5.8, we notice a different behaviour during the bias ramp up and down. While increasing bias, the current value does not follow immediately the bias evolution and value stays low resulting in a resistance of 1 MΩ. After the 10 min annealing, the current rises. The resistance falls down to 7.6 kΩ. Upon ramping down, the I(V) characteristic is almost linear revealing the conductor-like behaviour of graphene. Our interpretation is that during the annealing some species adsorbed to graphene had been removed or they have migrated out of the electron's path. No significant variations of the chamber pressure during the experiment have been noticed which is probably due to the small area of the sample.

Another interpretation is that only the tip-to-surface contact has been enhanced, even if probes were in contact and pushing down to graphene some amorphous carbon could have been removed from below the tips.

Figure 5.9 are STM scans before (a) and after (b) the electrical treatment. The surface is flatter and STM tip is significantly more stable. The affected area, if so, goes beyond the surface between the two probes, which could indicate that the graphene temperature was significantly raised by diffusion away from the direct probe-to-probe path. Yet, even after this final attempts imaging graphene with atomic resolution could not be obtained.

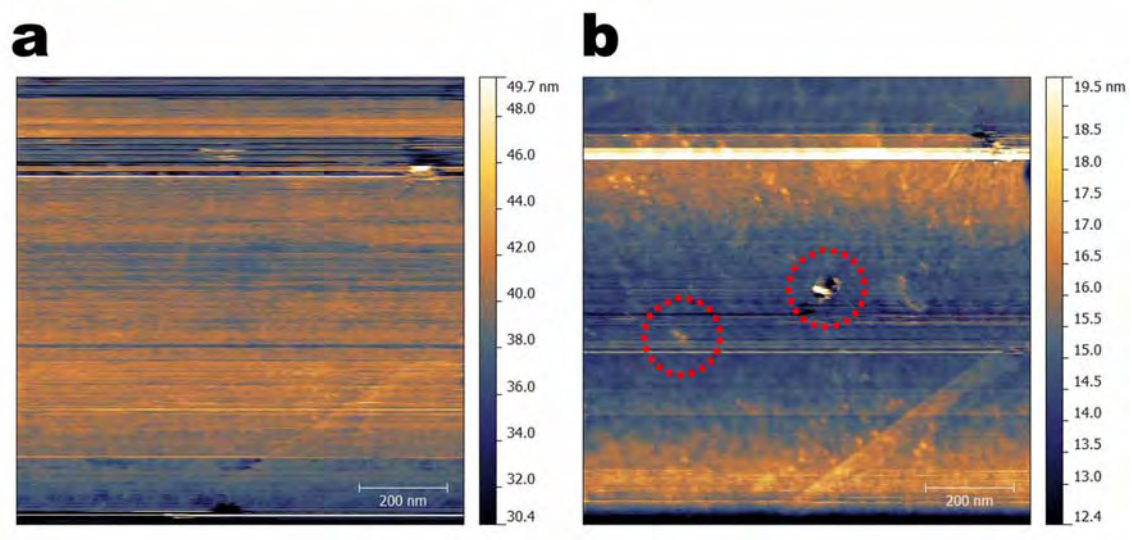


Figure 5.9: STM scans of the electrically annealed area before (a) and after (b) annealing. Red dotted circles in (b) correspond to the landing marks of the tips.

5.4 Electronic transport on graphene cross device

To measure a simple GNR electrically on a 4-probe station, one of the sides has to be electrically insulated from the other side to avoid shortcuts around the ribbon. If one of the sides is insulated it has to be supported, otherwise the ribbon would fall off and hang from the substrate. The supported area of the pattern has

then to be over an insulator, which is not the case for our samples. For this reason we considered a slightly more complex, but suspended, structure: a graphene cross. In this section is presented the preliminary SEM, STM and electrical analysis of an EBIE patterned cross (Figure 5.10). This cross is patterned on CVD graphene deposited over a TEM grid. This pattern has been chosen because, when placing one of the probes in the centre, electrons have to pass through a ribbon to reach the other electrode, thus the configuration is similar to an end to end measure of a GNR device. The device studied here is a cross composed by 2 GNR intersecting at 90° from each other. Each GNR is 290 nm long by 90 nm wide with a V-shaped connection each at $\pi/3$ of aperture angle. The pattern diagram shown in Figure 5.10a has been milled by EBIE under conditions defined in Chapter 3 as it is fully suspended. This also means that no gated transport measurements are possible in this substrate. STM (Figure 5.10b) and SEM (Figure 5.10c) imaging show that the intended complex pattern was successfully fabricated. The edges of the cross arms appear straight and smooth at the considered low magnification. Upon closer examination, one can notice the presence of several filaments hanging across the EBIE cuts. Such protrusions are observed when significant re-deposition occurs at the same time as the etching. We thus assume that the binding material most probably consists to rather insulating amorphous carbon.

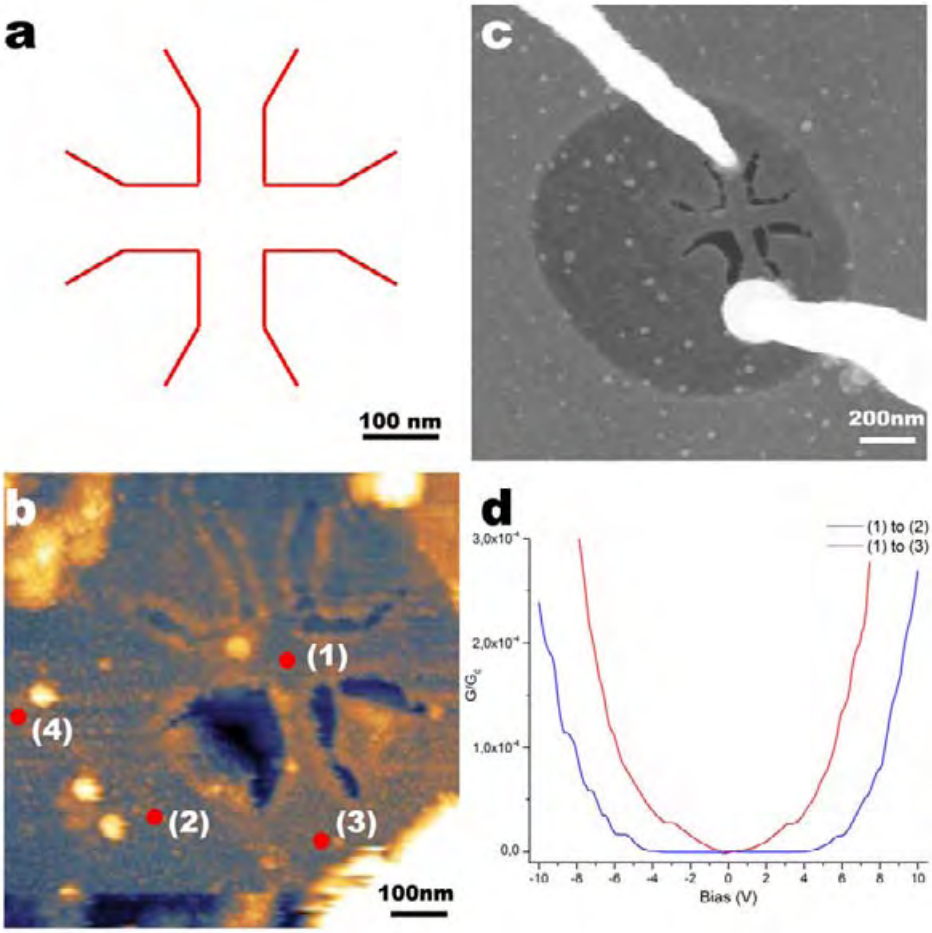


Figure 5.10: (a) SEM view of the configuration of the STM tips around a silicon sample in the 4-probe STM. (b) STM scan of the cross. Landing positions for the electric measurements are pointed with red dots and numbered from (1) to (3). (c) SEM image of the object analysed. The device is etched on suspended graphene on a TEM SiN grid. The tips 1 (low resolution, top left) and 3 (high resolution, bottom right) are used for imaging of the graphene nanoribbons cross and for the contact mode transport measurements. (d) Normalized conductance trough one leg of the graphene cross versus the drain-source bias. Red plot for measurements between positions (1) and (3), blue plot for measurements between position (1) and (2).

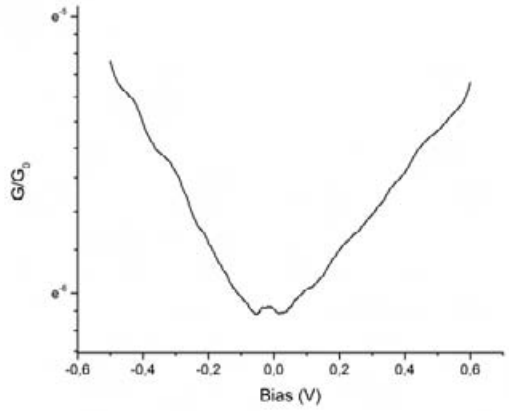


Figure 5.11: I(V) characteristic in Ln-scale of pristine graphene measured between positions (2) and (4)

The STM tips are positioned on the graphene by the procedure described before. For the characterization of the cross device, one tip is placed at the centre of the cross and set to ground voltage while another one is placed at location (2) or (3) and scanned on bias voltage.

The I-V characteristics for $V_{tip\text{-}tip}$ ranging from -10 V to +10 V are displayed in Figure 5.10d. Three different configurations are considered. The I-V of the non-patterned graphene is measured between positions (2) and (4) (Figure 5.11).

The cross pattern is first probed by measuring I(V) between the centre of the cross (1) and the end of an arm (3). The effect of the multiple arm pattern is further investigated by placing one tip at the centre of the cross (1) and the other one at the mid-distance between two arms terminations (2).

Conductance in pristine graphene is constant at any bias, yet the conductance measured is not constant and shows a minima at 0 V bias. This non-linearity is linear in logarithmic scale (Figure 5.11) indicating a tunnel or Schottky barrier. It could be due to amorphous carbon material that covers graphene despite of the desorption attempts and degrades the contact. The a-C or oxide on the tip would act as a barrier of lower conductance.

For the (1) to (3) measurement we can consider, as first approximation, only the direct path along the 100 nm long and 90 nm wide GNR and neglect the other three. For this width range a very little gap ($E_g \sim 2.2$ meV) is predicted. The measurement shows no flat region at this measurement resolution. The non-linearity is most probably due to the confinement in the GNR as in Chapter 4, but as the ribbons are wider and electronic transport measurements are made at low bias resolution, they do not allow to see if a meV range gap is present or not. In addition, if the contact resistance is the correct answer for the non-linearity in the pristine graphene, then this phenomenon can play a role in this measurement too.

Interestingly, the I-V curve (Figure 5.10d blue) reveals a different behaviour. The measurement shows a large plateau between -4 and +4 V of negligible conductance. This apparent gap is much wider than what could be expected for this range of GNR sizes. In addition we measure two equivalent GNR linking (1) and (2) which should double the conductance compare to the single ribbon ((1)-(3) characteristic). If we adopt an idealized view, we can hypothesize that graphene is still pristine in the cross pattern and supports ballistic transport. If so, the (1)-(2) measurement is equivalent to a double slit experiment, which could result in interference patterns in position (2). To test this hypothesis, we simulate the propagation of a classical wave in a medium shaped like the experimental sample. A Fortran script was written to simulate the wave propagation. The important parameter for this simulation is the wave frequency (or wavelength) compared to the device dimensions. The electron wavelength used is the de Broglie wavelength, calculated as follows.

$$\lambda_{dB} = \frac{h}{p} \tag{5.1}$$

$$p = m_0 v \tag{5.2}$$

$$v = \sqrt{\frac{2eU}{m_0}} \tag{5.3}$$

Here, λ_{dB} corresponds to the de Broglie wavelength, h is the Planck constant (h =6.626.10^{-34} m^2 kg/s), p kinetic momentum of the electron, m_0 its mass (m_0 = 9.109.10^{-31} kg), v its speed, e the elementary charge and U the bias. Some simulations at different energies are shown in Figure 5.12. The biases on a, b, c and d correspond respectively to 0.1, 0.5, 1 and 5 V. The green cross corresponds to the position (2) of the electrode. The amplitude of the signal at the position (2) is finite only at low (below 0.5 V) and high voltages (above 5 V). In between, the tip in position (2) is placed in the destructive interference region created by the angle of the cross pattern. The amplitude squared is plotted versus the bias and qualitatively shows the same features of the experimental data: the signal is cut until around 6 V. However the interferences are constructive at low voltages resulting in a signal not observed experimentally. As the (1)-(3) measurement of one arm show a very low or zero conductance at this range, the same phenomena may take place in this measurement too.

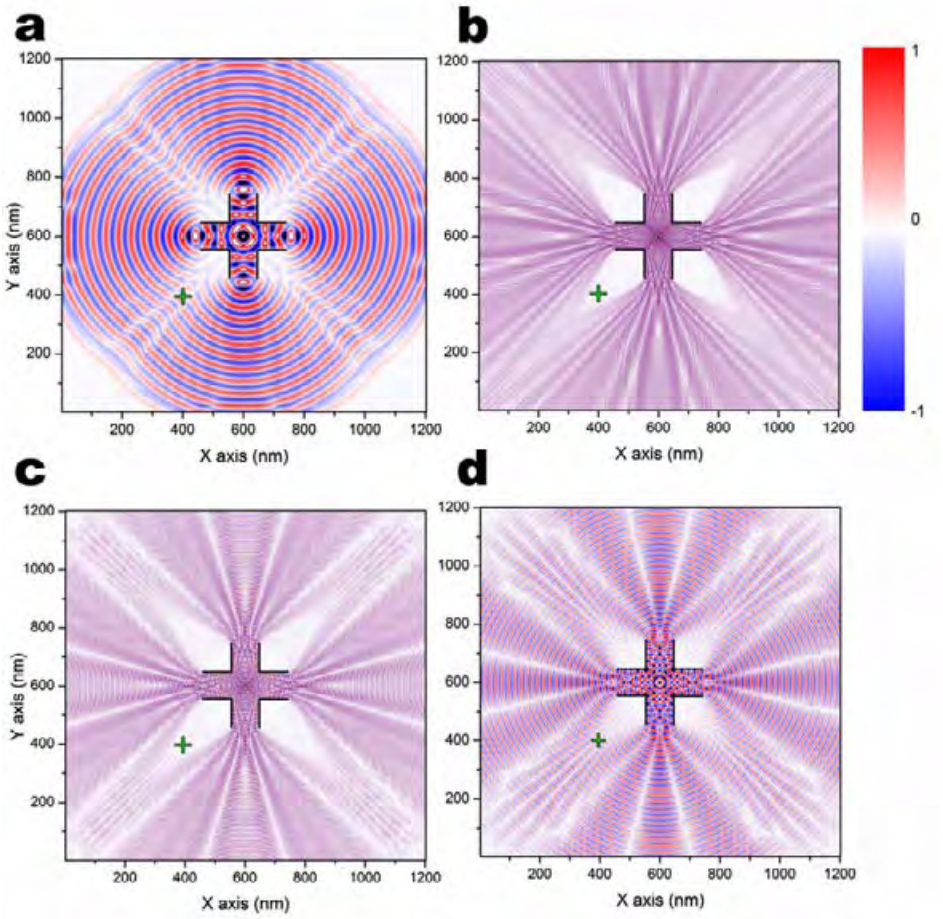


Figure 5.12: Simulation of the propagation of a wave through a graphene cross. The four simulations are for similar wave condition to 0,1 eV (a), 0.5 eV (b), 1 eV (c) and 5 eV (d) electron energy.

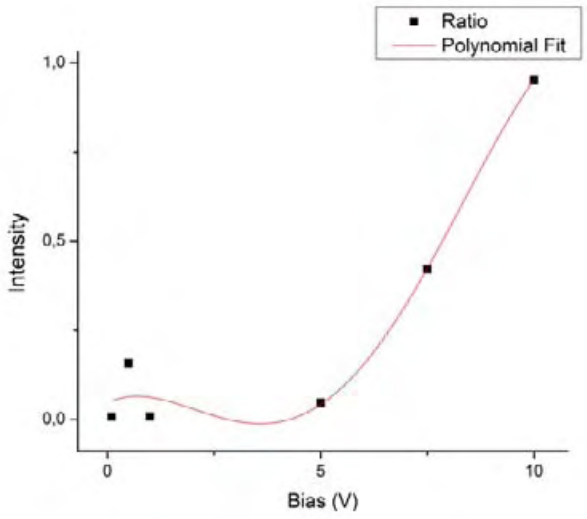


Figure 5.13: Graph of the normalized intensity (maximum normalized to 1) versus the bias voltage extracted from Figure 5.12.

At higher voltages, and lower wavelength, the diffusion from the two arms fill again the probed area and the signal raises over 5 to 6 V of bias.

In order to take into account both the measurement conditions of a single GNR represented by the tip-to-tip I/V curve between (1) and (3) and the possible interference through graphene between (1) and (2), we multiplied the simulated behaviour by the measurement through a single GNR. As a result we obtain the I/V curve displayed in Figure 5.14 (black) that we compare to the experimental (1)-(2) I/V curve.

The two plots are similar. The electronic interferences inducing a shadow at the tip position between 1 and ~5 V could indeed explain this large flat region measured on the Nanoprobe. This simulation is preliminary though, and a more precise model taking into account the lattice properties has to be used for more accurate comparison.

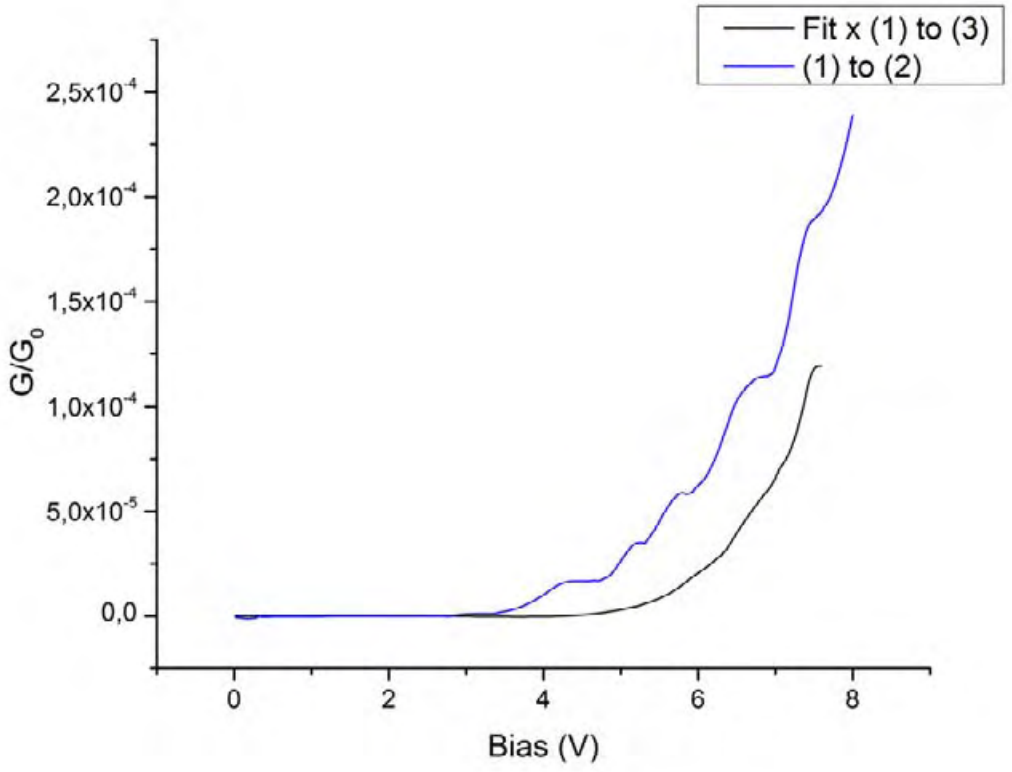


Figure 5.14: Comparison graphs between measurement on the cross between (1) and (2) and measurement between (1) and (3) corrected by the simulated electronic interference.

5.5 Conclusion

In this chapter an Omicron Nanoprobe 4-probe UHV STM has been used to analyse structural as well as electronic properties of a complex graphene device. The possibility of probing any patterned device on a TEM grid, without need of PMMA and lithography that induces contamination and the UHV environment are the main advantages of using a 4-probe UHV STM for the analysis of graphene devices.

The graphene cross studied seems to present electronic properties different from the GNR of the same width. A 90 nm wide GNR has theoretically a very little gap, whereas the cross presents an 8 eV flat region of suppressed conductance. We have explored one possible explanation. A similar behaviour has been simulated by preliminary calculations of electronic interferences on a cross-like medium of propagation.

Further experiments on the new Omicron Nanoprobe LT UHV STM will be carried. This higher resolution microscope at LHe temperature could supply supplementary measurements on our oxygen-assisted EBIE patterned devices.

5.6 References

[1] G. Binnig, H. Rohrer, Surf. Sci. 1983, 126, 236.
[2] M. Berthe, C. Durand, T. Xu, J. P. Nys, P. Caroff, B. Grandidier, in *Atomic Scale Interconnection Machines*, (Ed: C. Joachim), Springer Berlin Heidelberg, 2012, 107.
[3] R. Zan, C. Muryn, U. Bangert, P. Mattocks, P. Wincott, D. Vaughan, X. Li, L. Colombo, R. S. Ruoff, B. Hamilton, K. S. Novoselov, Nanoscale 2012, 4, 3065.
[4] F. R. Eder, J. Kotakoski, K. Holzweber, C. Mangler, V. Skakalova, J. C. Meyer, Nano Letters 2013, 13, 1934.
[5] R. Breitwieser, Y. C. Hu, Y. C. Chao, R. J. Li, Y. R. Tzeng, L. J. Li, S. C. Liou, K. C. Lin, C. W. Chen, W. W. Pai, Carbon 2014, 77, 236.
[6] A. Laitinen, M. Oksanen, A. Fay, D. Cox, M. Tomi, P. Virtanen, P. J. Hakonen, Nano Letters 2014, 14, 3009.
[7] M. Neek-Amal, P. Xu, J. K. Schoelz, M. L. Ackerman, S. D. Barber, P. M. Thibado, A. Sadeghi, F. M. Peeters, Nature Communications 2014, 5.
[8] P. Xu, M. Neek-Amal, S. D. Barber, J. K. Schoelz, M. L. Ackerman, P. M. Thibado, A. Sadeghi, F. M. Peeters, Nature Communications 2014, 5.
[9] J. K. Schoelz, P. Xu, V. Meunier, P. Kumar, M. Neek-Amal, P. M. Thibado, F. M. Peeters, Physical Review B 2015, 91.
[10] S. Marchini, S. Gunther, J. Wintterlin, Physical Review B 2007, 76.
[11] P. W. Sutter, J.-I. Flege, E. A. Sutter, Nature Materials 2008, 7, 406.
[12] S.-H. Ji, J. B. Hannon, R. M. Tromp, V. Perebeinos, J. Tersoff, F. M. Ross, Nature Materials 2012, 11, 114.
[13] A. Reina, X. Jia, J. Ho, D. Nezich, H. Son, V. Bulovic, M. S. Dresselhaus, J. Kong, Nano Letters 2009, 9, 30.
[14] Z.-Y. Juang, C.-Y. Wu, A.-Y. Lu, C.-Y. Su, K.-C. Leou, F.-R. Chen, C.-H. Tsai, Carbon 2010, 48, 3169.
[15] W. Regan, N. Alem, B. Aleman, B. Geng, C. Girit, L. Maserati, F. Wang, M. Crommie, A. Zettl, Applied Physics Letters 2010, 96.
[16] E. Moreau, S. Godey, F. J. Ferrer, D. Vignaud, X. Wallart, J. Avila, M. C. Asensio, F. Bournel, J. J. Gallet, Applied Physics Letters 2010, 97.
[17] M. Portail, A. Michon, S. Vezian, D. Lefebvre, S. Chenot, E. Roudon, M. Zielinski, T. Chassagne, A. Tiberj, J. Camassel, Y. Cordier, Journal of Crystal Growth 2012, 349, 27.
[18] A. Michon, S. Vezian, E. Roudon, D. Lefebvre, M. Zielinski, T. Chassagne, M. Portail, Journal of Applied Physics 2013, 113.
[19] B. Jabakhanji, A. Michon, C. Consejo, W. Desrat, M. Portail, A. Tiberj, M. Paillet, A. Zahab, F. Cheynis, F. Lafont, F. Schopfer, W. Poirier, F. Bertran, P. Le Fevre, A. Taleb-Ibrahimi, D. Kazazis, W. Escoffier, B. C. Camargo, Y. Kopelevich, J. Camassel, B. Jouault, Physical Review B 2014, 89.
[20] M. Sprinkle, M. Ruan, Y. Hu, J. Hankinson, M. Rubio-Roy, B. Zhang, X. Wu, C. Berger, W. A. de Heer, Nature Nanotechnology 2010, 5, 727.
[21] G. Lippert, J. Dabrowski, Y. Yamamoto, F. Herziger, J. Maultzsch, M. C. Lemme, W. Mehr, G. Lupina, Carbon 2013, 52, 40.
[22] C. Y. Su, A. Y. Lu, C. Y. Wu, Y. T. Li, K. K. Liu, W. J. Zhang, S. Y. Lin, Z. Y. Juang, Y. L. Zhong, F. R. Chen, L. J. Li, Nano Letters 2011, 11, 3612.

[23] Y.-C. Lin, C.-C. Lu, C.-H. Yeh, C. Jin, K. Suenaga, P.-W. Chiu, Nano Letters 2012, 12, 414.
[24] J. Moser, A. Barreiro, A. Bachtold, Applied Physics Letters 2007, 91.

Conclusion and Perspectives

A decade after graphene has been popularized, a vast effort is carried out worldwide to mass-produce it and to tailor its properties for a vast range of potential applications but also to reach yet unexplored physics.

Among possible ways to engineer the properties of graphene, nanoscale patterning will result in the confinement of the uniquely delocalized 2 DEG sustained by the flat sp^2 lattice.

In this thesis, we have developed a patterning technique that can reach atomic precision where graphene is cutted, while simultaneously offering the convening of arbitrary design and compatibility with the cleanest UHV environment. We have analysed the structure of the etching protocol in details and then transposed it to a partially suspended configuration that enabled to fabricate electronic devices based on graphene nanoribbons.

The patterning technique consists in a chemical etching of graphene by gaseous oxygen activated by the low-energy of an SEM electron beam. The Electron Beam Induced Etching removes carbon atoms from the lattice locally where the energy is supplied. The etching patterns can be of any arbitrary shape as it is reproduced by the programmed electron beam path. The etching by oxygen reveals to be effective. With a smallest feature size of about 10 nm and a capability to etch multimicrometre long lines.

The lines as well as ribbons down to 15 nm etched by oxygen EBIE are characterized using Spherical Aberration Corrected Transmission Electron Microscopy at low acceleration tension of 80 kV. The atomic resolution micrographs have shown, whether on cuts or ribbons, that the edges produced are non-amorphized and crystalline. The two edge arrangements, zigzag and armchair, had been observed. Moreover the graphene nanoribbons core is crystalline and no amorphized area has been observed.

Next, the etching technique has been successfully transferred to graphene partially suspended on backgated, silicon dioxide on silicon substrates. This adaptation requires an optimization of the suspended areas. In particular, the local pools had to be deepened to 6 µm to minimize the amorphization damages induced by backscattered and secondary electrons. Nanoribbons down to 60 nm in width were successfully produced and electrically contacted for electronic transport measurements.

Preliminary cryo-magneto-transport measurements were performed on one 60 nm wide and 320 nm long nanoribbon. The voltage-dependent measurements of the conductance show a non-linearity appearing as the temperature decreases down to 1.4 K with some indications of a small gap opening. The gap energy is estimated between 0.5 and 1 meV at unknown Fermi level, similar to the theoretical energy (3 meV). This indicates that other effects like electron hopping and edge disorder are weaker than the one measured in similar sized ribbons produced by EBL/RIE in addition of the absence of substrate. The field effect measurements at low temperature shown low coulomb blockade in the ribbon, we estimate the number of dots to six across the GNR. This number of dots is low giving around 50 nm islands of crystalline graphene. Field effect measurements also revealed mobility higher than 1200 cm^2/Vs and potentially up to 8000 cm^2/Vs. Finally conductance measurements under magnetic field showed a higher conductance when the current is confined along the edges. This result is in agreement with the SACTEM analysis confirming the good quality and crystallinity of the edges as conductance increase when electrons escape from some of the probable defects of the centre of the ribbon. Furthermore the magnetic field measurements show the presence of Shubnikov de Haas oscillation due to the presence of Landau levels in the sample, which is a sign of high mobility in the ribbon and thus good crystallinity.

In addition a perspective work has been explored: the 4-probe UHV-STM study of suspended graphene devices. The analysis using this machine has shown to be useful for two reasons: the SEM observation under UHV and thus low contamination environment, and for the possibility to perform probe-to-probe electronic transport measurements at any position on the sample without performing lithography or metal sputtering that contribute to contaminate the sample. The process of testing devices is then simplified in terms of production steps. We show that such analysis is possible by probing a graphene cross patterned by oxygen assisted EBIE. The transport properties show a behaviour reminiscent of simulated electron interference phenomena. The indication of electron interferences is one more property in agreement with high quality and crystallinity of nano-patterned graphene. Further experiments in the new LT 4-probe UHV-STM in CEMES could yield more indications on the actual potential of O_2 EBIE as patterning technique for atomic-scale graphene devices.

Based on this work, two perspectives can be suggested for future experiments. First of all, producing more GNR samples for electronic transport measurements in order to complete the measurements for a deeper knowledge of the objects produced by EBIE and further explore interpretations presented in this work. In addition, it is also important to produce and measure narrower GNR's. As presented in the SACTEM section in Chapter 3 our technique allows the reproducible fabrication of GNR's below 20 nm in width, which have not been produced yet over silicon dioxide on silicon samples for electrical measurements.

This would allow to access the energy gap E_G evolution depending on the GNR width. The second ones, and more long-term perspectives, are to continue the 4-probe measurements of fully suspended devices under UHV environment. This would be also a solution to work on cleaner samples and avoid contaminants during experiments. The capacity of this microscope to manipulate matter to the atomic level as well as a cleaner environment and low temperature (LHe) would improve quality as well as control on the ribbon nano-objects fabrication. Such evolution on graphene manipulation could allow one day the reproduction of already analysed molecules directly integrated in a graphene sheet for logic gate operations[1].

[1] C. Joachim et al. Physical Review B 83, 155443 (2011)

Nomenclature

ACE	Acetone
(SAC)TEM	(Spherical Aberration Corrected) Transmission Electron Microscope
2DEG	2-Dimensionnal Electron Gas
AFM	Atomic Force Microscopy
BF/DF	Bright Field / Dark Field
CTAB	Cetyl trimethylammonium bromide
CVD	Chemical Vapour Deposition
DOS	Density Of States
e-beam	Electron Beam
EBIE/D	Electron Beam Induced Etching / Deposition
EBL	Electron Beam Lithography
FEG	Field Emission Gun
FET	Field Effect Transistor
FIB	Focused Ion Beam
GIS	Gas Injection System
GNR	Graphene Nano-Ribbon
HAADF	High Angular Annular Dark Field
IPA	2-Propanol
LHe	Liquid Helium
LN_2	Liquid Nitrogen
NMP	1-Methyl-2-pyrolidone
PMMA	Polymethyl-methacrylate
RIE	Reactive Ion Etching
RT	Room Temperature
SAED	Selected Area Electron Diffraction
SE/BSE	Secondary Electrons / Backscattered Electrons
SEM	Scanning Electron Microscope
STM	Scanning Tunnelling Microscopy
TMP	Turbo Molecular Pump
UHV	Ultra High Vacuum
VLSI	Very Large Scale Integration
VTI	Variable Temperature Insert
WD	Working Distance

Annexe 1

Towards graphene/gold hybrid plasmonic systems

CONTENTS

1 INTRODUCTION 129
2 HYBRID PLASMONICS COMBINING GRAPHENE AND GOLD COLLOIDS 129
3 PARTICLE ENHANCED RAMAN SIGNAL 132
4 GREEN DYADIC SIMULATION 136
5 DISCUSSION 137
6 CONCLUSION 138
7 REFERENCES 139

1 INTRODUCTION

In addition to the intrinsic properties of graphene, this material allows an easy access to the bi-dimensional electronic gas. This is a unique opportunity to try and couple the electronic gas to other systems. One candidate is the coupling with a plasmonic system. The analysis of the coupling between graphene and plasmonic particles could lead to the possibility of using integrated graphene or graphene devices in plasmonic structures. To study the coupling of graphene with plasmonic particles we chose to investigate the evolution of the Raman signature of graphene in the vicinity of gold nanoparticles. Surface Enhanced Raman Spectroscopy studies on graphene coupled with nanoparticles have been published so far[1-7]. In this section we analyse the coupling between graphene and plasmonic gold particles. First we will describe the sample fabrication along with the particle description. Secondly we will focus on Raman mappings of a graphene sample on different beam conditions and on the three graphene Raman bands. Finally we present a theoretical study by simulation of conditions similar to the experimental sample to help understand the Raman results.

2 HYBRID PLASMONICS COMBINING GRAPHENE AND GOLD COLLOIDS

In this section, we make use of plasmonic colloidal gold nanoparticles in the graphene environment. The particles are crystalline gold rods. Their size varies between 140 and 350 nm long and their diameter is 18 nm. The rods are composed of 5 single crystals (Figure 1a) along a longitudinal axis resulting from the anisotropic growth of pentatermined seeds. The [1,0,0] faces are stabilized by

CTAB (Cetyl trimethylammonium bromide). During the growth, only faces [1,1,1] can collect metal and the seed grows into a rod shape (Figure 1b) nanoparticles are in solution and their faces still protected by CTAB.

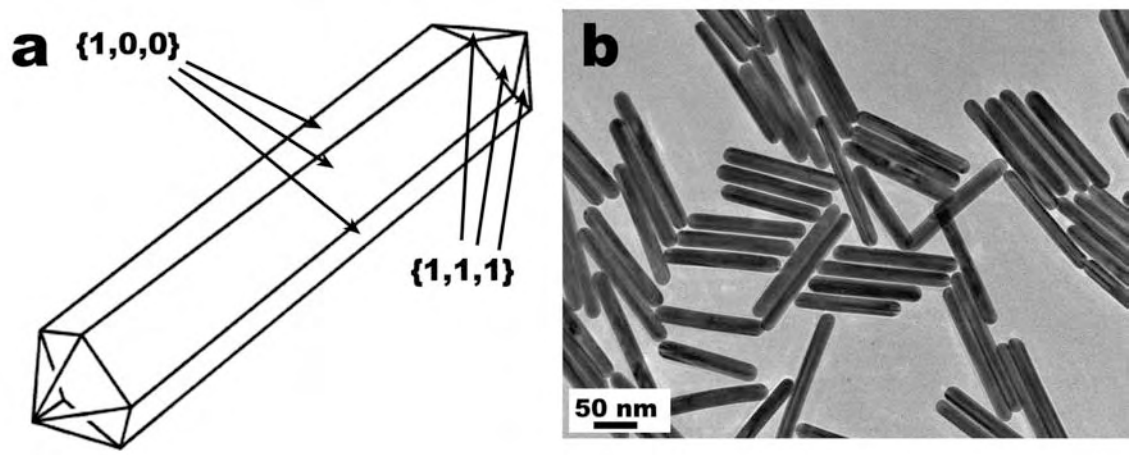


Figure 1: (a) Scheme of the gold nanorods morphology and crystals. (b) TEM micrograph of the gold nanorods on TEM grid. Courtesy of J. Sharma and E. Dujardin (CEMES, CNRS)

The sample fabrication begins by cleaning a flat silicon dioxide on silicon sample as described in Chapter 2. 15 μL of the rods solution is shacked is deposited over the substrate. Once dry, the substrate is rinsed with DI water. 20 min oxygen plasma is applied in order to remove CTAB of the nanorods and bring the surface plasmon in closer vicinity to the graphene 2DEG. As we want to excite graphene by the evanescent beam of the nanoparticles, the spacing must be as low as possible. Afterwards, we deposit graphene by the pealing technique (tape) described in Chapter 2 (Figure 2a). By this method we obtain a sample in which gold particles are covered by graphene, so graphene is fully accessible for measurements. The samples are first characterized by Raman mapping acquisition (Figure 2b). As the gold nanorods are not visible on optical microscopy, SEM could modify the graphene layer, and AFM would be longer to perform than Raman itself. The sample we will be interested on, in this chapter, is the sample in Figure 2c. It contains three spots of interest (1, 2 and 3). Number 1 is a pair of rods (Figure 2d left), the longer measures 333 nm long by 18 nm in diameter, and the shorter 237x19 nm. Number 2 is also a pair of rods (Figure 2d right) measuring 280x18 and 198x19 nm. Finally the third spot is a single rod measuring 243x18 nm.

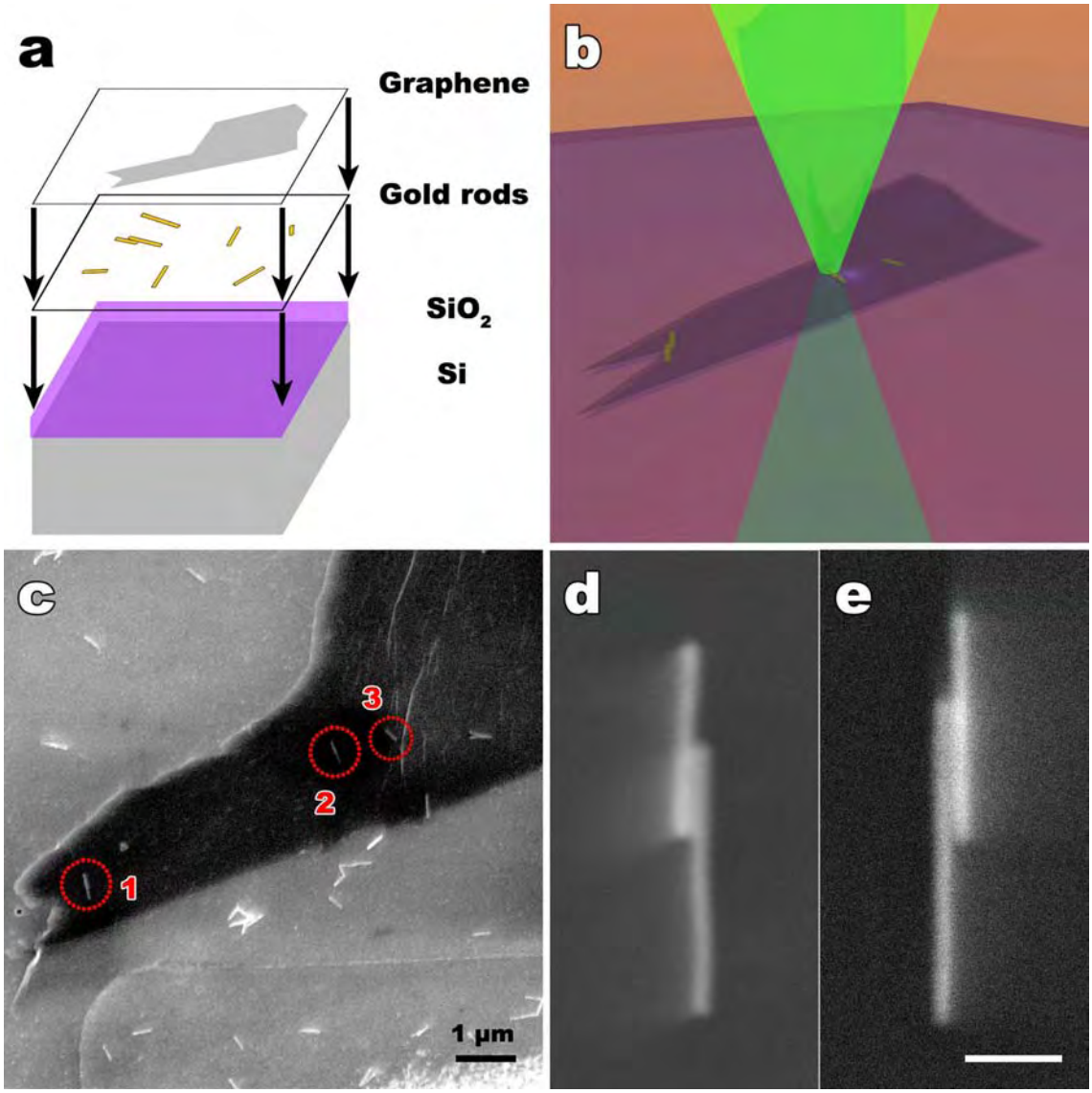


Figure 2: (a) Schematic of the sample's composition, with gold nanorods deposited over silicon dioxide on silicon sample covered by graphene. (b) Schematic of the experimental setup, the sample is excited by a Laser beam normal to the sample's surface and frequency shift is measured on the reflected beam. (c) SEM micrograph of the sample showing three spots were nanorods lie underneath the graphene. (d) Pair of nanorods of spot 2 and (e) Pair of nanorods of spot 1.

The amount of spectra is then analysed by a Fortran script. The script extracts the relative intensity, half high width and position of the three peaks D, G and 2D. The intensity is normalized by the second order of the silica signal to override laser intensity variations between experiments.

3 PARTICLE ENHANCED RAMAN SIGNAL

In this section some results of Raman mapping measurements on the sample presented before are analysed. We start by focusing on a Raman mapping of the upper part of the sample using a laser excitation at 638 nm of wavelength and horizontal polarization (Figure 3). We compare in this figure the SEM picture of the sample (Figure 3a), the map of the intensity extracted from the G band (Figure 3b), G' band (Figure 3c) and D band (Figure 3d).

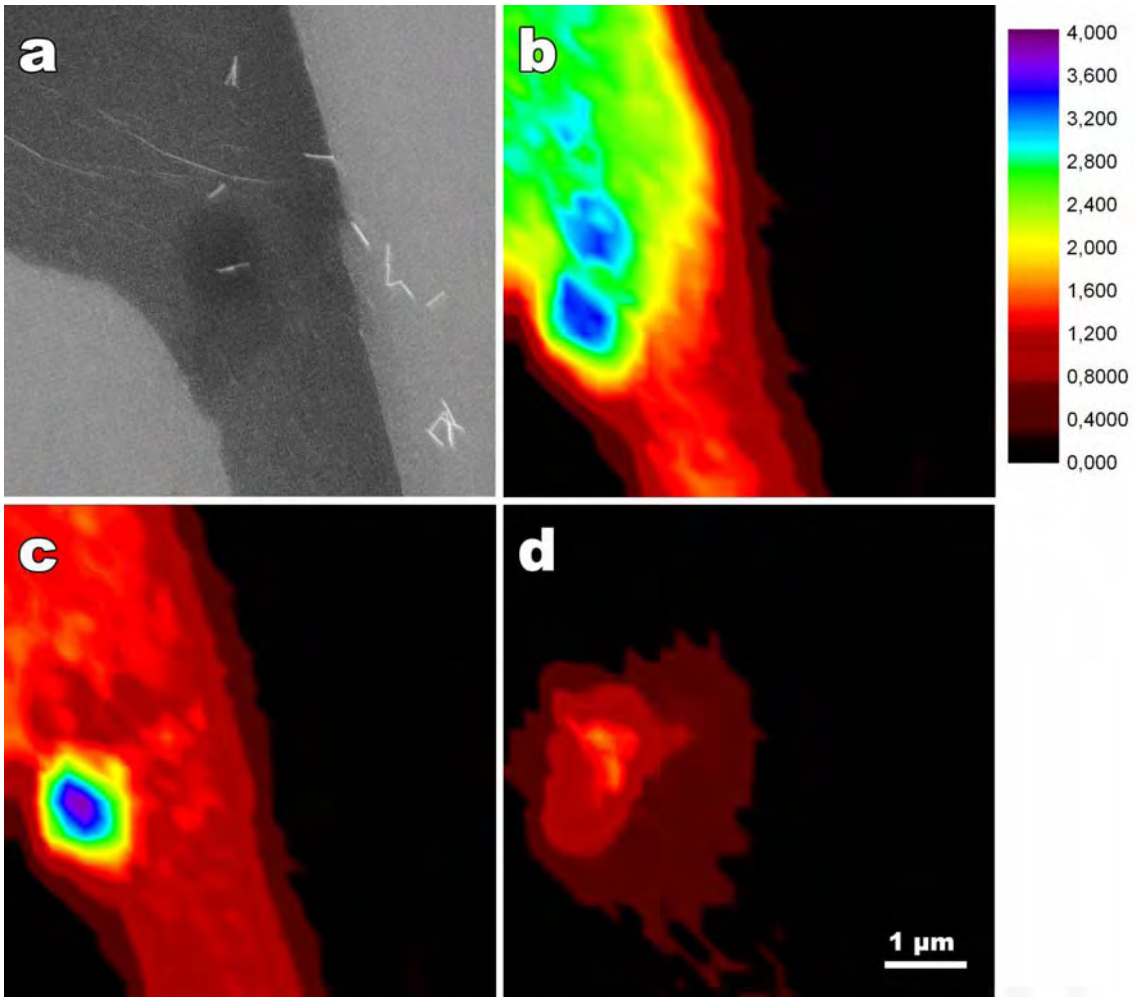


Figure 3: (a) SEM combined micrograph (classic + backscattered pictures) of the sample in the area of maps (b), (c) and (d). Raman mappings at 638 nm and horizontally polarized Laser excitation showing intensity in arbitrary units of (b) the G peak, (c) the G' peak and (d) the D band of graphene's Raman spectrum.

We observe different behaviours for G, G' and D peak mappings. Whereas for G peak two amplified lobes, that correspond respectively to the pair of rods (2) and to the isolated rod (3), the G' map shows only one single lobe. The lobe of G' mapping could correspond to the pair (2). As the stage positioning is not accurate and subject to drift (thermic drift and drift caused by the stage weight itself), it is hard to make a clear correspondence between Raman maps and the SEM

micrograph. In addition, the D band is also enhanced at the rod's pair position. The gold nanoparticles are then responsible of the enhancement of the Raman signal of graphene.

To test the frequency and polarisation dependency, we repeat this map at different lightings: 532 nm horizontal polarisation, 532 nm vertical polarisation, 638 nm horizontal polarisation and 638 nm vertical polarisation. By now we focus on the G' peak measurement of those 4 mappings (Figure 4).

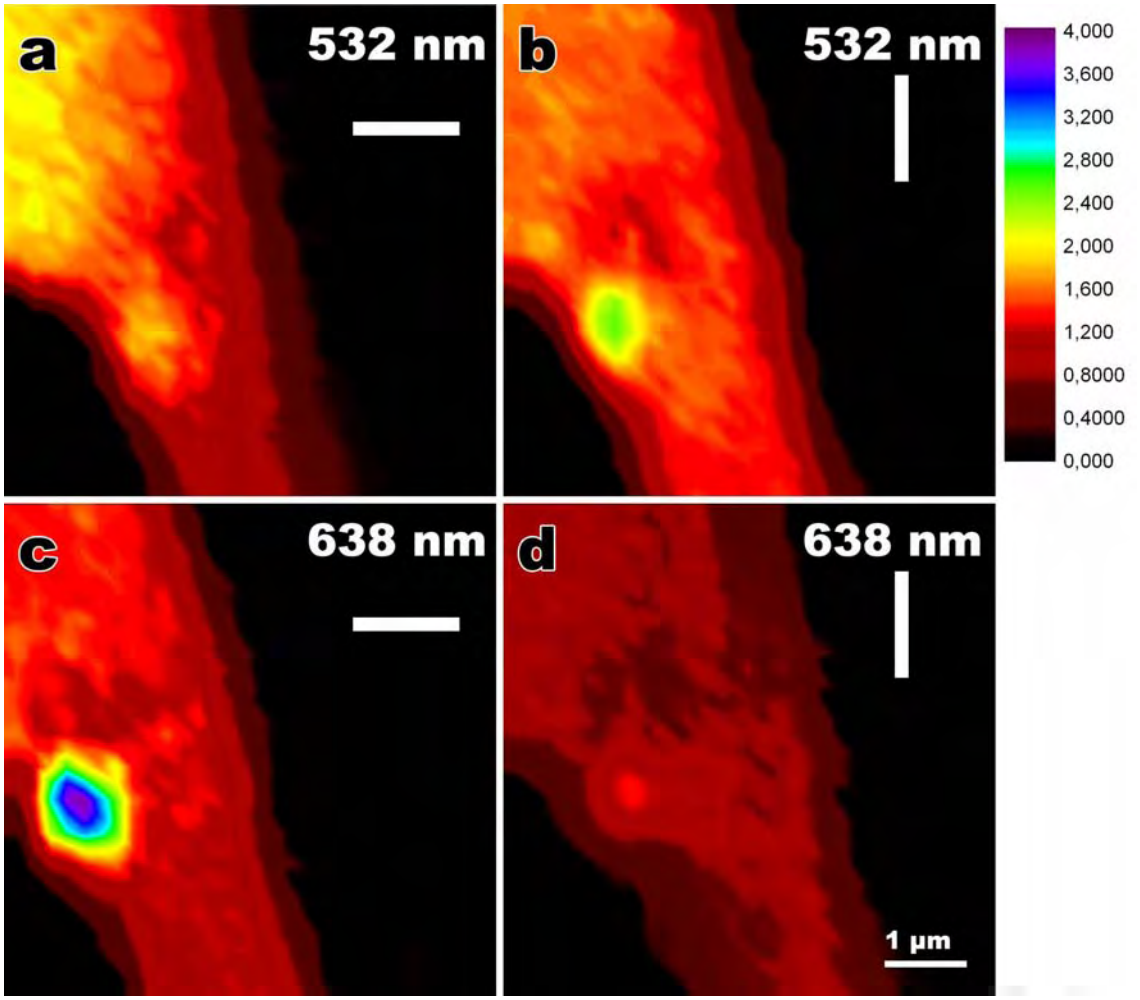


Figure 4: G' mappings of the sample at (a) 532 nm vertical polarisation, (b) 532 nm horizontal polarisation, (c) 638 nm horizontal polarisation and (d) 638 nm vertical polarisation.

In those measurements, the active spot looks to be the rods pair (2). The single rod (3) does not appear to induce any effect. The modification induced by the presence of the rods pair is different depending on the beam conditions. At 532 nm very little enhancement is observed (~40%). Whereas on the vertically polarized experiment the signal of the G' peak is enhanced to 71%. This enhancement is higher when we switch to the 638 nm beam with horizontal polarisation, where it reaches the value of 233 %. This lobe is switched back off again when the 638 nm beam is turned to vertical polarisation. Those results show that whether the rods pair or whether one of the rods alone is reacting to the

532 nm vertical polarized and to the 638 nm horizontal polarized beams. The energy of this resonance is transmitted to the graphene layer. Therefore the 532 nm should be close to the plasmonic resonance of the transverse mode of the pair, and the 638 nm should be close to the longitudinal resonance. As the enhancement is measured on a graphene peak (excluding background) the energy must've been transferred from the particle to the graphene layer. We now analyse the G band map of the same experiments.

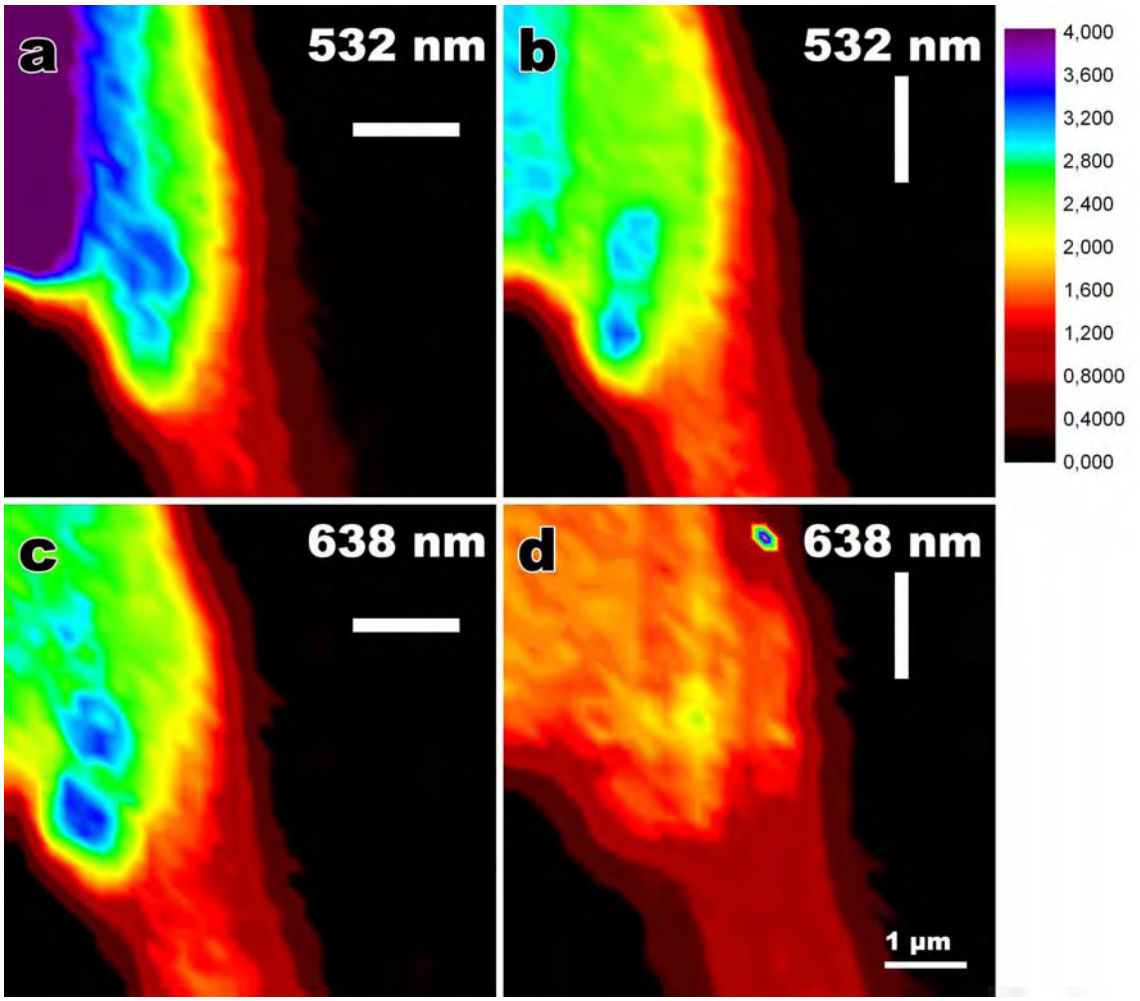


Figure 5: G mappings of the sample at (a) 532 nm vertical polarisation, (b) 532 nm horizontal polarisation, (c) 638 nm horizontal polarisation and (d) 638 nm vertical polarisation.

The results of the G band Raman mapping is very similar to the G', enhancement lobes are only observed if exciting beam is whether 532 nm vertical or 638 nm horizontal. The mean difference is that is that two lobes can be observed instead of one. The lobes correspond to positions (2) and (3). The rod in position (3) is similar to one of the rods of the pair. One explanation is that one single rod was responsible for the enhancement noticed in G' band (Figure 4), whereas the other one, comparable to the rod (3) is more likely effective enhancing the G peak. The size of the plasmonic particle determines the graphene band that is enhanced.

There is also a difference between the two lobes intensity. This intensity difference can be explained by the angle shift between particles in position (2) and (3) reducing the projection of the beam's polarisation.

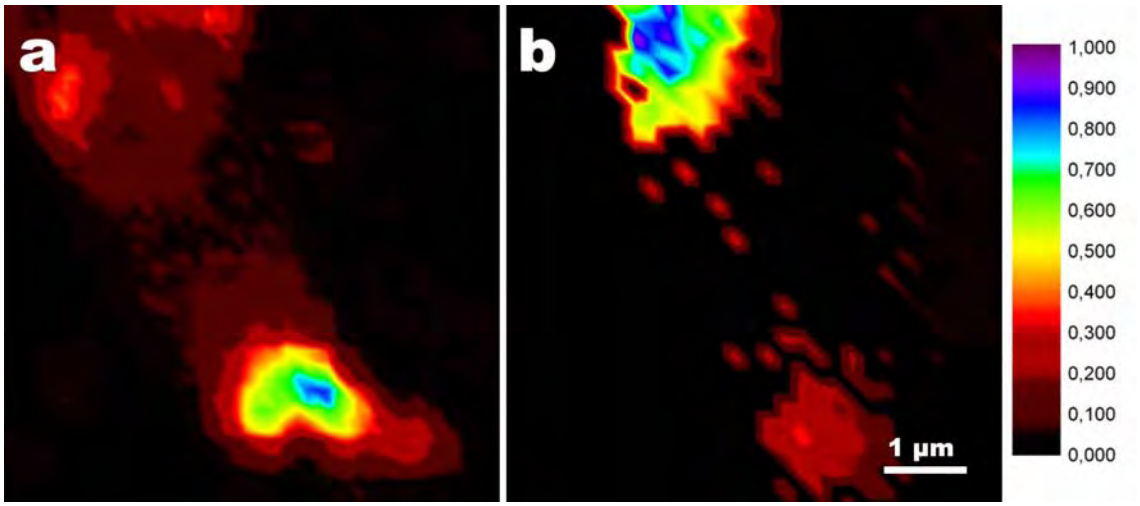


Figure 6: Raman mapping using 532 nm horizontal polarised laser beam of the D band of graphene before (a) and after (b) e-beam exposition.

This coupling can then be very useful for measuring graphene properties by Raman analysis. One of the most interesting measurements is the defects measurement on a graphene sheet. By measuring the D band intensity one can deduce the graphene quality, but this signal do not appear for low defected graphene, such as edges or folds.

We analyse the D band intensity of the entire sample (Figure 6). As it appears, two areas of the sample have a measurable D peak (Figure 6a). They correspond to the positions of the gold nanoparticles. The most relevant is at the bottom of the graphene sheet (position 1). In this area many edges and ripped graphene is present, which explains the high intensity D peak.

After this map the sample is entirely irradiated for SEM analysis. The same map is measured again (Figure 6b). But this time the roles have been switched. The upper area shows higher defects signal than the bottom. The e-beam irradiation has certainly caused damages at this area increasing the D signal. On the other hand the signal in position (1) has decreased. We understand this as the fact that D peak appears on defected graphene, but as too many defects are present, the sample does not reacts as graphene but more as amorphous carbon. This would cause the D band to grow up with increasing defects density at the start, but as graphene is too damaged, the D band starts decreasing[8].

4 GREEN DYADIC SIMULATION

In order to understand better the plasmonic coupling between graphene and the plasmonic nanoparticles we proceed to simulation of a similar system. The simulations are based in in Green Dyadic functions[9]. The simulated system correspond to a pair of gold nanorods of 280x18 nm and 198x19 nm disposed one compared to the other as the sample in Figure 2d. A graphene layer is placed on top of the nanoparticles. The laser excitation scans the area and signal from graphene only is calculated. The electric field irradiated by the nanoparticles induces modifications on the graphene signal. The simulation is performed for 532 mn (Figure 7a, b and c) and 638 nm (Figure 7d, e and f) of wavelength excitation. For each wavelength we show the calculation for three polarisations: 0º (Figure 7a and d), 45º (Figure 7b and e), and 90º (Figure 7c and f).

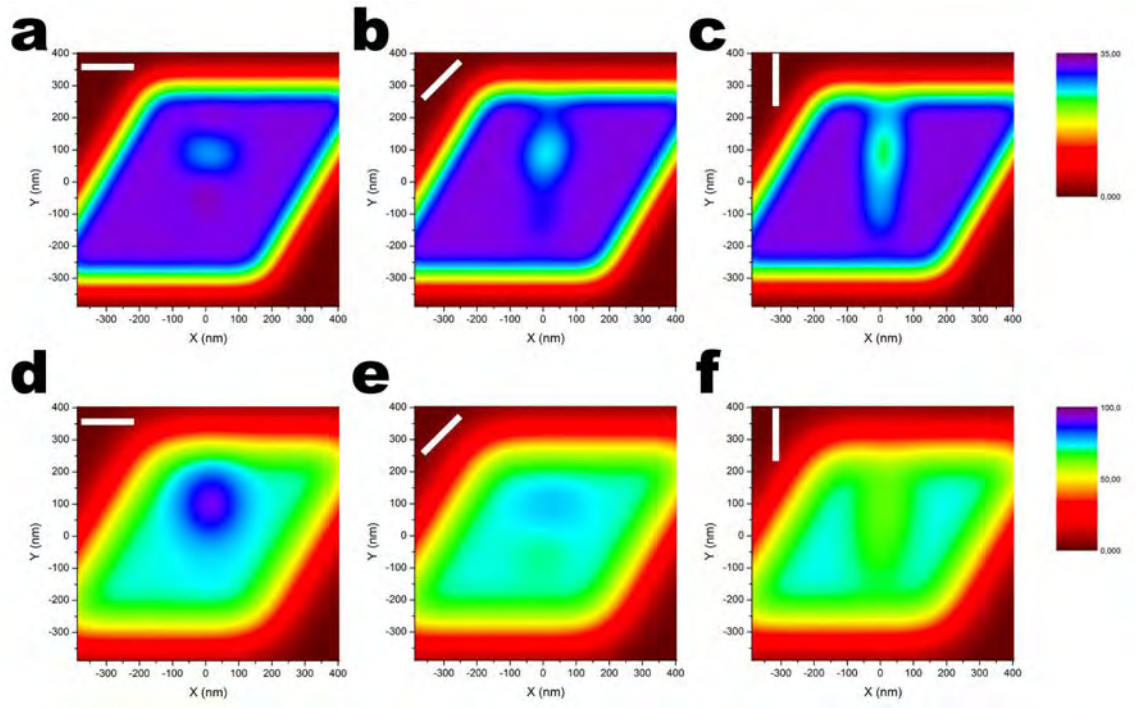


Figure 7: Green Dyadic simulations of the hybrid graphene and gold nanorods systems. Mappings for 532 nm with polarization at (a) 0º, (b) 45º, (c) 90º and 638 nm (d) 0º, (e) 45º, (f) 90º.

The simulations at 532 nm show very little on the transverse polarization of the nanorods (Figure 7a). For 45º polarized light (Figure 7b) only occultation is visible on the mappings as well as the longitudinal polarization (Figure 7c).

On the 638 nm wavelength simulation the situation is different. In the transverse polarization (Figure 7e) a relatively important exaltation (33%) of the graphene signal is observable at the nanoparticles location. This exaltation is lower on the 45º polarization simulation (Figure 7e) (10%). The mapping of the transverse polarisation only presents a little occultation.

5 Discussion

The simulations present some similarities with the experimental results. We will compare those results wit the mapping of G peak in Figure 4. It is important to point that in the experiment, the rods are not perfectly horizontal but present an ~18º angle. The 532 nm measurement shown no exaltation of the signal at longitudinal polarisation, and so does the simulation with some occultation of the electric field. On the other hand the transverse polarisation show in both cases an enhancement of the signal.

At 638 nm on longitudinal mode an exaltation lobe is noticed in the experiment whereas the simulation show occultation. The mapping at 45º does present an enhancement; the experimental situation should be in between those two situations. Finally the transverse polarisation at 638 nm presents experimentally a weak increasing of the Raman signal. This exaltation is reproduced in the simulation, but the ratios are not similar though. The experiment shown a higher enhancement (250%) on the longitudinal exaltation, which is not reproduced by the numerical calculations. The simulations of the 638 nm experiment result in mappings that seem shifted in 90º of polarisation compared to the experiments.

The first explanation is an experimental mistake during the measurements. But the polarization inversion in only one wavelength and not the other one looks improbable. The second one is that the simulation model of the sample is not exactly the same as the experimental distribution. The distance between two particles is not precisely known and thus the interaction could be different if not properly programmed. The same problem occurs with the graphene-nanoparticles distance and interaction. The simulation takes into account a hard flat surface one nanometre over the rods, whereas we know that graphene imitates the shape of its support as a cloth would do. Furthermore the simulations show the electric field induced by the graphene, but the experiments measure a precise Raman frequency shift evolution depending on the peak. The effect of the field modifications on the different kinds of phonons that cause the Raman signal is not well known, and thus not taken into account in the simulations. As the experimental data has shown, the exactly same excitation wavelength and polarisation, has spatially different effects on the G' signal compared to the G. Such phenomenon cannot be predicted by this simulation method as it is.

6 Conclusion

This Chapter shows a coupling between graphene and plasmonic nanoparticles. The effect on the graphene's Raman signal has been proved dependent of the field of the gold particles as it depends, in intensity and spatially, on the wavelength and the polarization of Laser exciting beam. The mechanism and results of the coupling has revealed a high complexity. The effect on the graphene signal does not only depends on the Lased beam properties, it also changes depending on which graphene signal is being observed. This is showing that this complex interaction between nanoparticles plasmons and graphene's electrons and phonons is still not understood. More research, and especially more experimental data is required in order to better describe the Raman signal dependencies at different frequency shifts.

7 References

[1] P. Wang, W. Zhang, O. Liang, M. Pantoja, J. Katzer, T. Schroeder, Y.-H. Xie, Acs Nano 2012, 6, 6244.
[2] P. Wang, D. Zhang, L. Zhang, Y. Fang, Chemical Physics Letters 2013, 556, 146.
[3] A. N. Sidorov, G. W. Slawinski, A. H. Jayatissa, F. P. Zamborini, G. U. Sumanasekera, Carbon 2012, 50, 699.
[4] F. Schedin, E. Lidorikis, A. Lombardo, V. G. Kravets, A. K. Geim, A. N. Grigorenko, K. S. Novoselov, A. C. Ferrari, Acs Nano 2010, 4, 5617.
[5] J. Lee, S. Shim, B. Kim, H. S. Shin, Chemistry-a European Journal 2011, 17, 2381.
[6] L. D'Urso, G. Forte, P. Russo, C. Caccamo, G. Compagnini, O. Puglisi, Carbon 2011, 49, 3149.
[7] C.-E. Cheng, C.-Y. Lin, H.-Y. Chang, C.-H. Huang, H.-Y. Lin, C.-H. Chen, C.-C. Hsu, C.-S. Chang, F. S.-S. Chien, Optics Express 2013, 21, 6547.
[8] D. Teweldebrhan, A. A. Balandin, Applied Physics Letters 2009, 94, 3.
[9] O. J. F. Martin, C. Girard, A. Dereux, Physical Review Letters 1995, 74, 526.

Annexe 2

Raman spectra of different graphene sources and transfer techniques

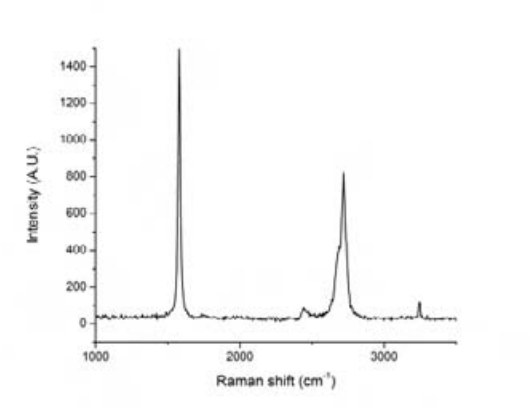


Figure 1: HOPG Raman spectrum

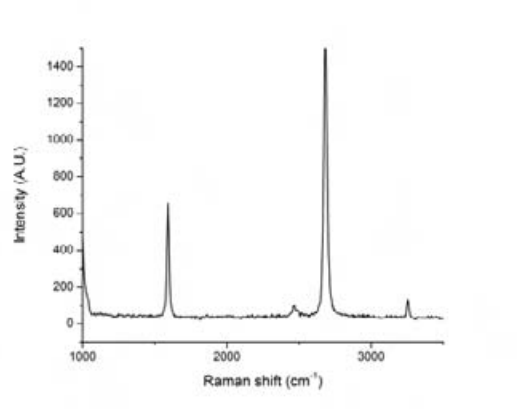


Figure 2: Raman spectrum of exfoliated graphene

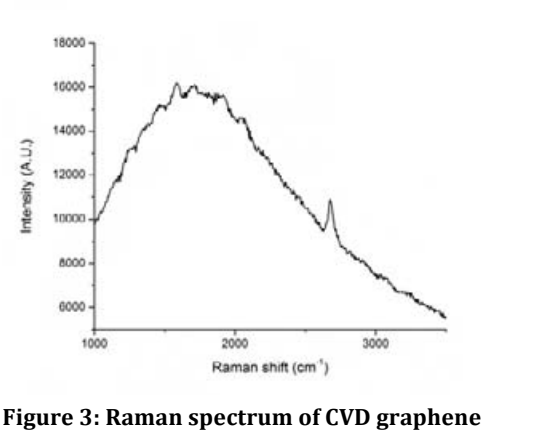


Figure 3: Raman spectrum of CVD graphene grown on copper

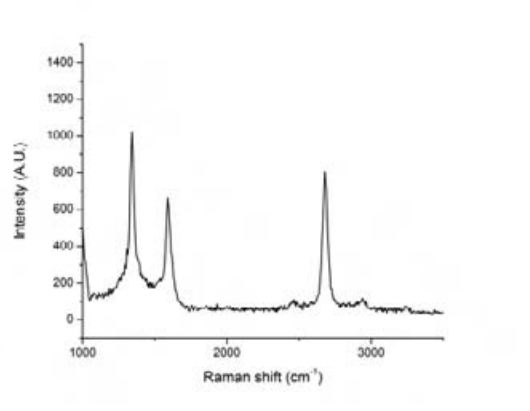


Figure 4: Raman spectrum of CVD graphene grown on copper transferred using Acetate Butyrate

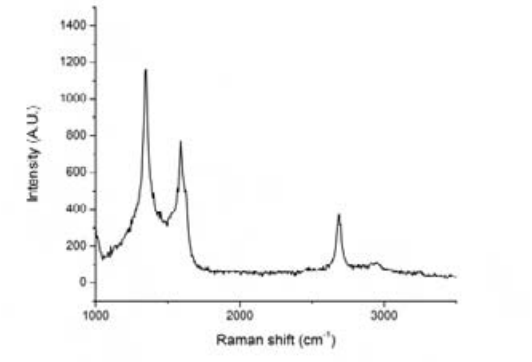


Figure 5: Raman spectrum of CVD graphene grown on copper transferred using PMMA

Résumé

Notre technologie actuelle est basée sur les processeurs et les calculateurs qui, eux mêmes, fonctionnent à partir de composants appelés transistors. Ces composants sont l'équivalent d'interrupteurs avec deux entrées, une sortie et une table de vérité extrêmement simple. C'est en utilisant ces composants dans une configuration et à travers une programmation ingénieuses que nos ordinateurs arrivent à en extraire le potentiel nécessaire pour réaliser des opérations complexes. Le basculement de cette électronique classique vers des composants électroniques moléculaires est prometteur et permettrait d'accéder à des composants plus élaborés correspondant chacun à une fonction particulière et donnerait aussi accès à des propriétés permettant d'utiliser des algorithmes pour réaliser des calculs impossibles à réaliser avec un ordinateur actuel, comme c'est le cas pour la factorisation de grands nombres. Dans ce manuscrit, nous proposons l'utilisation d'un matériau appelé graphène et d'une technique bien particulière de découpe induite par faisceau électronique afin de le façonner et de potentiellement induire des comportements électroniques non triviaux. Le graphène est un matériau cristallin carboné extrait du graphite avec des propriétés électroniques remarquables. Ce matériau présente des caractéristiques qui permettraient la fabrication de dispositifs à plus haute mobilité que ceux actuels. La thèse est déclinée en cinq chapitres commençant par les objectifs et le contexte de la thèse, suivis par les méthodes expérimentales et les équipements. La découpe électronique et sa caractérisation par microscopie à résolution atomique font l'objet du troisième chapitre, qui sera suivi par la caractérisation du transport électronique de dispositifs de graphène fabriqués par découpe induite par faisceau électronique. Enfin, un dernier chapitre décrit l'analyse du graphène et de dispositifs de graphène par microscopie à effet tunnel 4-pointes sous ultra-haut vide.

Chapitre 1 : Objectifs et contexte

Le graphène est un matériau d'un seul atome d'épaisseur formé par un arrangement hexagonal en nid d'abeille d'atomes de carbone (Figure 1a). La première zone de Brillouin est représentée sur la Figure 1b.

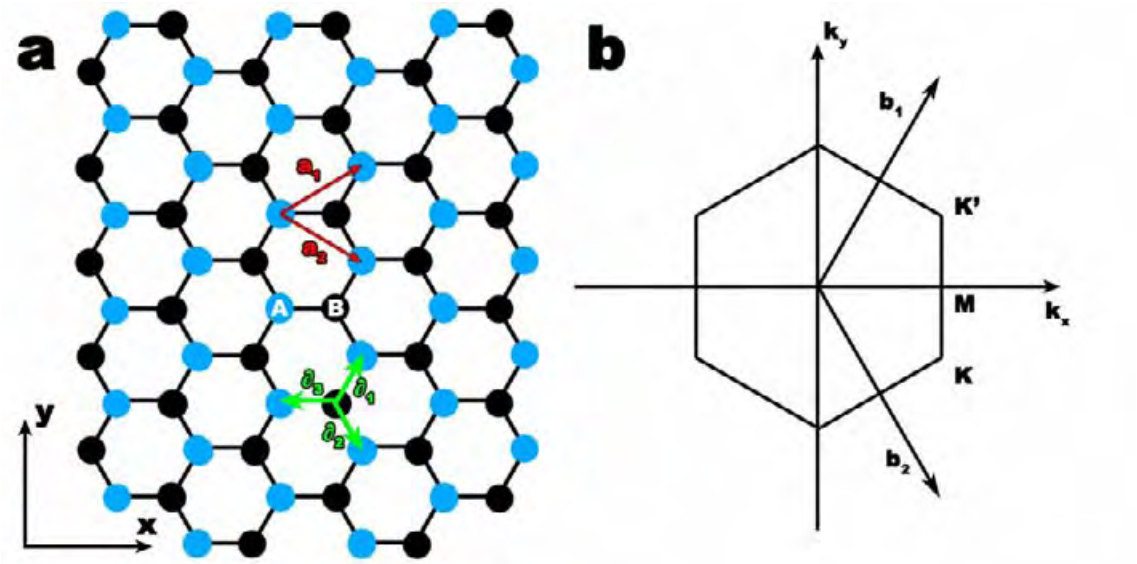


Figure 1 : (a) Représentation schématique de la structure atomique du graphène. (b) Première zone de Brillouin.

La structure électronique du graphène (Figure 2) comporte des points de Dirac aux positions K et K' de la première zone de Brillouin. Sur ces points, la dispersion des bandes est linéaire, c'est cette propriété qui donne lieu aux caractéristiques de transport électronique si particulières de ce matériau. Le graphène est donc un matériau avec un gaz bidimensionnel d'électrons libres en provenance des orbitales moléculaires π et π* non impliquées dans les liaisons atomiques.

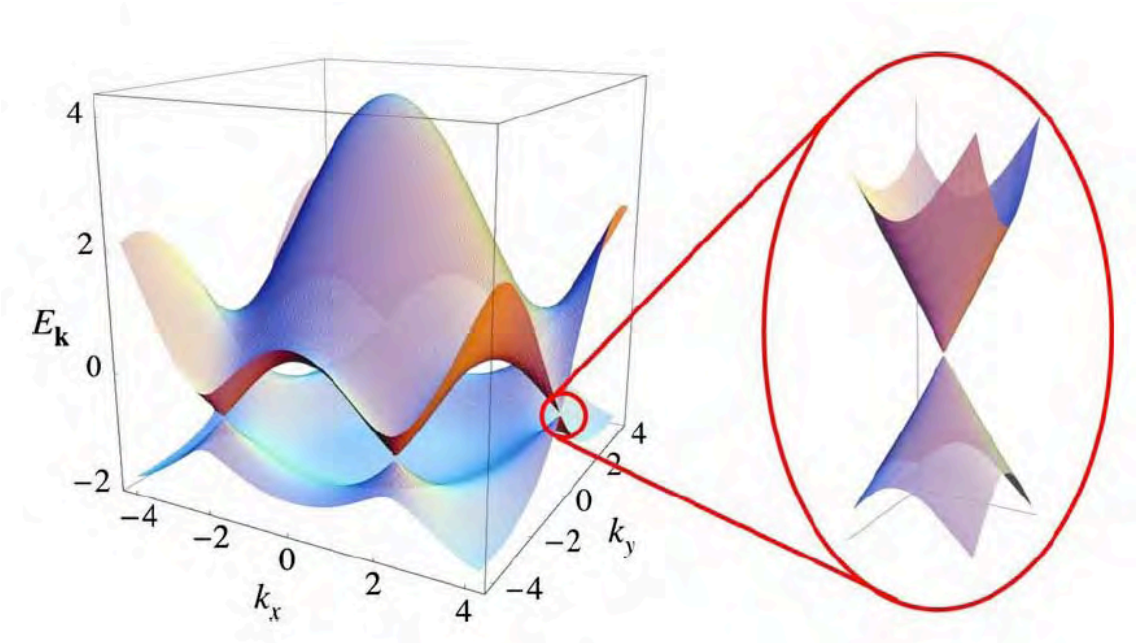


Figure 2 : Schéma de bandes électroniques du graphène représentant la bande de valence (inférieure) et la bande de conduction (supérieure) avec zoom sur un cône de Dirac

Les propriétés électroniques peuvent être modifiées. Un des moyens développé ici est celui par modification structurale. Un exemple est le confinement du gaz d'électrons à une dimension supplémentaire : un nanoruban de graphène. Le confinement à une dimension du gaz d'électrons dans un ruban de taille nanométrique aurait pour effet la création d'une bande d'énergie dans laquelle les interférences de l'électron sur lui-même lui empêcheraient de traverser le ruban, créant ainsi une bande interdite de faible conductance similaire à celle d'un semi-conducteur.

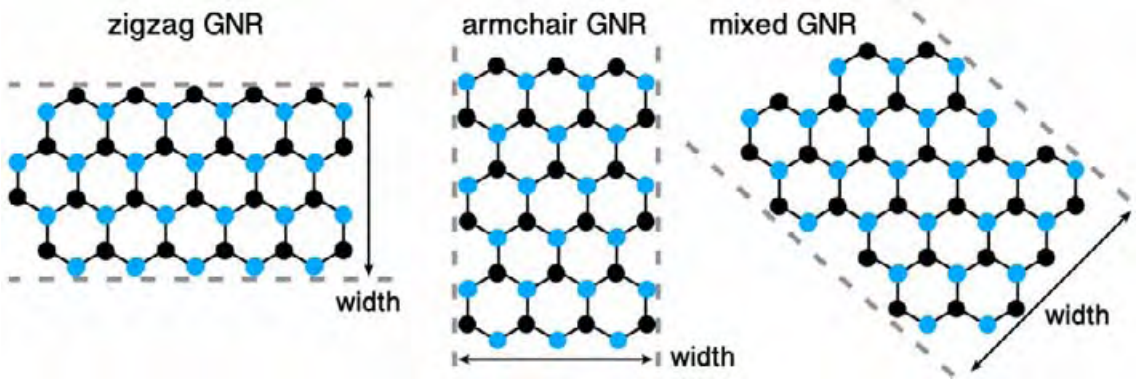


Figure 3 : Représentation schématique des trois familles de rubans de graphène : zigzag, armchair et mixte.

Plusieurs critères permettent de caractériser les rubans de graphène. La première caractéristique est sa largeur ainsi que sa longueur. Un second aspect concerne l'arrangement atomique des bords du rubans, pouvant être zigzag (direction y sur la Figure 1a), armchair (direction x sur la Figure 1a) ou bien mixtes (Figure 3). Finalement, la géométrie de la connexion entre le ruban et le reste du graphène peut aussi influer fortement les caractéristiques de transport à travers celui-ci (Figure 4).

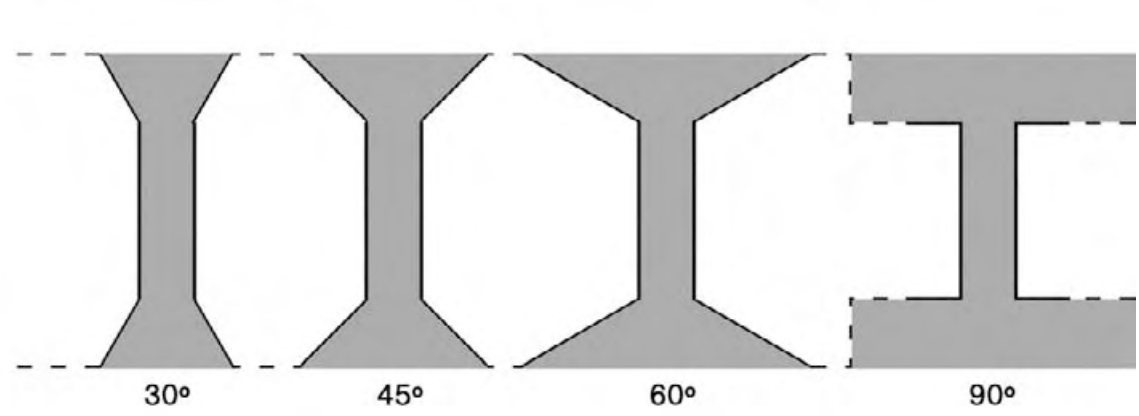


Figure 4 : Exemples de possibilités de connections sur un ruban de graphène

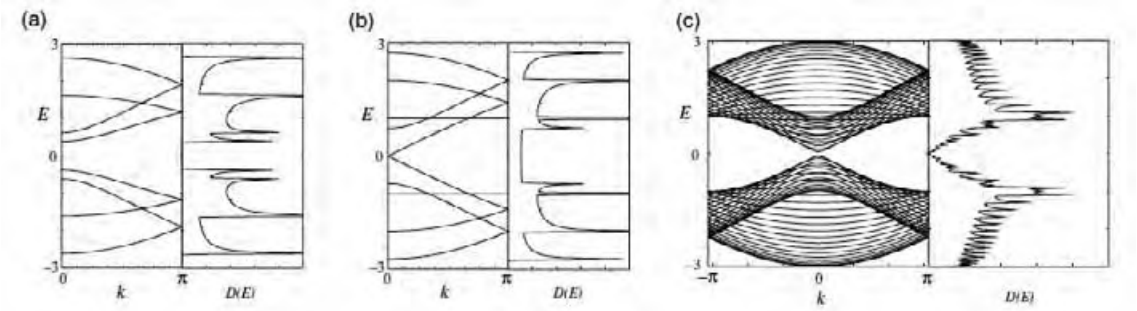


Figure 5 : Calculs de bandes électroniques pour des rubans de graphène armchair de (a) N=4 (b) N=5 et (c) N=30 rangées atomiques.

Autant la largeur que l'orientation cristalline du ruban influencent de façon directe les états électroniques du dispositif final. Un ruban type armchair pourra ainsi à certaines valeurs de la largeur avoir un gap entre les bandes de valence et de conduction (Figure 5). Par ailleurs, un ruban de type zigzag implique la présence d'états de bord en permanence au niveau de Fermi, et sont toujours métalliques quelle que soit leur largeur (Figure 6).

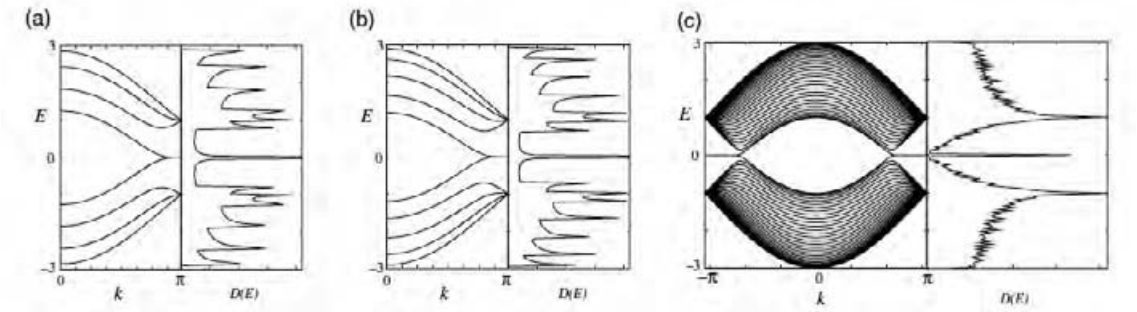


Figure 6 : Calculs de bandes électroniques pour des rubans de graphène zigzag de (a) N=4 (b) N=5 et (c) N=30 rangées atomiques.

Il existe plusieurs méthodes de fabrication de nanorubans de graphène dans la littérature. Quelques exemples sont la lithographie électronique suivie par un plasma ionique (EBL+RIE), la gravure par faisceau ionique focalisé, le knock-on direct par faisceau électronique à haute énergie (>100 kV), ou encore la gravure par diffusion de particules catalytiques et la synthèse chimique. Le but de ce manuscrit est de mettre au point une technique de gravure qui combine les avantages de la gravure par faisceau piloté afin de pouvoir graver des formes arbitraires, et la gravure par réaction chimique qui est potentiellement sélective par rapport aux directions cristallines et qui peut apporter une précision proche du niveau atomique. Dans le chapitre 3 est décrite notre technique de découpe induite par faisceau électronique à basse énergie (20 kV) assistée par de l'oxygène gazeux (oxygen assisted Electron Beam Induced Etching).

Chapitre 2 : Fabrication d'échantillons et méthodes expérimentales

Dans ce manuscrit, nous utilisons du graphène provenant de deux origines différentes. La première correspond au graphène fabriqué par exfoliation mécanique de flocons de graphite (Figure 7a). Le flocon est placé sur un morceau de bande adhésive (Figure 7b) puis clivé successivement (Figure 7c) jusqu'à recouvrir toute la surface adhésive (Figure 7d) afin de réduire l'épaisseur de la couche de graphite au maximum. Cette bande est ensuite appliquée sur un substrat de silice (290 nm) sur silicium afin de transférer une partie du graphite (Figure 7e). Cette méthode résulte en dépôts de graphène de haute qualité avec des tailles de feuillet aux alentours de 20x20 μm^2.

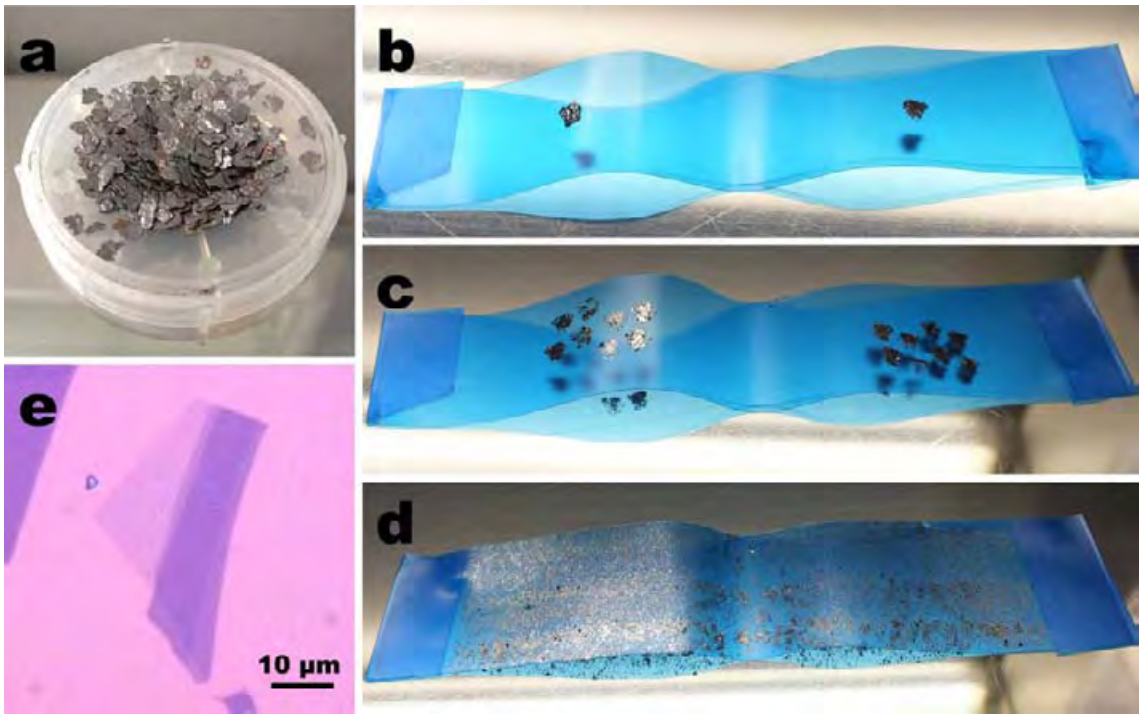


Figure 7 : (a) Flocons de graphite utilisé pour l'exfoliation mécanique. (b) Première exfoliation du flocon se poursuivant (c) jusqu'à l'étalement complet du graphite (d). (e) Dépôt de graphène sur un substrat de silice sur silicium.

La deuxième est l'utilisation de graphène CVD. Le graphène CVD est produit dans un four où des précurseurs de carbone sont cassés par réaction avec de l'hydrogène, déposés sur un métal catalyseur et réorganisés pour constituer une couche cristalline. Le métal catalyseur doit donc être gravé par réaction chimique afin de pouvoir déposer le feuillet de graphène sur le substrat de notre choix. Cette méthode produit des échantillons de graphène pouvant aller jusqu'à la taille d'un wafer de 4 pouces (en fonction de la taille du four), mais d'une taille de domaine cristallin et d'une propreté bien inférieure à celles de l'exfoliation de graphite. Il

est possible de nettoyer ces échantillons de la contamination par carbone amorphe en pratiquant un recuit sous atmosphère réductrice.

Il y a trois principaux appareils de fabrication et de mesure utilisés dans cette thèse. Le premier est un FIB/SEM FEI Helios Nanolab 600i dualbeam. Ce microscope, équipé d'une buse d'entrée d'oxygène, est utilisé pour la découpe électronique du graphène. L'analyse structurale à résolution atomique est mise à l'œuvre grâce à un microscope électronique en transmission FEI Titan cube équipé d'une caméra Gatan 4kx4k utilisé à une tension d'accélération de 80 kV. Le troisième est un cryostat Oxford à hélium liquide (^{4}He) (Figure 8a et c). Ce cryostat est équipé d'un insert à température variable (Figure 8b) capable de fixer la température de l'échantillon entre 1,4 K et 280 K. De même, un cryo-aimant permet d'établir un champ magnétique au niveau de l'échantillon jusqu'à 16 T (Figure 8d). Cet appareil est utilisé pour la caractérisation du transport et du magnéto-transport des dispositifs.

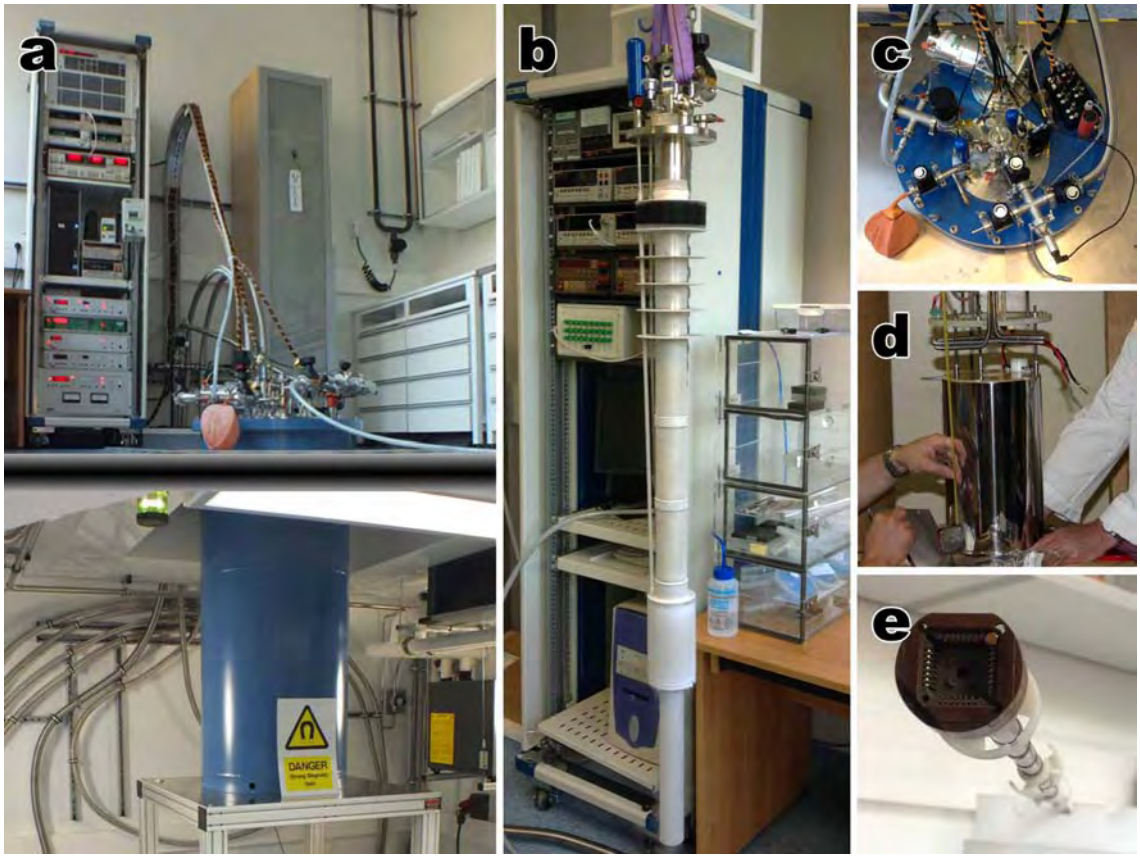


Figure 8 : (a) Cryostat Oxford à hélium liquide. (b) Insert à température variable. (c) Vue du haut du cryostat. (d) Cryo-aimant 16T. (e) Canne et socket porte-échantillon.

Chapitre 3 : Fabrication de nanorubans de graphène par découpe électronique assistée à l'oxygène

Le cœur de ce chapitre est consacré à la description, à la réalisation et à l'analyse des résultats obtenus par gravure induite par faisceau électronique (EBIE) assistée par oxygène sur échantillons de graphène CVD suspendu sur grilles TEM.

La gravure du graphène par EBIE à l'oxygène consiste en l'injection d'oxygène gazeux dans l'environnement proche de l'échantillon dans une chambre sous vide. La réaction entre l'oxygène et le graphène nécessite un apport d'énergie afin d'être activée. Cette énergie est apportée de façon locale par la sonde électronique du microscope. Dans cette étude, nous utilisons un faisceau électronique de 1,4 A accéléré jusqu'à une énergie de 20 keV. Sur la surface irradiée par le faisceau, les atomes de carbone du cristal vont réagir avec l'oxygène pour former des produits volatiles et seront donc extraits de la maille pour être évacués par le pompage du système. De la même façon, le faisceau électronique peut en parallèle casser des molécules présentes dans la chambre, ces contaminants peuvent provenir de l'échantillon, de la réaction de découpe ou de la chambre elle-même. En cassant, ces molécules se déposent sur le graphène provoquant une contamination par carbone amorphe. À vide limité, la seule option est de régler les paramètres au mieux pour la réaction, *i.e*. le courant de sonde, la tension d'accélération, le flux de gaz ainsi que les paramètres du motif : le recouvrement, le temps d'exposition et le nombre de scans. La géométrie du système est montrée sur le schéma de la Figure 9a.

Le microscope exécute les motifs digitalement et non analogiquement. Cela implique que des lignes ne peuvent pas être gravées en définissant un parcours et une vitesse, mais plutôt en définissant un ensemble de points d'irradiation qui éventuellement se recouvrent avec un temps d'exposition pour chacun. Afin de produire les bords les plus lisses possibles et éviter des formes en arc dûes à la forme circulaire de la sonde, le recouvrement utilisé ici sera de 95% de la taille de la sonde.

Le résultat d'un test de découpe sur un échantillon recouvert de carbone amorphe est un dépôt provoqué par le faisceau (Figure 9b). En revanche, pour un échantillon propre ayant subi un recuit, il en résulte une découpe nette de 10 nm de largeur en moyenne (Figure 9c).

Même si la largeur de la découpe est indicative de la précision, le plus important lors de cette étape est d'être capable de graver deux lignes côte à côte sans détruire le matériau entre les deux. Ceci est le paramètre le plus important pour la fabrication de nanorubans de graphène sans amorphisation du cristal.

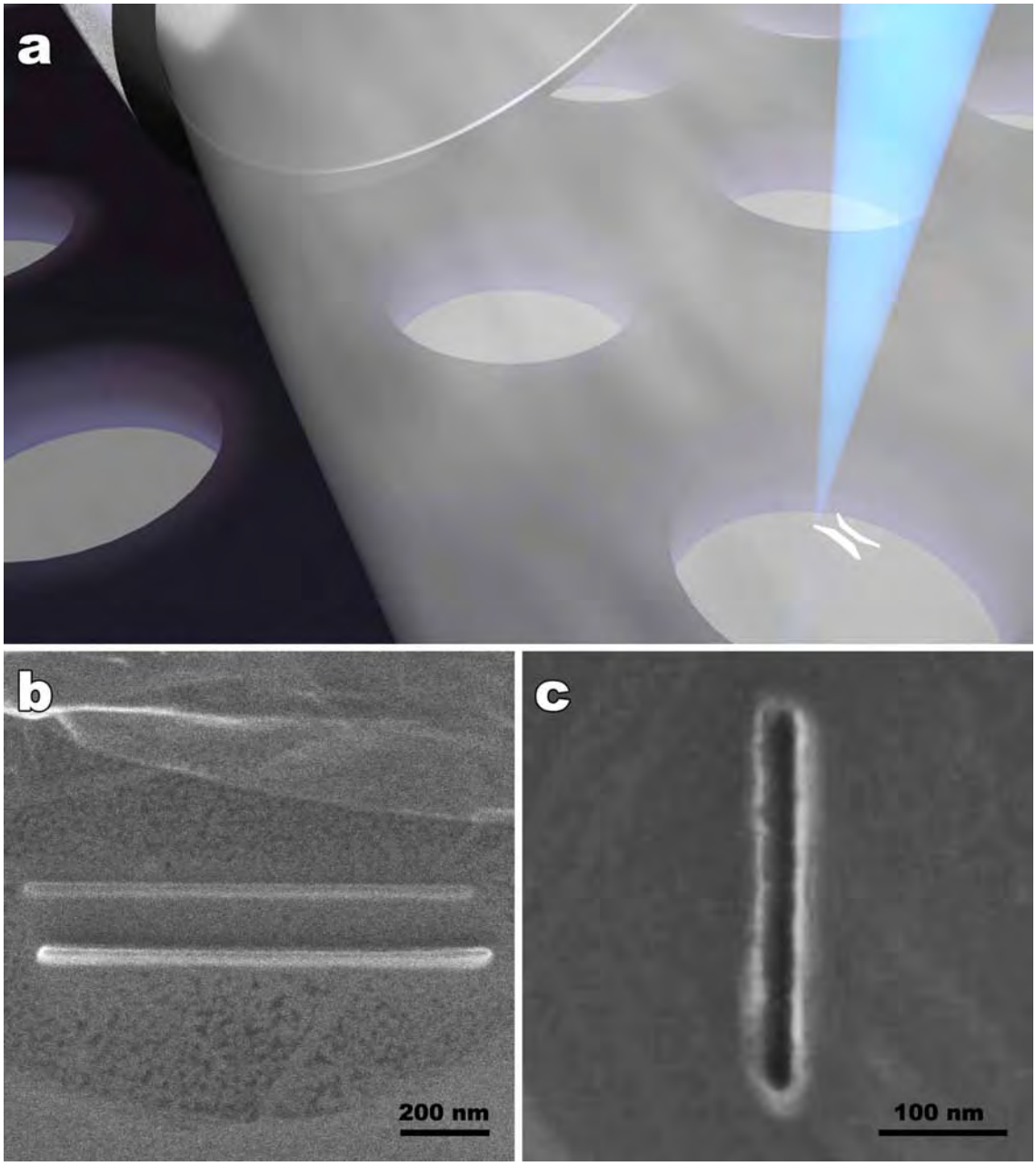


Figure 9 : (a) Schéma de la gravure induite par faisceau électronique assistée par oxygène du graphène dans le microscope. (b) Dépôt de carbone amorphe induit par le faisceau électronique. (c) Gravure d'une ligne sur le graphène.

Le motif choisit pour la découpe de rubans consiste en deux lignes parallèles (la plupart du temps de 300 nm de long) sur lesquelles sont rajoutés des entonnoirs d'entrée et sortie avec un angle de $\pi/6$ par rapport au ruban. La durée de gravure n'est pas affectée par le changement de largeur mais elle varie en lien direct avec la longueur. Des exemples de rubans de différentes largeurs et longueurs sont présentés sur la Figure 10.

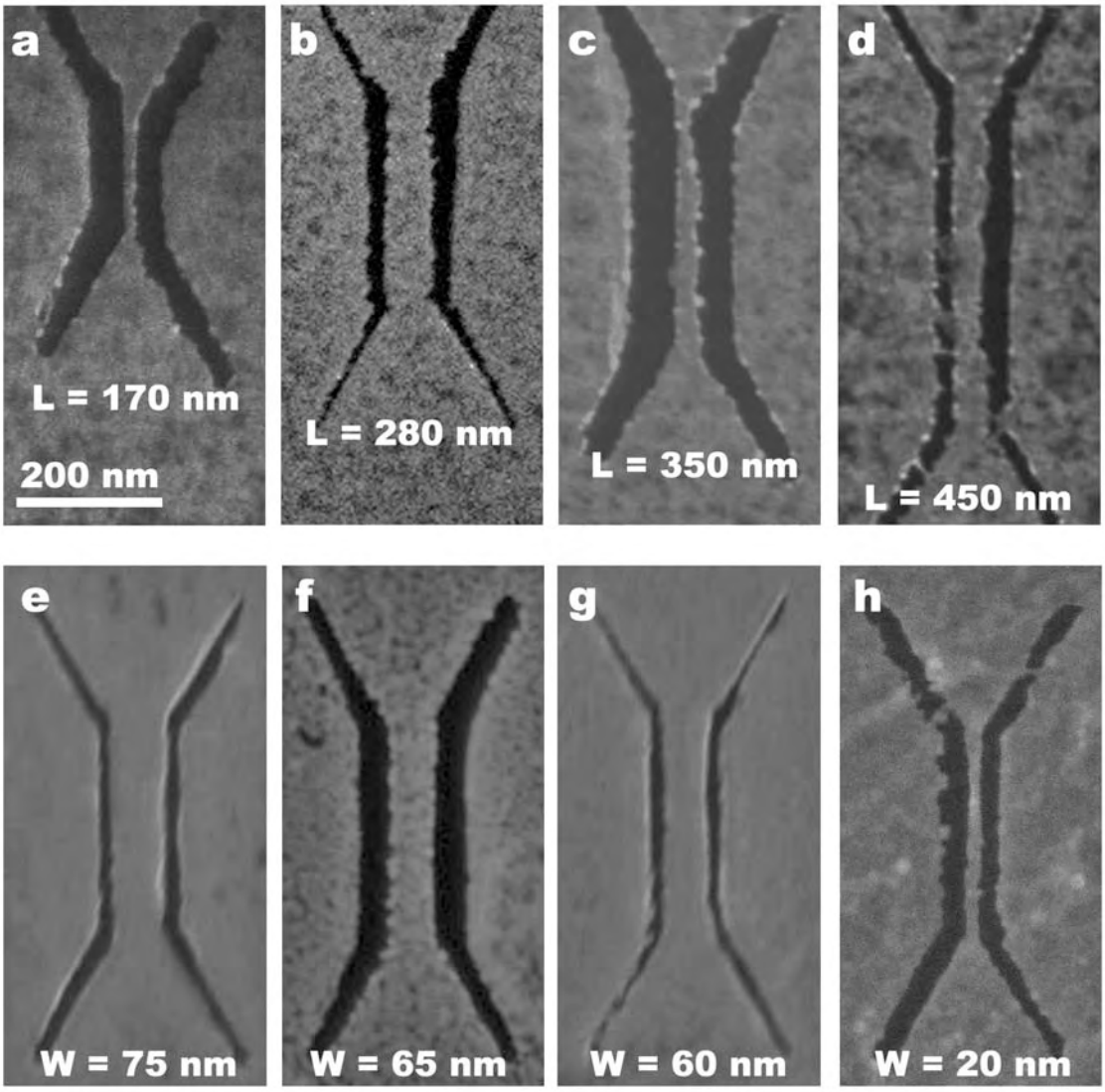


Figure 10 : Exemples de rubans gravés par EBIE à l'oxygène. La file du haut montre différentes longueurs entre 170 nm et 450 nm alors que la file du bas présente plusieurs largeurs entre 75 et 20 nm.

Un dépôt isolant est observable sur les zones de gravure, ce dépôt est produit pendant la gravure et est d'autant plus important que l'échantillon est sale ou que le vide est moins bon. Aussi loin que la résolution du SEM permet de l'analyser, les rubans sont droits, le motif est parfaitement reproduit et les bords semblent lisses même si le dépôt rend leur observation plus délicate.

Afin de rendre compte avec plus de précision de la qualité de ces objets, les rubans sur grille TEM sont analysés par microscopie électronique en transmission à résolution atomique. Afin d'éviter au maximum la modification de l'échantillon, la tension d'accélération est fixée en dessous de l'énergie minimale de knock-on pour des atomes de la maille du graphène (86 keV), soit 80 kV.

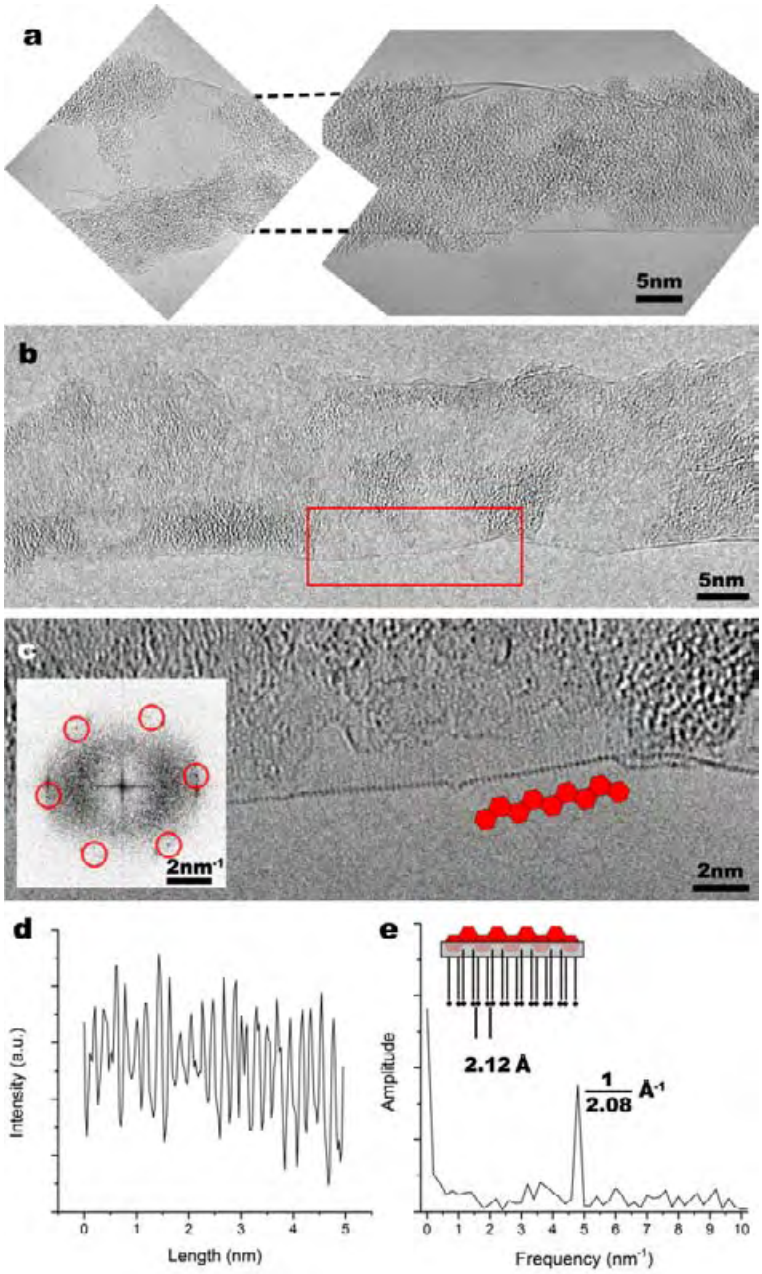


Figure 11 : Analyse par microscopie électronique en transmission corrigée en aberrations sphériques de rubans de graphène. (a) et (b) Deux exemples de rubans de graphène mesurant respectivement 14 et 16 nm de large par 320 nm de long. (c) Zoom sur la zone encadrée en rouge en (b) correspondant au bord du ruban, l'insert correspond à la transformée de Fourier de l'image. (d) Profil extrait du bord sur la figure (c) face au diagramme et (e) sa transformée de Fourier.

Les images enregistrées en TEM montrent encore une faible présence d'adsorbats sur les rubans (Figure 11a et b). Cela n'empêche pas la visualisation du graphène qui compose le vrai ruban. Celui-ci apparaît comme cristallin sans zone d'amorphisation ni interruption de bord à bord du ruban. De plus, les bords sont extrêmement lisses et suivent des directions cristallines. L'image TEM comparée à sa FFT ainsi que la périodicité du signal extrait du bord, montrent la présence de bords de type armchair. Par ailleurs, d'autres sections qui composent le bord, forment un angle par rapport à celui-ci, indiquant aussi la présence de bords de

type zig-zag. Étant donné la très faible probabilité que la direction de découpe soit parfaitement alignée à une direction cristalline, le bord est sans doute composé d'une combinaison linéaire de bords armchair et zigzag afin de s'aligner à la direction imposée par la gravure. Comparées à la littérature, ces qualités de ruban et de bords sont parmi les meilleures jamais publiées.

Chapitre 4 : Caractérisation par mesures de transport électronique des nanorubans de graphène

Même si les résultats par analyse SACTEM sont très encourageants, il est important de réaliser des mesures pour connaître les propriétés de transport électronique de ces objets. Pour cela, il est nécessaire de fabriquer des nanorubans de graphène électriquement isolés et contactés. Les substrats utilisés pour la microscopie ne sont pas adaptés à ce genre de mesures, nous procédons donc à une transposition de la technique de fabrication sur des substrats adaptés aux mesures de transport. Le type d'échantillon choisi est le graphène exfolié sur substrat de 290 nm de silice sur silicium. Afin de garder l'avantage principal de nos échantillons, des piscines de 5x1,5 µm par 6 µm de profondeur sont creusées sur les substrats. De cette façon, il est possible d'obtenir du graphène exfolié partiellement suspendu sur lequel nous pouvons graver nos motifs (Figure 12a). Une étape de lithographie électronique est mise en place, suivie par une évaporation de métal par faisceau électronique afin de déposer des électrodes métalliques pour contacter le graphène (Figure 12a et b). Par ailleurs, le motif initialement choisi est complété par deux découpes de part et d'autre du ruban, allant du ruban jusqu'au bord du feuillet, dont le but est d'isoler le ruban du reste du graphène pour éviter les court-circuits (Figure 12c). Un exemple de gravure de ce motif est présenté en Figure 12d.

Les simulations d'électrons rétrodiffusés sur de tels échantillons montrent que leurs effets sont faibles et proches de celui des gravures sur grilles TEM. L'utilisation de graphène supporté ou de piscines de profondeur inférieures à comme résultat une irradiation du graphène importante par les électrons secondaires et rétrodiffusés. Dans le cas du graphène faiblement suspendu, ces électrons créent une gravure EBIE parasite sur toute la surface suspendue. Par ailleurs, la gravure supportée résulte en une largeur de gravure fortement augmentée, endommageant le graphène jusqu'à un rayon de 400 à 500 nm autour de l'objectif. Ce cas de figure est utilisé pour l'isolation de l'objet lorsque les limites du graphène sont au-delà de la piscine. Nous considérons que cette rugosité n'a pas de grand effet sur le résultat final, puisqu'elle ne constitue pas une zone importante de conduction du courant.

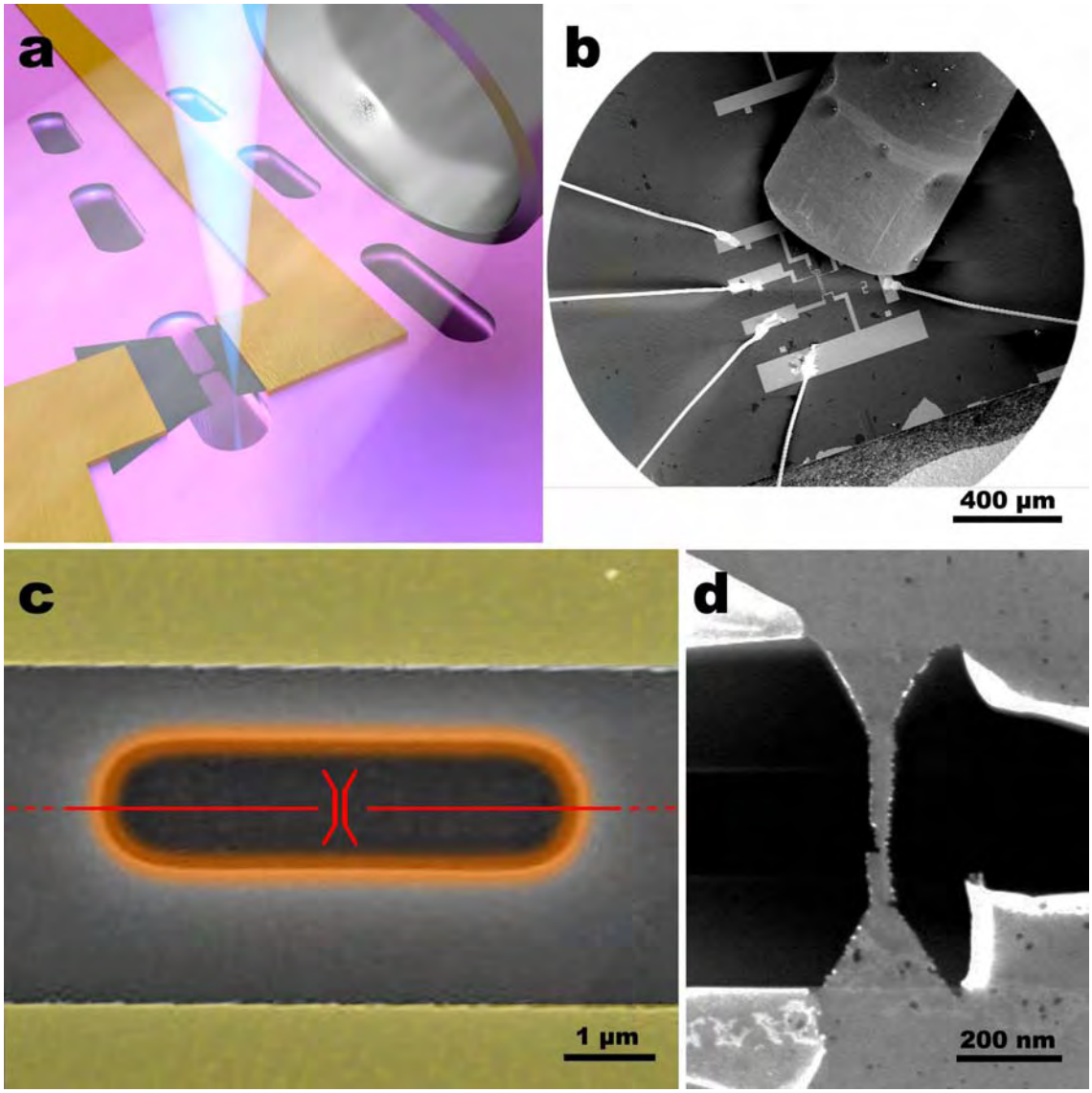


Figure 12 : (a) Diagramme de la gravure de rubans sur échantillons de graphène pseudo-suspendu et contactés sur silice sur silicium dans le SEM. (b) Image électronique de la configuration du microscope lors de la gravure d'un dispositif contacté.

Malgré un grand nombre de substrats préparés, de feuillets contactés et découpés, seulement deux dispositifs remplissaient les bonnes conditions pour être mesurés électriquement (Figure 16). L'un (ruban A) mesure 90 nm de large par 320 nm de long et est composé d'une bicouche (Figure 16a) présentant une résistance à température ambiante de 11,43 kΩ. Le deuxième (ruban B) mesure environ 60 nm par 320 nm et est monocouche, il présente une résistance à température ambiante de 5,4 kΩ. C'est ce dernier qui va permettre la plupart des mesures, ce sont donc les résultats mesurés sur le ruban B qui sont présentés par la suite.

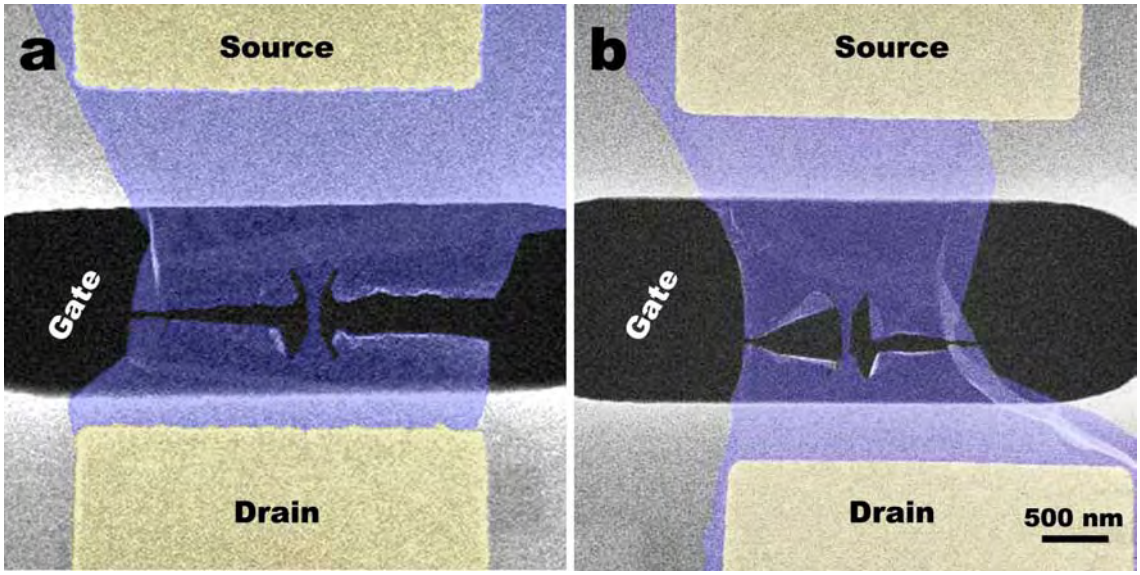


Figure 13: Nanorubans de graphène suspendu et contactés, fabriqués par EBIE à l'oxygène. (a) Ruban bicouche mesurant 90 nm de large par 320 nm de long. (b) Ruban monocouche mesurant 60 nm de large par 320 nm de longueur.

L'échantillon est inséré dans le cryostat et refroidit à 1,4 K. Des mesures I(V) sont enregistrées à différentes températures pendant le refroidissement (Figure 14a). Au fur et à mesure que la température diminue, une non-linéarité apparait. À 1,4 K, la mesure I(V) montre une zone autour de zéro ou la conductance est nulle (Figure 14b). Aucun plateau n'est visible, mais une zone bruitée où la pente est difficile à évaluer, apparaît. L'énergie, qui est représentée par l'espace les deux fortes pentes dans la mesure du courant en échelle logarithmique, est entre 0,5 et 1 meV. L'énergie théorique du gap de confinement pour un ruban de cette taille est de 3 meV. Nous sommes donc dans le même ordre de grandeur. Le fait que la mesure soit inférieure peut être justifié par le fait que la position du niveau de Fermi n'est pas connu à ce stade et donc que la tension de grille n'est pas réglée au niveau du pic de Dirac. L'absence d'un gap de confinement de grande énergie comme vu dans la littérature, peut montrer un régime de transport à haute mobilité sans, ou avec faible, blocage de coulomb, ce qui a déjà été observé dans des nanorubans de graphène produits par d'autres méthodes de gravure.

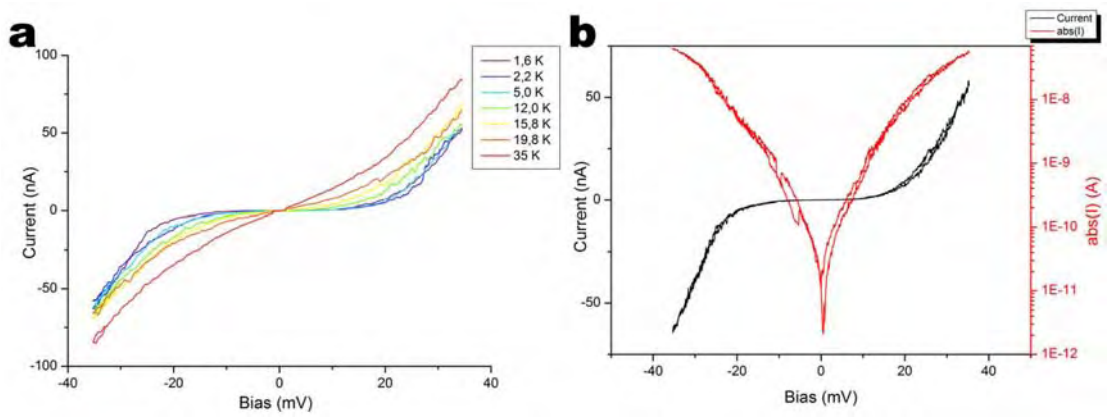


Figure 14 : (a) Mesures de courant en fonction de la tension source-drain à différentes températures pendant le refroidissement. (b) Mesure du courant en fonction de la tension source-drain à 1,4 K tracée en échelle linéaire (noir) ainsi qu'en échelle logarithmique (rouge).

Par ailleurs, les mesures du courant dans le ruban en fonction de la tension de grille arrière avec une tension source-drain constante (V_{SD} = 5 mV) donnent comme résultat une ligne de base en V dont le minimum se situe autour de V_g = 2 V sur laquelle sont superposées des oscillations (Figure 15a). Nous pouvons analyser la pente des deux segments de droite qui forment la ligne de base pour en extraire une valeur de mobilité pour les trous et les électrons. Les valeurs calculées tiennent compte d'un facteur d'efficacité réduite de la grille dû au manque de silicium sous le ruban, ce qui limite le potentiel électrique induit sur l'objet (Figure 15b). Les valeurs ainsi calculées donnent une mobilité de $\mu_{FET,e}$ = 3353 cm^2/Vs pour les électrons et de $\mu_{FET,h}$ = 8247 cm^2/Vs pour les trous. Ces valeurs sont calculées par le biais d'une approximation négligeant les parois de la piscine dans le calcul de la capacitance grille-ruban.

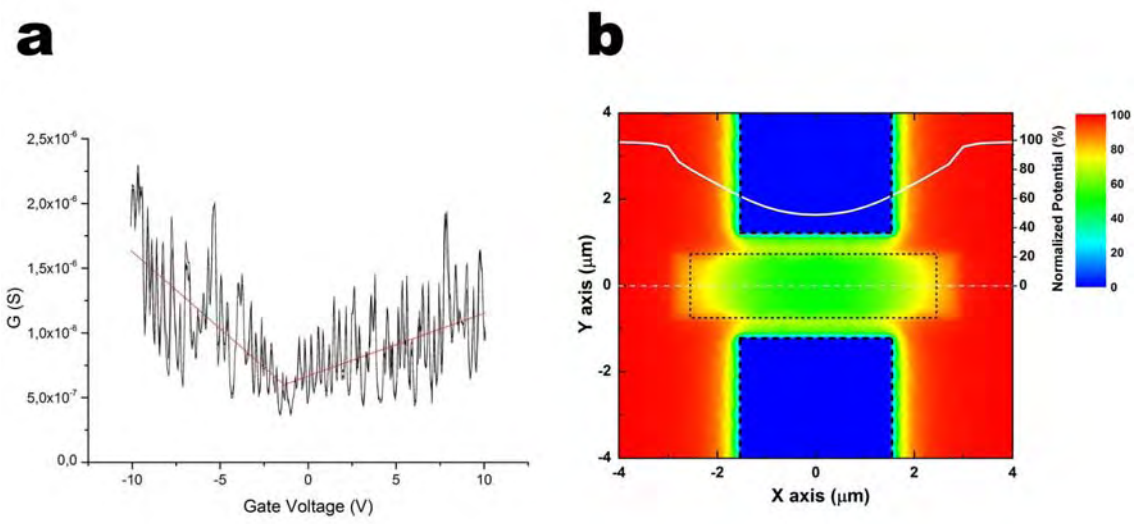


Figure 15 : (a) Mesure de la conductance en fonction de la tension de grille arrière avec une tension source-drain constante de 5 mV. (b) Simulation du potentiel électrique induit par la grille arrière à la surface de la silice (rouge : silice, jaune/vert : piscine, bleu : électrodes), superposé en blanc du tracé du potentiel sur l'axe y=0.

De leur côté, les oscillations peuvent être la signature de diamants de faible conductance qui indiqueraient un phénomène de blocage de Coulomb dans le ruban. Les creux de conductance sont en effet plus larges sur les mesures à 5 mV que sur les mesures faites à 20 mV de tension source-drain (Figure 16a). Il n'a pas été possible de réaliser la mesure complète du diagramme de conduction en fonction de la tension de grille et de la tension source-drain, nous avons donc procédé à une extrapolation de ces deux mesures afin d'en extraire des coordonnées approximatives de la position des diamants (Figure 16b). De la taille en V_{DS} de ces diamants peut être extraite une taille de dot à l'origine du blocage de Coulomb. D'après les calculs, la taille des îlots de graphène se situe entre 50 et 180 nm de long sur 60 nm de largeur. Ceci implique qu'il y ait environ 6 barrières tout le long du ruban.

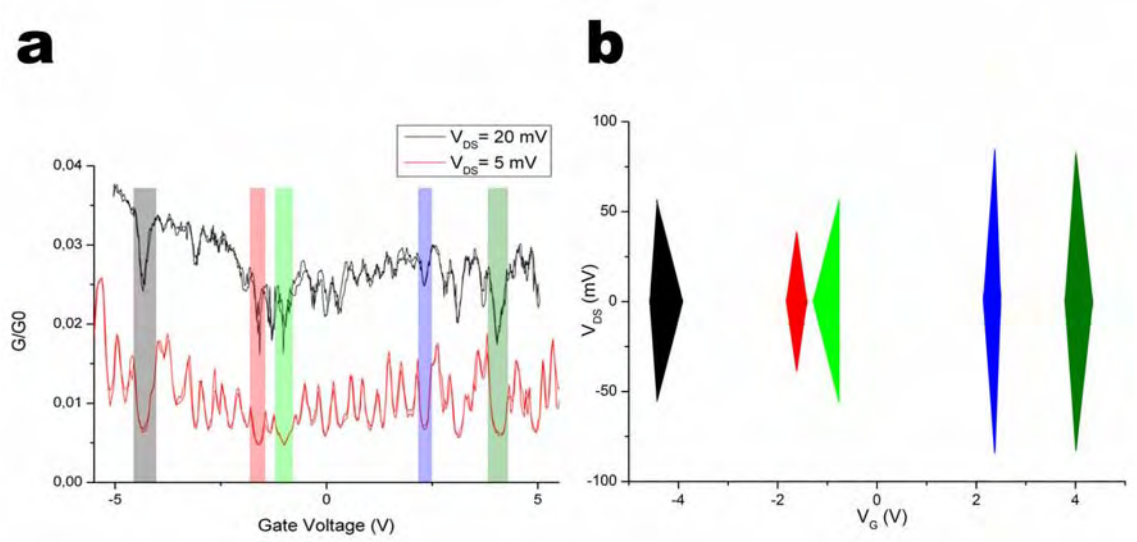


Figure 16 : (a) Mesures de conductance en fonction de la tension de grille à 5 et 20 mV de tension source-drain. (b) Diagramme des diamants de faible conductance extrapolé à partir des deux mesures en (a).

Nous observons également l'évolution de la conductance lorsqu'on applique un champ magnétique perpendiculaire au ruban. À bias constant, la conductance du ruban augmente avec le champ magnétique (Figure 17a). Cette magnéto-conductance positive indique que le ruban conduit mieux lorsque le champ magnétique est fort et que les porteurs de charge sont plaqués contre les bords du ruban. Les bords du ruban sont donc de bonne qualité. Le fait que la conductance augmente indique que les porteurs de charge rencontrent moins de défauts. De plus, la mesure faite à V_{DS} = 10 mV montre des oscillations se produisant avec une forme symétrique à -5 et 5 T. Étant donnés l'énergie et le champ appliqué pour leur observation, nous interprétons ces oscillations comme des oscillations de Shubnikov de Haas provoquées par le passage d'un niveau de Landau devant le niveau de Fermi lors du balayage en champ. Ces oscillations ne sont observables

que dans le cas d'un échantillon à haute mobilité. Ces résultats confirment les calculs faits précédemment ainsi que les observations TEM.

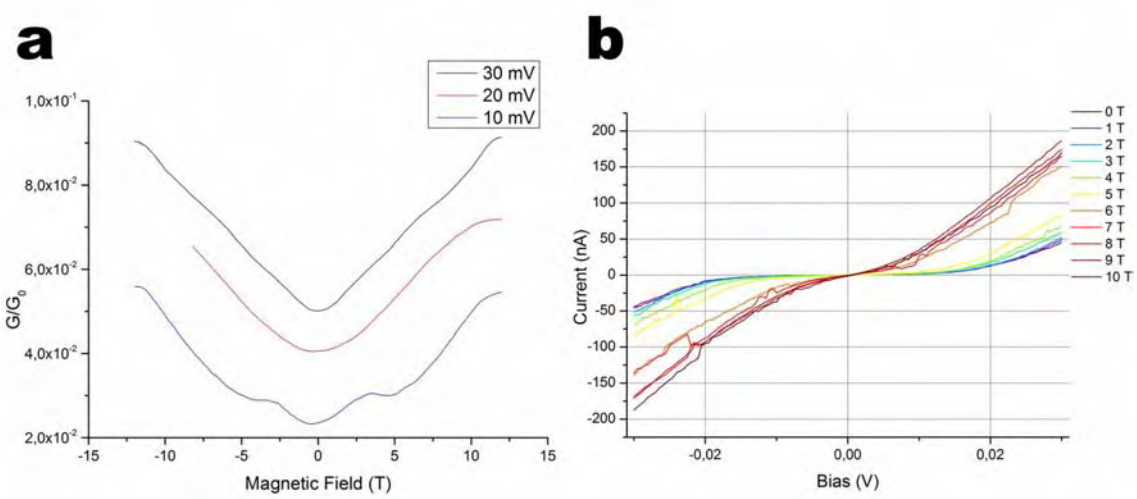


Figure 17 : (a) Mesures de la conductance en balayage en champ magnétique à tensions source-drain constantes. (b) Mesures du courant en fonction de la tension source-drain à différentes valeurs du champ magnétique.

Les mesures des caractéristiques I(V) en présence d'un champ magnétique constant montrent un affaiblissement de la non-linéarité avec l'augmentation du champ magnétique. Celui-ci agit comme un apport d'énergie au système donnant un résultat similaire à une augmentation de température.

Chapitre 5 : Étude du graphène et de rubans de graphène par microscopie STM 4 pointes sous UHV

Le cas idéal de sondage des propriétés d'un ruban de graphène est celui dans lequel aucune résine n'est utilisée pour le contact électrique, dans un environnement en ultra-haut vide, à basse température, dans un appareil capable à la fois de sonder les caractéristiques structurales et les propriétés de transport électronique et dans lequel un recuit de l'échantillon dans l'ultra-haut vide est possible. Ces cinq critères peuvent être réunis par l'utilisation d'un microscope à effet tunnel multisondes dans l'ultra-haut vide. Dans cette partie, nous décrivons les résultats obtenus par l'analyse d'échantillons de graphène CVD sur grille TEM et substrats de silicium dans le microscope Omicron 4-probe UHV-STM de l'IEMN à Lille. Cette étude va laisser de côté les basses températures pour se consacrer à deux points : l'analyse de l'évolution de l'échantillon sous un faisceau SEM en ultra-haut vide, et la faisabilité de l'analyse du transport électronique à travers un dispositif de graphène gravé par EBIE à l'oxygène.

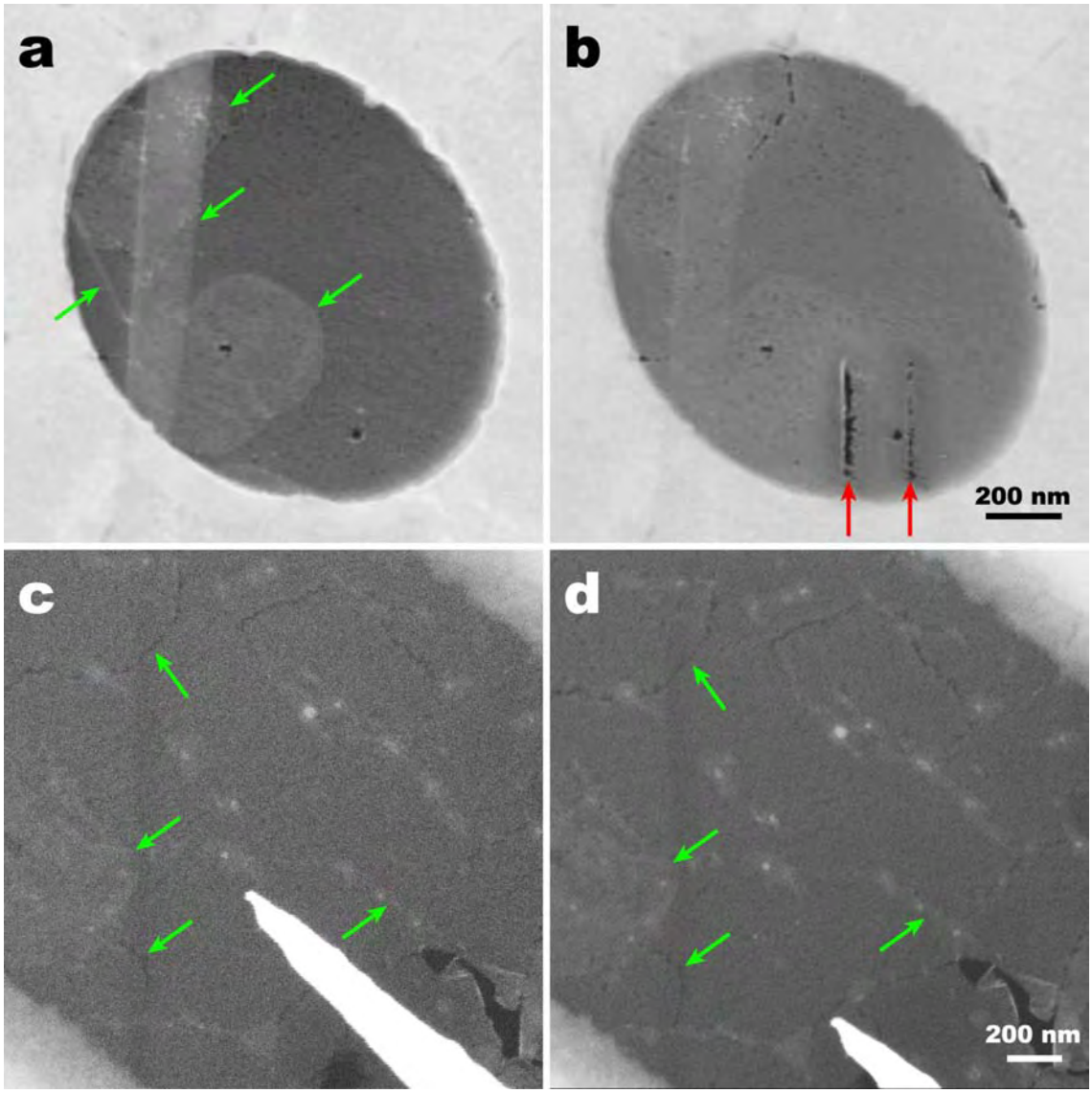


Figure 18 : (a) Image SEM de graphène suspendu (première irradiation) à P= 10^{-7} mbar. (b) Même zone imagée en (a) après une irradiation de D_1 = 7,86 10^{-9} C/µm². (c) Image SEM (première irradiation) de graphène suspendu à P= 10^{-10} mbar. (d) Même zone qu'en (c) imagée après une irradiation de dose D_2 = 6,07 10^{-8} C/µm²

Comme nous l'avons remarqué dans les chapitres précédents, l'irradiation par électrons dans un vide secondaire n'est pas anodine. En effet, cela provoque un dépôt de carbone amorphe qui contamine la surface du graphène (Figure 18a et b). En revanche, l'irradiation par électrons dans l'ultra-haut vide, même à dose et durée prolongées ne semblent avoir aucun impact sur la propreté du matériau et tous les détails sont parfaitement visibles (Figure 18c et d).

Par ailleurs, il est possible *in situ* de mettre en place un recuit électrique au moyen des sondes STM. Celles-ci placées au contact du matériau, nous pouvons nous en servir pour établir un bias qui va provoquer un courant à travers l'échantillon en le chauffant par effet Joule (Figure 19a).

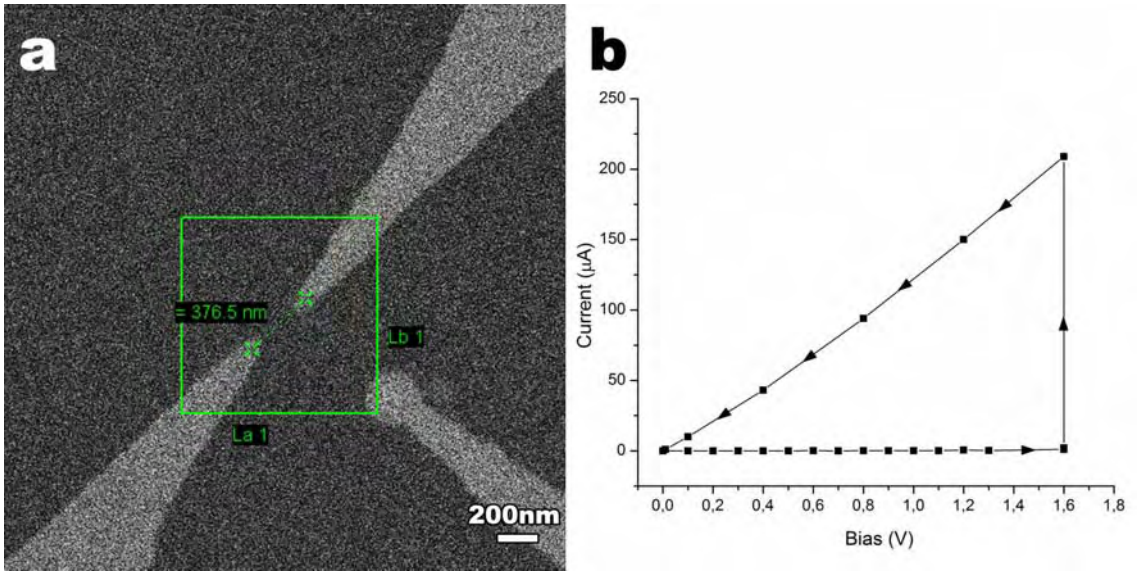


Figure 19 : (a) Image SEM de l'expérience de recuit électrique entre deux pointes séparées de 377 nm. (b) Parcours en tension/courant parcouru lors du recuit. La montée et la descente s'effectuent selon une rampe de quelques centaines de millivolts par minute et la tension maximale est maintenue pendant 10 min.

Dans le cas d'un échantillon contaminé, le courant initialement très faible et non linéaire par rapport à la tension va progressivement augmenter lors du recuit à tension constante, pour ensuite saturer. La redescente révèle ensuite un comportement linéaire typique d'un matériau ohmique (Figure 19b).

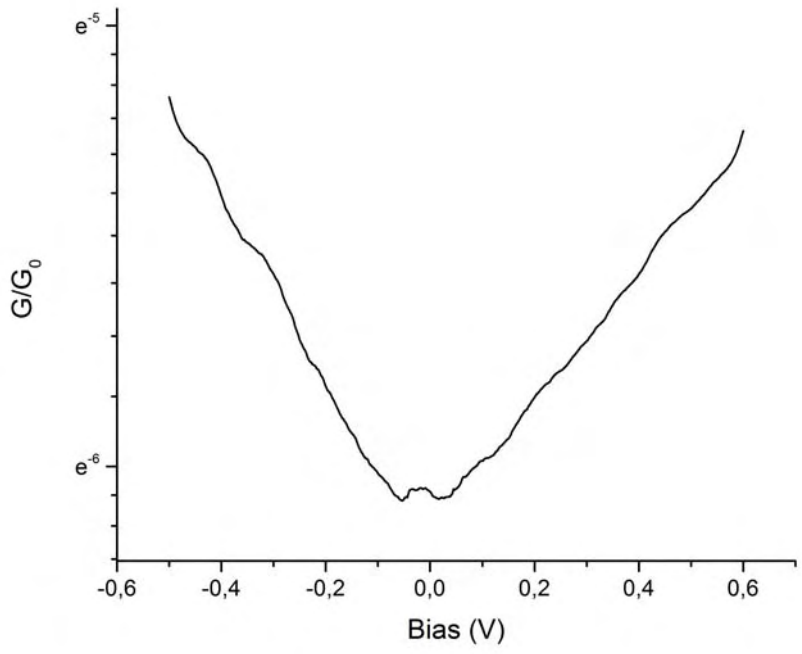


Figure 20 : Mesure de conductance en fonction du bias en échelle logarithmique

Nous nous intéressons maintenant à l'analyse d'une croix de graphène fabriquée par EBIE à l'oxygène. Le motif est intéressant dans notre cas car cela nous permet de mesurer l'effet des constrictions sans besoin d'isoler les deux bouts d'un ruban. Le motif utilisé correspond à deux rubans perpendiculaires (Figure 21a). L'objet est imagé à la fois par STM et par SEM (respectivement Figure 21b et c) afin de positionner les pointes pour les mesures désirées. Une première mesure entre (4) et (2) est réalisée afin d'avoir une référence et est présentée sur la Figure 19. Le résultat est une pente exponentielle que nous attribuons à des barrières Schottky entre les pointes et le graphène et qui sont provoquées par la contamination par des hydrocarbures.

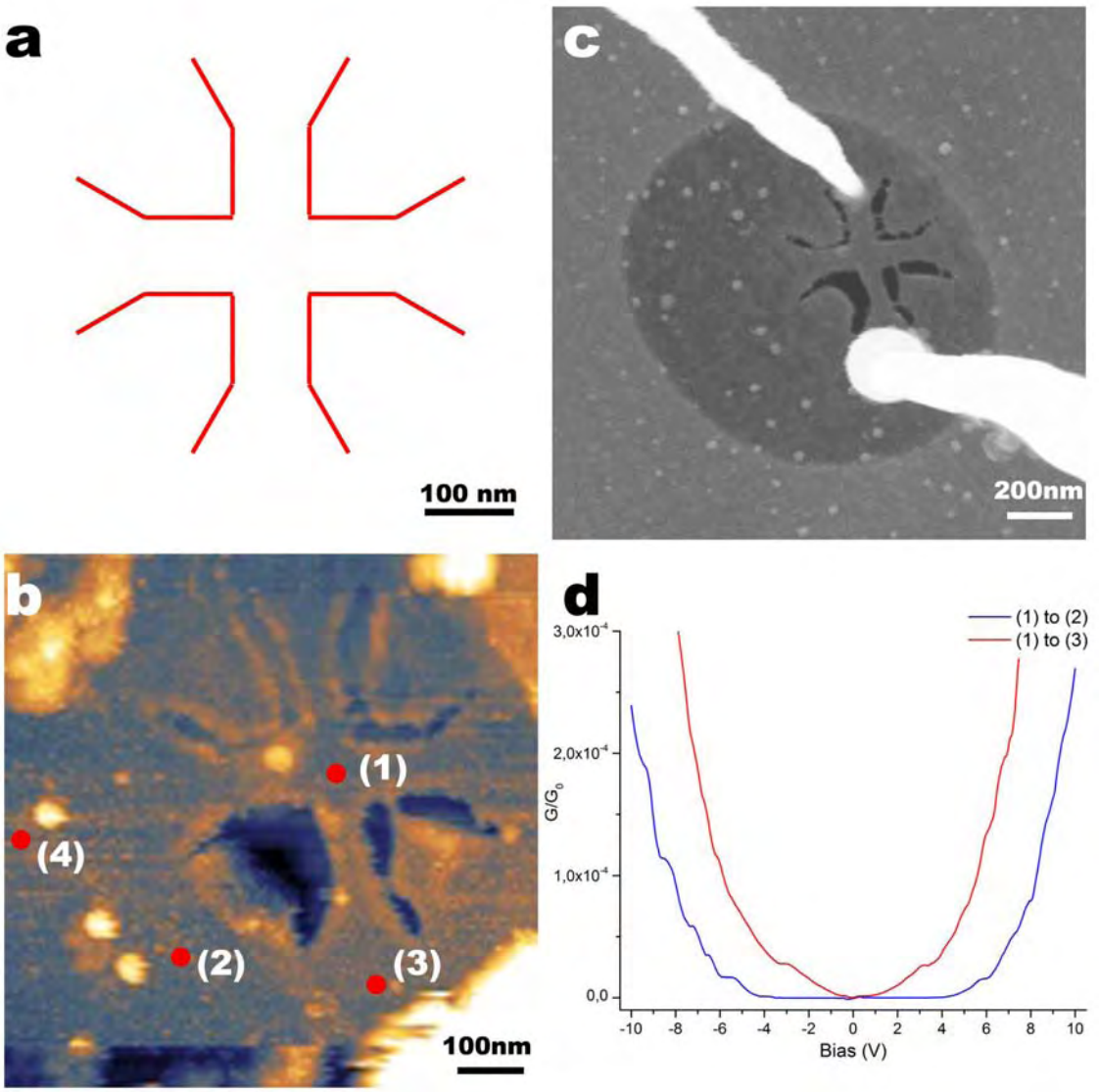


Figure 21 : (a) Motif utilisé pour la gravure EBIE à l'oxygène de la croix de graphène. Chaque bras mesure 90 nm de large par 100 nm de longueur. (b) Image STM de l'objet. (c) Image SEM de la croix et de l'approche des sondes. (d) Tracé des deux mesures de conductance en fonction de la tension pointe à pointe entre les points (1) et (2) en bleu et (1) et (3) en rouge de l'image (c).

Sur la croix, deux mesures sont faites. La première dont la conductance en fonction du bias est tracée en rouge sur la Figure 21d, correspond à la mesure entre (1) et (3). Nous approximons cette mesure à celle d'un simple ruban de 90 nm de large par 100 nm de long. Une annulation de la conductance est observée à bias nul. Aucun gap n'est observable à ce stade. La théorie prédit pour cette taille un gap de 2,2 meV, donc même s'il était présent, il ne serait pas visible à cause de la résolution de cette mesure. Par ailleurs, la mesure (1)-(2) tracée en bleu sur la Figure 21d montre un plateau de conductance nulle, très large comparée aux valeurs d'énergie de gap attendues pour un système de ces dimensions-là. Le plateau s'étend de -4 à 4 V de bias. Cette mesure peut être assimilée à une mesure de deux rubans en parallèle, ce qui devrait avoir comme résultat une résistance plus faible que lors de la mesure d'un seul ruban. Afin d'expliquer cela, nous avançons l'hypothèse suivante : étant donnée la géométrie de l'objet, le point de mesure (2) se trouverait, à une certaine plage de bias, soit dans une zone d'interférences destructrices provoquées par deux ondes électroniques en provenance des deux rubans, soit dans une zone d'ombre induite par la croix, ou soit dans une zone combinant les deux phénomènes.

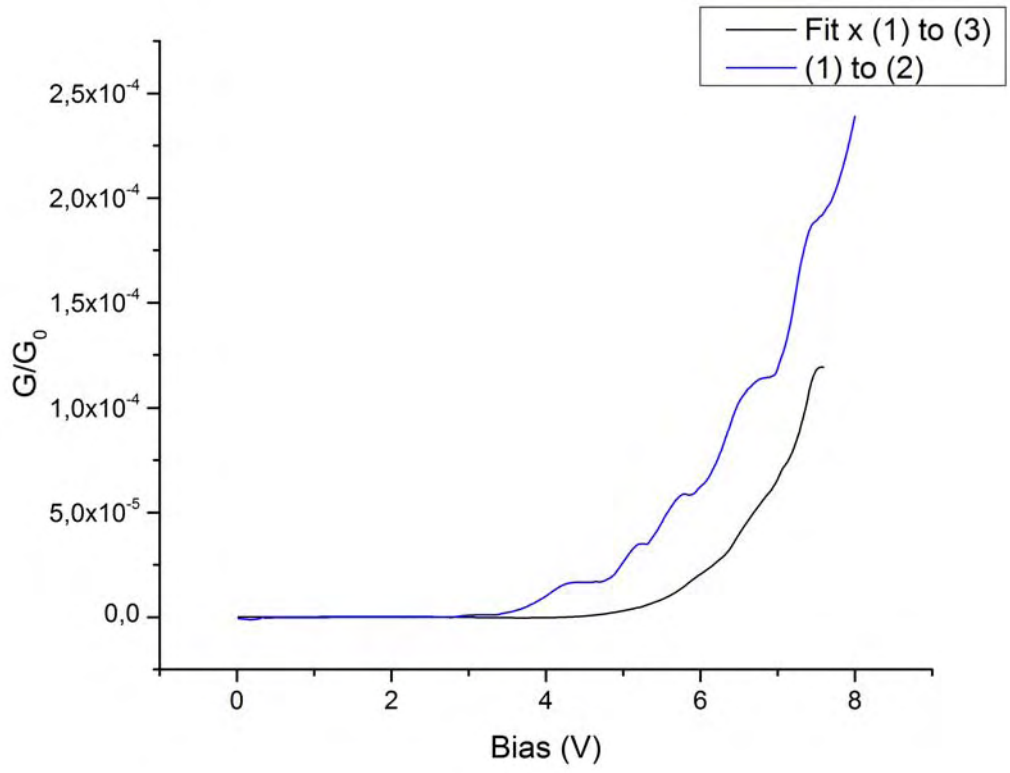


Figure 22 : Tracé comparatif de la mesure (bleu) des deux rubans de la croix et la mesure d'un seul bras convolué par les résultats de simulation d'interférences électroniques dans un milieu de géométrie similaire.

Nous effectuons donc des simulations de propagation électronique dans un milieu ayant une géométrie semblable à celle de la croix mesurée. Cette simulation nous permet d'extraire le ratio de l'intensité au niveau de la sonde placée en (2). La Figure 22 montre une comparaison entre la mesure (1)-(2) et la mesure (1)-(3) convoluée par les résultats de la simulation d'interférences électroniques. Les deux courbes présentent de grandes similarités. Une zone similaire d'occlusion du signal apparaît dans la simulation.

De plus amples analyses et des simulations plus précises et affinées sont nécessaires pour confirmer ou infirmer cette hypothèse. Cependant, ce résultat est encourageant et peut être encore un signe supplémentaire de la bonne qualité des objets produits en particulier sur des grilles TEM, comme cela fut prouvé déjà par l'analyse par microscopie TEM.

Conclusion

Dans ce travail de thèse, nous avons mis en place une technique de découpe de graphène combinée au pilotage d'un faisceau électronique et à l'activation d'une réaction chimique induisant la découpe. Les motifs de gravure sont ainsi arbitraires. Les analyses par la microscopie électronique en transmission à résolution atomique ont révélé des rubans cristallins, sans amorphisation et des bords droits, à très faible rugosité, et orientés selon des directions cristallines.

La technique de découpe a été transposée avec succès à des échantillons de graphène contacté pseudo-suspendu sur des piscines profondes creusées sur des substrats de silice sur silicium adaptés aux mesures de cryo magnéto-transport électronique. Deux rubans ont été mesurés, dont l'un de 60 nm de large, a révélé une forte non-linéarité avec la possibilité d'un gap en accord avec les prévisions théoriques. Les mesures en présence de tension de grille indiquent une mobilité importante à travers le ruban pouvant aller jusqu'à $\mu_{FET,h}$ = 8247 cm^2/Vs. Par ailleurs, des oscillations pouvant provenir d'un blocage de Coulomb indiqueraient la présence d'environ 6 barrières physiques le long du ruban car elles ne peuvent pas être attribuées à l'influence du substrat dans notre cas. Le magnéto transport contribue à prouver la bonne qualité des bords avec une conductance plus élevée lors du confinement du courant le long de ces derniers. De plus, des oscillations en champ magnétique très proches de la position des niveaux de Landau peuvent être attribuées à des oscillation de Shubnikov de Haas et donc à un régime de transport à forte mobilité.

En outre, les expériences de microscopie multisondes en ultra-haut vide ouvrent la voie à une nouvelle méthodologie d'analyse de ces objets, plus propre, évitant la lithographie et permettant de mesurer un grand nombre d'objets sur un même échantillon. Un autre microscope plus performant et permettant les mesures à basse température est déjà utilisé afin de poursuivre ces analyses.

Nanogravure et caractérisation structurale et électronique de rubans de graphène cristallins

Les principaux objectifs de cette thèse sont la fabrication et la caractérisation structurale à haute résolution de nanorubans de graphène à bords atomiquement lisses ainsi que leur intégration dans des composants et l'étude du transport électronique.

En premier lieu, nous montrons que des nanorubans de graphène cristallins de largeur inférieure à 100 nm et avec des qualités structurales supérieures l'état de l'art peuvent être découpé par un faisceau électronique focalisé d'énergie modérée en présence d'oxygène. Les caractéristiques des rubans obtenus sont également supérieures à l'approche précédente utilisant la vapeur d'eau.

Dans un deuxième temps, la structure des nanorubans est caractérisée jusqu'à l'échelle atomique par microscopie électronique en transmission corrigée des aberrations sphériques. Nous montrons que la cristallinité des nanorubans, tant en leur centre que le long des bords de découpe, est préservée. Les performances de notre approche atteignent l'état de l'art et sa reproductibilité permet de fabriquer des rubans longs de plusieurs centaines de nanomètres mais de largeur aussi fine que 16 nm.

Ensuite, nous avons transposé la découpe de nanoruban suspendus à une configuration partiellement suspendue sur substrat SiO_2/Si permettant de les intégrer dans des composants adaptés aux mesures de transport électronique à basse température et sous champ magnétique. Le transport électronique dans les rubans contactés de 60 x 300 nm présente un gap et des oscillations en balayage de grille arrière qui sont en accord avec un mécanisme de blocage de Coulomb dans un domaine de taille de l'ordre de la taille du ruban. Si ces résultats montrent la persistance de barrières tunnel, ses bords semblent de qualité suffisante pour ne pas induire de confinement supplémentaire.

Au-delà des composants mésoscopiques, notre méthode de fabrication des rubans par gravure électronique sous oxygène ouvre des perspectives dans deux domaines en émergence. Elle est compatible avec l'ultravide et parfaitement adaptée au développement d'une technologie atomique à base de graphène. Une caractérisation de la contamination du graphène ainsi qu'une caractérisation électrique de dispositifs de graphène qui a été fait par microscopie à effet tunnel multisonde en ultra vide.

Enfin, les rubans de graphène que nous produisons ont les dimensions et qualités structurales requises pour observer un comportement plasmonique du graphène dans le visible et ainsi interagir avec des structures plasmoniques métalliques. Ce couplage a été examiné en étudiant le signal Raman du graphène au voisinage de colloïdes d'or.

Mots clés : graphène, gravure induite par faisceau électronique, microscopie électronique en transmission, cryo-magnéto-transport, spectroscopie Raman, plasmonique, ultra vide, microscopie à effet tunnel.

Nanoetching and structural and electronic characterisation of crystalline graphene ribbons

The main objectives of this thesis are the fabrication and high-resolution structural characterisation of graphene nanoribbons with atomically smooth edges as well as their device integration and electronic transport study.

In first place, we show that crystalline graphene nanoribbons with width under 100 nm and structural properties better than the state of the art can be patterned by a focused electron beam in presence of oxygen. The structural characteristics of the ribbons are also better than the old process using water vapour.

Secondly, nanoribbons structure is characterized down to the atomic scale by spherical aberration corrected transmission electron microscopy. We show that the nanoribbons crystallinity, of the centre as well as along the cut edges, is preserved. The performance of our process reaches the state of the art and its reproducibility allows to produce ribbons with length of hundreds of nanometer but as narrow as 16 nm.

After that, we have transposed the suspended nanoribbon etching to a partially suspended configuration on a SiO_2/Si substrate allowing the integration in devices suitable for electronic transport measurements at low temperature and under magnetic field. The electronic transport in contacted ribbons of 60x300 nm shows a gap and oscillations on backgate scanning measurements that are in agreement with a Coulomb blockade mechanism with dot sizes in the range of the ribbon surface. Even though those results show the persistence of tunnel barriers, the edges quality look good enough to avoid additional confinement.

Other than mesoscopic devices, our ribbon fabrication process by electronic beam under oxygen atmosphere opens perspectives in two emergent fields. The process is ultra high vacuum compatible and perfectly adapted to the development of an atomic graphene based technology. A characterisation of contaminants of graphene samples as well as electrical characterisation of graphene devices has been performed in a multiprobe scanning tunnelling microscope in ultra high vacuum.

Finally, our graphene nanoribbons have the right dimensions and structural qualities required for the observation of plasmonic behaviour of graphene in visible light and so interact with metallic plasmonic structures. This coupling has been analysed by studying the Raman signal of graphene at the close environment of gold colloids.

Keywords : graphene, e-beam induced etching, transmission electron microscopy, cryo-magneto transport, Raman spectroscopy, plasmonics, ultra-high vacuum, scanning tunneling microscopy.